METHODOLOGIES FOR AUTOMATED MICROASSEMBLY

by

MOHAMMAD A. MAYYAS

Presented to the Faculty of the Graduate School of

The University of Texas at Arlington in Partial Fulfillment

of the Requirements

for the Degree of

DOCTOR OF PHILOSOPHY

THE UNIVERSITY OF TEXAS AT ARLINGTON

December 2007

Copyright © by Mohammad A. Mayyas 2007

All Rights Reserved

ACKNOWLEDGEMENTS

I would like to express my gratitude to all those who gave me the possibility to complete this Dissertation. I am deeply indebted to my supervisor *Prof. Panos S. Shiakolas* from the Mechanical & Aerospace Engineering Department, whose help, stimulating suggestions and encouragement helped me during the research and writing of this dissertation. I would like to gratefully and sincerely thank *Prof. Harry Stephanou*, the director of the *Automation & Robotics Research Institute* (*ARRI*), for his guidance and support. His visionary leadership and wisdom have always enlightened my intellectual progress through out my research activities.

My special thanks go to my wonderful advising committee, *Prof. A. Haji-Sheikh, Prof. Kamesh Subbarao* and *Dr. Woo Ho Lee.* Particularly, I am indebted to Dr. Lee whose support allowed me to work on state of the art research projects. I would like to acknowledge many people for helping me during my doctoral work, *Prof. Dan Popa, Dr. Jeongsik Sin, Dr. Raul Fernandez* and the wonderful *staff at ARRI.*

My acknowledgement goes also to *Hashemite University* for their continuous support during my higher education, particularly my colleagues in the *department of Mechatronics*. Certainly I am thankful to my friends with whom I share several pages of successes, *Hussam Al-Shammari, Iyad Al-Falujah, Murad Abu-Khalaf, Ayman AL-Rowashdeah, Mahmod Smadi, Nitin Appal,* and the list goes on.

This dissertation would not have been possible without the support of my *parents*. I am thankful to my wonderful sisters *Arwa, Ghada, Sawsan, Andaleeb, Fadia and Redab* and my brothers *Khaled and Feras*. Their encouragement advanced me forward following the footsteps of success.

November 4, 2007

ABSTRACT

METHODOLOGIES FOR AUTOMATED MICROASSEMBLY

Publication No. ______

Mohammad A. Mayyas, PhD.

The University of Texas at Arlington, 2007

Supervising Professor: Dr. Panos S. Shiakolas

The development of micromachining technologies has provided wide applications in micro sensing and actuation. However, most of the demonstrated devices are selectively constructed by fabrication processes that are limited to complexity, configuration, dimension, and material variation. The monolithic fabrication has limitations and does not allow the inclusion of multiple components of incompatible processes. Therefore, the construction of 3D microstructures by heterogeneous microassembly is an alternate manufacturing route. In deterministic, monitored or

controlled microassembly there has been considerable research in developing, analyzing and applying distributed algorithms for sensor and sensorless based assembly processes. Meso-scale teleoperated work-cells supported by Nano manipulators have been under development for two decades. This research focused on developing end-effectors which possess broader capabilities and yet based on reliable actuation principles. Specifically, different practical scenarios where the previous researchers have not addressed the design platforms for assembly and actuation conditions are considered. Thus, this research will aim at improving the performance of related MEMS devices through mathematical modeling and numerical simulations by coupling a range of electrothermal building blocks on deterministic serial to parallel microassembly, distributed manipulation and/or hybrid microassembly. However, these process are generally slow, complicated and require expensive equipments. Alternative methods for constructing and actuating 2½D to 3D microrobotic systems are emerging. The spontaneous assembly of 2½D micro-parts to form aggregate robotic structures will be examined. The locomotion of such constructed structures requires broader methodologies in actuation methods including concepts borrowed from physics, biology and chemistry. A promising platform is based on controlled microorganism for inexpensive and reliable sensing and actuation. The implementation of such actuation concept in the construction of micro-robotic systems, such as micro-pump is examined. Finally, methodologies for monolithic and selective detethering of micro-meso-parts that are vital for presenting massive blocks during assembly processes are introduced.

TABLE OF CONTENTS

ACKNOWLEDGEMENTS.......... iii

ABSTRACT v

LIST OF ILLUSTRATIONS.......... xv

LIST OF TABLES.......... xxi

Chapter

1. INTRODUCTION 1

1.1 Overview.......... 1

1.2 Motivation.......... 3

1.3 Contributions… 7

1.4 Summary.......... 12

1.5 Intellectual Merit and Broader Impact.......... 16

1.6 Applications.......... 17

1.7 Impacted Fields.......... 18

2. MICROASSEMBLY METHODOLGIES: SURVEY AND EXTENDED CONCEPTS.......... 19

2.1 Introduction.......... 19

2.2 Classification of Manipulations, Actuation and Assembly Techniques 21

2.3 Small Scale Manipulators as an Emerging Technology.......... 24

2.4 Dissertation Related Arts... 26

2.5 Modern Classification of Microassembly Methods 29

2.5.1 Deterministic Assembly 30

2.5.1.1 Parallel Assembly 31

2.5.1.2 Serial Assembly… 31

2.5.2 Stochastic Assembly 35

2.5.2.1 Self-assembly 36

2.5.3 Distributed Manipulation 38

2.6 Proposed Methodologies for Micro-Distributed Manipulation Systems (μDMS) for Assembly Process ……………..... 40

2.6.1 Proposed Definitions of (μDMS) 42

2.6.2 Proposed Definitions Based on Energy Methodology 43

2.6.2.1 Problem Formulation 45

2.6.2.2 Optimization Objectives 45

2.6.2.3 Assessment of μDMS Actuation Methods 46

2.6.2.4 Proposed Examples on μDMS 48

2.7 Chapter Summary …... 54

3. SERIAL TO HYBRID MICROASSEMBLY SYSTEMS ASSISTED BY IDENTIFICATION OF MULTI-PURPOSE ELECTRO-THERMO-ELASTIC GRIPPERS (METEG) … 55

3.1 Introduction 55

3.2 Design and Fabrication of METEG 56

3.2.1 Basic Building Blocks and Integration for Improved Assembly Capabilities.. 57

3.3.2 Methods for Attaching METEG 62

3.3.3 Process Based Powering of METEG 64

3.3.4 An Extended Teleoperated Work-cells for METEG Application..…………………………………... 66

3.3.5 Microassembly Applications Improvement Using METEG……………………….………. 68

3.4 Methodologies for Experimental Identification of METEG………….. 73

3.4.1 Electrothermoelastic Dynamic Response Identification of METEG…………………………………… 73

3.4.2 Static and Dynamic Structural Identification of METEG…...……………………………...…………… 75

3.4.2.1 Importance of Structural Modeling of a METEG in Assembly Process…………….. 76

3.4.2.2 Microassembly Work-cells Setup Based on Integrated METEG …..…………..………….. 78

3.4.2.3 The Deep Reactive Ion Etching of the Tested METEG …………….………….. 79

3.4.2.4 Static Structural Characterization of METEG……………………………………… 80

3.4.2.5 Dynamic Structural Characterization of METEG………………………..…………. 87

3.5 Further Considerations on Improving METEG…...……..…………….. 94

3.6 Summary and Conclusions……………….……………………………. 96

4. THERMAL MODELING AND PERFORMANCE ANALYSIS OF METEG COMPONENTS … 99

4.1 Introduction 99

4.2 Steady State Thermal Analysis of METEG Component. 101

4.2.1 U-Folded Beam "Heatuator" and V-Shape Beam "Chevron". 101

4.2.1.1 Theoretical Model 102

4.2.1.2 Numerical Comparison for V-Shape Actuator 108

4.2.1.3 Numerical Comparison for U-Shape Actuator 110

4.2.1.4 Thermal and Structural Failures 112

4.2.1.5 Experimental Observation on Actuators Failures 114

4.2.1.6 Summary of Steady State Thermal Analysis Method for METEG Blocks ………………. 117

4.2.2 Combined Blocks "Microgripper" 117

4.2.2.1 Theoretical Model 120

4.2.2.2 General Electrothermal Heat Conduction Equation 122

4.2.2.3 Steady State Heat Conduction Equation (S.S.H.C.E) 124

4.2.2.4 Simulation and Discussions 130

4.3 Thermal Cycle Analysis of U-(Folded beam) & V- (Chevron) Blocks 134

4.3.1 Transient H.C.E of Folded Beam Actuator 137

4.3.1.1 Charging Time Synthesis Using Trial Solution Method 137

4.3.1.2 Discharging Time from Steady State Conditions 145

4.3.2 Verification Methodologies of the Proposed Theories 148

4.3.2.1 SOI, PolyMUMPS and FLM Folded Beams Actuators.. 149

4.3.2.2 Verification of Trial Solution Method Using Finite Difference Approximation (FDA)................... 151

4.3.2.3 Verification of trial Solution Method for V-Shape Actuator 152

4.3.2.4 Verification of Lumped System Model Using Finite Element Modeling (FEM) 155

4.3.2.5 Charging and Discharging Time Simulations............ 157

4.3.2.6 Charging Simulation: Thermal Actuator with Beams of Uniform Widths................................. 158

4.3.2.7 Charging and Discharging Simulations: Temperature Responses of Thermal Folded Beam Actuator Using FDA and Lumped Model 161

4.3.2.8 Discharging Simulation: Temperature response of SOI Folded Beam Actuator Using FEM and Approximate Solution................................ 164

4.3.4 Relationship between Measured Mechanical and Approximated Thermal Cycle Responses 165

4.3.5 Discussion of Performance Analysis 171

4.3.6 Summary of Transient Analysis Methods 175

4.4 Chapter Conclusions 176

5. SELF-ASSEMBLY AND PARALLEL MANIPULATION OF MICRO SYSTEMS 178

5.1 Introduction 178

5.2 Self-assembly Assisted by Adhesive Forces (Microphysics) 180

5.3 Construction of 2½ D Structure: Principle of Self-assembly 181

5.4 Self-assembly Strategies for Non-conventional Actuation and Translocation of Micro-structures 184

5.4.1 Micro-robotic Assisted by Bacterial Translocation 186

5.4.2 Micro-robotic System Based on Micro Biological Organism 190

5.4.3 Bio-Micropump (BMP) 191

5.5 Feasibility Studies on Self-assembly 196

5.5.1 Method Requirements 196

5.5.2 Concept of Self-assembly Assisted by Agitation 198

5.5.3 Self assembly Based on DNA Recognition and Assisted by Wet and Dry Agitation 202

5.6 Chapter Summary and Conclusions 210

6. SELECTIVE AND MONOLITHIC DETETHERING METHOD FOR MESO- MICRO DEVICES 212

6.1 Introduction 212

6.2 Method Contributions 214

6.3 Applications for the Method 217

6.4 Description of the Method 219

6.4.1 General Concept of the Detethering Method 219

6.4.2 Vibratory Agitation System 224

6.4.3 Monolithic Detethering Concept 225

6.4.4 Selective Detethering Concept 226

6.4.5 Notes on Other Applications of Detethering 228

6.4.6 Summary of the Method 230

6.5 Design and Verification Methods 231

6.5.1 Experimental Feasibly Studies 232

6.5.2 Numerical Simulations 234

6.5.2.1 Modal Analysis... 235

6.5.2.2 Harmonic Analysis 236

6.5.2.3 Monolithic Detethering Using Harmonic Analysis for Array of Complex Devices ………….. 241

6.5.2.4 Monolithic and Selective Detethering Using Harmonic Analysis for Array of Complex Devices .. ……………………………….. 243

6.5.3 Mathematical Considerations for the Bending Vibration of Clamped-free Beams under Agitation …………………………………… 245

6.5.4 Lumped Modeling of Vibrating Cells in a Vibratory System.. 249

6.6 Chapter Conclusions 252

7. CONCLUSIONS AND FUTURE WORK….. 253

7.1 Dissertation Summary and Conclusions 253

7.2 Future Work 256

Appendix

A. MICROPHYSICS AT MICROSCALE 258

REFERENCES 266

BIOGRAPHICAL INFORMATION.. 285

LIST OF ILLUSTRATIONS

Figure Page

2.1 Proposed design flow diagram for
conventional MEMS development.. 41

2.2 Proposed μDMS based on agitation....49

2.3 Proposed μDMS based on micro elastic support... 50

3.1 Integrated electrothermal microgrippers.....58

3.2 Design and test analogy of the thermal gripper... 59

3.3 Optical microscopic image of an actuated micro-heater....60

3.4 Novel design of electrothermal actuator of integrated
microgripper, micro-heater and embedded strain sensor... 61

3.5 Calibration curve of the highly doped strain gauge that
is measured at room temperature... 62

3.6 Miscellaneous electrothermal MEMS devices....63

3.7 Suggested adapter for interfacing METEG
device to 3D microassembly stations 64

3.8 Extended microassembly system that is upgraded and configured
for serial to hybrid assembly applications.. 67

3.9 Sequential microassembly performed on MEMS die. 68

3.10 Active and passive gripping.....69

3.11 Active microassembly of 3D structure. 70

3.12 Hybrid to parallel microassembly.....71

3.13 Suggested arrangement of multiple METEG actuators performing parallel assembly 72

3.14 Electrothermoelastic dynamic response of the microgripper 74

3.15 Test platform configured in 3D Microassembly system......77

3.16 Integrated gripper attached to ceramic holder 81

3.17 Characteristic curves of force sensor 82

3.18 Experimental and theoretical spring constant of force sensor measured at tip. 82

3.19 Dynamical model of microgripper and sensor cantilever 83

3.20 Measurement of in-plane stiffness 85

3.21 Measurement of off-plane stiffness 85

3.22 FEM displacement and stress of a METEG 87

3.23 Adaptation law in self tuning estimation 88

3.24 Force sensor mode... 90

3.25 Sensor dynamical identification......91

3.26 Dynamical response of deflection and force measured at METEG tip... 93

3.27 METEG and its holder are fabricated on a silicon on insulator die 96

4.1 Schematic of three serially connected micro-beams......102

4.2 S.S thermal simulation of V-shaped actuator excited below critical voltages 108

4.3 V-shaped actuator excited at voltages beyond critical values 109

4.4 SOI and FEM model of a U-shape thermal actuator......109

4.5 Classification of S.S. Temperature profile in U- actuator 111

4.6 Theoretical exact S.S. temperature profile of U-actuator excited for a range of input voltages 112

4.7 FEM analysis of U-actuator at V=14.5. 113

4.8 Von Mises stress distribution in U-shape actuator. 115

4.9 Thermal failure observations. 116

4.10 Combined blocks forming a Microgripper. 121

4.11 1-D thermal model of symmetrical microgripper. 125

4.12 Current analogy model of microgripper. 125

4.13 Temperature distribution using FEM without airgap 130

4.14 Temperature distribution using FEM with airgap and handle wafer. 131

4.15 Comparison between FEM and analytical methods 131

4.16 Schematic drawing of a thermal folded beam actuator 139

4.17 Three fabrication methods of folded beam thermal actuators 150

4.18 Solid model of an attached thermal actuator of uniform widths (I-shape) 152

4.19 FEM model and boundary condition of an SOI folded beam actuator 155

4.20 Temperature response of a single SOI beam at 35mA current input (5V). 159

4.21 General temperature solution $T(x;t)$ of a folded beam actuator utilizing FDA 160

4.22 Slowest temperature response in a folded beam actuator using FDA and at different input current 162

4.23 Cooling temperature response of the lumped folded beam actuators at different input current 163

4.24 Steady state and discharging analysis. 164

4.25 Experimental dynamic response of the SOI thermal actuator for a range of frequencies from 15Hz to 1015Hz. 167

4.26 Identification of the SOI folded beam 168

5.1 The solid model of the encoded parts of dust size 181

5.2 Solid model of the Self-assembled micro-robotic system 183

5.3 Biological Micro Pump (BMP) based on the translocation
of microorganism in a control volume…………………………………….....…...191

5.4 Micro-scales BMP comprised of closed and open chambers 194

5.5 Macro-scale prototype of BMP...194

5.6 Meso-scale prototype of BMP 194

5.7 Proposed identification setup for performance measurement of BMP 195

5.8 Schematic of a setup combining two processes: simultaneous parallel
detethering and self-assembly of MEMS structures. 196

5.9 Micro-robotic building blocks of a fabricated on SOI 198

5.10 Schematic drawing of squeeze field with attraction regions *R's* 199

5.11 Trapping Meso-scale parts of large stiction forces 201

5.12 Machining on 55% porous copper layer used in
assembly assisted by agitation……………………………………………… ...202

5.13 Trapping small scale parts of large sticktion forces 203

5.14 Relocating the parts from one trap to another using
two different agitation conditions 203

5.15 Schematic for self assembly assisted by dry agitation 204

5.16 Schematic of self assembly assisted by wet agitation 205

5.17 Self assembly of aggregate under wet agitation 207

5.18 Preliminary results in self-assembly assisted by wet agitation
for DNA configured micro parts r wet agitation..208

5.19 Preliminary results in self-assembly assisted by agitation
for DNA configured micro parts...208

5.20 Effect of disturbance on self assembled aggregates 210

6.1 Method for releasing MEMS and semiconductors 213

6.2 Schematic for an array of two different devices
fabricated on same platform 221

6.3 Schematic of a tethered device in a unit cell 222

6.4 Illustrations for mechanical modeling and time
response of a tethered device 222

6.5 General schematic of a vibratory agitation system 223

6.6 Major components of a top-down vibratory agitation system 225

6.7 Concept of selective and monolithic detethering attained
from frequency response and stress analysis 226

6.8 Inertial-switch sensor: posse's mechanical signatures that
are excited at certain vibratory harsh-environment 229

6.9 An application on the need for releasing massive MEMS blocks 229

6.10 Blocks tethered by breadth cantilever beam and
results on detethering based on vibratory agitation 232

6.11 MEMS blocks fabricated from silicon in insulator using DRIE........................233

6.12 Harmonic response of Von Mises stress for
neglected damping coefficients...238

6.13 The stress harmonic response plotted for modals of model 1 and 2 240

6.14 Harmonic response of model 2 at different damping ratios 241

6.15 Harmonic Von Mises stresses at modal frequencies
for agitated unit cells 242

6.16 Harmonic responses of stresses measured at the
tether's neck for devices in figure 6.17...243

6.17 Array of identical devices which are anchored by different tethers 244

6.18 Uniform cross sectional cantilever beam of free mass at the end 246

6.19 Schematic drawing of clamped free tethers 246

6.20 Time response analysis of device displacement for a lumped model 251

LIST OF TABLES

Table Page

1.1 Summary of proposed methods and their extensions in the dissertation 15

2.1 Chronicle development of the teleoperated and semi-automated platforms 33

2.2 Actuation methods comparison. 47

3.1 Good of Fitting at each model of orders....74

4.1 Material properties of U-shape actuators... 107

4.2 Dimensions of U-shape actuators... 107

4.3 Material prosperities of Nickel-annealed, silicon and ceramic *Alumina* AD-85 129

4.4 Structure dimension used in steady state thermal analysis....129

4.5 Material properties of folded beam actuators 156

4.6 Dimensions of folded beam (U) and line-shape (I) actuators measured in μm 158

4.7 Natural convection coefficient used in simulation 158

4.8 Settling time of a folded beam with uniform widths based on 98% of final value 160

4.9 Thermal and structural time constants comparison for SOI folded beam actuators at 24V 170

4.10 Heating and cooling settling time constants for several Silicon models....172

4.11 Heating and cooling settling time constants
for several Nickel models 172

5.1 Mechanical and control properties of some microorganism…………………190

5.2 Properties of Yeasts used in the controlling
actuation for a tested BMP..193

6.1 Lock up table of basic tethers with mass at free end 236

6.2 Test lumped models for tethered devices in
vibratory agitation system 251

CHAPTER 1

INTRODUCTION

1.1 Overview

Microelectromechanical system (MEMS) deals with miniaturizing multiple components and microelectronics to design and construct electromechanical systems. Fast growing technologies have advanced the research to develop complex and diverse techniques to meet assembly requirements. Based on the available technologies, *Modern* microassembly can be classified into *deterministic, stochastic and hybrid* microassembly [1, 24, and 81]. In *Deterministic* microassembly**,** several semi or fully automated work-cells guided by vision, force and position feedback have been proposed [13- 20]. Employing control system architecture with integrated part handling from CAD layout enables performing complex manipulation tasks [21]. Deterministic microassembly can also be classified into serial and parallel. Depending on *a-priori* organization of the micro-parts, *parallel microassembly* provides for a large number of parts to be assembled simultaneously with micro-scale precision [5]. *Serial microassembly* or commonly called "pick and place" requires a well-defined infrastructure for end-effector and micro-part interface. The process is often related to the effects of stiction forces and is time-consuming. The *exponential assembly*

technique was recently introduced in [1] and refers to an ever-increasing numbers of assembled copies. In *Stochastic microassembly*, a large number of distributed micro-parts is spontaneously or algorithmically organized either by *Distributed arrays or* self-*Assembly. The Micro Distributed Manipulation System (μDMS)* of computational MEMS sensors and actuators or arrays include distributed manipulators which dynamically recruit the fixed neighborhood modules to work together [3, 4]. The varying relative location of modules refers to another class of *smart* distributed MEMS systems. The monolithic *self-assembly,* which is spontaneous or inspired by nature, includes agitation of membranes with signatures, bio-mimetic systems [4], fluidic assembly based on capillary, Van der Waals, and electrostatic forces [5, 6, 7]. *Hybrid microassembly* is defined as the process of combining the aforementioned techniques to perform the desired tasks.

There is a need to explore methodologies to enhance batch and hybrid assembly processes with the focus of developing complex and functional sensors and actuators. The trend of developing module or *hybrid devices,* capable of integrating several manipulation tasks and massive assembly communication, has led this research to the essence of investigating and analyzing their performances. Thus, developing devices capable of carrying complex microassembly and actuation requires interdisciplinary studies of several fields including mechanical, electrical, biological, and chemical and others. Several concepts found in the Macro and Nano domains could be potentially implemented in the Micro and Meso scales. Potential examples in such actuation and

microassembly mechanisms can generally be thought of bio-mimetic models, flexible surfaces, object guidance, modular distributed manipulator systems and so on.

1.2 Motivation

"Why head into new methodologies for microassembly, sensing and actuation techniques?" has not only often been a question for more profound impact on industrial fields from simple approaches, but also, it has been a requirement for increasing the diversity on manipulation capabilities while the bandwidth limitation is kept narrow.

The conventional assembly of micro-parts poses requirements and challenges in relative part manipulation with submicron precision. During the development of microassembly techniques, two major classifications were inspired by Macro assembly and are accordingly known as serial and parallel microassembly. Note that improved accuracy is limited to highly specialized machines with a limited set of tasks. Automated microassembly work-cells based on controlled vision are being developed to provide micro-part manipulation and high precision capabilities. Although automated task execution ensures robust assembly in a short cycle time, the automated assembly operations become difficult at massive and parallel tasks. The monolithic integration of micromechanics and electronic components requires subsystem for microassembly. The monolithic process suffers from yield losses due to high subcomponent counts and size differences. For example, usually a MEMS wafer requires dicing, passivation, assembly and encapsulation. In addition, the basic manipulation skills, such as pick, place and nonprehensile manipulation are very restrictive reference to the object shape.

The design concept for end-effectors is thus highly dependent on the task complexity which could encompass fundamental processes such as grasping, pushing, flipping, throwing, squeezing, twirling, smacking, blowing, and so on. The precise positioning of micro objects in a multi-scale scheme requires attention not only on the kinematic precision of the work-cell environment, but also on the mechanics of the interaction of the parts either among themselves and/or with the end-effector. *Microphysical forces* that dominate gravity at the micro scale include Van der waals, surface tension and electrostatic forces. In addition, open loop positioning is impossible to achieve under such an operating environment. The need for new concepts in microassembly also arises due to the limitations in the widely used silicon lithography and etching as platforms for MEMS. Specifically, building different scales of three dimensional and heterogeneous structures from surface micromachined components is almost impossible to obtain with a single fabrication method.

Key issues in developing successful techniques for constructing micro-robotic systems depend on the precession in constructing heterogeneous structures, process yield "Throughput," and manipulation capabilities. In precision requirements, a Meso-range workspace must be combined with submicron resolution and Micro-scale positioning accuracy. Throughput requirements would dictate the amount of parallel or sequential process flow and the complexity of the assigned assembly tasks. A successful assembly can be obtained employing both sensory and sensorless techniques. A sensory feedback subsystem for monitoring and guiding the manipulation tasks could be achieved through vision system, prehensile positioning and force sensing. Sensorless

assembly, on the other hand, is often guided by the self-assembly concept or geometrical constraints or control algorithms for open loop assembly.

The design of end-effectors should consider the complexity of the tasks and the objects to be manipulated. Electro-thermo-elastic MEMS devices are utilized as an actuation mechanism because of:

- Large and wide ranges in forces and deflections.
- Easy of fabrication in single layer of various materials.
- Several structural compliances can be obtained.
- Reliability, robustness and ease in packaging.
- Relatively fast thermal and structural responses.

While it is possible to fabricate micro-parts, it appears that it will be difficult to overcome the adhesion effects during conventional prehensile microassembly methods. The scaling effect of adhesive forces had been utilized in assisting the serial assembly processes [7]. In this research, it is proposed that new sensors and actuators could also be employed for and aid parallel microassembly processes. Methods developed for conventional Macro-scale assembly cannot be applied directly to microassembly. Therefore, part of this dissertation is to discuss micro-forces encountered for self-assembly processes. Consequently, handling techniques, assembly and task planning of micromanipulations could be optimized by regulating the attraction and repulsive micro-forces.

Actuation methods which are currently and widely considered include piezoelectric, electrostatic, electromagnetic, magneto-strictive, hydraulic/pneumatic,

thermal and shape memory materials. One particular measure of the fidelity of these actuators is the theoretical maximum amount of work and/or power that can be produced per unit volume occupied by the actuator (called the work density or when scaled by the dynamic bandwidth, power density) [127]. Identification of the scales at which different techniques dominate will help the designer to select the appropriate technology for a given application. Such analysis will provide information about other parametric scaling factors such as drive voltage amplitude and frequency, generated forces etc. Thus, development of methodologies for MEMS performance evaluation becomes important in order to develop approaches for the optimal design of sensors and actuators for particular parallel assembly applications.

A class of actuation methods is based on bio-mimetic models. The development of miniaturized mobile robots is mainly dependent on scaling the *on-board power supply*. The most significant bottleneck for further miniaturization of mobile robots requires miniaturizing the on-board power source and motility mechanisms. Bio-organisms with translocation ability are one of the most promising candidates for on-board bio-micro-motors which are advantageous over the hand made-man actuators. This is because of their high efficiency in directly converting chemical into mechanical energy. In addition, organisms range from Micro to Nano and also are capable of performing complicated motions.

One important consideration in construction of microrobotic systems is the fabrication of their building blocks. The drawbacks associated with the different fabrication processes could limit the post assembly techniques. In particular, it has been

difficult to introduce large quantities of Micro and Meso-scale parts in a single post fabrication process. Also, traditional methods, such as mechanical probing, were sought to release and singulate the devices into the assembly platform.

1.3 Contributions

This dissertation research is mainly focused on the development and enhancement of serial/parallel microassembly and manipulation methodologies through the development of novel hypotheses in actuation and translocation methods. Particularly, experimental and numerical performance analysis procedures are developed and employed to guide the design of not only designed sensor and actuator systems, but also to prove the concepts of the developed assembly methodologies. Current microassembly techniques will be categorized in order to help guide their future development. Herein, several parallel manipulation concepts, borrowed from macroscopic actuator array of a modular distributed manipulator system [3, 24, and 25] are hypothesized. Particularly, several hypotheses for the parallel "massive" manipulation and assembly techniques which mimic DNA Nano-assembly processes are developed and implement. Introducing such concept requires the development of methods to release massive quantities of parts. In this research, a preprocessor detethering method followed fabrication processes is introduced.

One objective of this dissertation is to develop definitions of various microassembly techniques. Assembly strategies guided by self-assembly principles are developed to enable stochastic and deterministic assembly at the presence of complex

interactive forces and constrains. Concepts based on energy methods are examined to allow the selection of actuators and assigned tasks in the manipulation domain. Particularly, distributed manipulation at micro-scale level or *Active surface devices* are investigated and classified according to their multi-physics working principles.

The dominant force is identified and the attractive nature of the dominant forces is studied under the scaling effect to enable self-assembly of micro objects. Assembly guidelines are formulated to allow generating suitable preconditions in task space and component space for assembly.

This research also aims at investigating and developing microassembly techniques for constructing different types of Microsystems. The contributions are summarized as follows:

- **Contribution 1. Developed End-effector with compliant structures for deterministic microassembly work-cells.** Several bulk Micromachined MEMS structures capable of performing advanced manipulations tasks were identified. The designed Silicon on insulator (SOI) electrothermal (E-T) devices are in-plane 2½D micro-parts. The characteristics of these multipurpose electrothermoelastic microgrippers (METEG) are as follows:

    (1-a) Pick and place of heterogeneous micro-parts (capabilities include remove, insert, grasp, place, push, pull, translate and orient from their substrates on a chip and join them to other micro-parts at a secondary location).

(1-b) The developed MEMS devices have two types of grasping modes: active gripping in which the tip is controlled by E-T elastic force, and passive gripping where the tip opens by the reaction imposed during the insertion process.

(1-c) An integrated micromechanism for Joule heating source designed for jointing, soldering or welding applications, capable of applying external uniform bonding pressure and reduces the adhesive forces.

(1-d) Sensory feedback to control, guide, and monitor manipulation tasks being performed. Two principles, first, strain gauge based on the resistivity change of highly doped silicon, and second, an electrostatic based sensing have been incorporated.

- **Contribution 2. Synthesized and analyzed METEG MEMS devices to identify their limitations and to enhance their functionality during the serial to parallel assembly of microstructures.** The thermal and struct**ural budgets** are studied. Particularly, the one dimensional temperature distribution at subsystem and system levels are modeled mathematically and numerically analyzed:

  (2-a) The steady state thermal behavior of E-T microstructures due to various input voltages in both amplitude and frequency was studied. Mathematical models are derived to evaluate the performance sensitivity

of serially connected microstructures mainly, U and I /V-shape building blocks.

(2-b) Comprehensive study on the thermal distribution of the integrated subsystems, particularly the "Microgripper": deriving mathematical models for both released and unreleased microgrippers under different boundary conditions.

(2-c) The transient heating (charging) and cooling (discharging) time constants of a U- and I/V-shape in METEG actuators are analytically approximated and lumped to allow for thermal cycle optimization.

(2-d) Introduced analogous multiphysical modeling techniques for METEG components. Mainly, Finite Element Approximation (FEA) and Finite Element Modeling (FEM) are utilized to compare and validate the developed mathematical models.

(2-e) A nonlinear mechanical analysis of a gripper thermal actuator was performed. The displacements in a microgripper, made of U and V shape structures, are experimentally measured and analytically derived to evaluate the large elastic deformation behavior of METEG devices in order to enhance and control manipulation and actuation during microassembly.

- **Contribution 3. Developed micro Self-assembly strategies inspired by DNA recognition concepts.** Particularly, developed methodologies for constructing 2½D structures to enable self and massive assembly of microrobotic devices.

- **Contribution 4. Deployed concepts for non-conventional actuation and translocation of micro-parts assembled or sub-assembled micro-structures.** Particularly, studied actuation methods based on microorganism locomotion for the assembled micro sensors and actuators. A meso-micro scale pump powered by translocation and reactions of the growing cultures of stimulated microorganisms, such as bacteria or fungi kingdoms was developed and demonstrated.
- **Contribution 5. Introduced expressions definitions for evaluating the performance of micro distributed manipulation system (μDMS)**. The Meso scale manipulation capabilities in μDMS are integrated with the METEG environment.
- **Contribution 6. Developed methodologies for releasing MEMS and semiconductor devices after fabrication.** The release method is a preprocessor technique that is mainly utilized to selectively and massively detether Meso and micro scale parts. Tethers possessing unique mechanical signatures are designed for conditional fracture during a controlled agitation process. The implementation of this release method provides parts for post assembly processes required for the construction of microrobotics and other micro and meso scale systems.
- **Contribution 7. Designed, implemented and used experiments for**:

    (7-a) Measurement and modeling the performance of the designed Meso-Micro-devices. Identify the static and dynamical performance of the

elastic and the electrothernoelastic MEMS structures using cantilever MEMS force sensors and non-contact dynamical profilometer.

(7-b) Methods on techniques for packaging and attaching the released electrothernoelastic MEMS devices.

(7-c) Monolithic detethering technique for micro to meso-scale MEMS parts on die and wafer level. Micro-parts of "dust size" fabricated on silicon and hanging over from device layer on a die level, are selectively but massively detethered by using proper mechanical design for resonating device.

(7-d) Introduced self-assembly of micro-parts in dry and wet media.

(7-e) Introduced setup for measuring aspects in the translocation performance of microorganism. The cell growth of microorganisms is experimentally evaluated for possible implementation in a controlled microactuation.

1.4 Summary

Following this introductory chapter, a comprehensive survey in the microassembly and manipulation techniques has been performed considering several interdisciplinary fields. The organization of the material presented in Chapter 2 aims at reformulating the presentation of the actuation and translocation methods and with the focus of allowing the researcher to properly select the most suitable method for their

required assembly tasks. The chapter concludes by formulating concepts in task selection based on energy method.

In Chapter 3, the tradeoffs in design, fabrication, packaging and the use of electrothermal MEMS devices for microassembly applications are discussed. Such fabricated designs of E-T end-effectors resulted in what is defined here as *Multipurpose Electro-Thermo-Elastic Gripper* or (METEG). METEGs may contain up to three basic design building blocks such as actuation mechanisms, heating elements, and feedback sensor.

In Chapter 4, the general heat conduction equation of micro E-T block design has been analytically solved to obtain the steady state temperature profile. Also, approximate analytical and lumped models have been proposed to solve for the thermal cycle of both METEG components which comprise U- and V-shape structures. These methods provide insight and comprehensive evaluation of the performance of METEG devices under different design and operational conditions. The experimental dynamical performance of METEG devices has also been analyzed for both passive and active modes and used to identify the system transfer function. The identified models could be directly utilized during the assembly process to improve system performance. Thus, the failure modes and operational conditions are predicted and employed in trouble shooting and identifying several issues in the design and experiment conditions, as discussed in Chapters 3 and 4. The capabilities of the developed devices have been successfully demonstrated for 3D assembly of heterogeneous structures. However, this slow deterministic process was extended and coupled with the distributed

manipulation concept. The Hybrid assembly process facilitated the fast positioning of micro-parts into their desired sites.

Although enhancements in assembly accuracy and time have been observed the enchacements resulted in increasing system complexity. Thus, parallel self-assembly of microstructures encoded by shape and micro attraction forces was explored and discussed in Chapter 5. Silicon in insulator micro-parts have been designed and fabricated to utilize the effect of their non-covalent forces. Techniques aiming at introducing the detethering and assembling of micro-parts to form aggregate structures based on spontaneous self-assembly were developed. In addition, several actuation techniques for such assembled devices were investigated. One of the promising actuation techniques is based on bio-mimetic models. Living species exhibit a variety of translocation mechanisms and can be found at different sizes. The forces, speeds and the controlling mechanisms could be easily customized based on the number of species available for usage. Consequently, a bio-actuation concept to power a micro-robotic device was experimentally explored where instead of translocating the micro-parts in open volume, the growth of the living species was utilized in an enclosed chamber as "a kind of locomotion" to deform an elastic membrane. This concept defined new generation of self powered and simple in actuation Bio-Micro-pump.

Novel methods for massively and selectively detethering of micro-parts are introduced in Chapter 6. The operational principle is based on the reverse engineering of the design of tethers of the devices, for example the MEMS structures designed in Chapter 3, 4 and 5, and then by agitating the tethered device at the designed tether

Table 1.1 Summary of proposed methods and their extensions in the dissertation.

Methods	Attributes	Challenges
(1) End-effectors for deterministic serial - assembly. Chapters (3 & 4)	1- Multi purpose electro thermal microgrippers (METEG) including grasping, sensing and heat sources. 2- Large forces and deflections. 3- Fast responses at micro scale. 4- Symmetrical and asymmetrical structures fabricated in one layer. 5- Active and passive based pick and place. 6- Compliant structures capable of handling micro and meso parts. 7- capable of constructing 3D structures.	1- Assembly process is sequential and slow. 2- Requires teleoperated work-cells. 3- Requires well-defined infra structures between part and METEG. 4- Packaging and powering. 6- Thermal failures.
(2) Deterministic parallel-assembly. Chapter (3)	1- Multiple of METEG.	----
(3) DNA based Self-assembly. Chapter (5)	1- Massive assembly based on fabrication of blocks having specified configuration and non-covalent forces. 2- Surface assembly is assisted by wet and dry agitation. 3- Implemented at micro to meso scale. 4- Capable of constructing 2 ½ D structures. 5- Repeated patterns.	1- Identifying setup parameters is crucial. 2- Probabilistic. 3- Stiction forces. 4- Limited robotic configurations. 5- Dependent on material and scale. 6- Stability during and after assembly. 7- Actuation after assembly.
(4) Micro-distributed manipulations system *μDMS.* Chapter (2,5)	1- Extended concepts of small scale active surfaces in continuous and discrete fashions. 2- Hypothesis for actuation selection based on energy and optimization criteria. 3- Continuous/discrete surfaces used to manipulate parts using minimum local energy assisted by agitation.	1- Requires extensive multiphysics synthesis and analysis. 2- Microphysical interaction.
(5) Hybrid assembly Chapter (3)	1- Combines methods (1, 2 & 3). 2- Work-piece is based on *μDMS* and used to allocate (template) parts into designed sites. 3- Teleoperated is automated to well-known sites located on *μDMS.* 4- Increase assembly **robustness** due to reduction in automation and processing time.	1- Increase system complexity.
(6) Release of MEMS and semiconductors. Chapter (6)	1- Selective and massive detethering of devices after manufacturing. 2- Based on mechanical signature designed tethers which resonate and break at specified agitation conditions. 3- Implementable at micro-meso-macro scales. 4- Independent of material. 5- Clean process which can be employed and introduced in a manufacturing process line. 6- Programmable process.	1- Inverse problem to identify the fracture conditions. 2- Reliable apparatus based on vibratory agitation.

fracture conditions. A massive number of microparts are arranged in unit cells fabricated on layer(s). The layers are positioned on an agitation vibratory system capable of transmitting lateral and/or longitudinal and/or out of plane motion to all tethered parts. At certain measured or calculated harmonic frequencies and amplitudes, the parts are massively separated at the designed notches through fracture, thus providing the released parts for the next assembly or packaging platforms. A summary of the discussed methodologies is summarized in Table 1.1.

1.5 Intellectual Merit and Broader Impact

The objectives of this work are to investigate new mechanisms and increase their capabilities over already existing microassembly, manipulation and actuation techniques. The research aims at developing new theoretical and experimental foundations for modeling, design and analysis of not only the end-effectors for serial-parallel microassembly work-cells, but also, for investigating and developing non-conventional actuation and monolithic microassembly processes based on revolutionized bio-mimetic concepts including the DNA recognition and the microorganism translocation and reactions.

The major merits of the proposed research efforts are (i) develop novel multipurpose electrothermoelastic gripper for serial to hybrid microassemby; (ii) develop mathematical analysis tools and experimental methodologies for evaluating the performance of the developed mechanisms; (iii) investigate translocation techniques and actuation mechanisms of microstructures; (iv) develop bio-micro-pumps (BMP) for

medical and other applications and (v) investigate the massive by selective detethering of microcomponents.

The results of this research effort will broadly impact not only engineering fields, but also broad areas of science and the society by (i) significantly enhancing the modern micro manipulation and actuation technologies; (ii) provide new dimension to the applications of *multiphysics*, including electro-thermo-elasticity, biomechanical and microphysics of microstructures**.**

1.6 Applications

The proposed research attempts to end at technologies and devices fabrication for the following specific applications:

(i) Multipurpose end-effectors for the assembly and construction of heterogeneous 2½D to 3D of active/passive microstructures.

(ii) Monolithic and selective detethering of MEMS structures and semiconductor devices:

- Unique procedure to massively dice the miniaturized integrated circuit devices, such as light emitting diodes (LEDs).
- Unique procedure to mechanically release MEMS based products such as laser detectors and modules for building robotics systems. For example, the method would release and provide massive quantity of meso- to micro-parts, which could be used for self-assembly and actuation of smart micro-particles for 2½D to 3D of active/passive microstructures.

- A potential preprocess that may provide a platform for self-assembly, templating and sorting.
- A methodology that be potentially implemented for a range of sensors and actuators including a claimed mechanical inertial sensor which may be utilized in existing applications related to systems safety.
- A methodology that may potentially solve common industrial limitations related to design and release of devices.

(iii) Smart sensor and actuator for biomedical and industrial applications. Particularly, bio-micro-pump (BMP) capsules based on microorganism actuation. This includes disposable drug delivery devices for respiratory and circulatory systems.

1.7 Impacted Fields

The outcomes of this research reinforce the importance of integrating several interdisciplinary fields. Students and researchers should be able to integrate skills of understanding different phenomena from Macro to Nano worlds. The specific influence of this research will impact:

(i) Engineering: synthesis and analysis of mechanical mechanisms, structural analysis and heat transfer models.

(ii) Biotechnology: biomedical and the related allied medical professions.

(iii) Industrial: the demand for fast product fabrication with techniques which are reliable, robust and inexpensive.

CHAPTER 2

MICROASSEMBLY METHODOLOGIES: SURVEY AND INTRODUCTION OF EXTENDED CONCEPTS

2.1 Introduction

The vastly growing micro-fabrication techniques increase the need for the development of microassembly methodologies for complex structures and hybrid MEMS devices. High aspect ratio parts and multilayer architectures were obtained by LIGA (lithography, electroplating, and molding) and explored in SUMMiT V (Sandia Ultra-planar, Multi-level MEMS Technology), respectively [134]. However, such processes are generally incompatible with the processing steps used for surface micromachining. Several groups developed flexible automated microassembly work-cells with the purpose of diversifying microassembly task capabilities, handling large volumes of devices and achieving submicron relative manipulations [33, 34 and 35]. The success of such multitasking systems depends not only on the robustness and repeatability of work-cells and fixtures, but also on the guidance by employing sensor feedback.

During the development of microassembly techniques, two major classifications inspired by Macro-assembly, evolved and are accordingly known as serial and parallel

microassembly. Serial microassembly or micron pick and place require a well-defined infrastructure for both the micro-tool and micro-part to interface with each other. In general, parallel microassembly processes enable large number of parts to be assembled simultaneously with micro-scale precision.

The need for heterogeneous microassembly in construction of MEMS and Semiconductor based devices is summarized as follows:

- Limitation of silicon lithography and etching as a platform for MEMS device fabrication.
- Monolithic integration of micromechanics and electronic requires developing and integration of several subsystem for micro-engineering. This process suffers from yield losses due to high counts and size differences. For example, a MEMS wafer requires dicing, passivation, assembly and encapsulation.
- Microassembly has been incorporated in sub cm-scale micro-system such as LEDs and silicon microstructures, and fluidic microelectronic packaging.
- Building three dimensional structures from surface micromachined thin films.

Obviously, the success of the developed technology depends on its capability to address the following *key issues*:

- Precision requirements: Meso- to Micro-range manipulation to achieve submicron relative positioning.

- The amount of parallel or sequential process flows and the complexity of delivering and performing the assigned assembly tasks.
- Sensor or sensorless assembly: sensor feedback to guide and observe manipulation tasks is handled by vision system, prehensile positioning and force sensing. Sensorless assembly, on the other hand, requires open loop or minimal ability control algorithm.

The material presented in this chapter surveys manipulation methods found in microassembly. More comprehensive classification of the available and potential techniques are introduced with the goal of initiating measures to improve the selection of assembly methods and their tools.

2.2 Classification of Manipulation, Actuation and Assembly Techniques

General manipulation of an object involves three basic tasks: singulation, orientation, and presentation [11]. Singulation is the process of separating mass of parts into individual parts. Orientation is the process of deterministically reorienting a randomly oriented part (typically one). Presentation is the action of moving the singulated and oriented part into a known location, where further processes might take place. Examples of singulation and presentation include, part pick and place, hitting, rolling, pushing, rolling, throwing, dropping, tumbling, pivoting, tilting, and flipping. Manipulation could be classified in accordance to:

1) *Quasi and Dynamic Manipulation*

In terms of dynamics, Yasumichi classified manipulation methods into *quasi-static and dynamic manipulations* [12]. In quasi-static manipulation applied external forces statically support an object which can be controlled by position trajectory. Conventional methods involve graspless and grasping manipulation or pick and place in robot end- effectors [13]. Graspless manipulation suffers from uncertainty of the frictional force at the contact locations, thus, stabilizing the object requires sensory feedback such as force and vision. Graspless manipulation includes point contact (i.e. pushing), line contact (i.e. tumbling) and face contact (i.e. pivoting). In dynamic manipulation, the dynamic characteristics of the applied external forces manipulate the object by considering the resultant of the inertial, gravity and micro impact forces. Such manipulation methodologies involve snatching, rolling, catching, releasing (or impulsive and throwing), repeated force (i.e. vibration, small impact, repeated movements). Swanson had analytically studied the vibration parameters which orient the randomly initial states of parts into vertical state or stable oscillation [11].

2) *Sensor and Sensorless Manipulation*

The uncertainty in the location of the objects can be reduced by either providing sensing or constrained motion strategies [14]. Accordingly, the control automation of objects can be classified into guided and sensorless manipulations. Guided manipulations in which the uncertainty of object location is adjusted by sensory feedback. Force and position sensors had been successfully implemented to locate and manipulate typical single objects [15, 16, 17 and 18]. Other types of feedback include

vision guided manipulation system operated in an SEM (Scanning Electron Microscope) and under CAD (Computer Aided Design) based approach microassembly [19, 20 and 21].

Sensorless manipulation or constrained motion strategies were introduced by Erdman and Mason [14] and Mason [22]. Generally, sensorless manipulation plays a role in assembly processes where sensing may not be feasible in general due to geometrical and scaling limitation. Sensorless complexity varies from superior, inferior to complementary based strategies. The gravitational force of a planar macro object to it by programming strategies for tray tilting [14]. Böhringer utilized a force field generated from a vibrating plate to orient and move objects into stable nodes [23]. Also, Böhringer et. al. developed algorithms for the manipulation tasks with an array of microelectromechanical structures on a limit surface [24], where an array of asymmetrical torsional resonators are utilized to generate an activation pattern for a specific motion.

3) *Contact and Non-contact Based Dry Manipulation*

Object manipulation can also be described by the mechanical interaction between the manipulated object and the supervising medium. In a dry medium, the situations of direct contact between an object and a surface are determined from the study of gravitational friction and sticktion forces (electrostatic, Van dar Wall). Luntz utilized the macroscopic frictional force of an array of motorized wheel actuators in order to move macro objects. Hence, a controlled *Modular Distributed Manipulation System* (MDMS) could enable dynamic manipulation of a resting object [25 and 26].

Other manipulation types based on dry medium involve non-contact manipulation such as electromagnetic levitation, electrostatic and air-flow distributed manipulation [27, 28, 29 and 30]. Huang induced magnetic force between perm-alloy magnetic flaps consisting of an external permanent magnetic mechanism and coil film where the levitated flap is utilized to steer the aerodynamic surface of a delta wing aircraft [29]. Satoshi fabricated an array of air-flow microactuators with electrostatically controlled nozzles [28].

4) *Surface and Volumetric Based Fluidic Manipulation*

Several assembly processes have been demonstrated either in planar or volumetric domains. Most non-contact or frictionless manipulation concepts are based on 3D aerobatic maneuver of objects. Manipulations assisted by a fluidic medium can take place on a wet surface or inside a solution. Böhringer demonstrated surface parallel micro-self-assembly of micro-parts floating above activated sites of substrate [31]. Gracias fabricated 3D microstructures by assembling large regular array of polymeric polyhedra suspended in water [32].

2.3 Small Scale Manipulators as an Emerging Technology

Small scale sensor and actuator concepts are merely a scale down version of conventional macro devices. The accuracy or precision of these small scale machines is at sometimes no better, and at worse than that of high- quality macro machines. In macroscopic scale, the range of accuracy is around 1 part of 10^5 or better [132]. It is obvious, that requirements of manipulators such as primary actuation method,

controlling manner, operating environment, low power consumption, resolution, bandwidth, compactness, cost, and positioning precision, for example, may be best achieved using different technologies. When assembling small parts, tolerance stack-up often leads to degradation in the earlier performance. Hence, the development of actuation systems and metrologies (such as sensors) are required to control the relative precision. Also, it is important for the device designer to be aware not only of the available technologies but also of the relevant performance measures as function of the dimensional scale of the device components. The dimensional scale of the classifications can be categorized into:

- Meso-systems, devices and processes whose major dimensions are typically measured in millimeters.
- Micro-engineering incorporate MEMS devices and processes that are measured in micrometers.
- Nano-engineering is considered for processes resulting in devices of defined structure or assembly in which nanometer is the most sensible unit of specifying dimensions or tolerance.

Most of the system features changes as dimensional scale reduces and often leads to advantageous behaviors that could be employed for assembly processes. For example

- With the available technologies so far, manual assembly is no longer viable at certain cut off dimension.

- Body surface interactions introduce significant mechanical forces that may change within the mechanisms. In small scale, the microphysics includes contact forces, Van der Waals, adhesion forces, electric dipoles, meniscus effect and Casimir forces [56].
- Scaling can change the relative dynamics of phenomena. For example, heat transfer and thermal response are often considerably comparable with mechanical response in micro scale. However, heat transfer in a macro scale machine is much slower than mechanical motion. Moreover, thermal expansion has more influence in micro devices than macro scale devices.
- The reduction of volumetric deposition or removal leads to economic tradeoff.

These key factors should guide the development of methodologies required to expand 2½D into 3D MEMS and semiconductor devices. In the following chapters, the scaling effects of forces are utilized to define new generations of microassembly for construction of microrobotic systems.

2.4 Dissertation Related Art

The majority of manipulations have been performed by microassembly work-cells which are considered as an alternate manufacturing route [16]. Particularly, the construction of heterogeneous 3D microstructures utilizing teleoperated work-cells has been under progressive development for more than two decades with the major contributions summarized in later sections. During such deterministic serial microassembly numerous methods for controlling the pick and place operations have

been utilized in the past, such as vacuum grippers based on micro-pipettes [33]; manipulators with heated micro holes acting as suction cups [39]; electrostatic force control method [40]; tweezers "grippers" and teleoperated assembly [41]; moisture and surface tension control methods [42]; and roughness change method and force controlled grasping based on an AFM (atomic force microscopy) [43].

A number of standard MEMS fabrication processes could be utilized to fabricate microgripper devices such as LIGA, SOI, MetalMUMPs, PolyMUMPs, FIB, EBL and DRIE [41 and 44]. An electrothermally (E-T) driven micromechanical device based on asymmetrical thermal expansion led to the development of many microactuators in microsystem technology [45 and 46]. This actuation principle is capable of providing larger deflections and forces compared to electrostatic, piezoelectric, and magnetic actuation principles [47]. However, the high power requirement of typical E-T building blocks such as monomorph, bimorph and chevron thermal actuators often cause thermal failures thus limiting the operating force, operating deflection, operating structural frequency, and the bonding conditions at the device pads. Thus, it is required to investigate design tradeoffs of E-T devices. The development of new end-effectors for teleoperated work-cells requires three main key issues; first, increasing the capabilities of the already existing end-effectors; second, developing mathematical models and numerical methods to measure and enhance the performance of the developed or of the already developed E-T end-effectors; third, introducing designs which could not only be used in serial and parallel manipulation, but also could be used

as modular or “building blocks” for an array for micro distributed manipulation which aid on performing hybrid assembly or locomotion.

This *Micro-Distributed Manipulator System* (μDMS) which in Macro-world is also referred to as modular distributed manipulation system (MDMS) where distributed manipulators with many small stationary cells or “modules” cooperate to manipulate larger objects [48, 49 and 50]. Typical manipulation addresses the task of bringing an object to a particular position and orientation. English Luntz [50] macroscopic MDMS was built upon the work of researchers in Microelectromechanical (MEMS) actuator array as found in Böhringer [51]. In his work, Luntz prototyped and demonstrated fully programmable and controllable cells consisting of motorized wheels supporting the object and generating traction forces [50]. Early development of microactuator control strategies is attributed to research work conducted by Bruce and Böhringer in which they investigated and developed sensorless parallel manipulation based on microactuators [51, 52 and 53].

The strategies of selecting the proper actuation method for specific micro object manipulations depend on understanding the multiphysics and the microphysics i.e. actuation principles and the behavior and effects of electrostatic and adhesion (capillary force, pull-off and Van-der Waals) forces [54]. Here, the surface forces are a function of the medium physical parameters like pressure, temperature, and humidity. Gracias [48] described static and dynamic self-assembly of Meso-Scale Self Assembly (MESA) to form 2D and 3D aggregates in a liquid medium assisted by electromagnetic forces. The key concept of static assembly is to allow the patterned object to float between a

hydrophobic liquid (perflourodecalin, PDF) and hydrophilic one (water). Positive and negative menisci are formed above and below the interface, respectively. At Meso-scale, the capillary force is weaker than menisci, thus menisci of the same shape attract each other and allow object interface. Generally, the microphysics of micro object is highly dependent on whether manipulation takes place on submerged medium or air. However, little attention has been paid in investigating the application, assembly function and actuating methods of such MESA aggregates. REF

Therefore, this dissertation continues on research differentiating the microassembly techniques and methods that address three types of actuation concepts

- Investigate electrothermoelastic structures to improve the manipulation in deterministic serial, parallel and distributed microassembly.
- Investigate the signatures for Micro-scale self-assembly and releasing of robotic systems.
- Investigate actuation methods for self assembled system, or for an existing structure, particularly, microorganism based actuation.

2.5 Modern Classification of Microassembly Methods

A microelectromechanical system relates to miniaturizing multiple components and microelectronics to design, assemble, and construct electromechanical systems. The miniaturization has advantages such as small and light weight devices with high resonant frequencies and band width. It also enables the integration of microelectronic devices. The fast growing technologies have advanced the research to develop complex

and diverse techniques to meet assembly requirements. Based on the available technologies, modern microassembly can be classified into deterministic, stochastic and hybrid. Hybrid microassembly combines the aforementioned techniques to perform a set of desired tasks.

The potential benefit of microassembly is encompassed in decoupling the process sequence which incorporates hybrid devices with optimal functionality. Tracking the development and tradeoffs of microassembly techniques are essential in establishing a well define structure for assembly classifications. The development of various assembly processes are discussed in the next subsections.

The computational challenges in the construction of MEMS based robotic systems are summarized as increasing the general intelligence and capability of machines and matter, comprising of first, construction of MEMS as computational blocks and second, methodologies and systems capable of performing analysis and assist in the design on multiple energy domains. Such mechanisms are required for manipulation and actuation of large number of distributed MEMS sensors and actuators, including coupling machine intelligence and the constructed system to the environment in real time event, and so the question arises for feedback sensors which are required to correlate for their motion.

2.5.1 Deterministic Assembly

Deterministic assembly refers to apriori planned assembly processes between parts and their destinations. Microassembly work-cells with integrated part handling

skills and vision based guided control system architecture enables performing deterministic manipulation tasks. Deterministic microassembly is also classified into serial and parallel assembly.

2.5.1.1 Parallel Assembly

Depending on the organization of the micro-parts, *Parallel microassembly* processes enable a large number of parts to be assembled simultaneously with micro-scale precision [24]. Parallel assembly comprises the simultaneous precise transfer and alignment of components into binding sites. It enables a large number of parts to be assembled simultaneously with micro-scale precision. Planned multiplicity, allows economic and massive MEMS component fabrication. Also, Parallel assembly has additional advantage in the flexibility in the design of massively parallel and interconnected microelectronics. Thus, allowing closed feedback, localized signal conditioning and control of massively parallel actuator array.

2.5.1.2 Serial Assembly

Serial microassembly or one by one micro pick and place requires well defined interface between end-effectors and micro-parts. Such successive process could be classified into automated and manual assembly, where manual assembly is operated by tweezers guided under a microscope. On the other hand, teleoperated**,** semi to fully automated microassemblies are operated by work-cells and assisted by proper

micrograppers. Methods for controlling the direct pick and place operations include [9, 81 and 95]:

- Roughness change method with vibration.
- Vacuum grippers based on micropipette.
- Manipulators with heated micro holes acting as a suction cup for pick up and place.
- Tweezers or microgripper actuator as fundamental tools for teleoperated assembly.
- Moisture and surface tension control method utilizing embedded micro-heater.
- Electrostatic force control method.

One major problem in pick and place is the sticktion problem and the time efficiency. Sticktion is caused by adhesive forces between end-effector surfaces and the micro-parts. Such forces appear in parts smaller than a millimeter, where electrostatic attraction, Van der Waals and surface tension are significant compared to gravitational force [34].

A well-designed work-cell in guided manipulation enables deterministic assembly for both serial and parallel tasks. The first kind teleoperated micromanipulation system was employed to high precision nano-robotic positioning [15]. It had full range of 15um with 10nm resolution and was driven by piezoelectric stack actuators. Extension of this manipulator incorporated force sensing, vision feedback, multi degree of freedom and high resolution positioning [16]. One of the first assemblies was performed utilizing micro-pipette gripper based vacuum [33].

Teleoperated and semi automated platform chronicle development is presented in Table 2.1.

In the next chapter, an upgraded version of an existing teleoperated manipulator that is developed to perform simple to hybrid microassembly tasks will be introduced. Generally, the serial assembly operated by deterministic teleoperated system requires the consideration of the following guidelines:

- High precision positioning is almost impossible to achieve in open loop manner. The development of control strategies for path planning is desired to be optimally selected for given tasks.
- The physical characterization of interaction of parts and their dynamics are complicated.
- Redundant sensors and degrees of freedom for general microassembly tasks are required to introduce handling flexibility.

Table 2.1 Chronicle development of the teleoperated and semi automated platforms.

Group/year	Features	Limitations	Ref.
1-Hatamura and Morishita/1990	1- 2D Coarse manipulator drive nanorobots 2- Piezoelectric stack nanorobot with 3D DOF of 10nm resolution and 15um full range. 3- Feedbacks are generated from a single DOF force sensor and SEM.	1- Manipulation tasks are conducted by teleoperator joystick.	[15]
2-Mitsuishi et al./ 1993	1- An extension of [1] but with high DOF force sensors. Optical microscope and CCD camera generate visual feedback.		[16]
3-Sato et al./1993	1- Stereo microscope was employed to guide microassembly task. 2- Vacuum gripper is developed based on drawn glass micropipette and vacuum pump.	1-small depth of field and field of view result in a limited viewable workspace	[33]
4-Sato et al./1995	1- Visually guided manipulation system operated under SEM. 2- Pick up and place of objects ranging from 5-15um.	1- Semi-autonomous. 2- Simple tungsten needle is used as a gripper.	[16]

Table 2.1-continued.

Group/year	Features	Limitations	Ref.
5- Koyano and Sato/ 1996	1- Guided microassembly work-cells with integrated SEM and optical microscope. 2-Multiple view with different optical resolutions. 3-Adhesive force based pick up and place was employed. 4-Manipulating 30um-40um solders balls.	1-Placement of object requires two tools.	[20]
6-Swiss Federal Institute of technology/1994, 1997	1-Multi DOF teleported and automated microassembly. 2-SEM with positioning resolution of 10nm over 1 cm^3.Two cameras and stereo light microscope provide feedback. 3- Virtual reality interface. 4- Two robots are equipped with tweezers and vacuum gripper while third robot functions as assembly surface.		[17,18]
7- Swiss Federal Institute of technology (EPFL)/ 1998	1- Automated assembly using visual feedback. 2-coarse to fine ranges with high precession (100×100 mm^2, Max. speed of 25 mm/s, fine resolution of 100 nm)	1- Off line processing. 2- Vacuum gripper	[34]
8-Uppsala University/ 1993-1997	1- Multi-degree of freedom under SEM. 2-Piezoelectrically actuated micro tweezers are used as end-effectors.	1- Manual and semi-automatic operation.	[35]
9-MITech Lab/ 1999	1- 3DOF micromanipulators with coarse (37×20×20mm^3 travel, 0.1mm resolution) and fine motion (10mm travel, 0.5-10um resolution, 0-200um/s speed) 2- Piezoelectrically actuated tweezers and vacuum gripper.	1- Similar to (EPFL) project.	[36]
10-Sandia National Laboratory/98	1- CAD based approach microassembly capable of assembling LIGA parts. 2- Visual servoying utilizing the off-line image synthesis. 3- 4 DOF robot, 4 DOF precision stages with 1um repeatability.		[21]
11-Sandia National Laboratory/1999	1- Parallel microassembly is performed on wafer level. 2- Work-cells include 4DOF assembly system, microscopes and tools for handling wafer.		[37]
12- Cohn/97	1- Deterministic parallel assembly using flip chip transfer assembly of micro-parts.		[38]
13- Zyvex corporation (200-2006) and RPI – until 2003	1- Complex micro machinery for constructing nano structures. 2- Exponential assembly methodology is suggested. 3- Robust algorithm for assembly sequence planning of microassembled systems. 4- End-effectors for handling hundred parts of hundred in microns down to ten nanometers.		[119, 120, 136, 131, 135, 137, 138]
14- ARRI/ 2004-2007	1- Three manipulator with high degree of freedom (19 DOF) 2- 6 DOF Nano cube manipulators for nano manipulation. 3- CAD based approach microassembly. 4-Vision system for stereo assembly 5- Semi to fully automated assembly sequences. 6- Assembly of heterogeneous 3D microstructures. 7- Successful assembly of Microsystems (Microspectrometer) 8- Hybrid microassembly assisted by active surface. 9-Integrated hot plate. 10- Multipurpose end-effectors.		[91, 94, 121, 122, 133]

- Successful task execution depends on suitable design of end-effectors and tools. It also requires regulated environment for vibration isolation and particle count.
- Semi-automatic operation or *remote teleoperation* must have user interface capability to allow for correction and compensation.

Another extension of deterministic technique is *Exponential assembly* [93] referring to the ever-increasing numbers of assembled copies, wherein the teleoperated system picks additional end-effectors in every sequential processes.

2.5.2 Stochastic Assembly

Stochastic Assembly refers to a large number of distributed micro-parts which are organized either by:

- Distributed arrays of computational MEMS sensor and actuator: Such array encompass, first: *Active Surface* manipulation which dynamically recruits the fixed neighborhood modules to work together and interact with environments. Second, smart MEMS devices which are distributed in the environment with relative locations varying with time.
- Monolithic self-assembly process which are inspired by laws of nature. Bio-mimetic system, fluidic assembly based on capillary force, and agitated membranes are examples that comprise simultaneous precise transfer and alignment of component organization into binding sites.

Stochastic parallel assembly, or most often referred by multiple self microassembly, is based on trapping micro-parts in defined binding site (etched hole,

chemical, electromagnetic, biomedical, electrostatic, etc.). It has been applied in industry for fabrication of LCD substrates with embedded silicon substrate. Such sensorless process enables massive fabrication of MEMS structures. However, stochastic parallel manipulation has the following limitations:

- Fabrication of devices and blocks that interact actively with changing environment. Requires universal singulation method that enables massive and selective releasing parts in assembly platforms.
- Unknown material and difficulty of modeling of micro-scale devices. Particularly, lack on comprehensive methodologies that guide proper selection of model based on simple simulation analysis
- Limitation in force output and motion ranges for small mechanisms. The translocation and actuation methods are not comprehensively studied for small but massive mechanisms.
- Lack of sensor information with regards to manipulation tasks.
- Geometric tolerances in the design due to fabrication limitations.

Next subsection surveys potential application of stochastic assembly in spontaneously arranging Meso- and Micro- scale parts. Contributions on this method are discussed in chapter 5.

2.5.2.1 Self-assembly

Self-assembly is the spontaneous organization of molecules or objects, under steady state or equilibrium conditions, into stable aggregates. These 2D and 3D

aggregate are not necessarily at the global minimum in energy. Here, the objects are driven by non-covalent forces that are selectively patterned to provide locking at the interface. The strategies of micro object manipulations rely on the behavior of electrostatic and adhesion (capillary force, pull-off and Van-der-Waals force) forces effects [40]. Here, the surface forces are a function of the medium physical parameters like pressure, temperature, and humidity. Gracias [15] described static and dynamic self-assembly of Meso-Scale Self-Assembly (MESA) to form 2D and 3D aggregates in a liquid medium, wherein the method relies on the selective patterning of the object faces into hydrophilic and hydrophobic sets. The key concept of static assembly is to allow the patterned object to float between hydrophobic liquid (perflourodecalin, PDF) and hydrophilic one (water). Positive and negative menisci are formed above and below the interface, respectively. Where, under Meso-scale, the capillary force is weaker than menisci. And thus menisci of the same shape attract each other and allow object interface. Generally, the microphysics of micro object are highly dependent on the whether manipulation takes place on submerged medium or air. The self-assembly can be classified as follows:

- Dry self-assembly.
- Electrostatic driven self-assembly.
- Wet self-assembly, examples in wet self assembly include surface tension driven self-assembly: Surface tension driven self-assembly has efficiently demonstrated the capability to accurately assemble and align micro parts on hydrophobic binding sites on a substrate. Xiong et. al. [41] illustrated binding

hydrophobic micro components on hydrophobic surfaces which exclusively act as binding sites on hydrophilic background. In their assembly processes, a hydrocarbon oil or melted solder lubricant is applied on the binding site of the substrate. And then it is immersed in water where the lubricant wets exclusively the hydrophobic binding sites and it assist the part's assembly.

2.5.3 Distributed Manipulation

Depending on the introduced concept of distributed manipulation, the technique could be classified by a deterministic serial to parallel assembly process with either sensory or senseless guidance. Extensive hypotheses will be introduced later on in this chapter.

The control methodology for distributed or organized modules array enables parallel manipulations. Takeshima and Fujita introduced the concept of distributed micro motion system (DMMS) which consists of an array of cooperating actuator modules [21]. Here, the actuator array forms an active two dimensional arrays on which the placed parts are manipulated by the force field. Selective computational MEMS modules can provide multiple energy domains capable of manipulating objects, performing analysis and design. Several new key concepts were employed to enable batch micromanipulation systems on surfaces. Here the distributed manipulator is grouped into two classes:

- *Smart particles*: Devices are distributed in the environment with relative locations varying with time. Challenges includes: determination of relative

location, network communication, synchronization, and an example includes smart dust.

- *Active surface devic*e: An automation device with High Precision to handle multiple objects utilizing massively parallel microactuators modules. Such devices are permanently attached to a surface and there is a fixed topography. The devices are coupled to dynamic of the medium which is causing the manipulation part. The challenge is to dynamically recruit neighborhoods of devices to work together to interact with environment.

Modular Distributed Manipulator System (MDMS) are distributed manipulators where many small stationary cells (modules) corporate to manipulate larger objects [15, 16, 17, and 122]. Typical manipulation addresses the task of bringing an object to a particular position and orientations. Distributed manipulation are not limited to known actuation methods but can accordingly be categorized into:

- Air-Flow Distributed Micromanipulation.
- Electrostatic Based Distributed Manipulations
- Electromagnetic Based Distributed Manipulations.
- Electrothermal Based Distributed Manipulations.
- Electrothermal Based Distributed Manipulations.
- Agitation Based Distributed Manipulations.
- Shape memory alloy based distributed manipulations.
- 2½ D flexible surfaces based distributed manipulations.

2.6 Proposed Methodologies for Micro-Distributed Manipulation System (μDMS) for Assembly Process

The actuation principles of the scaled down system result in response that could be approached for parallel manipulation. Actuator methods currently considered include piezoelectric, electrostatic, electromagnetic, magneto-strictive, hydraulic/pneumatic, thermal and shape memory. One particular measure of the fidelity of these actuators is the theoretical maximum amount of work and/or power that can be produced per unit volume occupied by the actuator (called the work density or when scaled by the dynamic bandwidth, called power density). However, the reduction in size limits both applications and functionality performances as function of scale changes from macro, meso-through micron down to nanometer level systems. Considering specific implementations, it is known that some of these methods maintain performance (piezoelectric, hydraulic, and electrostatic) as scales reduce while electromagnetic actuators tend to exhibit reduced work density and thermal-based actuators appear to improve. Chapter 3 will utilize such scale down improvement in thermal based actuation in order to develop multipurpose grippers capable of improved manipulation tasks. Identification of the scales at which different techniques dominate will help the designer to select the appropriate technology for a given application. Such analysis will also provide information about other parametric scaling factors such as drive voltage amplitudes, forces, etc.

Development of methodologies for assessment of MEMS performances becomes emerging in order to seek optimal design method for particular parallel assembly applications. The conventional MEMS design development, shown in Figure

(2.1), is primitively slow and difficult to predict because of fabrication limitations, system demands, testing requirement and design complexity. Thus, basic MEMS development was often based on numerical evaluation device level concepts and designs. However, there is a lack of insight between design parameters and key design factors governing the system.

Concepts based on energy method introduced in the next subsections aim to improve and guide the selection of the actuation and manipulation tasks. The presented hypotheses are based on of conservation of energy and optimality theories. We will restrict the investigation on possible concepts which could be further investigated in future work. However, practical examples are implemented by the end of this Chapter.

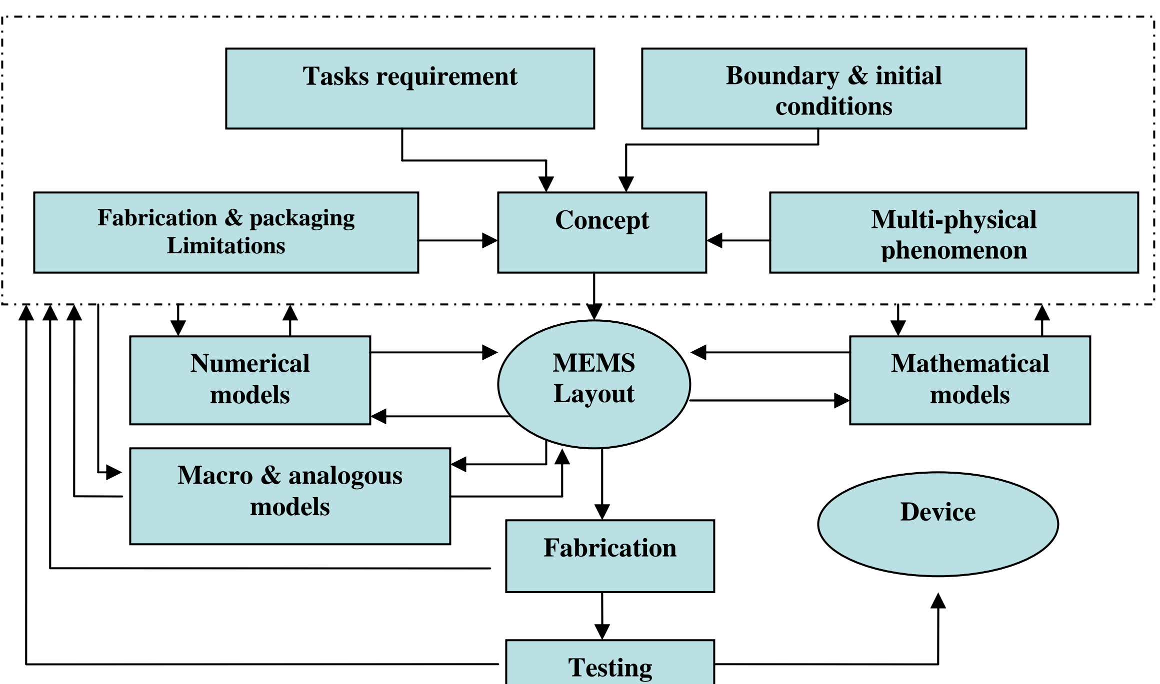

Figure 2.1 Proposed design flow diagram for conventional MEMS development.

2.6.1 Proposed Definitions of (μDMS)

The distributed manipulation environment (DME) is an interdisciplinary concept which was originally developed in Macro applications. The concept of DME for micro-scale systems might be defined here as

Micro-Distributed Manipulation Environment (μDME) is an expandable automation concept based on overall modularity of a micro-manipulation, micro-parallel assembly or micro-manufacturing system including actuation, sensing, control, computing hardware and software.

Alternative definition can also be portrayed as follows

The microscopic actuator array of a Modular Distributed Manipulator System (MDMS) is an enabling technology which can be performed in small scale systems. Its discrete dynamic motion allows the controlled manipulation and transfer of arbitrary object to desired locations.

The basic building block of DME is the Manipulation Module (MM) which consists of up to three units; including actuation, sensory, and processing. The strategies of selecting and exploiting MM across the environment are defined by

- Tasks and manipulation requirements must be achievable such that units must deliver sufficient amount of force. Better approach concepts include controllability, reliability, flexibility, reconfigurablility, versatility, maintainability, expandability to computing platform, power consumption, ease of manufacturing and compactability.
- Availability of Microsystems technologies including fabrication and production.
- The generic features of the actuators suitable for DME, for example, include electrostatic, electromagnetic, fluid power, shape memory alloy, piezoelectric

materials, magnetoresistive material, charge sensitive gel, electroheological fluids, electrothermal material, etc.

- For closed loop control, sensory units are required to determine the state of the location and orientation of objects. However, sensorless manipulation requires the knowledge of the inverse model of modular dynamic system.
- Mechanical and communication interface.

2.6.2 Proposed Definitions Based on Energy Methodology

Let N be a given set of tasks defined by power density cost functions ψ_i. *Assume that the k'th constraint of each available fabrication technology corresponding to an actuator* φ_j *and scale down phenomenon are given by a cost function* χ_{jk} & ω_{jk}, *respectively. Total of* k_j *constraint in each of M actuators is denoted by* γ_{k_j}. It *is desired to seek an optimal set of actuation method(s)* φ_j *such that for given tasks, the evaluation function* E *is optimal in a volume enclose by the MEMS array system.*

- Basic Definitions

The above statement reveals the following set of definitions:

Definition 1:

System consist of the set of M actuation methods that are enclosed in a continuous volume V .

Definition 2:

On each of the M actuation methods, there exist k_j *'th constraint denoted by* γ_{k_j}. *Such constrains are the result of either actuation phenomenon limitation or user defined conditions.*

Definition 3:

Power density or amount of work are candidate cost functions, φ_j*, which are continuous functions in V or subvolume* V_j. φ_j *is a function of L parameters which comprise all input constraints, material and geometrical parameters,* d_l*, that are enclosed in* V.

Definition 4:

The function $\varphi_j = f_j\left(d_1,...,d_L\right)$ *is a state function based on physical law or system identification. The well-defined laws are scalable in domain* Ω *and represent exact model* $\forall d_l \subset \Omega$. *While the identified system models are local in* Ω *and are either experimentally or numerically extracted in subdomain* $\Omega' \subset \Omega$.

Definition 5:

A MEMS array is classified into
First: Set of discrete modules over V given that each module occupies V_j *and is defined by single actuator principle,* φ_j.
Second: Set of discrete Modules over V given that each module occupies V_j *and is defined by set of actuation principles,* $\left\{\varphi : \varphi \subset \varphi_j \forall j\right\}$.
Third: A continuous module occupies V and is defined by single actuator principle, φ_j.
Fourth: A continuous module occupies V and is defined by set of actuation principles, $\left\{\varphi : \varphi \subset \varphi_j \forall j\right\}$.

Definition 6:

A task is defined as
First: a set of states defined by cost function(s) ψ_i*, the path of object motion is infinitesimally continuous on the region of manipulation* $V' \subset V$.
Second: subtasks defined by sets of states. The path in V' *is discrete due to discontinuity in cost function(s),* ψ_i.

Definition 7:

The scale down phenomenon of each actuator is given by ω_{jk} *with total constrain* P_j. ω_{jk} *is defined by*

First: The external force and phenomenon forces in V' including contact forces, van der Waals, adhesion forces, electric dipoles, meniscus effect and Casimir forces.
Second: Losses and transfer of energy to the complementary volume $\bar{V}'$, including heat, mechanical work, magnetic flux, photons, chemical reaction,,… etc.

2.6.2.1 Problem Formulation

Let φ, ψ and ω be the selected functions based on potential energies, then the following equation holds

$$\sum_{i=1}^{N}\int_{V}\psi_i\left(d_1,\ldots,d_L\right)dV=\sum_{j=1}^{M}\int_{V}\varphi_j\left(d_1,\ldots,d_L\right)dV-\sum_{j=1}^{M}\sum_{k=1}^{P_j}\int_{V}\omega_{jk}\left(d_1,\ldots,d_L\right)dV \tag{2.1}$$

Subjected to $\chi_{jk} \,\&\, \gamma_{k_j}$ for $j=1,\ldots,M$, $k=1,\ldots,P_j$.

It is desired to find rules such that requirements

- *"To find an optimal or nearly optimal set of actuations for given tasks and constrains"*
- *"To find the optimal distribution of actuator network given tasks and constrains"*
- *"To find number of actuators that are required to perform tasks under constrains for specified type of actuators".*

2.6.2.2 Optimization Objectives

Hypothesis: 1

Let evaluation function E be given by

$$\mathrm{E}=\sum_{j=1}^{M}\lambda_j\sum_{i=1}^{N}\kappa_i\frac{\partial\varphi_j\left(d_1,\ldots,d_L\right)}{\partial\psi_i} \tag{2.2}$$

Subjected to $\chi_{jk} \,\&\, \gamma_{k_j}$ for $j=1,\ldots,M$, $k=1,\ldots,P_j$.

where $\vec{\lambda}$ & $\vec{\kappa}$ are weight vectors corresponding to desired action and task, respectively.

Then

(1) The solutions of the sets

$$\frac{\lambda_1 \partial\varphi_1\left(d_1,\ldots,d_L\right)}{\partial\psi_i} = \ldots = \frac{\lambda_j \partial\varphi_j\left(d_1,\ldots,d_L\right)}{\partial\psi_i} = \ldots = \frac{\lambda_N \partial\varphi_N\left(d_1,\ldots,d_L\right)}{\partial\psi_i}, \qquad i=1,\ldots,N$$

correspond to extremes at which an actuation method change is sensitivity to a given task.

(2) $\mathrm{E}\left(d_1,\ldots,d_L\right)=0$ implies that task(s) can not be accomplished with the given actuation method(s). $\mathrm{E}\left(d_1,\ldots,d_L\right)=\infty$ indicates that there is no task assignment.

Hypothesis: 2

Let η_{jr} be a function that describes the relation between design parameters $\left\{d_1,\ldots,d_L\right\}$ and desired system characteristic f_{jr} of an actuation method described by φ_j i.e. $f_{jr}=\eta_{jr}\left(d_1,\ldots,d_L\right)$. A weight factor δ_r describes the scale of desirable actuation method. A near optimal actuator selection is the score that maximize weighted characteristic systems, the score is defined by function

$$S=\max_j\left\{\sum_{r=1}^{R}\delta_r\sum_{l=1}^{L}\frac{\partial\eta_{jr}\left(d_1,\ldots,d_L\right)}{\partial d_l}\right\}, j=1,\ldots,M . \tag{2.3}$$

2.6.2.3 Assessment of μDMS Actuation Methods

μDMS could be assessed from their actuation method which accordingly can be classified into

- *Electrostatic actuation.*
- *Fluidic and pneumatic actuations.*
- *Piezoelectric actuation.*
- *Electromagnetic actuation.*

- *Biological actuation.*
- *Chemical actuation.*
- *Shape memory alloy actuation.*

For example*, s*mall scale motion of micro actuator through the attraction of two parallel plates is given by $F = \varepsilon A V^2 / d^2$ [125], where *d, A, V and* ε are distance between plate, plate area, potential difference between two plates, and medium permittivity. On the other hand, MDMS based on electromagnetic actuation provides good driving force with reasonable ranges of frequency response. The major disadvantage is non-linear relationship between force and stroke, and heat generated in coil. An object of mass *m* in an electrical field generated by coil can be approximated by [126]

$$F = m\frac{d^2x}{dt^2} + b\frac{dx}{dt} + kx = \frac{I^2}{2}\frac{dL(x)}{dx} \qquad V_0 = IR + L(x)\frac{dI}{dt} + \frac{dL(x)}{dx}\frac{dx}{dt}$$

where, *x, I,k,b and L* are position of object, current in coil, spring constant, damping constant and inductance of air coil gaps. In summary, a comparison between the actuation methods is summarized in Table 2.2.

Table 2.2 Actuation methods comparison. [126, 127 and 128].

Actuator Technology	**Assessment Criterion**							
	Controllability	**Deriving force**	**Frequency Response**	**Cost per Element**	**Power Consumption**	**Reliability**	**Scalability**	**Approximate Order(J/cm^3)**
Electrostatic	Very Good	Very Good	Very Good	Very Good	Very Good	Very Good	Very Poor	~0.1
Electromagnetic	Fair	Fair	Good	Good	Poor	Poor	Good	~4
Fluid Power	Fair	Good	----	Poor	Good	Very Poor	Fair	--
SMA	Good	Good	Poor	Fair	Poor	Good	Fair	~10
Piezoelectric	Very Good	Very Good	Very Good	Poor	Good	Good	Good	~0.2
Magnetoresistive	Good	Very Good	Very Good	Very Poor	Poor	Good	Fair	--
Expanding Gels	Good	Poor	Poor	Very Good	Poor	Good	Very Good	--
Electrothermal	Good	Good	Good	Very Good	Fair	Good	Good at low scale	~5

2.6.2.3 Proposed Examples on μDMS

The dynamics of an object translating and rotating on particular supporting set of cells requires the synthesis of field traction forces. Such forces result from the in and out of plane forces which exist between cells and object. Several forces appear as a result of scaling down, including Van der Waal, elastic support, electrostatic forces, etc. The next examples portray the applications of the μDMS concept:

- **An Electrostatic μDMS**

We fabricate an active surface device based on the overall modularity of the resonating units which are able to rotate, position, and flip micro-object. Each building block is composed of four suspended cantilever beams with different compliances, shown in Figure (2.2). The basic goal of such array is to reduce the control complexity. In each building block, it is predicted that an identified input shape signal will electrostatically resonate each cantilever beam i. Thus, using the input of a single power supply is sufficient to provide a directional squeeze field force in all modules. This is accomplished by applying a voltage amplified signal between the handle layer of silicon die and the metal coated device layer. It is important to mention here that the SOI fabrication method allows only 2 microns of separation between the resonating cantilevers and the handle layer surface. Thus, backside etch holes will be fabricated to prevent both structural damping and shorting the circuit. Alternative method for simultaneous resonating of each cantilever in a unit is conducted by externally vibrating the die, wherein cantilever beam induce directional taping forces at structures

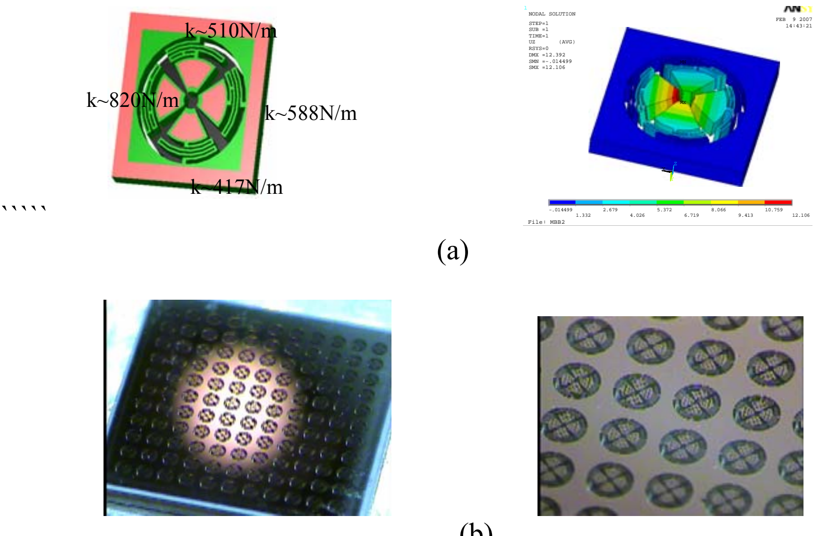

Figure 2.2 Proposed μDMS based on agitation. (a) Solid model and FEM of thebasic building unit. (b) Array of suspended cantilever cells fabricated on $1cm^2$ SOI die.

resonances. Vertical wave component is possible to obtain from piezoresonator attached to the die's base.

- **An Elastic Support μDMS**

More often, the application of object manipulation requires conformal support of a rigid object resting on a flat surface to surface contact, where the object surface is resting on set of n cells on domain Ω and shown in Figure(2.3). The gravitational forces at micro-scale become insignificant as compared to stiction, electrostatic, hydrophilic and magnetic forces. However, in this example, it is assumed that the gravitational force is dominant, particularly for objects of meson scale ranges. Consider an arbitrary object of weight W, whose center of mass is located at $\overrightarrow{X}_{cm} = \begin{bmatrix} x_{cm} & y_{cm} \end{bmatrix}^T$. The object is

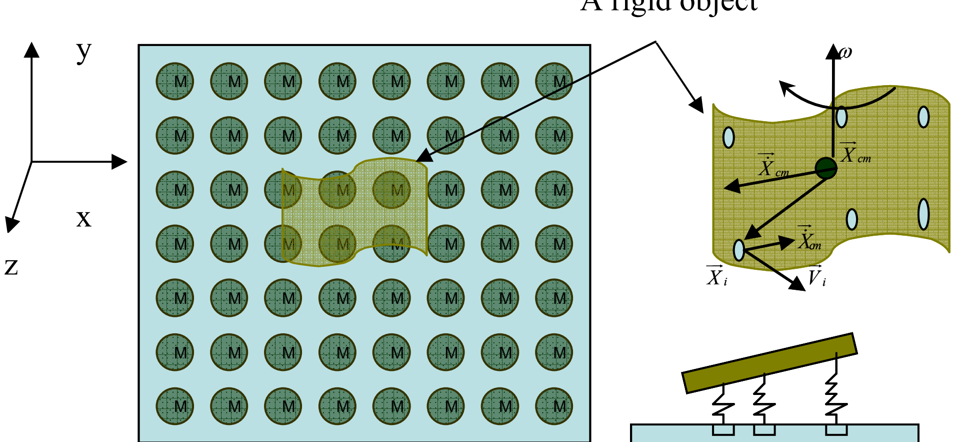

Figure 2.3 Proposed μDMS based on micro elastic support.

supported and is at rest, i.e. static, by the applied vertical normal forces $\vec{F}_g = \begin{bmatrix} F_1 & \dots & F_n \end{bmatrix}^T$ .Solving for *n* supporting forces requires the consideration of equilibrium of the object in both the vertical (*z*) direction and the rotation about the *x* and *y* axes. The center of locations of the *n* cells is arbitrarily arranged in x & y vectors

$$X = \begin{bmatrix} \vec{x} \\ \vec{y} \end{bmatrix} = \begin{bmatrix} x_1 & \cdots & x_n \\ y_1 & \cdots & y_n \end{bmatrix}^T = \begin{bmatrix} \vec{X}_1 & \cdots & \vec{X}_n \end{bmatrix}. \tag{2.1}$$

The vertical equilibrium of the object satisfies the following equation

$$\sum_{i=1}^{n} F_{gi} = W = I_{1\times n} \vec{F}_g^T \tag{2.2}$$

where $I_{1\times n}$ is a unit row vector. The equilibrium rotational moment induced by normal forces is formulated about x and y and satisfies

$$\sum_{i=1}^{n} F_{gi} y_i = W y_{cm} = \vec{y} \vec{F}_g^T \qquad \sum_{i=1}^{n} F_{gi} x_i = W x_{cm} = \vec{x} \vec{F}_g^T \ . \tag{2.3}$$

Thus far, three necessary conditions are imposed for the equilibrium of an object resting on *n* elastic modules. The remaining *n-3 unknown forces* can be solved by

considering the prototype flexibility of each module in the array. Consider each module to be an elastic spring, then each i'th module experiences a compression force given by $F_{gi} = K_{ei}\Delta z_i$. Assume rigid object whose body deformation in x and y is negligible, therefore we can write the plane equation of the object with respect to assigned coordinate. The plane equation is satisfied at any point in the object, thus

$$z_i = a_1' x_i + a_2' y_i + a_3' . \tag{2.4}$$

Where $a_1', a_2' \,\&\, a_3'$ are the coefficients of a planar surface. The balancing reaction force is obtained by multiplying equation 2.4 with prototype (modules) stiffness's

$$K_{ei} z_i = F_{gi} = a_1' K_{ei} x_i + a_2' K_{ei} y_i + K_{ei} a_3' . \tag{2.5}$$

Large portion of distributed manipulation is based on array of repeated modules, herein; it is assumed that the spring constant is the same for every unit of multiple-unit array. Similar assumption was followed for macro manipulators [50], and will be shown to be analogous with the result obtained herein for meson scale components. Therefore, in addition to previous 3 equilibrium equations, additional n equations are provided to solve for $n+3$ unknowns

$$F_{gi} + a_1 x_i + a_2 y_i + a_3 = 0 . \tag{2.6}$$

The set of algebraic equations can be represented in a compact matrix formulation

$$\left[\begin{array}{c} \vec{F}_g \\ \hline \vec{a} \end{array}\right] = \left[\begin{array}{c|c} I_{n\times n} & A^T \\ \hline A & 0_{3\times 3} \end{array}\right]^{-1} \left[\begin{array}{c} 0_{n\times 1} \\ \hline \vec{w} \end{array}\right] = \left[\begin{array}{c|c} I_{n\times n} - A^T\left(AA^T\right)^{-1} A & A^T\left(AA^T\right)^{-1} \\ \hline \left(AA^T\right)^{-1} A & -\left(AA^T\right)^{-1} \end{array}\right] \left[\begin{array}{c} 0_{n\times 1} \\ \hline \vec{w} \end{array}\right] \tag{2.7}$$

Where $0_{n\times 1}$ and $I_{n\times n}$ are column zero vector of length n and square identity matrix of size n, respectively. The unknown constants are augmented in column vector $\vec{a} = \begin{bmatrix} a_3 & a_2 & a_1 \end{bmatrix}^T$. $\vec{w}$ is a column vector given by $\begin{bmatrix} W & Wx_{cm} & Wy_{cm} \end{bmatrix}^T$. The A matrix corresponds to the individual module location in the coordinate system $A = \begin{bmatrix} I_{1\times n} & \vec{x} & \vec{y} \end{bmatrix}^T$.

In case of similar elastic spring constant, the reaction forces are independent of unknown vector $\vec{a}$. The normal forces are

$$\vec{F}_g = A^T \left(AA^T \right)^{-1} \vec{w}. \tag{2.8}$$

The unknown object slope

$$\vec{a}' = -\frac{1}{K_e} \left(AA^T \right)^{-1} \vec{w} = -\frac{1}{K_e} A^{-T} \vec{F}_g \tag{2.9}$$

In many distributed manipulation tasks, the modules can provide velocity field to object through friction contact of rotary and translational actuators. Examples include scratch drive actuator, vibratory micro-motor, electro-thermal mechanism, etc.

- **Active surface μDMS based on vibratory actuation**

An extended concept of an active surface capable of performing self-assembly and guided translocation could be mathematically expressed and optimized based on energy concept. Using similar notation described earlier, the problem is formulized as follows

Let M agitating load functions $\varphi_j \left(d_1, \ldots, d_L \right)$ *be well-distributed on a surface domain* Ω *such that the total energy field* E *generated on the surface is continuously*

differentiable of C^{-2} class and has a unique global minimum which is traceable in the domain Ω with respect to loads parameters.

On Cartesian domain, an equivalent energy field could be identified by logarithmic radial basis functions based on Thin plate Spline. The energy at *(x,y)* location may be found from

$$E_j(x,y) = a_0 + a_1 x_j + a_2 y_j + \sum_{i=1}^{M} F_i r_{ij}^2 \ln\left(r_{ij}^2 + \varepsilon\right) + C_j F_j = \overline{H}\overline{X}. \quad (2.10)$$

where $r_{ij}^2 = (x_i - x_j)^2 + (y_i - y_j)^2$, and $C_j = 16\pi D / K_j$ is the elastic constant at the interpolated point. K_j, D are the spring and rigidity constant. ε is an additional free constant ranging 10^{-3}-10^{-6} which smoothen the energy distribution.

The unknown vector $\overline{\boldsymbol{X}} = (\boldsymbol{F}_1, \boldsymbol{F}_2, ..., \boldsymbol{F}_N, \boldsymbol{a}_o, \boldsymbol{a}_1, \boldsymbol{a}_2)^T$ are computed from known quantities for the amount of energy produced by each load function $\overrightarrow{E} = (E_1(x_1, y_1)..., E_M(x_M, y_M), 0, 0, 0)^T$, and the unknowns is found by arranging the left hand side equations in (2.10) [129]

$$\boldsymbol{H} = \begin{bmatrix} \boldsymbol{C}_1 & r_{12}^2 \ln\left(r_{12}^2 + \varepsilon\right) & \cdots & r^2_{1,N-1} \ln\left(r^2_{1,N-1} + \varepsilon\right) & r^2_{1,N} \ln\left(r^2_{1,N} + \varepsilon\right) & 1 & x_1 & y_1 \\ r_{12}^2 \ln\left(r_{12}^2 + \varepsilon\right) & \boldsymbol{C}_2 & \cdots & r^2_{2,N-1} \ln\left(r^2_{2,N-1} + \varepsilon\right) & r^2_{2,N} \ln\left(r^2_{2,N} + \varepsilon\right) & 1 & x_2 & y_2 \\ \vdots & \vdots & \ddots & \vdots & \vdots & \vdots & \vdots & \vdots \\ r^2_{1,N-1} \ln\left(r^2_{1,N-1} + \varepsilon\right) & r^2_{2,N-1} \ln\left(r^2_{2,N-1} + \varepsilon\right) & \cdots & \boldsymbol{C}_{N-1} & r^2_{N-1,N} \ln\left(r^2_{N-1,N} + \varepsilon\right) & 1 & x_{N-1} & y_{N-1} \\ r^2_{1,N} \ln\left(r^2_{1,N} + \varepsilon\right) & r^2_{2,N} \ln\left(r^2_{2,N} + \varepsilon\right) & \cdots & r^2_{N-1,N} \ln\left(r^2_{N-1,N} + \varepsilon\right) & \boldsymbol{C}_N & 1 & x_N & y_N \\ 1 & 1 & \cdots & 1 & 1 & 0 & 0 & 0 \\ x_1 & x_2 & \cdots & x_{N-1} & x_N & 0 & 0 & 0 \\ y_1 & y_2 & \cdots & y_{N-1} & y_N & 0 & 0 & 0 \end{bmatrix}$$

(2.11)

This simplified approximation of energy field could be then be optimized to meet the energy criterion defined early in this section. This mathematical concept could

be employed to define new methods for translocation and assembly of micro parts which are attracted to the traceable minimum energy point. In particular, micro parts placed on a surface of a unique global minimum, would move towards that site and preferentially collide. For example, such sites could be used as an assembly platform for self assembly or sequential assembly as will be discussed next chapters. Moreover and if exist, having a tractable minimum energy site will allow one to tune the actuator parameters (mainly amplitude and frequency) such that micro parts could be attracted at any location in the surface. Feasibility study on the energy trapping could be revealed from the discussion provided in Chapter 5.

2.7 Chapter Summary

Modern classifications of the available micro actuation and translocation methods were introduced based on the related manipulation tasks and energy principles. The chapter has extensively illustrated the development of interdisciplinary assembly techniques which aimed at particularly constructing heterogeneous MEMS systems. It is concluded that although of the advanced progress and research experienced for sequential assembly, there are more promising techniques to be further explored. Thus, the scope of this chapter did not only organize materials for better understanding, but also provided platforms and conceptual methodologies necessary to guide the advancement in construction of microrobotic systems as will be discussed in this research.

CHAPTER 3

SERIAL TO HYBRID MICROASSEMBLY SYSTEMS ASSISTED BY IDENTIFICATION OF MULTI-PURPOSE ELECTRO- THERMO-ELASTIC GRIPPERS (METEG)

3.1 Introduction

The development of micromachining technologies has provided wide applications in micro sensing and actuation. Integrating and packaging of an MEMS device in electronic circuits have been demonstrated [5]. However, most of the demonstrated devices are selectively constructed by fabrication processes that are limited to complexity, configuration, dimension, and material variation. A monolithic fabrication has limitations and does not allow the inclusion of multiple components of incompatible processes. Therefore, the construction of 3D microstructures by heterogeneous microassembly is an alternate manufacturing route [95]. During assembly, numerous methods for controlling the pick and place operations have been utilized in the past. Such techniques include: vacuum grippers based on micro-pipettes [33]; manipulators with heated micro holes acting as suction cups [39]; electrostatic force control method [6]; tweezers “grippers” and teleoperated assembly [41]; moisture and surface tension control methods [7]; and roughness change method and force controlled grasping based on an AFM (atomic force microscopy) [43].

A number of standard MEMS fabrication processes could be utilized to fabricate “microgripper” devices, such as LIGA, SOI, MetalMUMPs, PolyMUMPs, FIB, EBL and DRIE [41, 96 and 120]. An electrothermally (E-T) driven micromechanical device based on asymmetrical thermal expansion has led to the development of many microactuators in micro-system technology [45, 46 and 119]. This actuation principle is capable of providing larger deflections and forces compared to electrostatic, piezoelectric, and magnetic actuation principles [47]. However, the high power requirement of typical E-T building blocks such as chevron, bimorph and monomorph thermal actuators causes thermal failures and limits operating force, deflection, heat loss, heat conduction, operating structural frequency, and contact resistance of pads. Thus the design tradeoffs of E-T devices are needed for their practical use. In this chapter we study design trade-offs for E-T microgrippers and exemplify how these end-effectors are fabricated, modeled, and attached onto precision robots for heterogeneous microassembly.

3.2 Design and Fabrication of METEG

Generally, automated task execution in assembly is used to ensure robust assembly and a short cycle time. These are desirable capabilities in microassembly as well. In addition, basic manipulation skills such as pick and place, and nonprehensile manipulation are generally restricted to specific objects. The design of end-effectors should consider the complexity of tasks that can encompass: grasping, pushing, flipping, throwing, squeezing, twirling, smacking, blowing, and heating.

3.2.1 Basic Building Blocks and Integration for Improved Assembly Capabilities

The proposed E-T designs are in-plane 2½D micro-parts form three building block: 1) V shape linear electro thermal actuator, 2) U-shape angular electro thermal actuator and 3) strain structure of square spring shape. The developed devices are categorized in accordance to their operation:

1-**Pick and place of heterogeneous micro-parts** (Silicon MEMS and non-Si MEMS). Examples of such designs are shown in Figure (3.1) Heterogeneous assembly is accomplished by: remove, insert, grasp, place, push, pull, translate and orient micro-parts from their substrates on a chip and join them to other micro-parts at the secondary location. For the microgrippers in Figure (3.1-a, b, and c), the mechanical structure is composed of two basic building blocks: first a V-shape actuator whose apex moves forward as a result force of the thermal expansion of the beams "Chevron" in a symmetrical geometry; and second, the U-shape structure or "folded beam" is based on the asymmetrical thermal expansion of connected beams. The thermal and mechanical operations are tested by capturing thermal image and testing for mechanical deflection, as shown in Figure (3.2). The narrow hot-arm pushes the wider cold-arm and causes the block-tip to open wider.

The Meso- Micro scale gripper in Figure (3.1-a) has a nominal opening of 960μm and it possesses high in plane stiffness which prevents the picked parts from sliding in a noisy translation. Meanwhile, the microgripper in Figure (3.1-b) has 90μm nominal opening and it is optimally designed using FEM simulation in order to provide wide tip opening at low temperature profile.

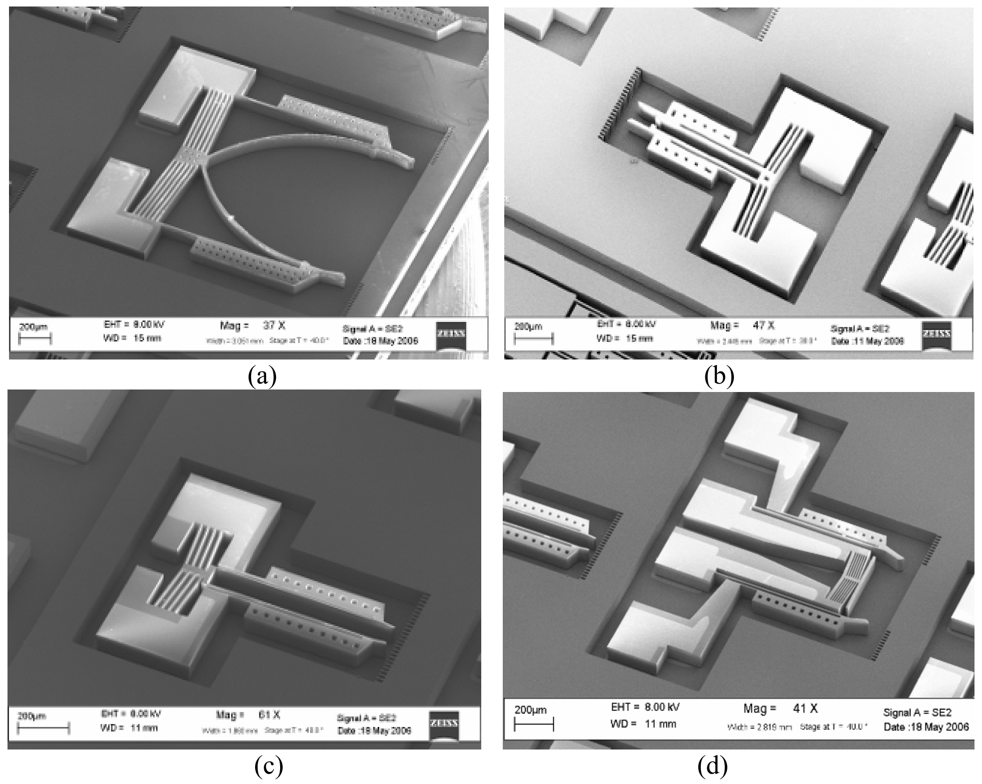

Figure 3.1 Integrated electrothermal microgrippers: (a) Stiff gripper for manipulation of 1000µm cubic blocks. (b) Active gripper with 90um nominal opening and low out of plane stiffness, the integrated block concept is due to work developed on [130]. (c) Active microgripper with 90µm nominal opening and high out of plane stiffness. (d)Micro-heater embedded microgripper with nominal opening of 240µm.

The microgripper structure in Figure (3.1-c) has better opening and out of plane stability than that on Figure (3.1-b). But such enhancement is on the expense of thermal budget which tends to cause much higher temperature at the symmetrical axis of chevron beams.

2- **Joule heating source for joining of micro-parts.** A resistive V-shape microactuator does not only transfer heat flux to the mated micro-part, but also provides external uniform bonding pressure “stroke” through the translation of the apex. Consequently, soldering and welding utilizing a micro-heater are promising techniques

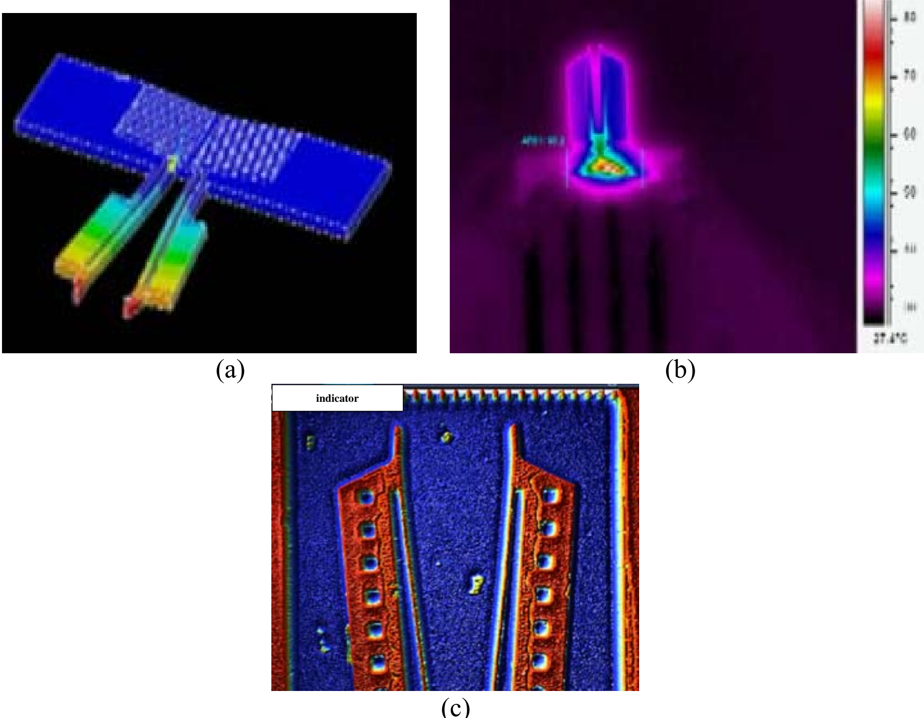

Figure 3.2 Design and test analogy of the thermal gripper: (a) designed of gripper using in ANSYS. (b) Thermal image of a powered gripper at measured steady state conditions. (c) Image captured from motion profilometer [84].

as they can provide an electrical interconnection in addition to a micromechanical joint in assembling 3D microstructures. Moreover, the heat conducted to the micro-part can be utilized as a controlling parameter to overcome adhesive forces that exist between the micro-parts and the tip of a gripper.

Figure (3.1-d) shows a multipurpose E-T MEMS gripper with combined capabilities: 1) basic pick and place which is achieved by the symmetrical opening of a compliant double-U thermal actuator; 2) heat generation element is provided by the dense V beams whose extreme flux “occurring at V shape center line” is conducted into the mating surface; 3) the axial deflection in the Chevron actuator exerts external force

onto the contact surface as shown in Figure (3.4). This bonding force provides good contact interface and thus enhances heat conduction transfer into the micro-part.

We experiment the micro heating concept in METEG devices. Under electrothermal loading the V-shape actuator, shown in Figure (3.3-a), works as a heat source. A porous copper block is machined using Femotosecond Laser Micromachining (FLM) system [124] (see also chapter 5). This micro-part is picked and then is thermally jointed by diffusing aluminum preform on a silicon substrate, as shown in Figure (3.3-b).

3- **Sensory feedback to control, guide, and observe manipulation tasks.** Embedded sensor elements can be calibrated to measure not only the in plane and/or out of plane deflections of MEMS end-effectors, but also the reaction forces which are caused during microassembly.

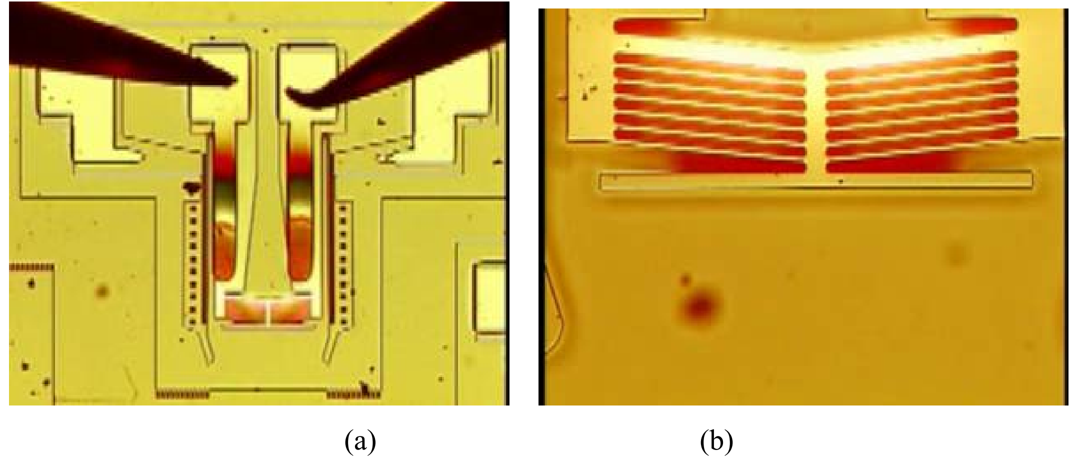

(a) (b)

Figure 3.3 Optical microscopic image of an actuated micro-heater: (a) Heat transferred from fused micro-heater. (b) Bonding and manipulation of small copper blocks.

The MEMS actuator in Figure (3.4) has 960µm nominal grip opening and can perform multi-tasks including pick and place, heating, and sensing. The sensory information is based on the resistivity changes of highly doped silicon [55]. Here, the electrothermal or external force/deflection causes elastic straining in the dual spring. The calibration curve of the sensory feedback is based on strain gauge fabricated in Figure (3.4), is measured at room temperature. Figure (3.5) shows the linear rate of resistance change per unit lateral deflection. The nominal resistance of the total effective strain is 948 ohm with total apparatus and pad resistance of 25 ohm. Other possible sensory feedback methods include combdrive fingers based on electrostatic changes [120], wherein such method has been also implemented in METEG device as will be shown in later sections.

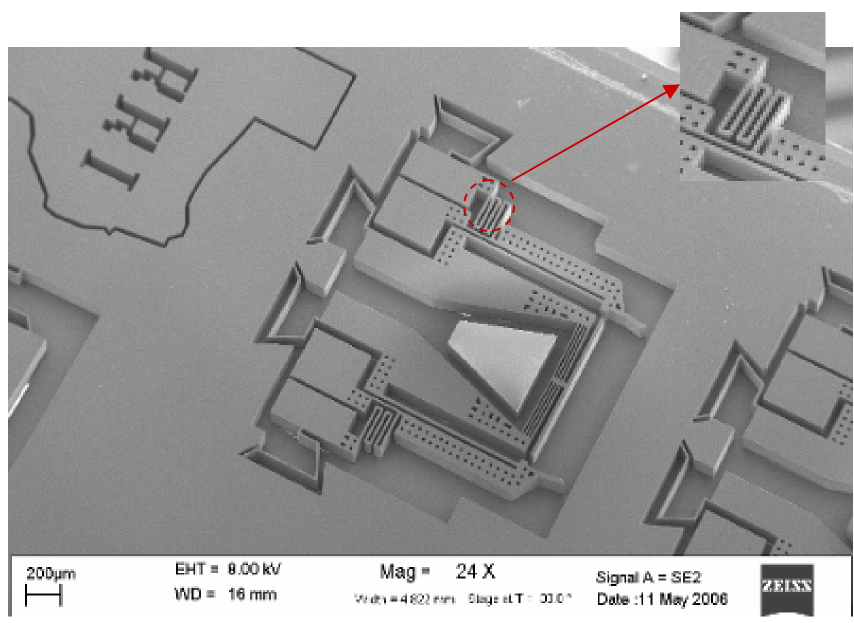

Figure 3.4 Novel design of electrothermal actuator of integrated microgripper, micro-heater and embedded strain sensor.

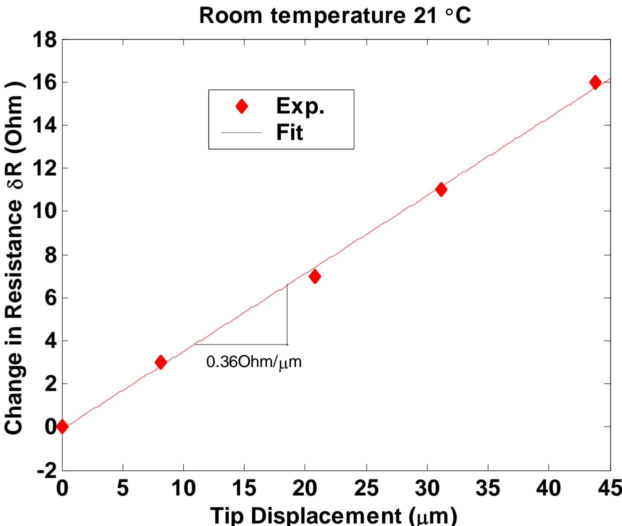

Figure 3.5 Calibration curve of the highly doped strain gauge that is measured at room temperature.

4- **Other types of operations to revert or enhance parts handling.** Examples include design of E-T micro-tweezers and complex integration of multiple E-T blocks. The opening direction of tweezers in Figure (3.6-a, b &cd) is the inverse of a normal gripper. Part picking is either performed by 1) passive insertion under which the gripper is inserted with non-zero contact force and zero input voltage; or 2) active picking with zero insertion force. Figure (3.6-d) shows integrated V and U-shape actuators with an embedded micro-heater.

3.3.2 Methods for Attaching METEG

The complexity of introducing MEMS devices into the 3D microassembly work-cells is illustrated by the need of providing electrical interconnection to their pads. A rigid double layer holder is thus interfaced between the microgripper and the manipulators. A high performance holder essentially provides a package for the

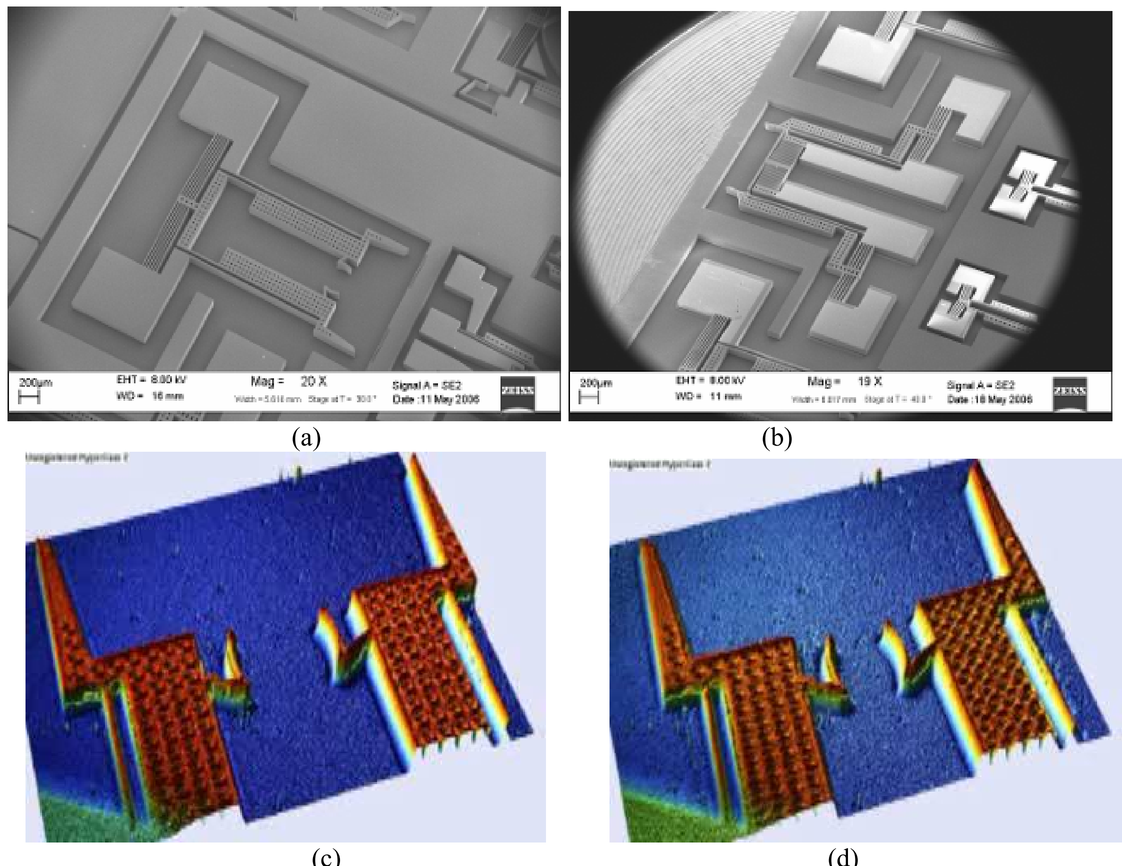

Figure 3.6 Miscellaneous electrothermal MEMS devices: (a) Micro-tweezers "inverted microgripper". (b) 3D motion profile of empowered gripper in 3.7-a. (c) motion profile for inverted motion at powered gripper.(d) Novel micro-heater and an integrated microgripper with V and U shape mechanisms.

interconnected microgrippers and requires mechanical, chemical and thermal stabilities. As a result, ceramic or silicon plates are candidate holder materials than traditional circuit board layers which are easily warped and melted.

Our E-T devices have three pad arrangements (2, 4 and 6). A ceramic holder with gold traces shown in Figure (3.7-a) is suggested. Several techniques can be deployed to firmly attach pads to the holder, which provides a low resistance at electrical interconnections:

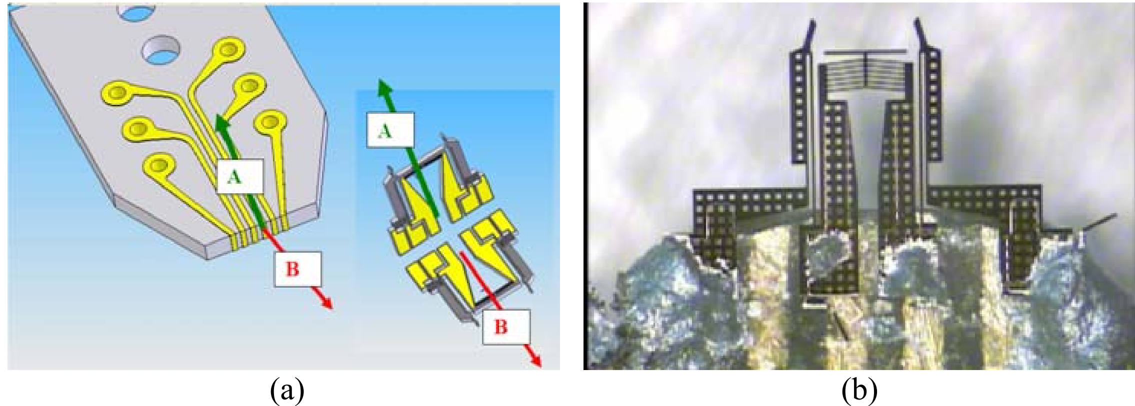

(a) (b)

Figure 3.7 Suggested adapter for interfacing METEG device to 3D microassembly station: (a) suggested ceramic holder with 6 interconnections. (b) A released E-T device is attached to the ceramic holder by conductive epoxy.

1- Applying thermal epoxy at the attachment area of a ceramic face. The microassembly stage is utilized to align and position the gripper relative to the holder. Curing the bonds at prescribed temperature is established by using a hot plate. Next step is to perform wire bonding between traces and gold coated pads on the MEMS gripper.

2- Applying electrical conductive epoxy on holder trace. The actuator is then aligned and attached electrically and mechanically at the same time as shown in Figure (3.8-b).

3.3.3 Processes Based Powering of METEG

After assembling packaged end-effectors, the E-T device can be externally excited by regulating the voltage according to the following classifications:

- *Two pads arrangement:* E-T device requires [0, V] excitation mode. An example is the combined Chevron and bimorph gripper as shown in Figures (3.1-a,b&c and 3.6-a).

- *Four pads arrangement*: E-T devices in Figures (3.1-d and 3.6-d), allow two modes of actuation mechanisms.

a. Sequential excitation of actuators is easily applied by choosing either the gripper or the heater to operate. In this case the pads are excided as follows:

i. To excite the gripper alone, we chose the following strategy: [V-0-0-V] or [0-V-V-0], where V is the voltage excitation corresponding to pad sequence, *i.e.* from right to left (1-2-3-4).

ii. To excite micro-heater/micro-stroke alone requires passing power to the Chevron beam by the following mechanism: [0-V-0-0] or [0-0-V-0], where V is the voltage supplied across the micro-heater pads of the following sequences (1-2-3-4).

b. Simultaneous excitation of a heater and a gripper is obtained by feeding the four pads with the following sequence:

i. [0-V-0-V] provides same voltage for both actuators.

ii. [0-V-(-V)-0] or [0-(-V)-V-0] will provide double voltage to the heater relative to the gripper.

iii. [V-0-V/2-(-V/2)] provides double voltage across the gripper relative to the heater.

- *Six pads arrangement E-T devices* in Figure (3.4): Additional strain sensors are included to correlate the gripping force and deflections. The principle of actuation and pad strategies are similar to four pads and it can be interrupted by the following examples:

i.Excite grippers by [0-0-V-V-0-0]

ii.Excite heater/stocker by [0-0-0-V-0-0]

iii. Excite gripper, heater/stocker by [0-V-0-V-0-0]

iv. Excite sensor alone by [V-0-0-0-0-V]

v. Excite all by [Vs1-V-0-V-0-Vs2], where for quarter bridge strain gauge Vs1=V+Vs2.

3.3.4 An Extended Teleoperated Work-cells for METEG Application

The developed MEMS-based E-T microgrippers are the end-effectors for robotic manipulator work-cells that is sequentially deterministic in principle. 3D-microassembly work-cells have been originally developed at the Texas Microfactory™ [130,133]. In this research we further reconfigure and upgrade system, shown in Figure (3.8), to enable the implementation of serial and hybrid microassembly. Herein, integrated multi degree of freedom manipulators comprise the work-cells illustrate for METEG application:

- Base manipulator with down to top stages arranged as follows: tilt stages, XY translational stages and rotational stage, wherein the work piece is replaceable with two kinds of platforms: (i) a passive workpiece, on which the assembly takes place (ii) high performance hot-plate as a miniaturized assembly platform which is compatible with the cleanroom environment. The assembly field, which is located on the hot plate surface, provides an adjustable temperature that is primarily cooled under natural convention. The said later system comprise of a core conductive material "Aluminum" with through holes drilled for electrical heating-elements and thermocouples. The core metal is insulated by high performance

structure which is machined on low thermal-conductive ceramic. A force sensor is integrated below the hot plate mechanism in order to monitor the exerted force during assembly processes (reaction force between end-effectors and the work piece).

- Two 9-DOF arm-manipulators with the stages arranged from bottom to top as follows: XYZ translational stages, XYZ Nano-positioning Piezocubes, rotational stage and two manual tilt stages. We design a fixture for one arm required to integrated work-cells with the Zyvex ceramic holder [131], This holder has electrical conductive traces on which a our designed microgrippers are attached. The other arm-manipulator has a fixture that we designed here to enable vacuum based gripping. Herein, a micropipette needle produces suction pressure and its tip is utilized to pick micro-devices during assembly process.

The μ^3*-microassembly system* at the Texas Microfactory™ is currently composed of a set of three precision robots with 19 DOFs and described in more detail with most updated configuration is available in reference [91].

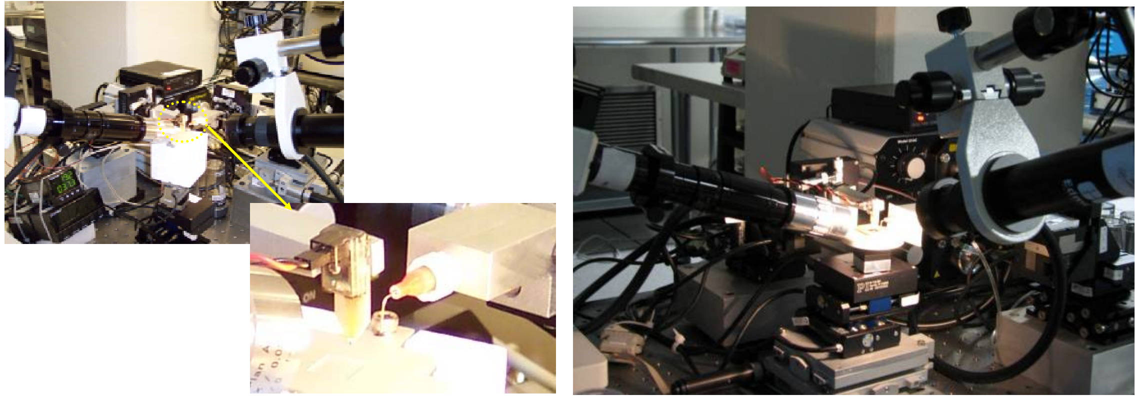

Figure 3.8 Extended microassembly system that is upgraded and configured for serial to hybrid assembly applications.

The μ^3 system relies primarily on serial microassembly process. However, parallel and exponential microassembly and hybrid microassembly have also been implemented in this research on the said μ^3microassembly. We pursue an integrated end-effectors design, thus accomplishing several tasks at once, such as active gripping, heating, and force sensing.

3.3.5 Microassembly Applications Improvement Using METEG

In this section, we demonstrate the use of E-T microgrippers for heterogeneous microassembly. The robots within μ^3 microassembly system bridge the gap between meso, micro, and nano scales. The E-T device is fixed at the end of the flexure arm and attached to a ceramic holder. The silicon pads of E-T device are attached and fixed to the ceramic holder by using conductive silver epoxy. First, an E-T microgripper is interfaced to μ^3 system. Figure (3.9-a) shows the E-T device of 960μm nominal opening that is designed to grasp a metal block $(1000 \pm e_1 \times 1000 \pm e_2 \times 500 \pm e_3)\mu m^3$ in dimension.

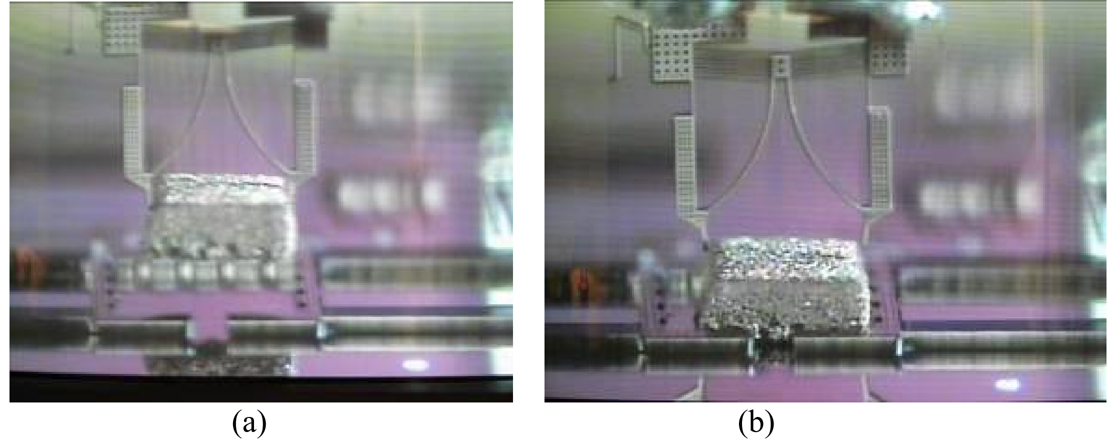

(a) (b)

Figure 3.9 Sequential microassembly performed on MEMS die: (a) Pick up a metal block. (b) Placing metal block onto specified site.

The stiffness of in plane structure provides reaction and clipping force. Releasing or placing task is performed by actuating the device as depicted in Figure (3.9-b).

This gripper and those in Figure (3.10) operate in two modes; *active and passive mode*. Depending on the gripper tip design, an active gripper is electrothermally driven to open and close the tip as shown in Figure (3.10-c), wherein the E-T deflection allow pick and place operations for blocks of manufacturing dimension uncertainty (e_1, e_2). On the other hand, the *passive* gripper, alternative to dummy grippers described in [120], demonstrates the ability to grip parts by forced insertion of trapezoidal tip. Thus, the careful design of METEG structure several applications based on passive pick, push and one-by-one *detethering* tasks, as shown in Figure (3.10-a&b).

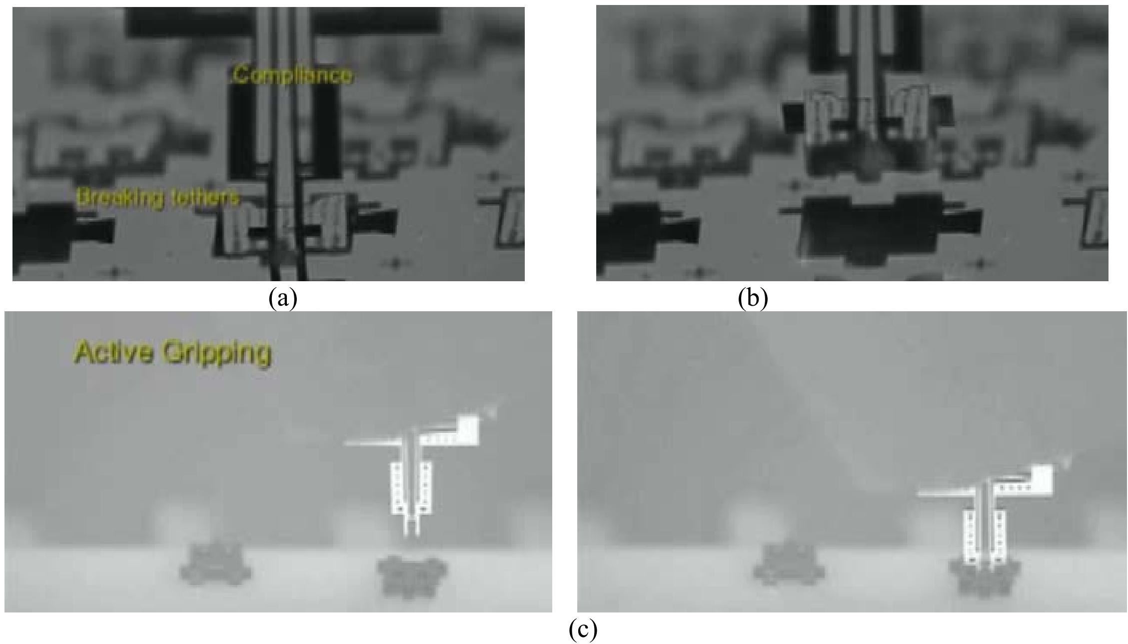

Figure 3.10 Active and passive gripping: (a) detethering from fabricated die and using in plane or out of plane structure compliance. (b) Passive pick up using in plane compliance. (c) Active gripping of a released jammer.

A second demonstration involves fashioning of a micro-part “jammer” assembled into the substrate. The E-T gripper tip is designed to grasp the jammer from the neck of etched holes. The process of grasping a released or tethered jammer, shown earlier in Figure (3.10), requires teleported system equipped with vision system. This is necessary to perform multi-degree of freedom assembly using the developed grasper. A top view of the assembly process is shown in Figure (3.11-a). Such an assembly requires several process sequences: activate the gripper, pick the micro-part, locate and position them to the desired assembly site, activate locking mechanisms on an MEMS die, place the micro-part, deactivate lock on an MEMS die, and finally activate the microgripper in order to release and place the micro-part on its final position as shown in Figure (3.11-b).

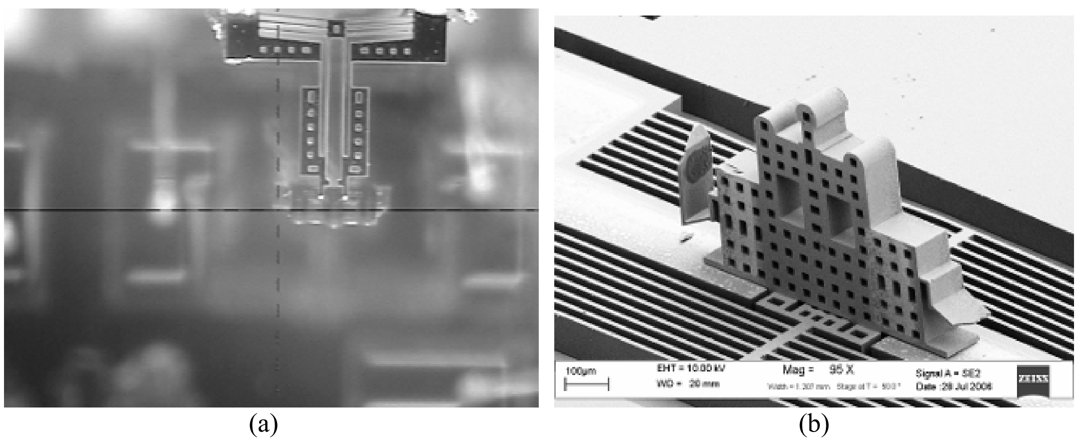

(a) (b)

Figure 3.11 Active microassembly of 3D structure: (a) Top view of a microgripper handling a micro-part. (b) Assembling a micro-part into a locking mechanism on a MEMS die.

Hybrid microassembly is used at the third experiment, by combining sequential pick and place with E-T grippers for the parallel orientation of micro-parts on the substrate. The process is summarized as follows:

- A silicon die with etched holes is agitated to trap and orient the distributed Micro-Meso parts near hole-sites. These sites have local minimum vibration-energy while the unetched surface has higher energy. Figure (3.12-a and b) shows the “spontaneous” positioning of a $1\times1\times0.025mm^3$ metal preform onto the binding sites of an agitated silicon substrate. Piezo-resonators are utilized to create a force field that overcomes sticktion to locate at binding site.

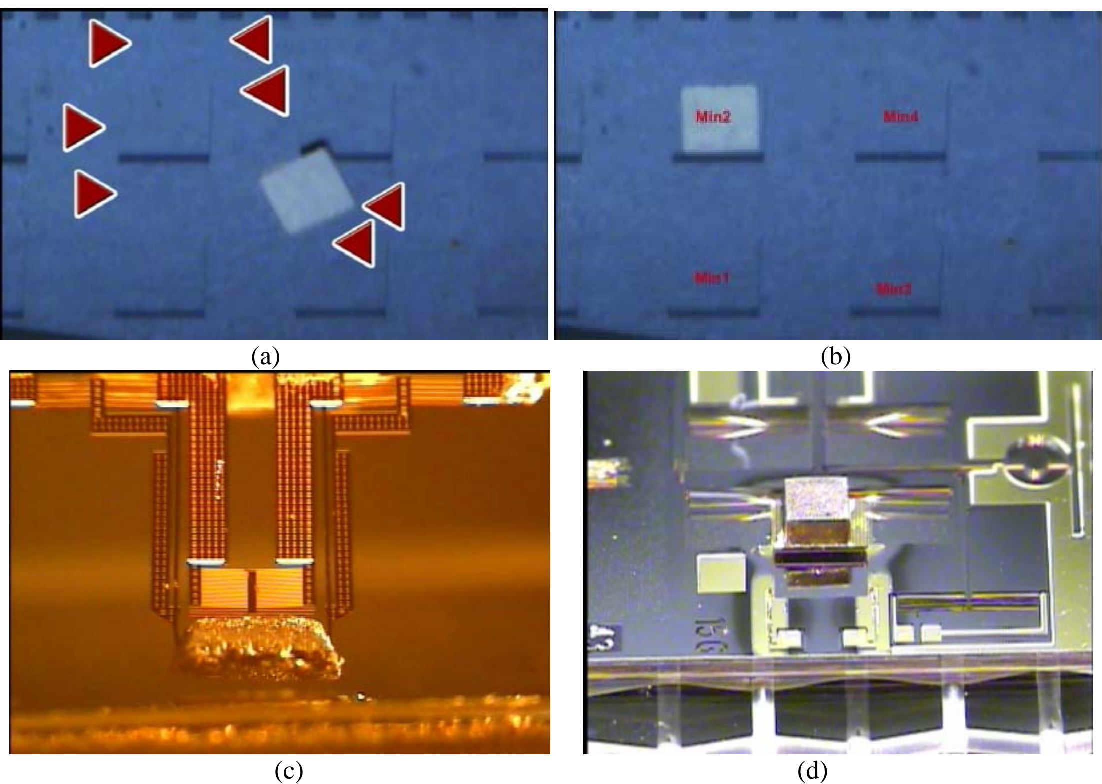

(a) (b)

(c) (d)

Figure 3.12 Hybrid to parallel microassembly: (a) Initial position, the monolithic self-assembly utilizing a piezo based agitation for silicon substrate of etch holes array. (b) Milliseconds after agitating plate. (c) Continuing the sequential assembly on the metal preform which is positioned on a movable structure.

- The silicon substrate is fixed in position and thus the process of detecting parts becomes easier and can be automated (Figure (3.12-c)). Here, the end-effector is translated into binding site to continue the assembly processes.
- The binding site is located at different MEMS die, wherein it is desired to bind place and solders block to the movable structure on the said MEMS die. Herein, the reflow temperature, necessary to solder the copper block onto the movable structure, is provided either by: first heat produced from the METEG joule heating source. Second the heat flux produced from the hot plate the heat developed for MEMS application, as mentioned earlier.

Multiple of METEG end-effectors devices can perform parallel assembly, where the said end-effectors are arranged and embedded on an interface holder as proposed on the Figure (3.13). In such arrangement, quantified pick and place operation could be simultaneously performed, wherein the location of target parts are configured/templated on the sites located on workpiece surface.

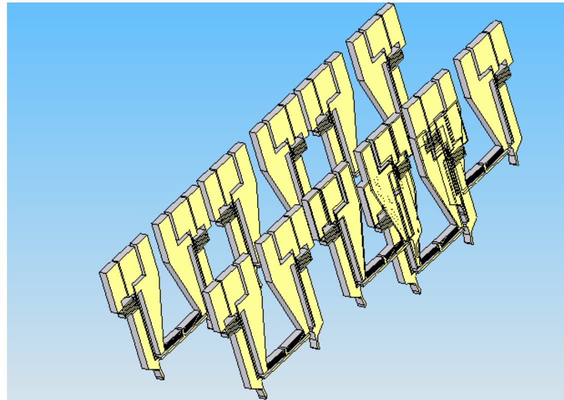

Figurer 3.13 Suggested arrangement of multiple METEG actuators performing parallel assembly.

3.4 Methodologies for Experimental Identification of METEG

3.4.1 Electrothermoelastic Dynamic Response Identification of METEG

The E-T MEMS devices can be characterized using measured electro-thermo-elastic responses. We used two methods to extract a "black box" model for the proposed microgrippers: first, parametric identification based on minimization of the prediction error/Maximum Likelihood method; and second, frequency response analysis. The microgripper in Figure (3.1-b) is *identified* using test signal inputs with 50% duty cycle square shape at amplitude of 16V at frequencies of [20, 70, 100, 180, and 1000] Hz. A 3D MEMS profilometer (WYKO-NT1100) [84] is utilized to measure the static and dynamical deflections of one side of a gripper tip, and they are plotted in Figure (3.14-a and b).

The SISO measurements are identified for several models utilizing MATLAB identification toolbox [85] including ARX, ARMAX, OE and general form models (for more details, see Ljung [86]). Table 3.1 depicts the good fit at different frequency measurements. The parametric identification for the measured outputs due at 20Hz frequency input is plotted for different models as shown in Figure (3.14-c). Higher fitting values show better results as they are defined according to [85, 86]:

$$fit = \frac{100 \times (1 - norm(\hat{y} - y)}{norm(y - mean(y))} . \tag{3.1}$$

where y is the gripper tip displacement at one side and measured in μm.

The simplest representation of a stable continuous transfer function is extracted from OE of order [1 1 1] and at 91% fit:

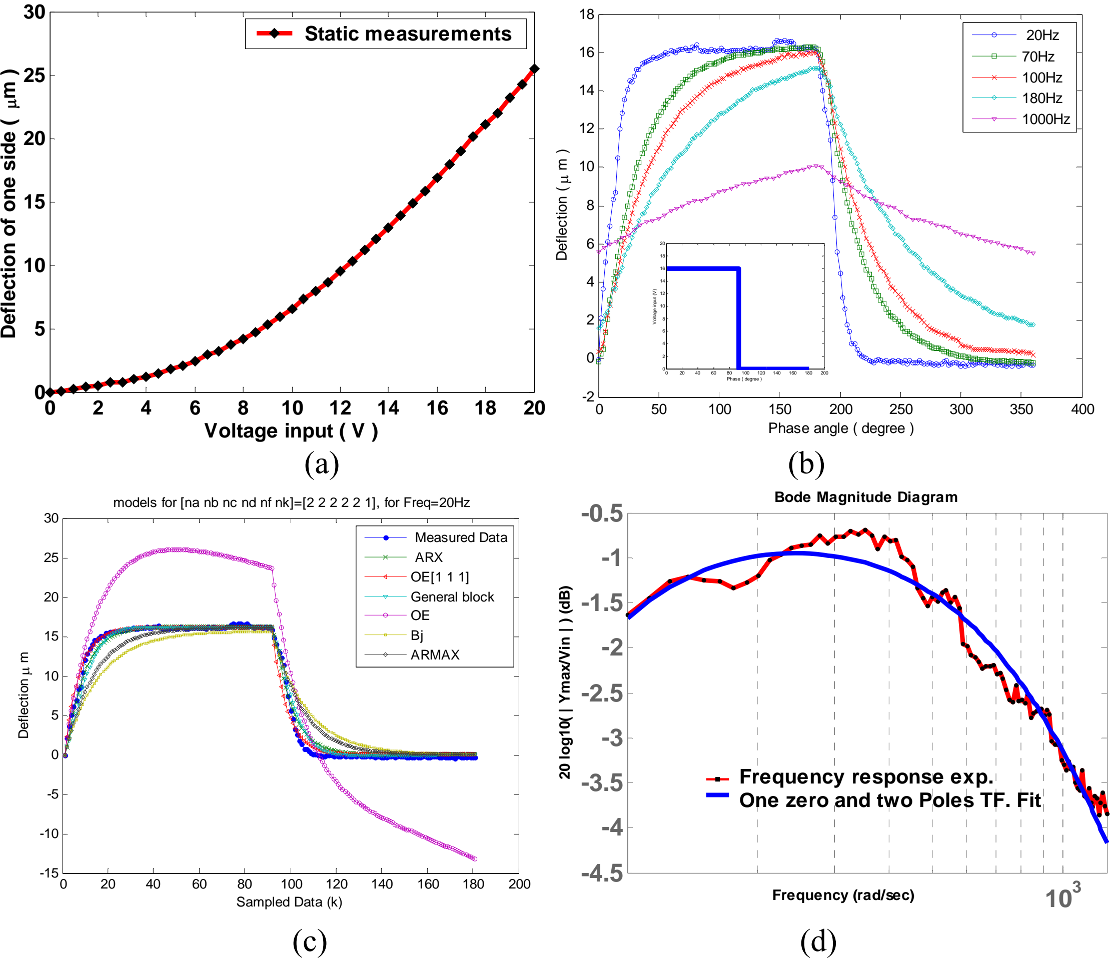

Figure 3.14 Electrothermoelastic dynamic response of the microgripper, in Figure (3.1-b), attached to silicon substrate. (a) Static DC input voltage vs. deflections. (b) The measured deflection responses of one side of gripper tip under square excitation signals and with several frequencies. (c) Estimated tip deflections utilizing several structures and for the sampled measurements under 20Hz square voltage input. (d) Frequency response analysis.

Table 3.1 Good of Fitting at each model of orders: [na,nb,nc,nd,nf,nk]= [2,2,2,2,2,1]

	20Hz	**70Hz**	**100Hz**	**180Hz**	**1kHz**
ARX	91.8060	95.6334	96.8333	96.4295	86.3838
ARMAX	82.0472	97.6175	98.0074	94.8550	82.1597
OE	3.2239	98.0498	98.3867	96.6863	95.4888
OE**	91.2608	94.8697	96.0809	96.2083	86.1107
Bj	78.6741	98.4945	97.7333	96.1127	96.4152
GF	92.0422	97.2156	96.7365	94.6612	85.4628

** The output error order is modified into[1 1 1].

$$y(s) = \frac{3576}{(s+3535)} V(s) + e(s) \,. \tag{3.2}$$

Figure (3.14-b) shows that for this attached microgripper, the maximum operating frequency at which it will recover a full structural cycle (no heat accumulation) is 100Hz.

The frequency response of an E-T microgripper is more informative in identifying the dynamics of a system. A gain curve Bode plot for the microgripper is established by measuring the dip deflection response to pure sinusoidal voltage input, *V(t)*. In Figure (3.14-d), the deflection response, *Y*, of the dip deflection, is plotted for a desired frequency range from 16Hz to 200Hz. It is clear that the response starts damping (roughly as 20 dB/decade) after approaching resonant frequency of 52Hz, hence a first order model is adequate for a good fit. It is important to note that different gripper designs may require higher order models and different model fits at various frequency ranges due to lower resonant frequencies and more nonlinear characteristics.

3.4.2 Static and Dynamic Structural Identification of METEG

The performance of any micro-component affects the overall performance of the system especially in the micro-level. In this section, the thermal and structural performances of a microgripper based on silicon are studied. The present study is part of a larger effort in developing, modeling and characterization procedures toward understanding the behavior of microgripper. This is essential to develop better control algorithms and to facilitate the study of robot arms dynamic on gripping performance.

The structural stiffness and failure of microgripper in static loading are characterized for two actuation modes: in-plane and off-plane. Moreover, building block attempts are introduced for dynamical modeling of microgripper/sensor/ and environment. The electromechanical system model of sensor is experimentally identified and utilized in identifying the performance of hypothesized lumped models of microgripper.

This section addresses the design, manufacturing and testing of a silicon microgripper based on electro-thermal actuation. A method of identifying gripper stiffness is introduced by utilizing a calibrated force sensor. The approach for evaluating static linear stiffness of the microgripper is introduced. In the later subsection we continue presenting methodology for characterizing structural failures in a microgripper.

The dynamic models and the experimental results of the microgripper are also developed. Here, the parametric identification techniques employed to extract unknown parameters in dynamic structures are first introduced. Subsequently, system identification of force sensor/ microgripper are modeled and discussed.

3.4.2.1 Importance of Structural Modeling of a METEG in Assembly Process

Microgrippers are usually designed with micro-precision and controlled in an open loop actuation due to the difficulties associated with obtaining sensory feedback information. Better control of micro-grippers will not only further enhance the assembly of miniaturized devices, but also allow pick and place of heterogeneous micro parts. Effective grasping of delicate objects, such as biological elements [97, 98, 99],

compliant MEMS devices and fibers, requires stable grasping for micro assembly. Thus a controlled force and position at the tip are required in order to keep the components undamaged during manipulation. Therefore, one must first characterizes the failure conditions of the operating microgripper at low operating frequency.

Failures can be defined by structural failure which is caused by overloading and compliance mismatch which is revealed during pickup and place operations [100, 102]. Second, the essence of obtaining dynamic models encompassed in utilizing them in – predicting the behavior of system [103], determining the fault and causes of malfunctions, developing control techniques which increase observability of unknown parameter [101], and finally optimize system . Such models identify the grasping and manipulation conditions of sub-millimeter parts which are not only limited to the robotic but also to the compliant gripper.

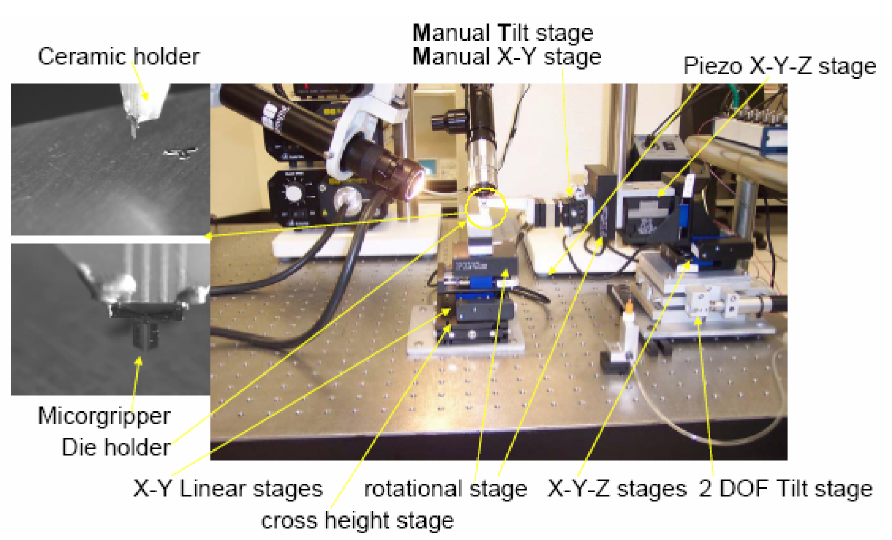

Figure 3.15 Test platform configured in 3D Microassembly system.

The goal of microgripper static and dynamical characterization is to successfully augment microgripper in a precise 3D micro-assembly robot configured to perform the dynamical and static identification. The developed platform has micro-stages and piezo actuators of nano resolution that are operating at macro level workspace, as shown in Figure (3.15).

3.4.2.2 Microassembly Work-cells Setup Based on an Integrated METEG

The design of flexible end-effectors capable of grasping micro-parts made of different materials must encounter the dynamic of robot arms. Researchers assumed approximate models for sensor – manipulator – environment for system identification with a fourth order plant that was used for control law [103, 104]. However, in micro-scale, the plant could be more complex in nature and the resulting models might not provide enough physical insight. Hence, individual analyses of the decoupled systems may serve the goal in modeling and optimizing micro-assembly processes. The complication is referred to the need of end-effectors "microgrippers" capable of performing two main tasks: first, compliant gripper capable of handling micro-part, before and after grasping, without damaging the part in a "passive" mode [100], and second, an "active" mechanism to open and close the gripper tip in order to accommodate a range of grasping and releasing capabilities.

Particularly, this serial microassembly refers to the process of constructing complex micro-systems. It provides for the manipulation of components from their original location of fabrication into their final location in the micro-system. Thus, the

embedded microgripper with the assembly work cells will mainly perform sequential processes to remove, insert, grasp, translate and orient micro-parts from their substrate on a chip and join them to other micro-parts at the secondary location. Moreover, at low rate serial micro-assembly, complex microstructures could be created utilizing high degree of freedom (DOF) robotic stations for assembly. The testing platform setup, shown in Figure (3.15), consists of two manipulators with a total of 16 DOF, vision systems, and controllers operated through LabVIEW. Primarily, and under certain dynamical consideration, such setup will be utilized to characterize the performance of microgripper under static and dynamic loading as introduced in the next subsections.

3.4.2.3 The Deep Reactive Ion Etching of the Tested METEG

The wafer-level MEMS fabrication approach provides simple miniaturized components. A variety of integrated MEMS processes could be utilized to fabricate a microgripper device, such as LEGA, SOI, MetalMUMPS, PolyMUMPS, FIB, EBL and DRIE [97 and 99]. The most basic end effectors used for micromanipulation are made either of tungsten or steel probes. These probes are used to push against micro-objects to move them from one place to another or to reorient them. For example, such probes are used to break tethers which hold micro-parts connected on silicon chips as part of the fabrication process.

The microgripper used in this experiment is fabricated using deep ion reactive etching (DRIE) of silicon. The $1590 \times 1300 \times 50\,um$ structural component is released from the substrate by breaking the tethers. Figure (3.16) shows an electrothermally

actuated gripper attached on a ceramic holder. As current passes through the pads, the current intensity or thermal expansion in hot and chevron beams are higher than cold arm. Thus, the structure configuration combines two actuation mechanisms; first, it allows the chevron mechanism to push the hot arm around a fixture pivot for wider opening, and second, the one hot arm mechanism will provide for wider opening. The microgripper is packaged on ceramic holder and mounted on the robotic arm. This active and passive end-effector or grasper is embedded on the fixture and used for the assembly process.

3.4.2.4 Static Structural Characterization of METEG

Static characterization is described here by defining the equivalent stiffness constants of microgripper and identifying the maximum deflection and loading conditions at which failures take place. In this section, we limit the static analysis to force sensor and microgripper. The environment and robot arm effects have been deliberately minimized in studying the characteristics of force sensor and the off-plane stiffness in microgripper.

- **Force sensor calibration**

A cantilever beam force sensor based on silicon strain gauge [105] is utilized to directly measure the resisting structural and thermal force of microgripper, as shown in Figure (3.16). Proper half bridge completion and data acquisition card have been equipped to this MEMS sensor. Initially, the sensor is experimentally calibrated through

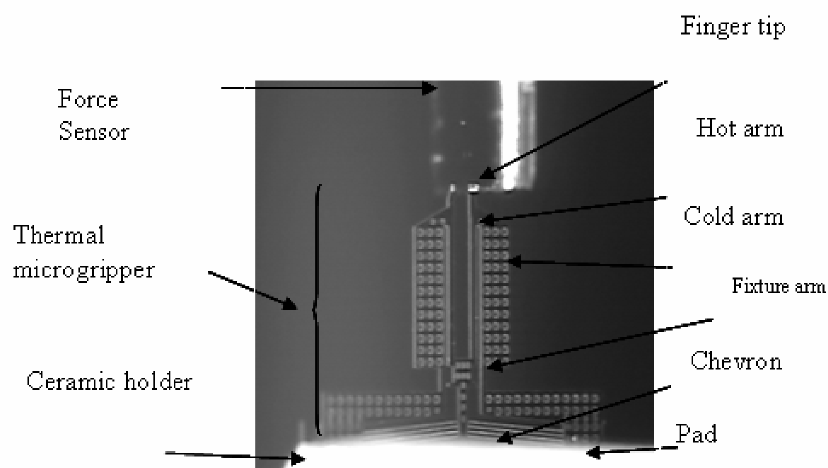

Figure 3.16 Integrated gripper attached to ceramic holder.

two calibration tests. In the first test, a controlled translational displacement is imposed at the tip of the sensor cantilever beam using a rigid edge carried by motorized micro-stages.

The sensor Root Mean Square "RMS" voltage is recorded at each static displacement and plotted in Figure (3.17-a). It is noticed that the sensor operation can be classified into either parabolic stiffness or into two linear regions: 0~40 um with stiffness 917 N/m. and ~40-140 um with stiffness of 1618 N/m. The increase in spring constant might be explained by the appearance of stiffness in the force sensor fixation "environment" which is attached in series with cantilever equivalent spring or to due to slippage caused by a compliant joint.

The second characterization relates sensor voltage output to external forces applied at the cantilever tip by gradually stacking measured weights with the results plotted in Figure (3.17.b).

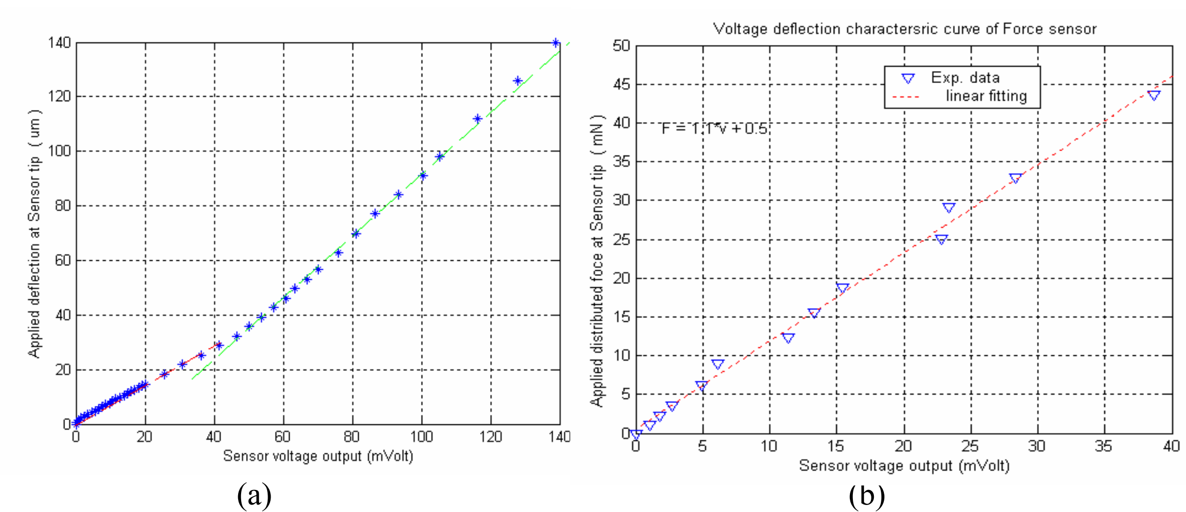

(a) (b)

Figure 3.17 Characteristic curves of force sensor: (a) Displacement-voltage. (b) Force-voltage.

The sensor deflection-force diagram is constructed and exhibits good linearity for both force and deflection sensing as shown in Figure (3.18). The theoretical and experimental stiffness constant of sensor are also shown.

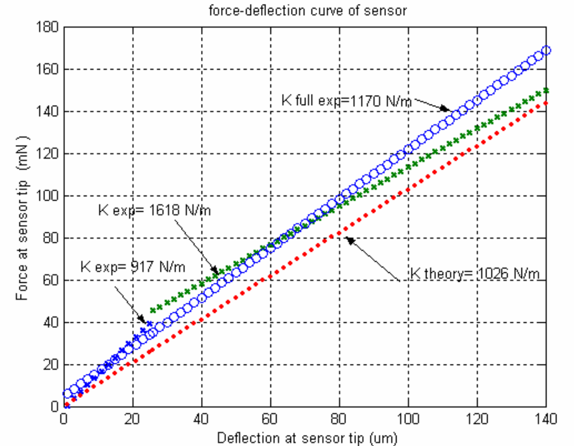

Figure 3.18 Experimental and theoretical spring constant of force sensor measured at tip.

The linear fit of all data reveals a slope of 1170 N/m where the theoretical one is 1026 N/m. This calibrated sensor will be used to measure gripper displacement and reaction force in order to characterize the dynamic behavior of the thermal actuator.

▪ **Microgripper Modeling "*Passive to Active modes*"**

A passive gripper is also defined here by its performance given zero input voltage i.e. no thermal forces. This performance is analyzed upon studying the open loop response for two separate excitations: off-plane force or perpendicular force/deflection excitation applied at tip, and in-plane force or force/deflection excitation applied at tip, as shown in figure 3.19.

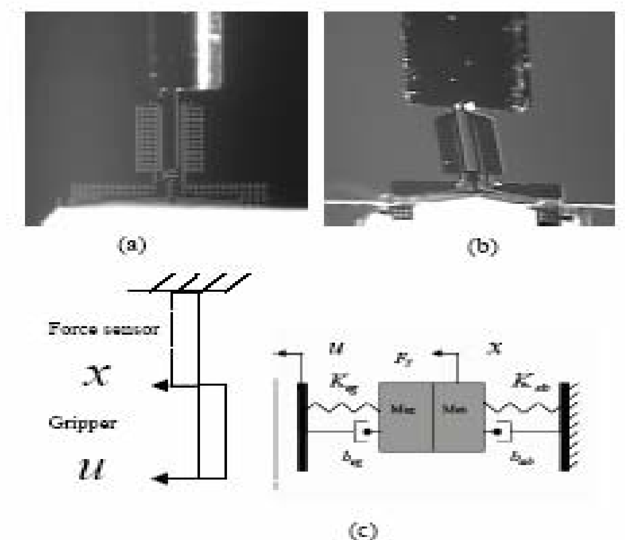

Figure 3.19 Dynamical model of microgripper and sensor cantilever: (a) In-plane and (b) Off-plane microgripper in contact with sensor cantilever tip, and (c) Mechanical equivalent model.

At low frequencies and known force sensor spring constant, the assumed system dynamic models are utilized to extract microgripper spring constants. The microgripper is approximated by a spring mass and damper system. The gripper base is excited (*u*

translation) while the sensor base is held firm as shown in Figure 3.19. The system model is described by

$$M_{eb}\ddot{x} + b_{eb}\dot{x} + K_{eb}x = F_G \tag{3.3}$$

$$M_{eG}\ddot{x} + b_{eG}\left(\dot{x} - \dot{u}\right) + K_{eG}\left(x - u\right) = F_b - F_T\left(v\right) \quad (3,4)$$

$$F_G + F_b = F_T\left(v\right) \tag{3.5}$$

$$\left(M_{eb} + M_{eG}\right)\ddot{x} + \left(b_{eb} + b_{eG}\right)\dot{x} + \left(K_{eb} + K_{eG}\right)x = b_{eG}\dot{u} + K_{eG}u + F_T\left(v\right) \tag{3.6}$$

where, F_T is the equivalent thermal force at gripper tip which is a function of gripper material, geometry and voltage excitation v . $K, M \ \& b$ are the equivalent spring, mass and damper coefficients. Subscripts *G, b* refer to Gripper and force sensor, respectively. F is the reaction force at contact assuming no relative displacement at contact point.

One should notice that if it is desired to control the position of gripper tip, a proper controlled thermal input may be selected according to equation (3.6) – control law development is beyond the scope of this paper but the developed models will be used for control law development. Thus, for a linear system (constant parameters), a pole placement by output feedback may be selected to drive system into a desired position. A practical example of such need in control is in sensitive surgical operation where it is desired to avoid damaging neighborhood area.

At equilibrium, the stiffness of microgripper is calculated from equation (3.6) by setting

$$\ddot{x} = \dot{x} = \ddot{u} = \dot{u} = F_T = 0 , \quad K_{eG} = \left(\frac{x\left(v_i\right)}{u_i - x\left(v_i\right)}\right)K_{eb} \tag{3.7}$$

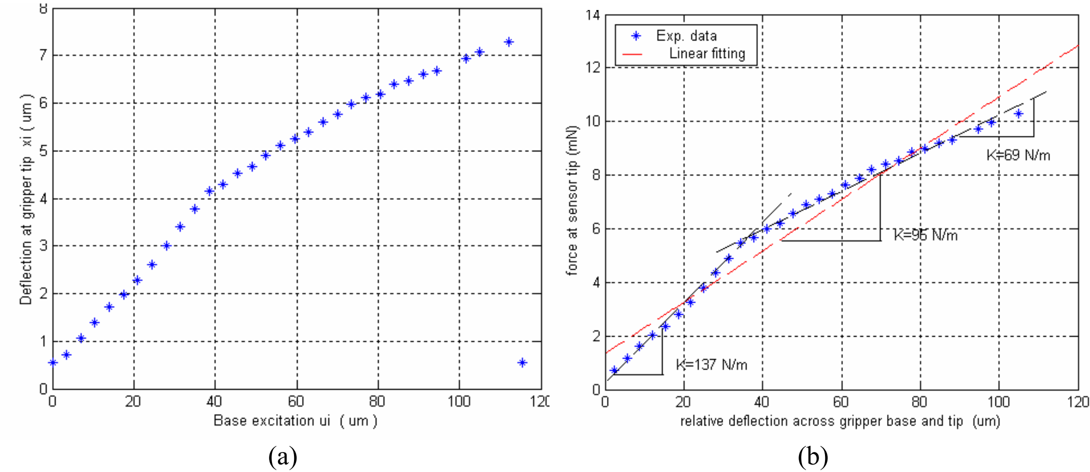

(a) (b)

Figure 3.20 Measurement of in-plane stiffness: (a) Base and gripper displacements for arrangement in fig (3.19-a). (b) Stiffness of in-plane gripper.

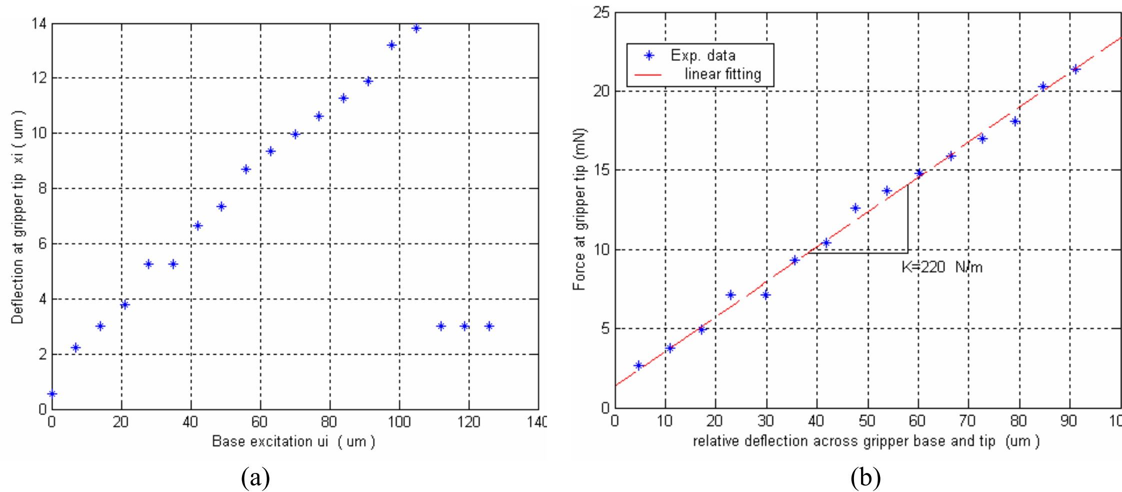

(a) (b)

Figure 3.21 Measurement of off-plane stiffness: (a) Base and gripper displacements for arrangement in fig (3.19-b). (b) Force deflection curve.

where, the contact displacement x is recovered from force sensor characteristic curves. The two stiffnesses for off-plane and in-plane passive gripping are evaluated by relating displacement $x(v_i)$ (a function of sensor voltage) to the controlled base displacement u_i where i indicates a single static measurement. Herein, the said displacements relationship is measured and plotted in Figure (3.20-a) and (3.21-a). It is interesting to

notice that microgripper has nonlinear in-plane stiffness which is attributed to the stiffness contribution of hot beam and chevron structure on flexure arm. The in-plane stiffness of microgripper is obtained by applying equation (3.7) for data in Figure (3.20-b). The average K_{eG}^{In} is ~ 96 N/m for one end-effector tip, i.e. symmetrical portion of gripper**.** The in-plane and off-plane performance of the microgripper were also analyzed using finite element (FE) analysis using ANSYS [92]. The FE models were analyzed for a number of applied loads and the tip displacements recorded. An instance of one analysis is shown in Figure (3.22). For constant parameters, the FE analysis yields an equivalent on-plane spring constant of 307 N/m. It is our belief that the sensor attachment point is not rigid but flexible causing inaccurate data collection. We are currently working on identifying a procedure that would minimize environmental interference and the results will be reported once obtained.

On the other hand, the off-plane stiffness K_{eG}^{off} for both end-effector tips is ~ 220 N/m and depicted from measurement plot in Figure (3.21-b). The off-plane stiffness of microgripper obtained through FE analysis was 212 N/m. An instance of FE analysis is shown in Figure (3.22-b). Here, the environment effects were minimized and the experiment is in good agreement with FE.

The structural failure for in-plane loading is experimentally determined to occur at ~ 110 um tip displacement and ~ 12 mN tip reaction force. The FE analysis reveals that the maximum local stress occurs on fixture pivot for both in- and off-plane loading modes. An in-plane force of ~ 15 mN applied at the tip causes a failure corresponding to 1GPa as obtained from FE analysis. Similarly, the experimental off-plane structural

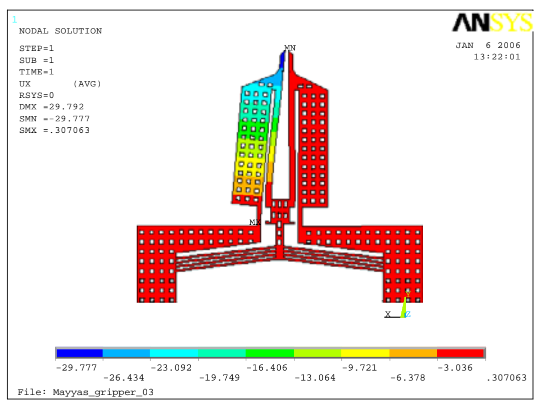

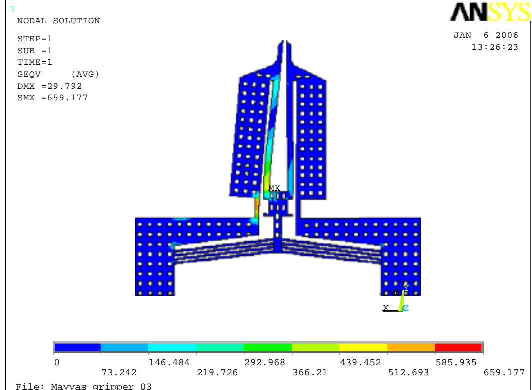

(a)

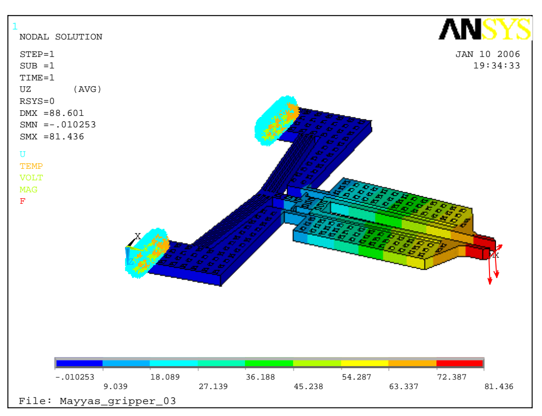

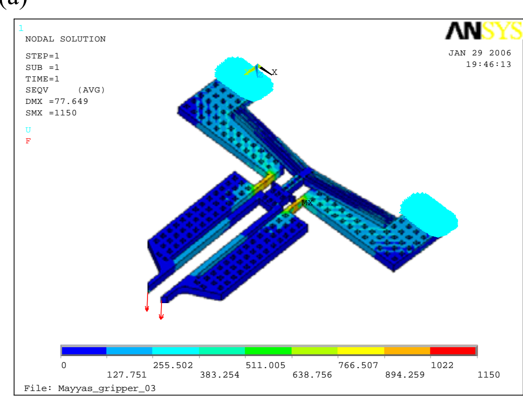

(b)

Figure 3.22 FEM displacement and stress of a METEG (a) in-plane loading. (b) off-plane loading.

failure occurs at tip deflection ~ 98 um and external force 22 mN. The FE model showed that the maximum stress of 1 GPa occurs at the flexure beam corresponding to an off-plane force of 17.4 mN.

3.4.2.5 Dynamic Structural Characterization of METEG

The grasping performance, e.g. stability and accuracy of assembly process, could be substantially improved by selecting proper control techniques which in turn

requires better understanding of the interaction between microgripper and its environment. Examples include picking, placing, insertion, pushing, breaking tethers, etc. Hence, 3D micro-assembly automation primarily requires identifying the plant transfer function. In this section, preliminary work on system identification for force sensor is presented. Brief results of microgripper dynamics are also showed and discussed.

- **Self-Tuning Controller for Parametric System Identification**

The actual dynamic model of a complex system might be approximated or "fitted" into a desired "predicted" model. For example, one shall estimate the parameters of the second order ODE for each active gripper. The spring, mass damper system coefficients could be obtained by coupling a controller with an online "recursive" or off-line parameter estimator that is called self-tuning controller. The process of finding a set of parameters that fits the available input-output data from a plant is shown in Figure (3.23). The most popular identification technique is based on least-squares method and its extension found in ARX, ARMAX, NARMAX, Output-error (OE), Box-Jenkins (BJ), state-space and user defined structure models [101, 86].

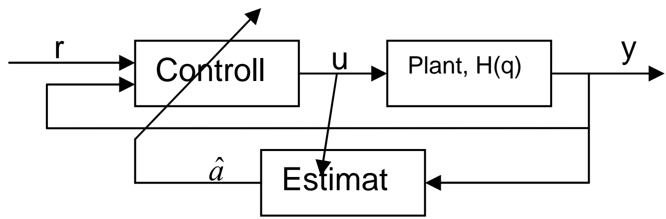

Figure 3.23 Adaptation law in self tuning estimation [86].

The goal of system identification is to utilize input/output experimental data to determine a system model for that operating range. In this work, the identification of system parameters is performed based on the OE model which relates system response to plant and some external error whose dynamic is independent of original plant. For example, one may apply to the system a specific discrete-time input *u(k)*, measure the observed discrete-time output *y(k)* and try to determine the OE's system transfer function from

$$y(t) = \left[B(q)/F(q)\right]u\left[t-nk\right] + e(t) \tag{3.8}$$

where, the plant transfer function is $B(q)/F(q)$, and *e(t)* is the external disturbance caused by either circuits or external vibrations.

- **Identifying sensor dynamic**

The MEMS force sensor is cantilever silicon with strain gauge doped on the neck. The strain gage comprises two resistive elements of approximately $1K\Omega$ each. Half bridge strain measurement circuit is developed and interfaced with a data acquisition card. It is important to note that the sensor should exhibit a faster response than the system to be measured. Therefore, the sensor dynamics should be identified.
The dynamic deflection response shown in figure 3.24, *y*, of sensor cantilever beam due to a ramp input deflection, *u*, applied at the tip is modeled as a second order ordinary differential equation "ODE"

$$M_{eb}\ddot{y} + b_{eb}\dot{y} + K_{eb}y = F_{ext} \approx b\dot{u} + Ku \tag{3.9}$$

The linear transfer function for the plant representing the model in figure 10 is rewritten from equation 3.9 as

$$H(s) = \frac{y(s)}{u(s)} = \frac{(b / M_{eb})s + (K / M_{eb})}{\left[s^2 + (b_{eb} / M_{eb})s + K_{eb} / M_{eb}\right]} \tag{3.10}$$

where, M_{eb}, b_{eb}, K_{eb} are approximate parameters for the equivalent electromechanical system. F_{ext} is the external force due to input velocity and displacement generated by b and K coefficients.

The experiment was conducted as follows: first, the sensor was rigidly mounted against a rigid translating micro-stage with 0.067 um resolution. Then, the micro-stage block was brought in contact with the force sensor tip. A ramp excitation signal is fed to micro-stage in order to translate in a known and controlled manner. Both response and excitation signals were synchronized and stored using a sampling rate of 10^{-6} sec.

The estimation criterion is sensitive for outliers and noise. Thus, two signal preprocessing techniques were used in an effort to enhance Least Square fitting. First, a band stop filter of [0 10] rad/s range is applied in order to capture the dynamics in the defined frequency band and to reduce the effect of white noise.

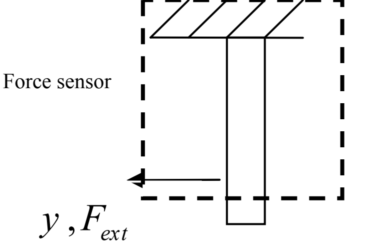

Figure 3.24 Force sensor model.

Second, resampling the output at slower sampling rate of 10^{-4} sec. This is particularly useful if disturbance dynamics have high frequencies compared to MEMS actuator. Figure (3.25) shows the measured, filtered and fitted signals responses to a ramp input excitation. The second order system is extracted using the conditioned signal and estimated using OE discrete model. The equivalent continuous transfer function using first order hold with the slower sampling rate is found to be

$$H(s) = \frac{17.98\ \mathrm{s} + 338.9}{\mathrm{s}^2 + 35.16\ \mathrm{s} + 378.7} \quad . \tag{3.11}$$

The transfer function model in equation (3.11) was simulated with the input from filtered data and compared with measured one. The percentage of the output variation that is produced by the model has a 96.8% fit as shown in Figure (3.25-a). The cross and auto

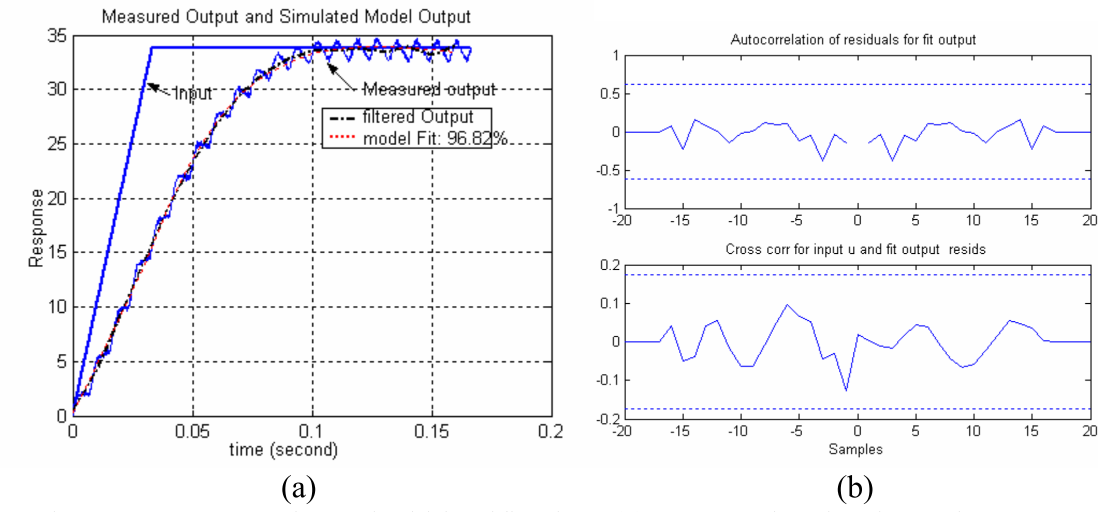

(a) (b)

Figure 3.25 Sensor dynamical identification: (a) measured and estimated system position response at 96.8 % fit. (b) model validation.

correlation functions between input and residuals lie within acceptable confidence region as shown in Figure (3.25-b).

- **Identifying Microgripper dynamics**

As mentioned the microgripper would perform several tasks and at different actuation modes. Mainly, a passive structure mode with no electrical excitation for in-plane grasping. Thus, it is important to understand how the gripper would respond to external in-plane force or deflection due to the microassembly process. Also, the off-plane dynamics of gripper would play a major role in serial and parallel assembly especially for high rate insertion processes. Therefore, the electrothermal and structural interaction should be modeled and analyzed using a representative model due to an excitation voltage that would open the gripper for grasping. An excitation voltage is supplied to the microgripper and the off-plane response is measured with the force sensor using a sampling rate of 9.9e-5 sec.

In Figure (3.26-a), the off-plane gripper and sensor combination is plotted and it exhibits an overshoot. The noisy signal was again conditioned by first using a band pass filter of order 10 with operating frequencies of [0, 10] rad/s, and second by resampling the filtered signal with a slower sampling rate of (9.9e-5 sec) * 110. The resampled signal is fed into Output Error (OE) least square optimization in order to identify the parametric model transfer function.

This model is shown in Figures (3.26- b&c), and relates the gripper tip deflection, x, and base excitation u for open loop system without any thermal forces. The transfer function of this dynamic system based on equation (3.6) is

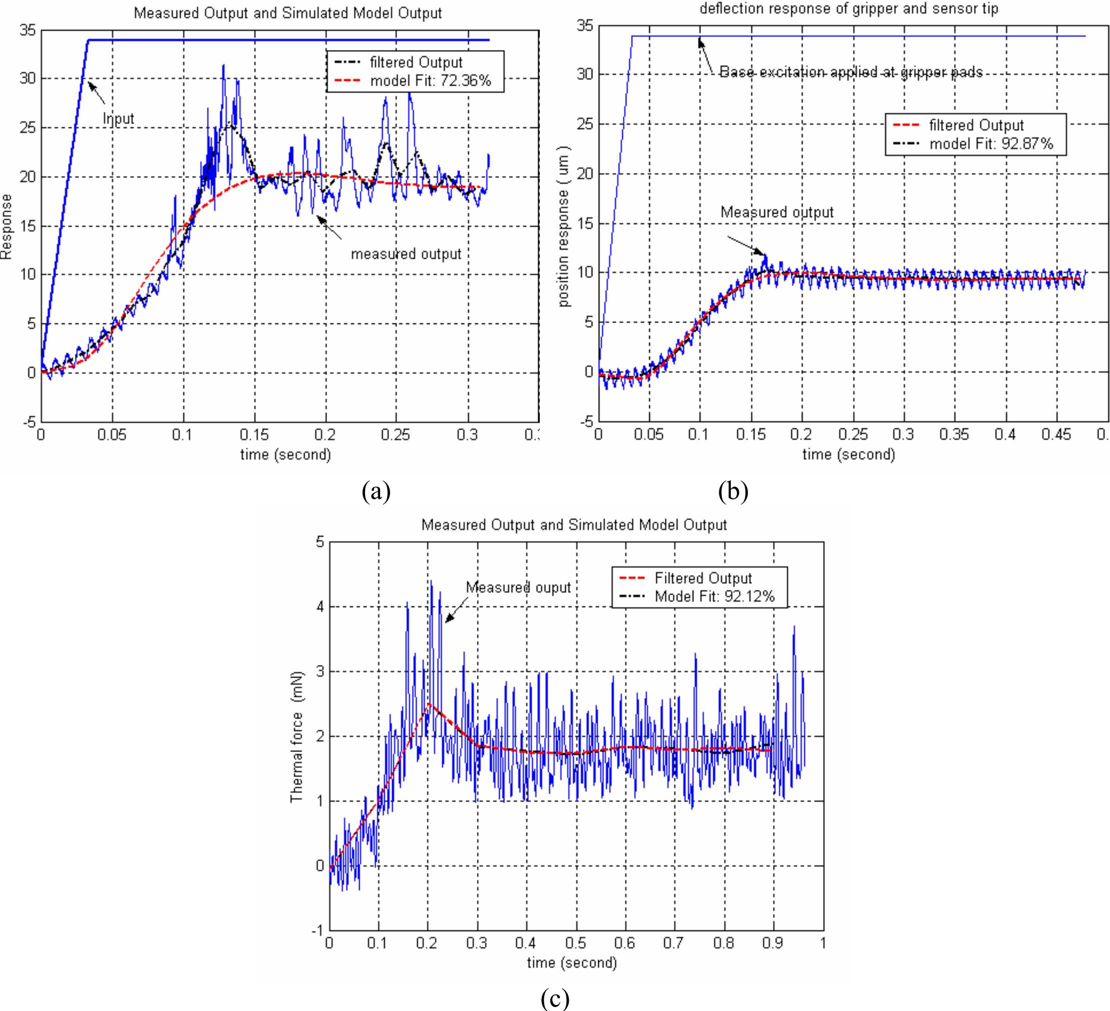

(a) (b)

(c)

Figure 3.26 Dynamical response of deflection and force measured at METEG tip: (a) Off-plane position response. (b) In-plane position response. (c) in-plane thermal force response due to electrothermal input.

$$\frac{X(s)}{U(s)} = \frac{\left[b_{eG}s + K_{eG}\right]}{\left[\left(M_{eb} + M_{eG}\right)s^2 + \left(b_{eb} + b_{eG}\right)s + \left(K_{eb} + K_{eG}\right)\right]}. \tag{3.12}$$

The equivalent fitted transfer function is

$$\frac{X(s)}{U(s)} = \frac{\text{-0.6189 s + 398.7}}{\text{s}^2 + 33.75\text{ s} + 710.8} \quad . \tag{3.13}$$

Similarly, for in-plane operations the combined dynamics are similarly described by equation (3.12). The experimental data obtained for in-plane analysis are shown in Figure (3.26-b). Similar analysis as the off-plane one yields the results in figure 3.26-b and an in-plane transfer function of

$$\frac{X(s)}{U(s)} = \frac{\text{-4.412 s + 190.9}}{\text{s}^2 \text{ + 34.43 s + 694.2}} \quad . \tag{3.14}$$

The dynamic system response due to a thermal force input caused by a 10 V voltage step input was also analyzed. The measured raw data is shown in Figure (3.26-c). The analysis using band filter and resampling using values similar to the off-plane analysis was performed. The transfer function which relates the approximated linear dynamics due the thermal force input is evaluated to be

$$H(s) = \frac{F_{Ther}(s)}{V(s)} = \frac{\text{0.002815 s + 0.03732}}{\text{s^2 + 16.99 s + 291.5}} \quad . \tag{3.15}$$

The equations described in equations (3.12-3.14) assume that there is no environment interference. However, it is apparent from the good of fit obtained with these order models that the fit has a relatively low number (~ 72%, ~ 92%, and ~92%) indicating that higher order models should be used to recover all non parameterized variables.

3.5 Further Considerations on Improving METEG

The voltage drop associated with contact resistance at the E-T gripper contact pads becomes an important issue because of the generated heat. This is apparent for E-T devices that require especially large input power. As a result, the microgrippers become

unreliable after repeated operations, or de-bonded from the holder. We illustrate challenges for the microgripper in Figure (3.1-a) whose characteristics were evaluated by parabolic shape static deflection with total opening of 20μm at 23V, damping deflection in the range of 15-150Hz and resonance frequency at 120Hz. Although electrical conductive epoxy used to attach the gripper has low electrical resistivity, its low melting point can be exceeded when the current drawn by the E-T actuator is large. Accordingly, the overall resistance and mechanical resonance of the E-T gripper varies during continuous or intermittent operation. Solution can be addressed by:

- We can reduce the pad resistance by coating the pad area with metal layers. In addition, coat the entire device face with metal. A 20nm thick chromium layer and a 100nm thick gold layer are used. This metal coat decreases the device power consumption and increases the linear ranges of total resistance. On the other hand, the short circuit, which is caused by metal layers, is disconnected at point that possesses a high melting point. This phenomenon is observed at the longest and the narrowest arm of the microgripper. For a released microgripper operating in an ambient environment, the coated gripper has saturated at 16.33V and 0.156Amp. Meanwhile current of the uncoated gripper saturates at a higher value of 23.4V and 0.274Amp. At saturation, the corresponding total openings of uncoated and coated are 44μm and 32μm, respectively. Obviously, drawbacks in a metal coated silicon microgripper include early current saturation which decreases the deflection.
- An alternative design introduces the package during fabrication process, by fabricating the holder itself out of silicon with DRIE. Figure (3.27) shows the design of

a multipurpose E-T actuator that is attached on the silicon substrate. This device has the capability of combined V and U actuation mechanisms for gripping, V shape resistive heating element and a reliable electrostatic feedback sensor.

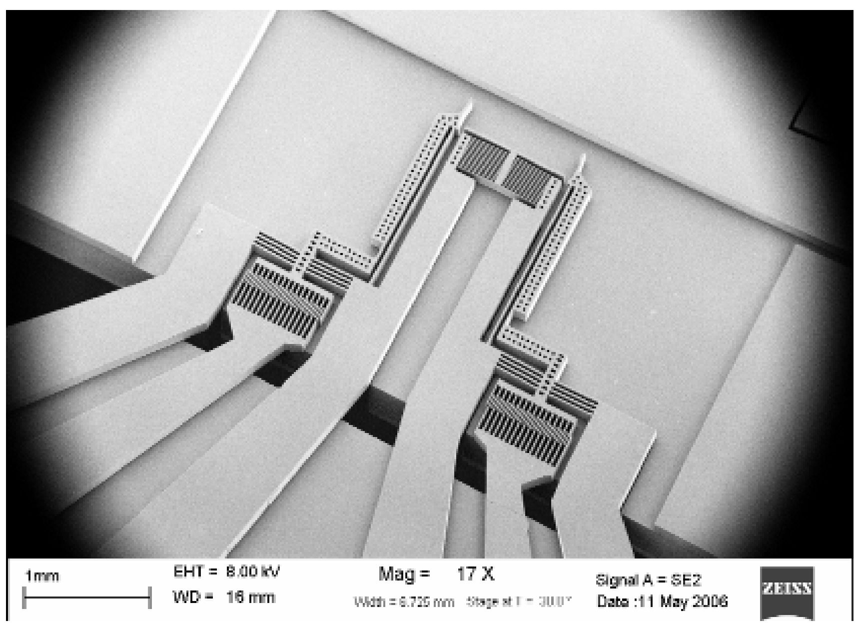

Figure 3.27 METEG and its holder are fabricated on silicon on insulator die.

<u>3.6 Summary and Conclusions</u>

This chapter discussed tradeoffs in design, fabrication, packaging and use of electrothermal MEMS devices for microassembly applications. Examples of E-T end-effectors are fabricated containing three basic design building blocks: actuation mechanisms, heating elements, and feedback sensor blocks. Methodologies to model static and dynamic responses of passive and active microgrippers were also formulated and examined in order to better understand the METEG dynamics for improving 3D sequential micro-assembly processes. The methods described in experimental allowed

determining the static failure of tested microgripper for in- and off-plane modes respectively. The gripper stiffness was also analyzed and compared with FE results indicating good correlation for off-plane but not for in-plane measurements attributed to the influence of the environment. The dynamic models provide a better understanding of microgripper response at high assembly rates. Simplified second order linear models were employed for the force sensor and microgripper and then compared with experimental results indicating that higher order models should be analyzed in an effort to improve the good of fit. The dynamical performance of packaged end-effectors was assessed. Practical challenges in attaching and exciting E-T devices were also discussed. The dynamical performance of packaged end-effectors was assessed. Practical challenges in attaching and exciting E-T devices were also discussed.

The major conclusions of this chapter are summarized as follows:

- The integrated electrothermal end-effectors, which are designed here for sequential microassembly, had broadened the manipulation capabilities during assembly process.
- Sequential microassembly is complex and slow process. Hybrid assembly can enhance process efficiency through integrating auxiliary system capable of massively organizing the micro component on the assembly work piece.
- Experimental identification of devices is essential to efficiently deploy them during assembly processes. Particularly, the fidelity of end-effector can be tested by determining structural responses and failure loads.

- The characteristic of end-effectors varies according to design parameters and packaging conditions. Thus, it is recommended to characterize the electrothermoelastic from their parameters in order to create a platform for optimization. Wherein such optimization increase the yield process of assembly.
- Performing multiple assemblies for several kind of meso- and micro-parts often requires changing the end-effectors. There are no efficient methods available for replacing the electrothermal end-effector during assembly process. However, the fixture which is holding the end-effector could be replaced during the offline modes.

CHAPTER 4

THERMAL MODELING AND PERFORMANCE ANALYSIS OF METEG COMPONENTS

4.1 Introduction

The micro-assembly process of the micro-system technology has recently demanded the development of microgrippers which are capable of handling and manipulation of various micro-components. In the case of electro-thermal driven microgrippers, thermal analysis should be investigated to enhance the performance of microgrippers. Electro-thermal (E-T) micromechanical actuation based on asymmetrical thermal expansion has led to the development of the driving elements in micro-systems technology [106 and 75]. E-T microgrippers have been getting more attention in recent years. Where, the integrated arrays of thermal actuator are capable of providing combined large deflection and force as compared to electrostatic, piezoelectric, and magnetic actuation [75]. However, the input power range of typical building block, such as, chevron, bimorph and monomorph thermal actuators, is limited to thermal failures [80], operating force, deflection, heat loss, heat conduction, the operating structural frequency and most importantly the contact resistance of pads. Thus and similar to most of actuation types, the design of electro-thermal devices are limited to their intended applications.

Several actuation methods, which are utilized in microassembly, were discussed in chapter 2. The emerging phenomena of scaling down of actuator based on thermal expansion are much affected as compared to other types of actuation. Particularly, micro-electrothermal devices posses a faster responses and improved geometrical sensitivity. Such phenomena have been utilized in chapter 3 of this dissertation, wherein the methodology approached had focused on designing multipurpose grippers for sequential microassembly.

This chapter aims at deriving mathematical expression for the modeled of the METEG components. The building block comprising any METEG constitutes of V and U-shape actuators and identified most end-effectors structures discussed in chapter 3. In addition, we have introduced an integrated grippers containing combined performance of U and V shape, wherein a microgripper or micro-tweezers were efficiently utilized in assembly process. In the next sections of this chapter, the thermal performance of the designed electrothermal grippers, or METEG, is established by finding methods to compute: First, the steady state analysis of U-V and integrated grippers. Second, computing the thermal cycle of U and V-components that determines their structural time responses. Third, investigating on the thermal failures that cause METEG to fail during assembly process. Fourth, feasibility studies on the effect of system parameters on the overall performance of a device.

The purpose of the material presented is aligned with the need to optimize the capabilities of the invented METEG. Particularly, such analysis improves the sequential and hybrid assembly themselves, wherein in the previous chapter, we highlighted new

methods that identify structural response of passive METEG. Meanwhile, the next material deals with active components (powered devices) and focuses on exhaustive analytical and numerical approaches for steady state and transient thermal responses.

4.2 Steady State Thermal Analysis of METEG Component

4.2.1 U-Folded Beam "Heatuator" and V-Shape Beam "Chevron"

In a Microelectromechanical System (MEMS), the dimensions of the active and passive components must be properly designed to yield optimized components for manufacturing and functionality. Electrothermal actuators have been active building-blocks in MEMS devices because of the capability to generate large forces and displacements as compared to other types of actuation [41,107,108 and 69]. However, such thermally driven devices have performance limitations which are constrained by the maximum temperatures and allowable thermal stresses [45].

Three types of microstructures identify thermal actuators in micro-systems [70]; overhanging microstructures fabricated by bulk micromachining, suspended microstructures fabricated by surface micromachining; and attached microstructures generally fabricated by IC technologies. In this section, the thermal responses of overhanging microactuators are studied by examining the steady state temperature response/profile caused by varying the magnitude of the pulsating input voltage.

4.2.1.1 Theoretical Model

In a single micromachined layer, the structural layer of thermal device can be thought of as micro-beams connected in series and/or parallel as shown in Figure (4.1) The micro-beams are mostly rectangular bars of different widths and lengths and uniform heights. The thermal response of three sequentially connected micro-beams of different widths is analytically derived for a device hanging over a substrate spaced by a conductive air gap layer. The temperature variation is governed by a nonlinear PDE equation with an input energy source due to current *(I)* with density $J = I/wh$ [69]. A rectangular bar of width w and height h is attached at the anchors and kept at fixed airgap relative to the substrate. The rate of heat change per area is equal to heat production per unit volume per time minus heat losses yielding

$$\rho_d C_p \frac{\partial T}{\partial t} dx = \left(\frac{I}{wh}\right)^2 \rho_o \left[1 + \xi\left(T - T_s\right)\right] dx - \left[-\psi_o \frac{d^2 T}{dx^2} dx + \frac{S}{h}\left(\frac{T - T_s}{R_T}\right) dx + \left(wh_{cu} + 2hh_{cs}\right)\left(T - T_{amb}\right) dx\right] \tag{4.1}$$

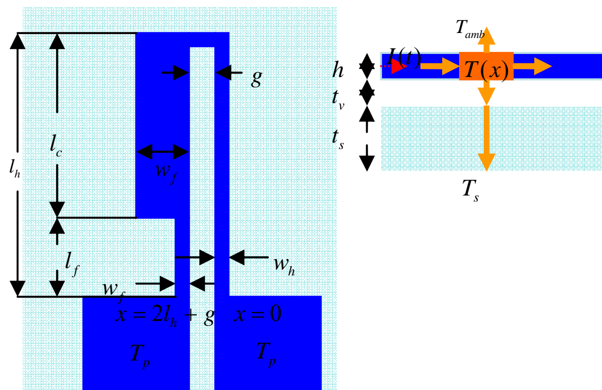

Figure 4.1 Schematic of three serially connected micro-beams.

The shape factor, $S = h/w\left(2t_v/h+1\right)+1$, amplifies the heat flow into substrate[70 and 71]. For micro-beam attached on substrate and spaced by an air gap, the thermal resistance between the micro-beam and the substrate is given by $R_T = t_v/k_v + t_s/k_s$. t_v and t_s are the air gap and substrate thickness respectively. k_v and k_s are the thermal conductivity of air and substrate, respectively. The resistivity of moving material is related to temperature and here it is assumed to have a linear thermal coefficient ξ. The thermal conductivity of the actuator material is ψ_o, and in the current analysis is assumed to be independent of temperature variation. T_s is the temperature of the bottom surface of the substrate and is assumed to be constant. Convection coefficients h_{cs} and h_{cu} correspond to thermal convection heat loss of micro-beam side wall and upper face respectively.

The Steady State Heat Conduction Equation (SSHCE) is obtained by dropping the time partial derivative in equation 4.1. For *n* serially connected micro-beams, the temperature profile is determined by the flowing current I_i or β_i criterion

$$\begin{cases} I_i == \sqrt{\dfrac{k_v k_s \xi w_i \rho_0\left(2t_v + h + w_i\right) + \left(k_v t_s + k_s t_v\right)\left(w_i h_{cui} + 2h h_{csi}\right)}{\xi h \rho_0\left(k_v t_s + k_s t_v\right)}} \\ \beta_i == \left(\dfrac{S}{hR_T} + w h_{cu} + 2h h_{cs} - J^2 \rho_o \xi\right) \end{cases} \quad i == 1,2...n \tag{4.2}$$

In bimorph or U-shaped actuators, *n=3,* the temperature distribution along the three micro-beams is continuous, starts from pad temperatures at hot arm ,*h*, and ends

up with pad temperature at the end of flexure arm, *f*. The total boundary conditions needed to solve the unknown constants in temperature profiles is $2(n-1)+2$.

The temperature profile at considerably low input voltage has been discussed in [69]. In this work, the temperature profile along the microbeams is defined by an exponential function given that $\beta_h, \beta_c, \beta_f > 0$ corresponding to $I_h, I_c \& I_f < I$, and the input current is greater than the right hand side in equation (4.2),

$$T_i(x_i) = T_{\infty i} + C_{1i} e^{\sqrt{\frac{\beta_i}{\psi_o}} x_i} + C_{2i} e^{-\sqrt{\frac{\beta_i}{\psi_o}} x_i} \quad , i = h, c, f \tag{4.3}$$

where $T_\infty = \left(T_s + {J^2 \rho_o}/{\beta} \right)$ and the unknown constants are extracted from temperature profile continuity and boundary conditions. The temperature distribution of a three beam microstructure is continuous starting from pad temperature at hot arm and ending up with pad temperature at the end of flexure arm, and the heat flux is continuous across the arms. The following Dirichlet conditions are applied and used to solve for the six unknown constants,

$$\begin{aligned}
&\boldsymbol{T_h}(0) = \boldsymbol{T_s} \\
&\boldsymbol{T_h}(\boldsymbol{L}+\boldsymbol{g}) = \boldsymbol{T_c}(\boldsymbol{L}+\boldsymbol{g}) \\
&\boldsymbol{w_h} \frac{\boldsymbol{dT_h}(\boldsymbol{L}+\boldsymbol{g})}{\boldsymbol{dx}} = \boldsymbol{w_c} \frac{\boldsymbol{dT_c}(\boldsymbol{L}+\boldsymbol{g})}{\boldsymbol{dx}} \\
&\boldsymbol{T_c}(\boldsymbol{L}+\boldsymbol{g}+\boldsymbol{L_c}) = \boldsymbol{T_f}(\boldsymbol{L}+\boldsymbol{g}+\boldsymbol{L_c}) \\
&\boldsymbol{w_c} \frac{\boldsymbol{dT_c}(\boldsymbol{L}+\boldsymbol{g}+\boldsymbol{L_c})}{\boldsymbol{dx}} = \boldsymbol{w_f} \frac{\boldsymbol{dT_f}(\boldsymbol{L}+\boldsymbol{g}+\boldsymbol{L_c})}{\boldsymbol{dx}} \\
&\boldsymbol{T_f}(2\boldsymbol{L}+\boldsymbol{g}) = \boldsymbol{T_s}
\end{aligned} \tag{4.4}$$

Applying the boundary conditions into the SSHCE gives the unknown constants C_{ij},

$$\begin{bmatrix} C_{1h} \\ C_{2h} \\ C_{1c} \\ C_{2c} \\ C_{1f} \\ C_{2f} \end{bmatrix} = \begin{bmatrix} 1 & 1 & 0 & 0 & 0 & 0 \\ e^{\sqrt{\frac{\beta_h}{\psi_o}}(L+g)} & e^{-\sqrt{\frac{\beta_h}{\psi_o}}(L+g)} & -e^{\sqrt{\frac{\beta_c}{\psi_o}}(L+g)} & -e^{-\sqrt{\frac{\beta_c}{\psi_o}}(L+g)} & 0 & 0 \\ e^{\sqrt{\frac{\beta_h}{\psi_o}}(L+g)} & -e^{-\sqrt{\frac{\beta_h}{\psi_o}}(L+g)} & -\frac{w_c}{w_h}\sqrt{\frac{\beta_c}{\beta_h}}e^{\sqrt{\frac{\beta_c}{\psi_o}}(L+g)} & \frac{w_c}{w_h}\sqrt{\frac{\beta_c}{\beta_h}}e^{-\sqrt{\frac{\beta_c}{\psi_o}}(L+g)} & 0 & 0 \\ 0 & 0 & e^{\sqrt{\frac{\beta_c}{\psi_o}}(L+g+L_c)} & e^{-\sqrt{\frac{\beta_c}{\psi_o}}(L+g+L_c)} & -e^{\sqrt{\frac{\beta_f}{\psi_o}}(L+g+L_c)} & -e^{-\sqrt{\frac{\beta_f}{\psi_o}}(L+g+L_c)} \\ 0 & 0 & e^{\sqrt{\frac{\beta_c}{\psi_o}}(L+g+L_c)} & -e^{-\sqrt{\frac{\beta_c}{\psi_o}}(L+g+L_c)} & -\frac{w_f}{w_c}\sqrt{\frac{\beta_f}{\beta_c}}e^{\sqrt{\frac{\beta_f}{\psi_o}}(L+g+L_c)} & \frac{w_f}{w_c}\sqrt{\frac{\beta_f}{\beta_c}}e^{-\sqrt{\frac{\beta_f}{\psi_o}}(L+g+L_c)} \\ 0 & 0 & 0 & 0 & e^{\sqrt{\frac{\beta_f}{\psi_o}}(2L+g)} & e^{-\sqrt{\frac{\beta_f}{\psi_o}}(2L+g)} \end{bmatrix}^{-1} \begin{bmatrix} T_s - \alpha_h \\ \alpha_c - \alpha_h \\ 0 \\ \alpha_f - \alpha_c \\ 0 \\ T_s - \alpha_f \end{bmatrix} \tag{4.5}$$

One common case in addition to $\beta_h, \beta_c, \beta_f > 0$ is when $\beta_h, \beta_f < 0$ and $\beta_c > 0$. This normally takes place because the width of cold arm in a U-shaped actuator is always greater than hot and flexure arms. This causes the exponential thermal responses of hot and flexure arms to drift into a distribution as the input current increases, $I_h, I_f < I \;\&\; I_c > I$, and the cold arm exhibits an exponential response. The temperature profiles are given by

$$T_i(x_i) = T_{\infty i} + C_{1i}\cos\left(\sqrt{\frac{|\beta_i|}{\psi_o}}x_i\right) + C_{2i}\sin\left(\sqrt{\frac{|\beta_i|}{\psi_o}}x_i\right) \quad i = h, f$$

$$T_c(x_c) = T_{\infty c} + C_{1c}e^{\sqrt{\frac{\beta_c}{\psi_o}}x_c} + C_{2c}e^{-\sqrt{\frac{\beta_c}{\psi_o}}x_c} \tag{4.6}$$

The unknown constants are then evaluated according to

$$\begin{bmatrix} C_{1h} \\ C_{2h} \\ C_{1c} \\ C_{2c} \\ C_{1f} \\ C_{2f} \end{bmatrix} = \begin{bmatrix} 1 & 0 & 0 & 0 & 0 & 0 \\ \cos\left(\sqrt{\frac{|\beta_h|}{\psi_o}}(L+g)\right) & \sin\left(\sqrt{\frac{|\beta_h|}{\psi_o}}(L+g)\right) & -e^{\sqrt{\frac{\beta_c}{\psi_o}}(L+g)} & -e^{-\sqrt{\frac{\beta_c}{\psi_o}}(L+g)} & 0 & 0 \\ \sin\left(\sqrt{\frac{|\beta_h|}{\psi_o}}(L+g)\right) & -\cos\left(\sqrt{\frac{|\beta_h|}{\psi_o}}(L+g)\right) & \frac{w_c}{w_h}\sqrt{\frac{\beta_c}{|\beta_h|}}e^{\sqrt{\frac{\beta_c}{\psi_o}}(L+g)} & -\frac{w_c}{w_h}\sqrt{\frac{\beta_c}{|\beta_h|}}e^{-\sqrt{\frac{\beta_c}{\psi_o}}(L+g)} & 0 & 0 \\ 0 & 0 & e^{\sqrt{\frac{\beta_c}{\psi_o}}(L+g+L_c)} & e^{-\sqrt{\frac{\beta_c}{\psi_o}}(L+g+L_c)} & -\cos\left(\sqrt{\frac{|\beta_f|}{\psi_o}}(L+g+L_c)\right) & -\sin\left(\sqrt{\frac{|\beta_f|}{\psi_o}}(L+g+L_c)\right) \\ 0 & 0 & e^{\sqrt{\frac{\beta_c}{\psi_o}}(L+g+L_c)} & -e^{-\sqrt{\frac{\beta_c}{\psi_o}}(L+g+L_c)} & \frac{w_f}{w_c}\sqrt{\frac{\beta_f}{\beta_h}}\sin\left(\sqrt{\frac{|\beta_f|}{\psi_o}}(L+g+L_c)\right) & -\frac{w_f}{w_c}\sqrt{\frac{\beta_f}{\beta_h}}\cos\left(\sqrt{\frac{|\beta_f|}{\psi_o}}(L+g+L_c)\right) \\ 0 & 0 & 0 & 0 & \cos\left(\sqrt{\frac{|\beta_f|}{\psi_o}}(2L+g)\right) & \sin\left(\sqrt{\frac{|\beta_f|}{\psi_o}}(2L+g)\right) \end{bmatrix}^{-1} \begin{bmatrix} T_s - \alpha_h \\ \alpha_c - \alpha_h \\ 0 \\ \alpha_f - \alpha_c \\ 0 \\ T_s - \alpha_f \end{bmatrix}$$

(4.7)

However, at high input current, $\beta_h, \beta_c, \beta_f < 0$ or $I_h, I_c \,\&\, I_f > I$, to the three beams, the solution becomes

$$T_i(x_i) = T_{\infty i} + C_{1i} \cos\left(\sqrt{\frac{|\beta_i|}{\psi_o}} x_i\right) + C_{2i} \sin\left(\sqrt{\frac{|\beta_i|}{\psi_o}} x_i\right) \quad , i = h, c, f \tag{4.8}$$

And the unknowns are evaluated according to

$$\begin{bmatrix} C_{1h} \\ C_{2h} \\ C_{1c} \\ C_{2c} \\ C_{1f} \\ C_{2f} \end{bmatrix} = \begin{bmatrix} 1 & 0 & 0 & 0 & 0 & 0 \\ \cos\left(\sqrt{\frac{|\beta_h|}{\psi_o}}(L+g)\right) & \sin\left(\sqrt{\frac{|\beta_h|}{\psi_o}}(L+g)\right) & -\cos\left(\sqrt{\frac{|\beta_c|}{\psi_o}}(L+g)\right) & -\sin\left(\sqrt{\frac{|\beta_c|}{\psi_o}}(L+g)\right) & 0 & 0 \\ \sin\left(\sqrt{\frac{|\beta_h|}{\psi_o}}(L+g)\right) & -\cos\left(\sqrt{\frac{|\beta_h|}{\psi_o}}(L+g)\right) & -\frac{w_c}{w_h}\sqrt{\frac{\beta_c}{\beta_h}}\sin\left(\sqrt{\frac{|\beta_c|}{\psi_o}}(L+g)\right) & \frac{w_c}{w_h}\sqrt{\frac{\beta_c}{\beta_h}}\cos\left(\sqrt{\frac{|\beta_c|}{\psi_o}}(L+g)\right) & 0 & 0 \\ 0 & 0 & \cos\left(\sqrt{\frac{|\beta_c|}{\psi_o}}(L+g+L_c)\right) & \sin\left(\sqrt{\frac{|\beta_c|}{\psi_o}}(L+g+L_c)\right) & -\cos\left(\sqrt{\frac{|\beta_f|}{\psi_o}}(L+g+L_c)\right) & -\sin\left(\sqrt{\frac{|\beta_f|}{\psi_o}}(L+g+L_c)\right) \\ 0 & 0 & \sin\left(\sqrt{\frac{|\beta_c|}{\psi_o}}(L+g+L_c)\right) & -\cos\left(\sqrt{\frac{|\beta_c|}{\psi_o}}(L+g+L_c)\right) & -\frac{w_f}{w_c}\sqrt{\frac{\beta_f}{\beta_h}}\sin\left(\sqrt{\frac{|\beta_f|}{\psi_o}}(L+g+L_c)\right) & \frac{w_f}{w_c}\sqrt{\frac{\beta_f}{\beta_h}}\cos\left(\sqrt{\frac{|\beta_f|}{\psi_o}}(L+g+L_c)\right) \\ 0 & 0 & 0 & 0 & \cos\left(\sqrt{\frac{|\beta_f|}{\psi_o}}(2L+g)\right) & \sin\left(\sqrt{\frac{|\beta_f|}{\psi_o}}(2L+g)\right) \end{bmatrix}^{-1} \begin{bmatrix} T_s - \alpha_h \\ \alpha_c - \alpha_h \\ 0 \\ \alpha_f - \alpha_c \\ 0 \\ T_s - \alpha_f \end{bmatrix} \tag{4.9}$$

In the cases presented, the six unknown constants in temperature profile equation $T_i(x_i)$ are obtained by solving the six Dirichlet boundary conditions in equation 4.4. A uniform width U-shaped actuator could be thought of as an V-shaped microactuator. Therefore, the equations derived for U-shape can be applied to V-shape given that $w_h = w_c = w_f$. For micro-beams of same width, or I-shaped actuators, the critical condition $\beta_h, \beta_c, \beta_f == 0$ gives constant temperature distribution $T_h(x) = T_c(x) = T_f(x) = T_s$ in which case, the amount of heat generation is equal to the amount of heat lost across substrate. The parameters considered in the presented derivation include the geometric (see Figure (4.1) and material properties of the microactuator, the air gap, and thermal conductivity of the substrate as show in Tables 4.1 and 4.2. The obtained equations along with boundary conditions determine the steady state temperature profiles along

the microactuator. The derived expressions are then used to study the effect of the input voltage magnitude (low to very high) on the steady state temperature distribution along the actuator. The voltage input causes different temperature profiles in the microactuator, thermal stresses and thermal failures.

Table 4.1 Material properties of U-shape actuators [69,109].

	SOI		
Layers / **parameters**	*Si Device*	*Si wafer Handle*	*Air*
Density, ρ_d (Kg/m^3)	2330	2330	0.524
Thermal conductivity, $(Wm^{-1}\,{}^oC^{-1})$	100	30	3.37e-2
Thermal Expansion, α $(10^{-6}\times{}^oC^{-1})$	3.1	3.1	1.49e3
Thermal Capacity, C_p $(J\ Kg^{-1}\,{}^oC^{-1})$	787	787	1013
Temperature coefficient, ξ $(10^{-3}\times{}^o\mathrm{C}^{-1})$	1.25	1.25	-
Electrical resistivity, ρ_o $(\Omega.m)$	1.5e-4	2.5e-2	3e13
Modules of Elasticity, E (Gp)	169	169	-
Poison ratio, ν	.22	.22	-

Table 4.2 Dimensions of U-shape actuators.

Parameter	**SOI(** μm **)**
air gap, t_v	2
thickness of substrate layer, t_s	300
width of the hot arm , w_h	10
width of cold arm , w_c	52
width of cold flexure arm, w_f	10
length of hot arm, L	370
length of cold arm, L_c	271
length of flexure arm, L_f	99
structure thickness, h	100
gap distance between cold and hot arm, g	20

4.2.1.2 Numerical Comparison for V-Shape Actuator

The purpose of this section is to illustrate the drawback of numerical approaches which are widely used to simulate electrothermal temperature response. Specifically, finite difference method (FDA) and finite element modeling (FEM) are utilized and compared with the exact solutions which are obtained at different voltage conditions.

In FDA, the general solution of a rising temperature distribution could be obtained by Forward-Time Centered- Space method (FTCS). In micro-electrothermal actuators

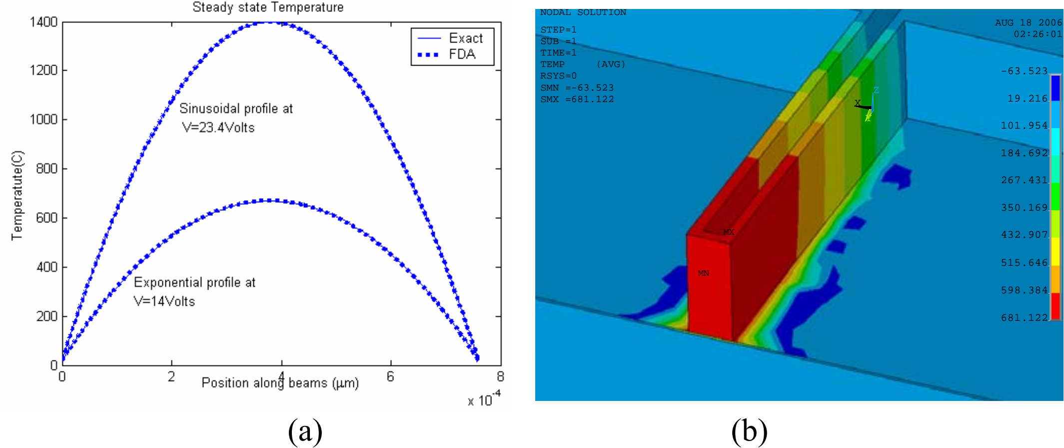

(a) (b)

Figure 4.2 S.S thermal simulation of V-shaped actuator excited below critical voltages: a) Temperature profiles comparison between FDA and Exact solution. b) FEM at 14Volts.

whose n beams are serially connected, the finite difference equation of equation 4.1 is given by

$$T_{\chi}^{\omega+1} = \left(\frac{{}^{i}\alpha_{p}\Delta t}{\Delta x^{2}}\right)\left(T_{\chi-1}^{\omega} - T_{\chi}^{\omega}\left(2 + {}^{i}\varepsilon\Delta x^{2} - \frac{\Delta x^{2}}{{}^{i}\alpha_{p}\Delta t}\right) + T_{\chi+1}^{\omega} + {}^{i}T_{\infty}\,{}^{i}\varepsilon\Delta x^{2}\right), i = 1, \ldots .n \quad (4.10)$$

where, $\varepsilon = \beta/\psi_{o}, \varepsilon > 0$ and ω & χ are integers which refer to time and space mesh, respectively. Δx & Δt are space and time grid resolution, respectively.

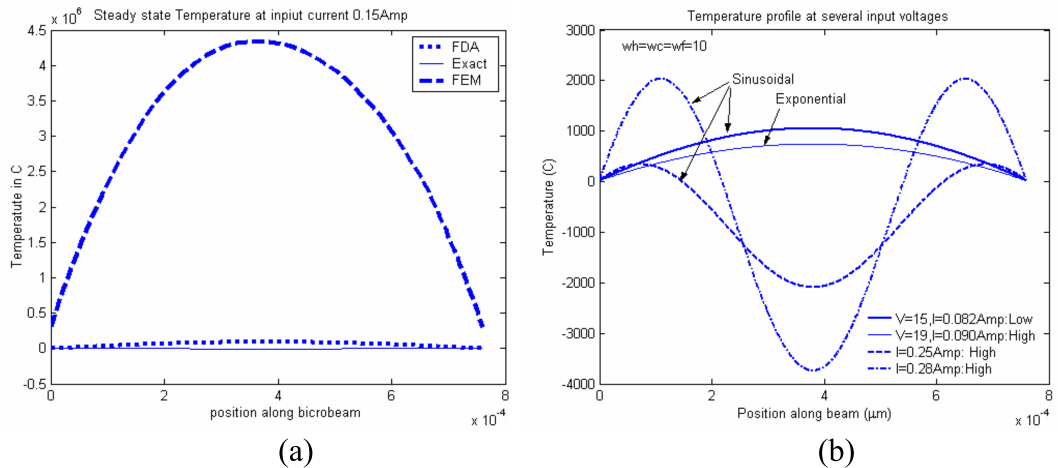

(a) (b)

Figure 4.3 V-shaped actuator excited at voltages beyond critical values: (a) temperature profiles comparison between FEM, FDA and exact for high input voltage. (b) The theoretical exact S.S. temperature profile for several input voltages.

Numerical simulations are performed with the material properties and dimensions of the device layers which are tabulated in table 4.1 and table 4.2, respectively.

In I-shaped “single micro-beam” actuator the SOI dimensions in table 4.2 are used except that all beams have *10um* width, wherein I-shape is thermally equivalent to V-shape actuator known as Chevron. The voltage at which temperature changes its

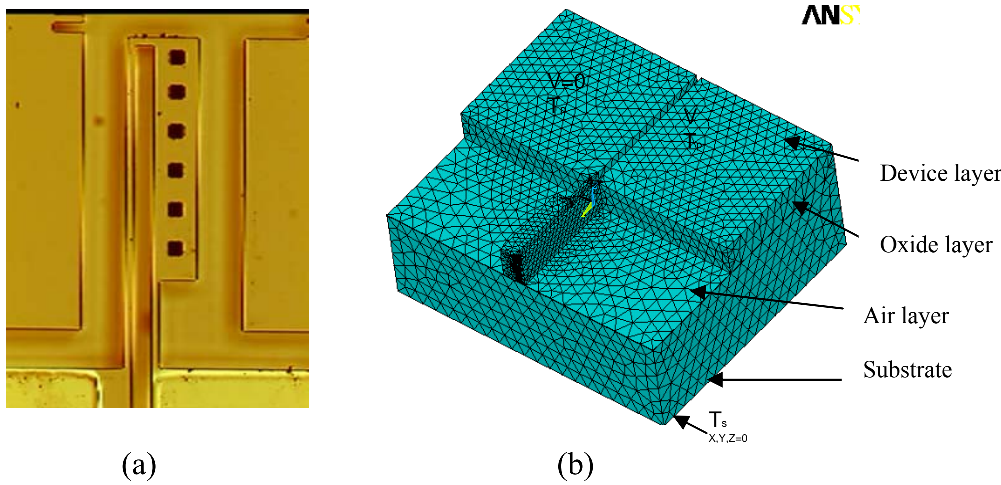

(a) (b)

Figure 4.4 SOI and FEM model of a U-shape thermal actuator. (a) Fabricated on SOI wafer (b) FEM of tetrahedral meshing.

profiles is 15V. For low to high input voltage, the simulation revealed that both the exponential and sinusoidal cases result in a peak at the micro-beam center as shown in Figure (4.2-a). FDA is utilized to compare with exact solution at different voltage excitation magnitudes. The exact, FEM and FDA methods agree for low input voltage with exponential temperature profile, and they also agree for high voltage input with sinusoidal temperature profiles, as shown in Figure (4.2-a,b). However, the exact temperature profile appears to have several peaks (propagating temperature wave) starting at the very high input current 125mAmp (~754Volt). Both FDA and FEM fail to capture the sinusoidal behavior at very large input voltage, as shown in Figure (4.3-a). The steady state temperature profiles are plotted for several input voltages and revealed either pure exponential or pure sinusoidal responses, as shown in Figure (4.3-b).

4.2.1.3 Numerical Comparison for U-Shape Actuator

Bimorph microactuator is fabricated on silicon substrate utilizing deep reactive ion etching DRIE process with $100\mu m$ SOI (silicon on insulator) wafers, shown in Figure (4.4-a). The exact analytical solution of S.S. temperature profiles of bimorph are also compared with FDA and FEM solutions. Unlike I-shaped actuator, a difference in computing the S.S. temperature profile along micro-beam is observed, as shown in Figure (4.5-a). These differences are attributed to mathematical assumptions and physical modeling, and numerical approximation. The exact average temperature of micro-beams has been simulated for variable step input voltages as shown in Figure

(4.6-a). The electrothermal average temperature is defined for *n* serially connected micro-beams of length l_k and temperature profile $T_k(x), l_k \geq x \geq l_{k-1}$

$$\bar{T} = \sum_{k=1}^{n}\left(l_k T_{\infty k} + \int_{l_{k-1}}^{l_k} T_k(x)dx \right) / \sum_{k=1}^{n} l_k \qquad (4.11)$$

The simulation is stopped at the average of ~860 ^{o}C where the silicon actuator has a hot arm peak temperature that is close to silicon melting point (1414 ^{o}C). At about 8.3 V input, the average temperature is smooth and the temperature profile along the beams changes from exponential distribution into a combined profile where the hot and flexure arms experience sinusoidal profiles while the cold arm has an exponential profile as shown in Figure (4.5-b). The temperature response at high voltage input is more sensitive than at low voltages. At combined temperature responses, temperature magnitude highly respond to input current and the profile changes.

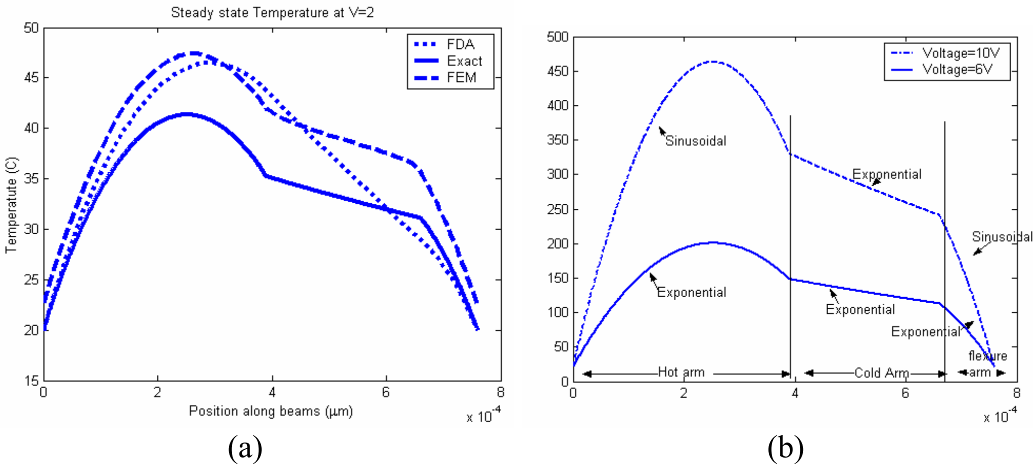

(a) (b)

Figure 4.5 Classification of S.S. Temperature profiles in U- actuator. a) Comparison of methods at low input voltage. b) Exponential and combined temperature profiles.

Particularly, when input current reaches the second critical current of bimorph ($I_c = 219mAmp$). A higher current excitation, $I > I_c, I >> I_h, I >> I_f$, the temperature profile becomes totally sinusoidal as shown in figure (4.6-b). The steady state profile is propagating in wave fronts and both the frequency and magnitude will change as the magnitude of the input current changes.

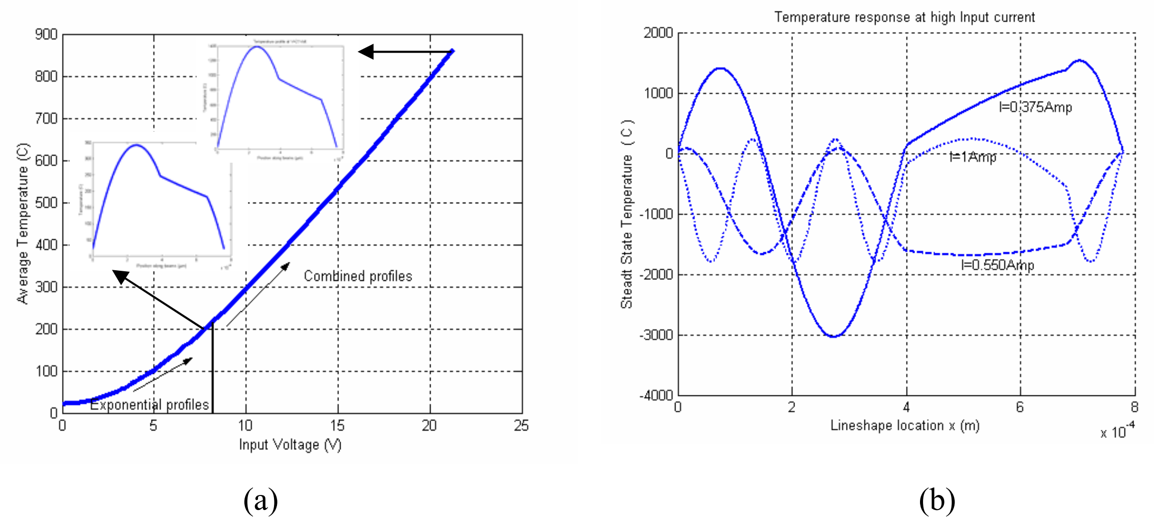

(a) (b)

Figure 4.6 Theoretical exact S.S. temperature profile of U-actuator excited for a range of input voltages. (a) Average temperature vs. voltage input simulated over the working condition of silicon. (b) Theoretical sinusoidal response to high input current, silicon fails to withstand high temperature due to early melting.

4.2.1.4 Thermal and Structural Failures

The derived exact solution of temperature profiles to various input voltages determines the failure mode in electro- thermal actuators. In general, early failures occur either because of structural yield or thermal yield. The failure conditions for bimorph actuator are summarized as follows:

- At low input voltage, the exponential temperature profile along the beams yields the maximum temperature at the longest and narrowest beam (hot

beam), where only one maximum temperature takes place around the hot beam center. Depending on the configuration and material properties, failure in this mode is likely to occur as a result of thermo-structural coupling. If a low temperature gradient causes a large asymmetrical expansion, then fracture would occur as a result of yield stresses at the hot arm neck.

- At high input voltage, a combined sinusoidal at narrow beams and exponential at wide beams profile is observed. If structural stresses do not yield the material, then failure is due to thermal stresses. Specifically, the gradual ramping of the input voltage would increase the maximum temperature at the narrowest and longest beam (center of hot beam). This temperature ramping continues until the actuator beam fails due to melting as concluded in Figure (4.6-a) and Figure (4.7-a).

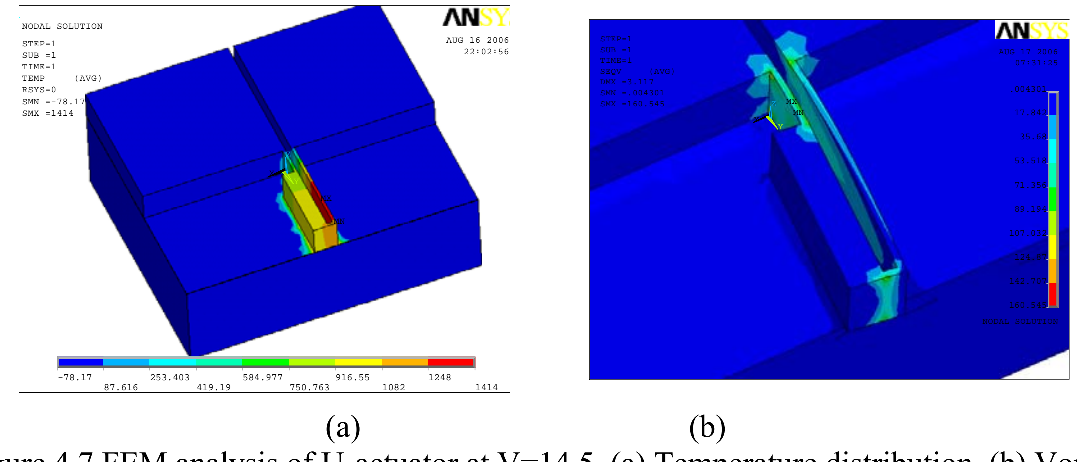

(a) (b)

Figure 4.7 FEM analysis of U-actuator at V=14.5. (a) Temperature distribution. (b) Von Mises stress distribution.

- At very high input current, heat flow along the device structure will theoretically undergo successive charge and discharge across the substrate. This leads to both high localized thermal and structural stresses and also high peaks which could explain the multi failure modes in a single structure. Such failures are observed in short and large magnitude pulsating input.
- Combined low to high input voltages cause thermal and structural stresses that cause buckling.

4.2.1.5 Experimental Observation on Actuators Failures

For the fabricated SOI bimorph, the finite element modeling procedure using ANSYS.9 [92] has been utilized to obtain the input voltage at which maximum temperature reaches silicon melting points. Figure (4.7-a) shows that for input voltage of 14.5 Volts, the FEM yielded a maximum temperature of 1414 ^{o}C which occurs on the hot arm. For the same input conditions, the Von Mises stress distribution along the beam is plotted in figure 8. The simulation suggests that the local maximum stress magnitude is significant and close to the compressive yield stress of silicon (120 MPa). This analysis is experimentally verified by incrementally increasing the voltage across bimorph pad as shown in Figure (4.9-a). At an input voltage ~14.4 Volts, the bimorph had two distinct failures as shown in Figure (4.9-b); first, a thermal failure due to maximum temperature at hot arm, and second structural failure due to buckling at the hot and flexure neck.

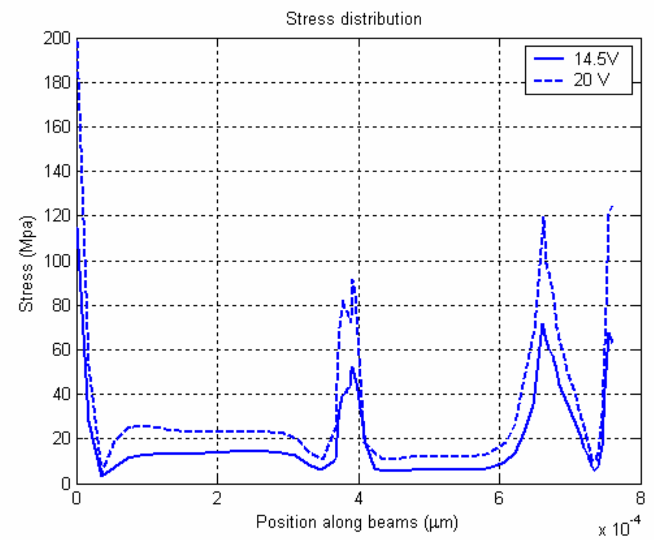

Figure 4.8 Von Mises stress distribution in U-shape actuator.

On the other hand, a short duration and high input voltage is applied across the bimorph and the failure is captured in Figure (4.9-c&d). It is clear that the combined thermal stresses and temperature have cause fracture at several locations. Meanwhile, an ultrafast and relatively high voltage (~30 Volts) caused high temperature peaks close to the hot arm end as shown in Figure (4.9-e). This suggests that the heat propagation along beams was quick to cause thermal failure as compared to structural buckling.

Thermal failures due to temperature peaks and gradients (local thermal stresses) are more common in electrothermal actuators whose thermal stresses are at minimum. For example, in Figure (4.9-f&g), a vertical actuator based on double layer arm is fabricated on PolyMUMPS and tested for thermal failures. It is observed that a single peak temperature caused melting of the center beam of actuator as shown in Figure (4.9-f). A high amplitude voltage caused several failure points due to localized temperature peaks and thermal stresses as shown in Figure (4.9-g).

A failure in I-shape copper layer fabricated by Femtosecond Laser Machining is shown in Figure (4.9-h). The thermal failure takes place at the micro-beam center for moderate voltage range predicted from the analytical work and experimentally verified as shown in Figure (4.9-i). The developed analysis could be employed in identifying the effect of material properties, dimensions, and boundary conditions on the performance of a microactuator or could be used in an inverse process of designing a microactuator with certain performance specifications.

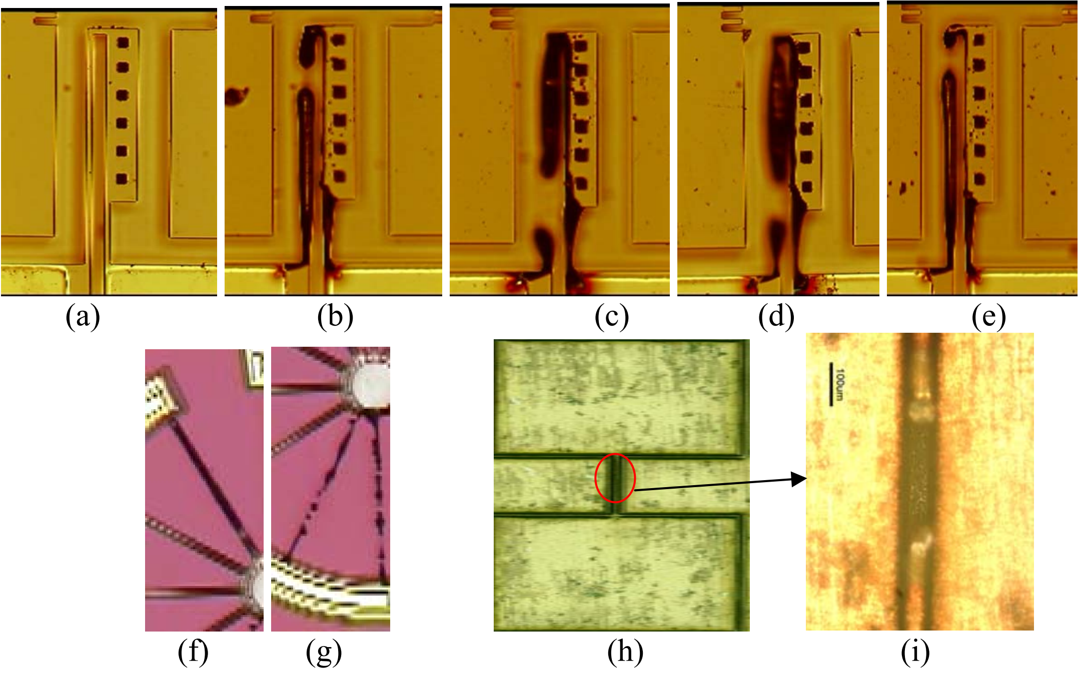

Figure 4.9 Thermal failure observations:
(a) An SOI U shape actuator. (b) Failure on hot arm due to (~14.4 Volts) . (c) Multi failures in hot and flexure arms due to (~18 Volts). (d) Multi failures in hot and flexure arms due to (~20 Volts) . (e) Failures due to very high voltage input (~30 Volts). (f)Single peak melting failure in PolyMUMPS. (g)Multi failures due to temperature peaks and thermal stresses. (h) I-shape actuator laser machined on copper. (i) Thermal failure due to peak temperature.

4.2.1.6 Summary of Steady State Thermal Analysis Method for METEG Blocks

The steady state temperature profiles of U- and I-shaped electrothermal microactuators were analytically derived. The temperature profiles could be used to evaluate the performance sensitivity of the microactuator due to various parameter changes. Wherein, the analysis assumed a packaged and unpackaged silicon microactuator with an air gap between the actuator and substrate and the profiles are evaluated for various input voltage amplitudes. It was found that at low voltage inputs the temperature profile is exponential in nature with the failure being due to thermo-structural stresses and/or structure melting. At voltages larger than a critical value, a combined sinusoidal and exponential temperature profile is observed with the failure being strongly due to structural melting as well. However, higher voltage excitation causes a fully distributed sinusoidal temperature profile. In this mode, failures occur at different locations and due to high localized thermal stresses causing the temperature to exceed the material melting point. The behavior of U- and I-shaped microactuators based on silicon on insulator (SOI) fabrication and Femotosecond Laser Micromachining was experimentally examined with the results corroborating the conclusions drawn from the analysis.

4.2.2 Combined Blocks “Microgripper”

The microassembly process of the micro system technology has recently demanded a development of microgrippers which are capable of handling and

manipulation of various microcomponents [58]. In plane Microgripper has recently been effectively used in industry [59].

Various micro-fabrication processes have been employed to construct microgripper structures, such as DIR, IC-based silicon processing, LIGA techniques, SU8, MUMPS, micro-EDM, molding methods, femtosecond surface micromachining processes FLM [60], and other methods.

Microgripper based on array of thermal actuators, discussed in pervious sections, provides powerful force and wide overall deflection [58 and 61]. Here, closing and opening of gripping are performed by two integrated thermal actuators with two opposite actuation direction. Temperature distributions along structure, structural stiffness's and end effecter deflection are some design parameters that govern the selected material and dimension of a prescribed structure.

Such microactuators have therefore attracted a lot of attention in recent years [62]. Lerch et al [60] have reported an a finite element (FE) analysis based on microactuator for maximum temperature in the device. Lin and Chiao [63] have used FE simulation to study electrothermal response of line-shape microstructure, Heatuator. Nilesh [61] introduced comprehensive thermal model for and electro-thermal complaint ETC studied by finite element simulation.

Temperature distribution in microgriper is significant in specifying and optimization of the opening displacement capabilities. Moreover, analytical solution of thermal microgripper is more robust than FEM simulation and facilitate designer to expect the constrains of thermal failure including melting and buckling.

This section investigates thermal distribution of a proposed planner microgripper mechanism. The study derives the core analytical response of steady state temperature distribution from a non homogenous, one dimensional structural layer under heat conductions. The analysis scope is to investigate the feasibility of modeling thermal response of a microgripper for micro-assembly purposes.

The design of many thermal MEMS actuators is often based on Finite Element Analysis, but lacks analytical insight. In this section we present a systematic methodology for analyzing combined electro- thermal microactuators by analytically deriving and solving 1-D steady-state equations. Because of the variety of microgripper fabrication technologies and applications, 3 different thermal boundary conditions are considered. In the first one, heat conduction to the substrate through a thin airgap layer depends on its thickness, and our model reveals an exponential temperature distribution in the microgripper. In the second case, if heat convection and radiation are neglected, such as if the microgripper operates in vacuum at moderate or low temperatures, the temperature profile are sinusoidal. In the third case, corresponding to a microgripper lifted off the substrate for use in assembly, the resulting natural convection conditions lead to an exponential temperature profile that has a similar, but shifted shape compared to the second case. The method prescribes the governing PDE's of each uniform segment in the actuator structure. In a constrained problem, continuous temperature and heat flux profiles ensure the compatibility response of the gripper structure. The thermal response of thermal gripper is simplified into a one dimensional problem. Here, the resistive electro-heat power generated in the element is equal to heat conduction,

convection and radiation which lost out of the element. The generalized heat conduction partial differential equations are exclusively implemented in different models. Three lumped models are built without consideration of heat radiation. In the first model, microgripper bottom face is brought close to substrate with few micron of airgap. In the second model, heat loss by free convection is considered for microgripper faces. Third model solves for microgripper under no heat loss.

The approach is conventional in reducing FEM simulation time and constructing analytical thermo-structural model. ANSYS MEMS design software package is employed to perform theoretical thermal analysis and used to validate the presented model.

4.2.2.1 Theoretical Model

The diagram shown in Figure(4.10) is microgripper based on array of monomorph thermal actuators. Motion with this actuator end effecter is combined by one hot arm actuator, linkage arm and shuttle actuator. In the one hot arm actuator, which is called Heatuator, the requirement to achieve rotational tip motion is to have one hot arm expanded more than cold arm. On the other hand, the thermal expansion of linkage arm pushes one hot arm structure for a wider opening. Similarly, the shuttle array of actuators performs linear vertical motion which pushes linkage arm-end vertically and then gripper tip deflects for a wider opening. The pads are anchored to base substrate. Two designs of microgripper could be obtained: first the movable structure is kept in gap with silicon substrate.

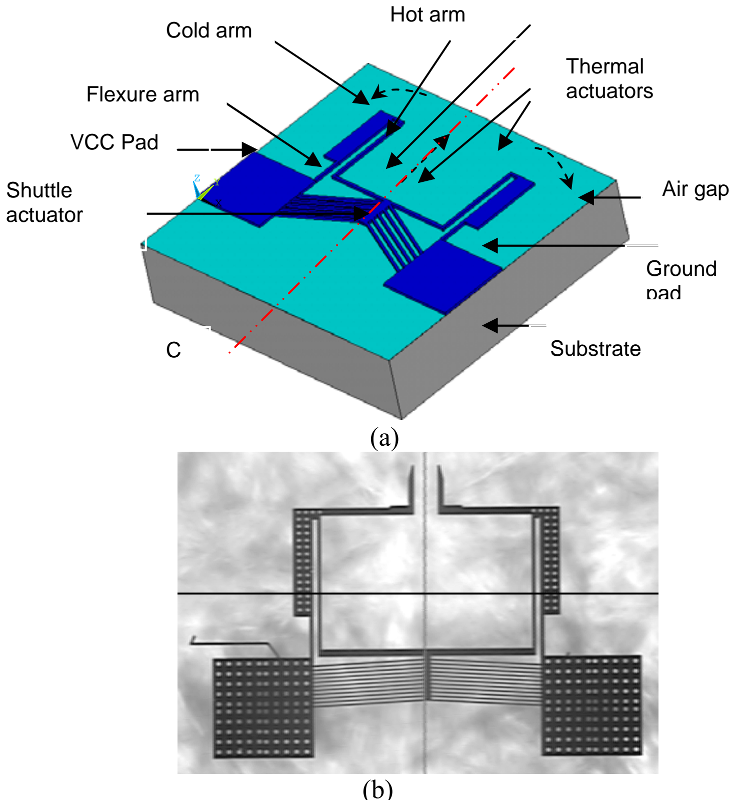

(a)

(b)

Figure 4.10 Combined blocks forming a Microgripper: (a) 3D model of an attached microgripper. (b) Fabricated and released microgripper.

Such air gap is obtained through introducing a removable intermediate layer while bonding the pads. Because the airgap height is small, it can be modeled by a conductive layer with zero modules of elasticity and infinite electrical resistivity. Second, extending moving structure into the ambient to let only free heat convection, i.e. Figure1 without air and substrate layers.

A source current is wired to pads. The current density at hot, linkage and shuttle arms cause higher thermal expansion as compared to cold arms. The actuator tip will freely bend toward cold arm resulting a bilateral force actuation to any attached passive micro-device. The shuttle actuator supports monomorph thermal

actuator and not only provides a momentum force to gripper tips but also structural stiffiness.

4.2.2.2 General Electrothermal Heat Conduction Equation

The thermal response of actuator is simplified into a one dimensional problem because the size in the length direction is much larger than that of its cross-section, Figure1. The resistive heat power generated in the element is equal to heat conduction, convection and radiation which are lost out of the elements. Temperature variation is governed by a nonlinear PDE equation which is resulted from an energy source of current input that has a density of , $J = I/wh$. The rate of heat change per area is equal to heat production per unit volume per time minus heat losses

$$\rho_d C_p \frac{\partial T}{\partial t} dx =$$
$$\left(\frac{I}{wh}\right)^2 \rho_r dx - \left[\frac{d}{dx}\left(-k_p \frac{dT}{dx}\right)dx + \left(T - T_p\right)\left(\frac{S}{hR_T}\right)dx + \left(\frac{2h_{cs}}{w} + \frac{\lambda h_{cf}}{h}\right)\left(T - T_\infty\right)dx + \frac{\lambda \varepsilon_e \sigma}{h}\left(T^4 - T_a^{\ 4}\right)dx\right] \tag{4.12}$$

Equation (4.12) is a general 1-D transient heat conduction that combines the nonlinearity of heat conduction coefficient and the effect of radiation heat transfer. Each face and side area of microgripper are convecting heat to air. Where, h_{cf} , h_{cs} are heat convection index at prescribed side and face areas of a structural bar. In free convection process, λ factor is equal to one if heat conduction through airgap is considered. However, λ is two when structure is experiencing convection from all side with no conduction to other layers, i.e. S=0.

The shape factor of heat conduction shape, s, [60] impacts the shape of the element on the excessive heat conduction to the substrate. Shape factor is defined by the total heat flux out of the line-shape microstructure per unit length divided by heat flux going directly under the width of microstructure [63]. It is given by

$$S = \frac{h}{w}\left(\frac{2t_v}{h} + 1\right) + 1 \tag{4.13}$$

R_T is the thermal resistance between the thermal micro-beam and the substrate is given by

$$R_T = \frac{t_v}{k_v} + \frac{t_s}{k_s} \tag{4.14}$$

where t_v and t_s are the air gap elevation and the thickness of substrate, respectively. k_v and k_s are the thermal conductivity of air and substrate, respectively.

The resistivity of moving material, ρ_r, is related to temperature and here it is assumed to have linear thermal coefficient, ξ, that is

$$\rho_r(T) = \rho_o\left[1 + \xi(T - T_s)\right]. \tag{4.15}$$

Thermal conductivity, k_p, of silicon is assumed here to be dependent on temperature variation and is approximated in a third degree polynomial [64], that is

$$k_p = \psi_o + \psi_1 T + \psi_2 T^2 + \psi_3 T^3 . \tag{4.16}$$

Surface heat radiation by convection and radiation become important at height operating temperature, above 500K [61] and at small physical devices. The radiation

heat transfer is especially important in devices that can see each other and have closely spaced parts of 1-10um and with high temperature difference between them [65].

There is a limited amount of published data on natural convection correlation for heated horizontal plates, suspended over a semi enclosed, losing heat from exposed surfaces [66]. In the next section we neglect the effect of radiation and free convection. Also we assume constant heat conductivity of moving structure so that a closed form solution is viable.

4.2.2.3 Steady State Heat Conduction Equation (S.S.H.C.E)

At steady state condition, a simplified version of equation 4.12 is reduced into simple linear ODE problem with both radiation heat convection transfer are negligible. Heat conduction coefficient being independent on temperature, $k_p = \psi_0$.

The structure and boundary conditions symmetry yields symmetrical temperature distribution of microgripper about middle axis. This imposes adiabatic line where the temperature is at least local maximum. The temperature distribution in along arms are linearly solved in a line shape, *x,* starting from pad and ending into same pad as shown in Figure 4.11. Upon solving the following ODE, we yield

$$T_i(x) = \alpha_i + C_{1i} e^{\sqrt{\frac{\beta_i}{\psi_o}}x} + C_{2i} e^{-\sqrt{\frac{\beta_i}{\psi_o}}x}, \; i == f, c, h, l, s \tag{4.17}$$

where

$$\beta = \left(\frac{S}{hR_T} - J^2 \rho_o \xi \right), \alpha_d = T_s + \frac{J^2 \rho_o}{\beta} \tag{4.18}$$

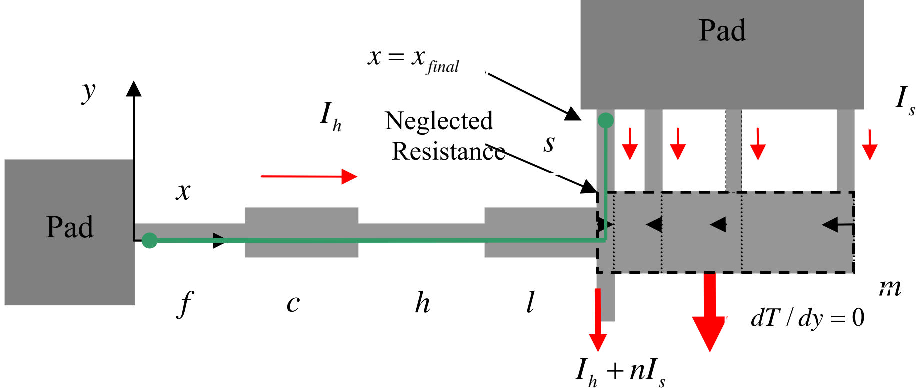

Figure 4.11 1-D thermal model of symmetrical microgripper.

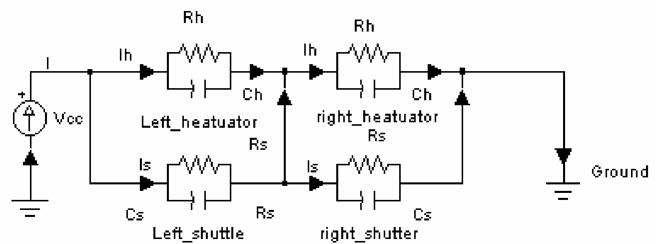

Figure 4.12 Current analogy model of microgripper.

The unknown constants, $c_{1f},...,c_{2s}$, are found by guaranteeing the continuity of steady state heat conduction and temperature profiles.

Microactuator is governed by exponential steady state, in equations 4.17, if $\beta_f, \beta_c, \beta_h, \beta_l,, \beta_s > 0$ are held for the all beams (normally occurs at low input current) .i.e. The allowed current which produces steady state exponential response is related to beam of width w_i and determines thermal distribution along each beam

$$I_i < \sqrt{\frac{k_v k_s}{\xi \rho_0} \frac{\left(hw_i^2 + \left[h^2 + 2ht_v\right] w_i\right)}{\left(k_v t_s + k_s t_v\right)}}; i == f, c, h, l, s\,. \tag{4.19}$$

The steady state current passing in each beam is extracted from the lumped model with neglected middle link resistance, shown in Figure (4.11&4.12). Current passing through heatuator links, which are encompassed with flexure *f*, cold *c*, hot, *h*, and linkage *l*, is

$$I_h = \frac{IR_s}{\left(R_h + R_s\right)} \tag{4.20}$$

Similarly, the current passing in each of the *n* shuttle links, *s*, is given by

$$I_s = \frac{IR_h}{n\left(R_h + R_s\right)} \tag{4.21}$$

The calculations of currents are simplified by pre-evaluating structure resistance at an average spatial temperature rather than taking it as a function of temperature profile. The resistances are calculated by resistivity at average temperature, ρ_a ,as follows:

$$R_h = \frac{\rho_a}{h}\left(\frac{L_f}{w_f} + \frac{L_c}{w_c} + \frac{L_h}{w_h} + \frac{L_l}{w_l}\right), R_h = \rho_a \frac{L_s}{hw_s n} \tag{4.22}$$

However, The ODE’s reduced from Equation (4.12), describes temperature dependent resistance.

Moreover, the resistance and the temperature profile of middle link ,m, and along with the current flowing in joints between shuttle arms $I_{m_j} = I_h - I_s(n-j)$ have insignificant impacts on solution of each shuttle link. So we assume similar heat profile at each links. The temperature distributions of multi beam microstructures are continuous, start from pad temperatures at flexure arm and ends up with pad

temperature at the shuttle arms end. Continuous heat flux is valid among arms, the following Dirichlet conditions solve for the 10 unknown constants,

$$
\begin{aligned}
&T_f(x) = T_s(x) = T_p\,, && \text{at } x = 0, L_f + L_c + g + L_h + L_l + L_s \\
&T_f(x) = T_c(x), \quad w_f \frac{dT_f(x)}{dx} = w_c \frac{dT_c(x)}{dx}, && \text{at } x = L_f \\
&T_c(x) = T_h(x) \quad w_c \frac{dT_c(x)}{dx} = w_h \frac{dT_h(x)}{dx}, && \text{at } x = L_f + L_c \\
&T_h(x) = T_l(x), w_h \frac{dT_h(x)}{dx} = w_l \frac{dT_l(x)}{dx} && \text{at } x = L_f + L_c + g + L_h \\
&T_l(x) = T_s(x), && \text{at } x = L_f + L_c + g + L_h + L_l \\
&w_l \frac{dT_l(x)}{dx} = w_s \frac{dT_s(x)}{dx} && \text{at } x = L_f + L_c + g + L_h + L_l
\end{aligned}
\tag{4.23}
$$

Applying Boundary condition into SSHCE gives unknown constants

$$
\begin{bmatrix} C_{1f} \\ C_{2f} \\ C_{1c} \\ C_{2c} \\ C_{1h} \\ C_{2h} \\ C_{1l} \\ C_{2l} \\ C_{1s} \\ C_{2s} \end{bmatrix}
=
\begin{bmatrix}
1 & 1 & 0 & 0 & 0 & 0 & 0 & 0 & 0 & 0 \\
e^{\sqrt{\frac{\beta_f}{\psi_o}}L_f} & e^{-\sqrt{\frac{\beta_f}{\psi_o}}L_f} & -e^{\sqrt{\frac{\beta_c}{\psi_o}}L_f} & -e^{-\sqrt{\frac{\beta_c}{\psi_o}}L_f} & 0 & 0 & 0 & 0 & 0 & 0 \\
\sqrt{\frac{\beta_f}{\psi_o}}e^{\sqrt{\frac{\beta_f}{\psi_o}}L_f} & -\sqrt{\frac{\beta_f}{\psi_o}}e^{-\sqrt{\frac{\beta_f}{\psi_o}}L_f} & -\frac{w_c}{w_f}\sqrt{\frac{\beta_c}{\psi_o}}e^{\sqrt{\frac{\beta_c}{\psi_o}}L_f} & \frac{w_c}{w_f}\sqrt{\frac{\beta_c}{\psi_o}}e^{-\sqrt{\frac{\beta_c}{\psi_o}}L_f} & 0 & 0 & 0 & 0 & 0 & 0 \\
0 & 0 & e^{\sqrt{\frac{\beta_c}{\psi_o}}(L_f+L_c)} & e^{-\sqrt{\frac{\beta_c}{\psi_o}}(L_f+L_c)} & -e^{\sqrt{\frac{\beta_h}{\psi_o}}(L_f+L_c)} & -e^{-\sqrt{\frac{\beta_h}{\psi_o}}(L_f+L_c)} & 0 & 0 & 0 & 0 \\
0 & 0 & \sqrt{\frac{\beta_c}{\psi_o}}e^{\sqrt{\frac{\beta_c}{\psi_o}}(L_f+L_c)} & -\sqrt{\frac{\beta_c}{\psi_o}}e^{-\sqrt{\frac{\beta_c}{\psi_o}}(L_f+L_c)} & -\frac{w_h}{w_c}\sqrt{\frac{\beta_h}{\psi_o}}e^{\sqrt{\frac{\beta_h}{\psi_o}}(L_f+L_c)} & \frac{w_h}{w_c}\sqrt{\frac{\beta_h}{\psi_o}}e^{-\sqrt{\frac{\beta_h}{\psi_o}}(L_f+L_c)} & 0 & 0 & 0 & 0 \\
0 & 0 & 0 & 0 & e^{\sqrt{\frac{\beta_h}{\psi_o}}(L_f+L_c+g+L_h)} & e^{-\sqrt{\frac{\beta_h}{\psi_o}}(L_f+L_c+g+L_h)} & -e^{\sqrt{\frac{\beta_l}{\psi_o}}(L_f+L_c+g+L_h)} & -e^{-\sqrt{\frac{\beta_l}{\psi_o}}(L_f+L_c+g+L_h)} & 0 & 0 \\
0 & 0 & 0 & 0 & \sqrt{\frac{\beta_h}{\psi_o}}e^{\sqrt{\frac{\beta_h}{\psi_o}}(L_f+L_c+g+L_h)} & -\sqrt{\frac{\beta_h}{\psi_o}}e^{-\sqrt{\frac{\beta_h}{\psi_o}}(L_f+L_c+g+L_h)} & -\frac{w_l}{w_h}\sqrt{\frac{\beta_l}{\psi_o}}e^{\sqrt{\frac{\beta_l}{\psi_o}}(L_f+L_c+g+L_h)} & \frac{w_l}{w_h}\sqrt{\frac{\beta_l}{\psi_o}}e^{-\sqrt{\frac{\beta_l}{\psi_o}}(L_f+L_c+g+L_h)} & 0 & 0 \\
0 & 0 & 0 & 0 & 0 & 0 & e^{\sqrt{\frac{\beta_l}{\psi_o}}(L_f+L_c+g+L_h+L_l)} & e^{-\sqrt{\frac{\beta_l}{\psi_o}}(L_f+L_c+g+L_h+L_l)} & -e^{\sqrt{\frac{\beta_s}{\psi_o}}(L_f+L_c+g+L_h+L_l)} & -e^{-\sqrt{\frac{\beta_s}{\psi_o}}(L_f+L_c+g+L_h+L_l)} \\
0 & 0 & 0 & 0 & 0 & 0 & \sqrt{\frac{\beta_l}{\psi_o}}e^{\sqrt{\frac{\beta_l}{\psi_o}}(L_f+L_c+g+L_h+L_l)} & -\sqrt{\frac{\beta_l}{\psi_o}}e^{-\sqrt{\frac{\beta_l}{\psi_o}}(L_f+L_c+g+L_h+L_l)} & -\frac{w_s}{w_l}\sqrt{\frac{\beta_s}{\psi_o}}e^{\sqrt{\frac{\beta_s}{\psi_o}}(L_f+L_c+g+L_h+L_l)} & \frac{w_s}{w_l}\sqrt{\frac{\beta_s}{\psi_o}}e^{-\sqrt{\frac{\beta_s}{\psi_o}}(L_f+L_c+g+L_h+L_l)} \\
0 & 0 & 0 & 0 & 0 & 0 & 0 & 0 & e^{\sqrt{\frac{\beta_s}{\psi_o}}(L_f+L_c+g+L_h+L_l+L_s)} & e^{-\sqrt{\frac{\beta_s}{\psi_o}}(L_f+L_c+g+L_h+L_l+L_s)}
\end{bmatrix}^{-1}
\begin{bmatrix} T_p-\alpha_f \\ \alpha_c-\alpha_f \\ 0 \\ \alpha_h-\alpha_c \\ 0 \\ \alpha_l-\alpha_h \\ 0 \\ \alpha_s-\alpha_l \\ 0 \\ T_p-\alpha_s \end{bmatrix}
\tag{4.24}
$$

The resistance of micro gripper depends on temperature change and it is estimated as follows:

$$R_h = \int_0^{L_f+L_c+L_g+L_l} dR(T) = \frac{(L_f)}{w_f h}\rho_o\left(1+\xi\left(\overline{T}_f - T_s\right)\right) + \frac{(L_c)}{w_c h}\rho_o\left(1+\xi\left(\overline{T}_c - T_s\right)\right) + \frac{(L_h+g)}{w_h h}\rho_o\left(1+\xi\left(\overline{T}_h - T_s\right)\right) + \frac{(L_l)}{w_l h}\rho_o\left(1+\xi\left(\overline{T}_l - T_s\right)\right)$$

$$R_s = \frac{1}{n}\int_{L_f+L_c+L_g+L_l}^{L_f+L_c+L_g+L_l+L_s} dR(T) = \frac{(L_s)}{n w_s h}\rho_o\left(1+\xi\left(\overline{T}_s - T_s\right)\right) \tag{4.25}$$

One should noticed that the previous temperature are resistances dependent and were not included in the calculation of currents, A more accurate result is obtained by iterating and comparing resistances

The voltage across the microgripper actuator is computed using resistances in equation (4.25)

$$V = \frac{2I\left(R_s R_h\right)}{R_s + R_h} \tag{4.26}$$

On the other hand, the extended microgripper structure is lumped by conduction and free convective heat transfer.

Here we assume convection at all sides and faces of microgripper. Equation (4.17 ,4.19 through 4.26) are still valid for this case giving that $T_\infty = T_s$ and

$$\beta_i = \left(\left(\frac{2h_{cs}}{w_i} + \frac{\lambda h_{cf}}{h}\right) - J_i^2 \rho_o \xi\right) \quad i == f,c,h,l,s \tag{4.27}$$

where T_∞ is ambient temperature and h_{cs} & h_{cf} are the convection coefficients which are measured experimentally.

Finally, temperature propagate in a spatial wave front if the microgripper is experiencing no heat loss, the governing equations are

$$T_i(x) = \alpha_i + C_{1i}\sin\sqrt{\frac{\beta_i}{\psi_o}} + C_{2i}\cos\sqrt{\frac{\beta_i}{\psi_o}} \quad i == f,c,h,l,s \tag{4.28}$$

Table 4.3 Material prosperities of Nickel-annealed, silicon and ceramic *Alumina* AD-85.

Parameter	air	silicon	Ceramic	Unit
Density, ρ_d	2e7	2330	3400	Kg/m^3
Thermal conductivity,	0.025	30	16	$Wm^{-1}\,{}^oC^{-1}$
Free convection, h_c	35	--	--	$Wm^{-2}\,{}^oC^{-1}$
Thermal Expansion, α	--	2.7×10^{-6}	7.6×10^{-7}	${}^oC^{-1}$
Thermal Capacity, C_p	--	705	920	$J\ Kg^{-1}\,{}^oC^{-1}$
Temperature coefficient, ξ	--	1.3×10^{-3}	--	${}^oC^{-1}$
Electrical resistivity, ρ_o	--	1.1×10^{-5}	10×10^{12}	$\Omega.m$

Table 4.4 Structure dimension used in steady state thermal analysis.

Parameter	μm
width of cold flexure arm, w_f	50
width of cold arm ,w_c	150
width of the hot arm ,w_h	50
width of the linkage arm , w_l	50
width of the middle arm , w_m	100
width of the shuttle arm , w_s	50
length of flexure arm, L_f	200
length of cold arm, L_c	500
length of hot arm, L_h	700
length of linkage arm, L_l	500
length of shuttle arm, L_s	651
air gap, t_v	10
thickness of substrate layer, t_s	500
structure thickness, h	25
gap distance between cold and hot arm, g	100
gap distance between shuttle arms, g_s	50

with $\beta_i = J_i^2 \rho \xi$ and $\alpha_i = T_s - \frac{1}{\xi}$. The constants are found by solving previous continuity of flux and temperature in equations 4.23. we yield equation

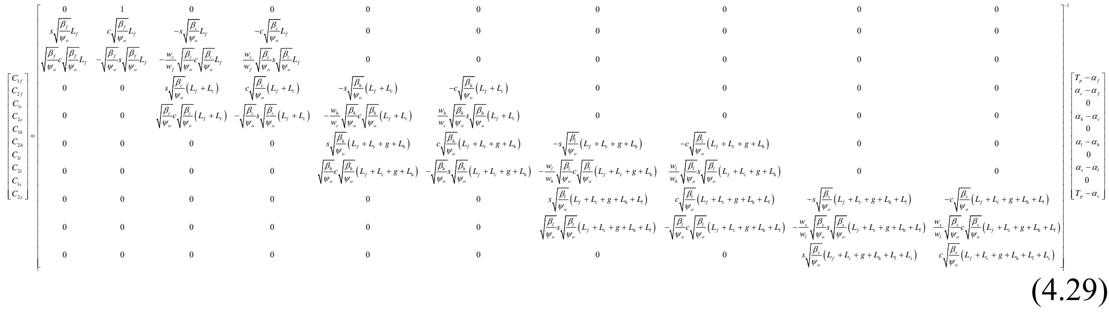

(4.29)

4.2.2.4 Simulations and Discussions

The primary objective of this analytical and FEM simulations is to validate the temperature profile behavior and the physical property of the proposed microgripper. In

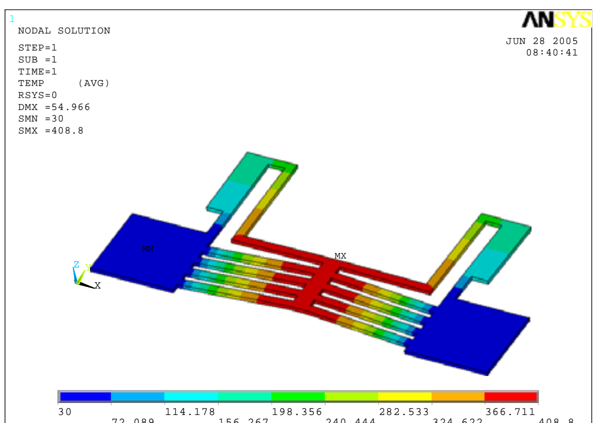

Figure 4.13 Temperature distribution using FEM without airgap.

this numerical example, microgripper structure is silicon and could be fabricated by DIR process. Three examples are discussed here, a microgripper operating in vacuum with negligible heat loss. Second, microgripper conducting heat to airgap and substrate. Finally microgripper freely convicting heat to air.

Structure dimensions and material properties of models are shown in Tables 4.3&4.4. Figure (4.13 & 4.14) is the FEM temperature result obtained by using ANSYS

package. It simulates the steady state temperature response of 1volts applied across pads. Symmetrical temperature results are obtained with maximum temperature is located on the adiabatic line. And so heat is adiabatic at this middle bar, i.e. no heat flows across symmetrical structures. One shall notice that when no heat loss is associated with model, the maximum temperature is located between the first upper links of shuttle actuator. This is because current density is large compared to other locations. Here in the FEM simulation, the value of thermal resistively, ρ_o , is

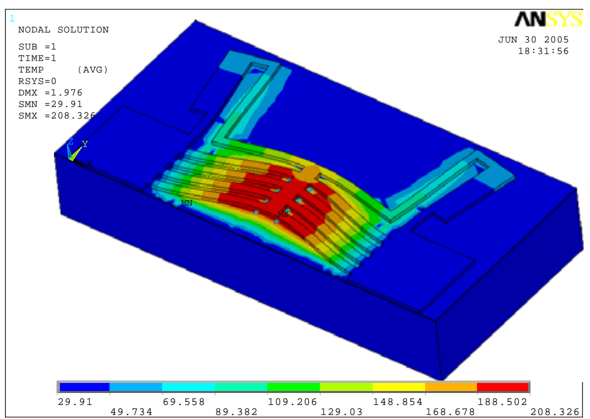

Figure 4.14 Temperature distribution using FEM with airgap and handle

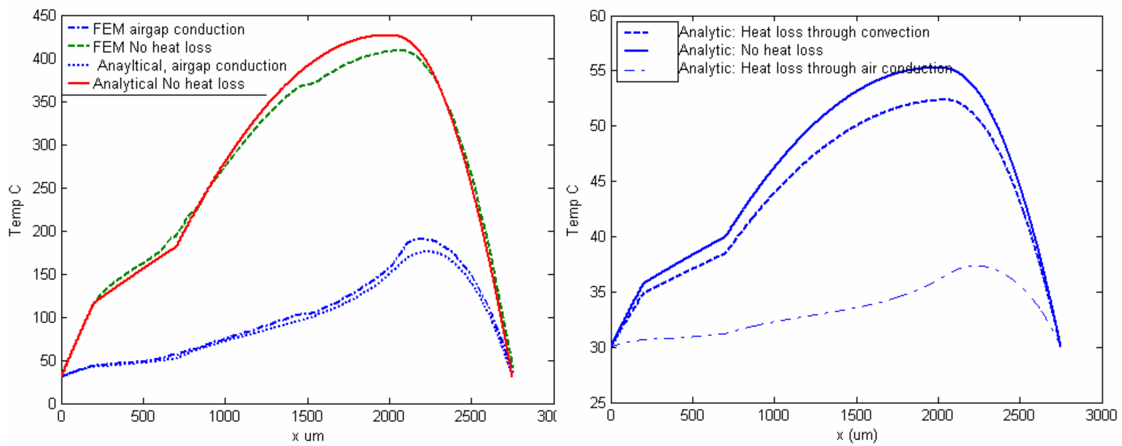

Figure 4.15 Comparison between FEM and analytical methods: (a)FEM and analytical thermal responses at 1 V, (b) Analytical thermal responses at 0.25 V

temperature independent and assigned at T_p.In Figure (4.15-a). FEM temperature distribution is plot wafer. linearly with location, x, starting from one pad, flexure arm, cold arm, gap and hot arm, linkage arm, fist shuttle and ending to same starting pad. Numerically, the analytical equation in 4.28 plots sinusoidal response and is compared with FEM. Both results are in good agreement. The profiles are very close at low temperature however, analytical results exceeds at higher temperature. This might be explained by the sensitivity of the resistivity to temperature where higher linear resistance in analytical model is computed and compared with constant resistivity in FEM model.

In the second example, heat conduction through airgap and substrate is imposed to microgripper structure. FEM model is carefully built with all layers elements are connected at different material sets. FEM solution is obtained in Figure (4.15-b) for lower substrate temperature being constrained to T_p and a voltage of 1V in magnitude is applied. Significant temperature drop is noticed and plot in Figure (4.15-a). The temperature profile is no longer dominated by sine wave but with exponential distributions. In this model, microgripper heat flux becomes steep as it compared to no heat loss model and thus low average temperature on each beam. The steady state temperature and heat flux have exponential response at low input voltage. FEM agrees analytical model at low temperature level. However, FEM temperature response has slightly exceeded analytical response at high temperature either because high current density and resistivity accounts for more heat loss at adiabatic regions. Or of the approximate assumption made for neglecting middle bar resistance in analytical model.

Temperature profile responds sinusoidally when the condition described in equation (4.19) is violated in an arm as a cause of voltage increase, material or geometry changes. More increase in airgap decreases heat loss and may violates condition which prescribes the exponential temperature response. And thus system is no longer governed by airgap heat conduction. However, the conduction loss across substrate increases as air gap decrease and so microgripper temperature decreases.

A final numerical example compares the significance of heat loss between air fee convection and airgap conduction. Figure (4.15-b) depicts the thermal response of same structure but with 0.25 input voltages. The free convection temperature profile is governed by exponential distribution and yet has caused a little shift when compared with sinusoidal response of no heat loss. Meanwhile significant temperature dropped is depicted when structure is losing heat into airgap and substrate.

We conclude that the proposed methods for thermal microgripper actuator has proposed closed form solutions which are were in good agreement with the finite element results. The most important heat transfer mechanism is considered through the heat conduction of non homogenous structure through air and substrate formulates system of ODE. However, heat convection is insignificant if the microgripper is few microns in gap with substrate. The analytical methods discussed in this section are computationally efficient which facilitate the design and optimization of elctrothermo-coupled problems. The derived electro-thermal driving principle is essential in defining the expansion and motion actuation of micrgripper. Moreover, the phenomena of plastic

deformation and back-bent mode which occur in current saturation mode at extreme temperature zone could be predicted and avoided.

4.3 Thermal Cycle Analysis of U-(Folded beam) & V- (Chevron) Blocks

An electrothermal (E-T) micromechanical actuation based on asymmetrical thermal expansion has popularly been adopted as one of the major actuation principles in microsystems. Such a technique is capable of providing the required large deflection and force compared to other actuation principles such as electrostatic, piezoelectric, and magnetic. However, the performance of electrothermal building blocks such as bimorph and monomorph thermal actuators at a given operating force and deflection are primarily limited to thermal budget at micro-scale. Such limitations are a result of thermal failures and thermo-elastic coupling effects in the MEMS structure which are functions of thermal boundary conditions, scaling effect, materials and the operating power input.

In general, the thermo-dynamical cycle of E-T microactuators consists of heating, dwell (engaging) and cooling times. The determination of the maximum operating frequency of E-T actuators relies on the successive thermal heating and cooling rates. Thus, MEMS building blocks have fast response times compared to macro scale actuators [110]. It is desired to drive thermal actuators with a power input cycle time less than or equal to thermal cycle (full duty) otherwise, the actuator will be unable to dissipate the heat generated by the high frequency and amplitude current signal [45]. This might cause the actuator to either retain a perturbed static deflection - as if it were almost driven by DC

input current - or the energy will periodically accumulate in the structural layer causing temperature rise and eventually thermal failure. Thus, the structural dynamic response of an E-T microactuator is largely determined by its heating and cooling time.

The thermal duty cycle can be obtained by deriving mathematical model based on micro-physics of E-T MEMS devices. However, it is not only difficult to obtain accurate time and spatial dependent models, but also elegant closed form solutions are often infeasible. Hence, exhaustive finite element approximations and modeling techniques based on lumped and exact physical models have often been sought to analyze the static and dynamic behaviors of thermal MEMS devices. Black box models based on the direct measurement of thermal response of microactuators are currently limited by the bandwidth and spatial resolution of sensors used to collect data such as an infrared camera. Such numerical and parameterization methods lack the physical insight that relates to E-T microphysics and which could assist on optimizing E-T thermal performance and provide design guidelines.

In case of E-T actuators with a narrow air gap, fast cooling can be achieved by heat conduction across a substrate; for example, in an E-T vibromotor the bandwidth of thermal-elastic response can be up to 1.0 kHz in range at a low voltage input [111]. It is also reported that the bandwidth of a lateral thermal actuator fabricated by MUMPs process is up to several kHz [45]. The enhancement of structural frequency response is thus highly dependent on minimizing rising and cooling time constants. The thermal response of MEMS device has been calculated using numerical and lumped models, whereas little attention has been given to the measurement of transient thermal

responses due to the limitation of current sensing capability [110]. A SPICE model was developed to incorporate electrical loading, transient responses, and deflections of a polysilicon thermal actuator [45], and the reduced order dynamic model of a MUMPs thermal actuator obtained using experimental data and finte element (FE) approximation simulation demonstrated high speed actuation up to hundreds of kHz with input shape control [112]. Other modeling efforts include the use of simplified partial differential equation (PDE)/ordinary differential equation (ODE) formulation of a lineshape and U-shape microstructure [70 and 110] and the FE model of thermal microgrippers [107]. Although the aforementioned techniques relate to thermal cycle, the thermal transient analysis of complex microstructures is difficult to obtain analytically and also requires time consuming computation. Furthermore, these techniques might not clearly illustrate a procedure to relate efficient high speed performance to transient thermal conditions.

This section presents a methodology that enables the transient synthesis and subsequent verification for computing thermal cycle in serially connected micro-beams particularly, folded beam actuators. First, system of PDEs is obtained to describe general E-T heat conduction equations (HCE) of the three connected E-T beams or "folded beam" actuator. The PDEs are then transformed into ODEs from which trial solution procedures are performed based on a weighted residual method. The polynomial shape functions are chosen to approximate the solution of ODE in Laplace domain [79].The general time-domain response and heating time constants of folded beam are derived from the inverse of Laplace domain. An approximate cooling time constant is derived from the lumped model of a folded beam actuator driven by low

input voltage under steady state conditions. The fabrication of E-T actuators used for subsequent experimental verification of the proposed procedures is discussed. The rising time obtained from the proposed analytical approaches for folded beam actuators is compared with finite element (FE) approximations and finite element modeling using ANSYS® coupled field module. The heating time response of uniform width “single line-shape” or as widely known V-shape actuator is also obtained and compared with the available exact solution obtained in [70]. Section V introduces the mechanical response measurement of an SOI folded beam actuator used to compare between the mechanical time constants with computed thermal time constants. The section concludes with the performance analysis of the folded beam actuator utilizing the derived approach that allows one to determine the thermal cycle as function of thermal states, material and geometry.

4.3.1 Transient H.C.E of Folded Beam Actuator

E-T MEMS actuators may undergo an entire cycle of charging and discharging when the input power switching time is slower than the corresponding heating and cooling times of an the actuator. In practice, it is recommended that the thermal actuator be operated at frequencies that neither cause thermal failure nor a static deflection offset.

4.3.1.1 Charging Time Synthesis Using Trial Solution Method

The resistive joule heating of an element in an E-T device is equal to the heat conduction through and heat loss out of the element. The resulted thermal distribution will

cause expansion in the connected beams causing the actuator to deflect based on the structural configuration.

The modeling of a thermal actuator can be simplified into a one dimensional problem when the length scale of a beam is much higher than its width and thickness [69]. In case of a packaged micro-device operating at low temperature, heat losses caused by radiation and convection are negligible compared to heat losses due to conduction to the substrate. In this analysis, it is assumed that the heat conduction coefficient is constant ($k_p = \psi_0$) and not a function of temperature, and that the temperatures of the pads and substrate are constant at T_s.

The temperature variation of an actuator is governed by a nonlinear PDE with an input current density *J=I/wh,* where *I* is input current. A beam structure of uniform cross section (width w and height h) floats on a substrate with an air gap and with the two ends anchored at the pads. The rate of heat change per area is equal to heat generation per unit volume per time minus heat losses and is give as:

$$\rho_d C_p \frac{\partial T}{\partial t} dx = \left(\frac{I}{wh}\right)^2 \rho_o \left[1+\xi\left(T-T_s\right)\right] dx - \left[-\psi_o \frac{d^2 T}{dx^2} dx + \frac{S}{h}\left(\frac{T-T_s}{R_T}\right) dx + \left(wh_{cu} + 2hh_{cs}\right)\left(T-T_{amb}\right) dx\right] \tag{4.30}$$

where, the shape factor $S = h/w(2t_v/h+1)+1$ amplifies the heat flow into the substrate [70, 78]. R_T is the thermal resistance between the micro-beam and the substrate separated by an airgap, and is given by $R_T = t_v/k_v + t_s/k_s$, where t_v and t_s are the thicknesses of the air gap and the substrate, and k_v and k_s are the thermal conductivities of the air and the substrate, respectively. Convection is considered on the upper face of a thermal actuator

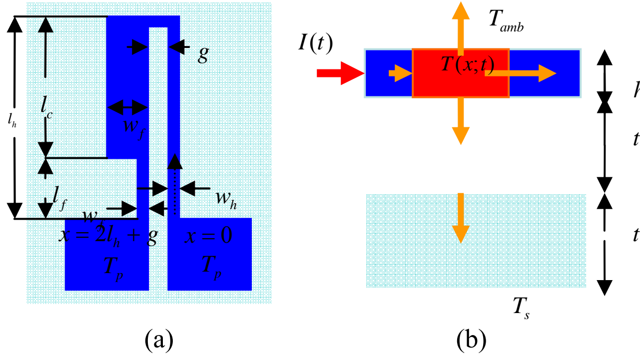

(a) (b)

Figure 4.16 Schematic drawing of a thermal folded beam actuator. (a) Top view and (b) side view.

with the convection coefficient h_{cu} and film temperature $T_{film} = T_{amb} = T_s$. While convection through side walls can be negligible to a thermal actuator with a thin device layer like those fabricated by PolyMUMPs, the convection heat transfer of a thick device layer must be considered. It is assumed that the resistance of the beam material is linear to temperature changes, where the thermal coefficient ξ, and the thermal conductivity of the beam material ψ_o, are constant.

The transient parabolic heat conduction PDE of an element in equation 4.30 is expressed as,

$$\frac{\partial^2\theta}{\partial x^2} = \frac{1}{\alpha_p}\frac{\partial\theta}{\partial t} + \varepsilon\theta \tag{4.31}$$

where

$$\theta = (T - T_\infty)\ \alpha_p = \frac{\psi_o}{\rho_d C_p}, \qquad h_e = wh_{cu} + 2hh_{cs},$$

$$\varepsilon = \left(\frac{S}{hR_T\psi_o} + \frac{h_e}{\psi_o} - \frac{J^2\rho_o\xi}{\psi_o}\right),\ T_\infty = \left(T_s + \frac{J^2\rho_o}{\varepsilon\psi_o}\right) \tag{4.32}$$

A folded beam micro-actuator shown in Figure 4.16 could be represented as three serially connected beams representing the hot, cold and flexure arms. The

temperature distribution of this folded beam micro-actuator is continuous. The temperature profile starts from the temperature of the right side pad at the hot arm, continuous at the cold arm, and ends at the left side pad at the flexure arm end. The condition that the heat flux through the arms must be continuous yields the following necessary but not sufficient Dirichlet conditions expressed in the transformed serial model as follows

$$\begin{cases} W(0,s)=\dfrac{T_s-T_{\infty h}}{s}, \quad W_h(L+g,s)-W_c(L+g,s)=\dfrac{T_{\infty c}-T_{\infty h}}{s} \\ w_h\dfrac{dW_h}{dx}(L+g,s)-w_c\dfrac{dW_c}{dx}(L+g,s)=0,\ W_c(L+g+L_c,s)-W_f(L+g+L_c,s)=\dfrac{T_{\infty f}-T_{\infty c}}{s} \\ w_c\dfrac{dW_c}{dx}(L+g+L_c,s)-w_f\dfrac{dW_f}{dx}(L+g+L_c,s)=0,\ W_f(2L+g,s)=\dfrac{T_s-T_{\infty f}}{s} \end{cases} \tag{4.33}$$

where $W=\Im\{\theta\}$.

The major difficulty in solving the Laplacian of equations (4.31) and (4.33) is the need to simultaneously solve the three systems of PDEs which correspond to the number of connected beams. Mathematically speaking, the conditions ($\varepsilon<0$, $\varepsilon=0$ & $\varepsilon>0$) hold for a particularly designed E-T actuator giving different excitation signals [80]. Practically, the low temperature profile along a beam is exponentially distributed if $\varepsilon>0$. Otherwise, it is critically constant for $\varepsilon=0$ or sinusoidally distributed for $\varepsilon<0$. In all situations, high order numerical approximations are required to avoid the suppression and numerical oscillation of time dependent temperature distribution. Hence, an approximate analytical solution that can optimize and fit different conditions is proposed.

The temperature boundary conditions (BCs) at the pads are not necessarily the same as the initial condition for all beams as $T(x;0)=T_i$. These BCs are transformed from

the time domain into the Laplace domain, thus transforming the equations into only function of x. The ordinary differential equations of the three systems are rewritten in Laplace domain as

$$\frac{d^2W_k\left(x,s\right)}{dx^2}-\left(\frac{s+\alpha_p\varepsilon_k}{\alpha_p}\right)W_k\left(x,s\right)+\frac{T_i}{\alpha_p}=0,\quad k==h,c,f \tag{4.34}$$

A trial solution in terms of finite sum of basis-functions could be formulated using the independent space variable x, time phase lag, and the indeterminate coefficients. A second order polynomial approximation is chosen as the basis function for the current analysis

$$\tilde{W}_k\left(x,s,T_{\infty k},\alpha,\varepsilon\right)=a_{ok}+a_{1k}x+a_{2k}x^2,\quad k==h,c,f \tag{4.35}$$

A second order polynomial function is chose since it could approximate the exponential function in the x-domain. This normally occurs for $\varepsilon>0$, a condition that represents the majority of operations of E-T actuators.

The residuals are obtained by substituting equation 4.35 into equation 4.34 for hot, cold, and flexure arms

$$\begin{aligned}
&R_h\left(x,s\right)=T_i/\alpha_p+a_{oh}\Psi_{1h}+a_{1h}\Psi_{2h}+a_{2h}\Psi_{3h} && L+g\geq x\geq 0\\
&R_c\left(x,s\right)=T_i/\alpha_p+a_{oc}\Psi_{1c}+a_{1c}\Psi_{2c}+a_{2c}\Psi_{3c} && L+g+L_c\geq x\geq L\\
&R_f\left(x,s\right)=T_i/\alpha_p+a_{of}\Psi_{1f}+a_{1f}\Psi_{2f}+a_{2f}\Psi_{3f} && 2L+g\geq x\geq L+g+L_c
\end{aligned} \tag{4.36}$$

where, the coefficients of undetermined residuals are

$$\begin{aligned}
&\Psi_{1k}=\left(-\frac{s+\alpha_p\varepsilon_k}{\alpha_p}\right),\quad \Psi_{2k}=\left(-\frac{s+\alpha_p\varepsilon_k}{\alpha_p}x\right),\\
&\Psi_{3k}=\left(2-\frac{s+\alpha_p\varepsilon_k}{\alpha_p}x^2\right)\qquad k==h,c,f
\end{aligned} \tag{4.37}$$

The next step is to find the best set of parameters of the basis function approximation for which the approximated solution of the transformed independent variable is as close as possible to the exact solution of the transformed dependent variable. This is performed by using weighted residual method which includes the collocation, subdomain, least square and Galerkin criteria [79].

The subdomain optimization method is utilized to generate the remaining equations that are needed to solve for the undetermined coefficients of an approximated function. This method is based on setting the residual integrals to zero over the subdomains. A reasonable choice is used to divide the domain into intervals based on the length of the hot, cold, and flexure arms

$$\int_{0}^{(L+g)} R_h dx = 0 \qquad \int_{(L+g)}^{(L+g+L_c)} R_c dx = 0 \qquad \int_{(L+g+L_c)}^{(2L+g)} R_f dx = 0 \tag{4.38}$$

The undetermined coefficients are evaluated by substituting the approximate functions $\tilde{W}$ into both the auxiliary conditions in equation 4.33 and optimization criteria in equation 7 yielding a series of algebraic equations expressed in matrix form as

$$[a] = \begin{bmatrix} A_a \\ --- \\ A_b \end{bmatrix}^{-1} [b] \tag{4.39}$$

where, the undetermined coefficients of the three micro-beams in approximated functions are $a = [a_{0h} \quad a_{1h} \quad a_{2h} \quad a_{0c} \quad a_{1c} \quad a_{2c} \quad a_{0f} \quad a_{1f} \quad a_{2f}]^T$, and b is a constant matrix in spatial and Laplace domains given by

$$b = \left[\frac{T_s - T_{\infty h}}{s} \quad \frac{T_{\infty c} - T_{\infty h}}{s} \quad 0 \quad \frac{T_{\infty f} - T_{\infty c}}{s} \quad 0 \quad \frac{T_s - T_{\infty f}}{s} \right.$$
$$\left. -\frac{T_i\left(L+g\right)}{\alpha_p} \quad -\frac{T_i\left(L_c\right)}{\alpha_p} \quad -\frac{T_i\left(L-L_c\right)}{\alpha_p} \right] \tag{4.40}$$

The boundary conditions and flux continuity between the micro-beams yield the following matrix

$$A_a = \begin{bmatrix} 1 & 0 & 0 & 0 & 0 & 0 & 0 & 0 & 0 \\ 1 & (L+g) & (L+g)^2 & -1 & -(L+g) & -(L+g)^2 & 0 & 0 & 0 \\ 0 & 1 & 2(L+g) & 0 & -\left(w_c/w_h\right) & -2(L+g)\left(w_c/w_h\right) & 0 & 0 & 0 \\ 0 & 0 & 0 & 1 & (L+g+L_c) & (L+g+L_c)^2 & -1 & -(L+g+L_c) & -(L+g+L_c)^2 \\ 0 & 0 & 0 & 0 & 1 & 2(L+g+L_c) & 0 & -\left(w_f/w_c\right) & -2(L+g+L_c)\left(w_f/w_c\right) \\ 0 & 0 & 0 & 0 & 0 & 0 & 1 & \left(2L+g\right) & \left(2L+g\right)^2 \end{bmatrix}$$

(4.41-a)

The subdomain optimization method in equation 4.38 completes the indeterminism of the approximate function coefficients. Consequently, the matrix A_b in spatial and Laplace domains is given by

$$A_b = \left[\begin{matrix} -\frac{(L+g)}{\alpha_p}\left(s+\alpha_p\varepsilon_h\right) & -\frac{(L+g)^2}{2\alpha_p}\left(s+\alpha_p\varepsilon_h\right) & 2L+2g-\frac{(L+g)^3}{3\alpha_p}\left(s+\alpha_p\varepsilon_h\right) & 0 \\ 0 & 0 & 0 & -\frac{L_c}{\alpha_p}\left(s+\alpha_p\varepsilon_c\right) \\ 0 & 0 & 0 & 0 \end{matrix} \right.$$
$$\left. \begin{matrix} 0 & 0 & 0 & 0 & 0 \\ -\frac{(L+g+L_c)^2-(L+g)^2}{2\alpha_p}\left(s+\alpha_p\varepsilon_c\right) & 2L_c-\frac{(L+g+L_c)^3-(L+g)^3}{3\alpha_p}\left(s+\alpha_p\varepsilon_c\right) & 0 & 0 & 0 \\ 0 & 0 & -\frac{(L-L_c)}{\alpha_p}\left(s+\alpha_p\varepsilon_f\right) & -\frac{(2L+g)^2-(L+g+L_c)^2}{2\alpha_p}\left(s+\alpha_p\varepsilon_f\right) & 2\left(L-L_c\right)-\frac{(2L+g)^3-(L+g+L_c)^3}{3\alpha_p}\left(s+\alpha_p\varepsilon_f\right) \end{matrix} \right]$$

(4.41-b)

The $\left[A_a|A_b\right]^T$ matrix is the coefficient matrix for the system of polynomial that describes the thermal behavior of the actuator. The Eigenvalues of this coefficient matrix are used to evaluate the time constants of the thermal actuator.

$$\Delta(s) = \left| \left[A_a \middle| A_b \right]^T \right| \tag{4.42}$$

In a stable thermo-dynamical system, the magnitude of the real part of the Eigen-values is the inverse of time constants. The three fundamental and dominant rising time constants, τ_1, τ_2, and τ_3 correspond to the three connected beams and determine the approximated averaged rise time in the exponential components of the time varying coefficients.

The general solution of the temperature distribution of the thermal actuator is obtained by computing matrix a in the time domain and substituting it into the approximate shape function.

Matrix a is obtained in time domain by taking the inverse Laplace of the right hand side in equation 4.39

$$\left[a(t) \right] = \Im \left\{ \begin{bmatrix} A_a(s) \\ --- \\ A_b(s) \end{bmatrix}^{-1} \left[b(s) \right] \right\}^{-1} \tag{4.43}$$

The general solution consists of both the transient and steady state temperature distributions and is obtained by substituting equation 10 in the temperature model

$$\tilde{T}_k(x;t) = T_{\infty k} + a_{ok}(t) + a_{1k}(t)x + a_{2k}(t)x^2 \quad , \quad k == h, c, f \tag{4.44}$$

Although this analysis is obtained for three sequentially connected folded beams, the presented approach can be easily extended to any finite number of connected micro-beams. In such a case, the matrices in equations (4.41-a and 4.41- b) are

augmented while meeting the conditions for temperature continuity and residuals relaxation.

4.3.1.2 Discharging Time from Steady State Conditions

The steady state heat conduction equation (S.S.H.C.E) is obtained by dropping the time partial derivative in equation 4.30, yielding a set of simple linear ordinary differential equations (ODEs) which are found in the literature [69, 80]. Here, the steady is derived for $\varepsilon > 0$ to be state temperature distribution for the hot, cold, and flexure arms

$$T_k(x) = \alpha_k + C_{1k} e^{\sqrt{\frac{\beta_k}{\psi_o}}x} + C_{2k} e^{-\sqrt{\frac{\beta_k}{\psi_o}}x} \qquad k == h, c, f \tag{4.45}$$

where, $\beta = \left(\frac{S}{hR_T} + h_e - J^2 \rho_o \xi\right)$, $\alpha_d = T_s + \frac{J^2 \rho_o}{\beta}$, and $C_{1h}, \ldots, C_{2f}$ are constants found by solving the steady state heat conduction equation. A microactuator reaches stable steady state in equation 4.45 if $\beta_h, \beta_c, \beta_f > 0$ is held for the three beams (normally occur at low input current), i.e., the maximum allowed current that produces an exponential steady state response is

$$I = \min\left\{ I_i = \sqrt{\frac{k_v k_s \xi w_i \rho_0 \left(2t_v + h + w_i\right) + \left(k_v t_s + k_s t_v\right)\left(w_i h_{cui} + 2hh_{csi}\right)}{\xi h \rho_0 \left(k_v t_s + k_s t_v\right)}} \right\}_{i == h, c, f} \tag{4.46}$$

The continuity condition in the temperature distribution of a three beam microstructure is also imposed for the discharging time starting from steady state conditions starting from the pad temperature at hot arm and ending at the pad

temperature at the flexure arm. The heat flux continuity condition between the arms yields the following Dirichlet conditions used to solve for the six unknown constants

$$
\begin{aligned}
&T_h(0)=T_s && w_h\frac{dT_h(L+g)}{dx}=w_c\frac{dT_c(L+g)}{dx}\\
&T_h(L+g)=T_c(L+g) && T_c(L+g+L_c)=T_f(L+g+L_c)\\
&T_f(2L+g)=T_s && w_c\frac{dT_c(L+g+L_c)}{dx}=w_f\frac{dT_f(L+g+L_c)}{dx}
\end{aligned}
\tag{4.47}
$$

Applying the boundary conditions into S.S.H.C.E solve for constant which are expressed in the following matrix

$$
\begin{bmatrix} C_{1h}\\ C_{2h}\\ C_{1c}\\ C_{2c}\\ C_{1f}\\ C_{2f}\end{bmatrix}=
\begin{bmatrix}
1 & 1 & 0 & 0 & 0 & 0\\
e^{\sqrt{\frac{\beta_h}{\psi_o}}(L+g)} & e^{-\sqrt{\frac{\beta_h}{\psi_o}}(L+g)} & -e^{\sqrt{\frac{\beta_c}{\psi_o}}(L+g)} & -e^{-\sqrt{\frac{\beta_c}{\psi_o}}(L+g)} & 0 & 0\\
e^{\sqrt{\frac{\beta_h}{\psi_o}}(L+g)} & -e^{-\sqrt{\frac{\beta_h}{\psi_o}}(L+g)} & -\frac{w_c}{w_h}\sqrt{\frac{\beta_c}{\beta_h}}e^{\sqrt{\frac{\beta_c}{\psi_o}}(L+g)} & \frac{w_c}{w_h}\sqrt{\frac{\beta_c}{\beta_h}}e^{-\sqrt{\frac{\beta_c}{\psi_o}}(L+g)} & 0 & 0\\
0 & 0 & e^{\sqrt{\frac{\beta_c}{\psi_o}}(L+g+L_c)} & e^{-\sqrt{\frac{\beta_c}{\psi_o}}(L+g+L_c)} & -e^{\sqrt{\frac{\beta_f}{\psi_o}}(L+g+L_c)} & -e^{-\sqrt{\frac{\beta_f}{\psi_o}}(L+g+L_c)}\\
0 & 0 & e^{\sqrt{\frac{\beta_c}{\psi_o}}(L+g+L_c)} & -e^{-\sqrt{\frac{\beta_c}{\psi_o}}(L+g+L_c)} & -\frac{w_f}{w_c}\sqrt{\frac{\beta_f}{\beta_c}}e^{\sqrt{\frac{\beta_f}{\psi_o}}(L+g+L_c)} & \frac{w_f}{w_c}\sqrt{\frac{\beta_f}{\beta_c}}e^{-\sqrt{\frac{\beta_f}{\psi_o}}(L+g+L_c)}\\
0 & 0 & 0 & 0 & e^{\sqrt{\frac{\beta_f}{\psi_o}}(2L+g)} & e^{-\sqrt{\frac{\beta_f}{\psi_o}}(2L+g)}
\end{bmatrix}^{-1}
\begin{bmatrix} T_s-\alpha_h\\ \alpha_c-\alpha_h\\ 0\\ \alpha_f-\alpha_c\\ 0\\ T_s-\alpha_f\end{bmatrix}
\tag{4.48}
$$

As the thermal actuator reaches steady state, the heat is stored in the structure and kept constant unless the input current is removed. The structure mainly dissipates energy by heat conduction from the lower device surface to the substrate surface. The folded beam structure is lumped as a single block element under average temperature given by

$$
\bar{T}=\frac{1}{2L+g}\left[\alpha_h(L+g)+\alpha_c(L_c)+\alpha_f(L_f)+\int_0^{L+g}T_h(x)dx+\int_{L+g}^{L+g+L_c}T_c(x)dx+\int_{L+g+L_c}^{2L+g}T_f(x)dx\right]
\tag{4.49}
$$

Specifically, when $\beta > 0$ the average temperature is computed from equations 4.46, 4.48 and4.49 as,

$$\overline{T} = \frac{1}{2L+g}\left[\alpha_h(L+g) + \alpha_c(L_c) + \alpha_f(L_f) + \sqrt{\frac{\psi_o}{\beta_h}}\begin{bmatrix} C_1\left(e^{\sqrt{\frac{\beta_h}{\psi_o}}(L+g)} - 1\right) - \\ C_2\left(e^{-\sqrt{\frac{\beta_h}{\psi_o}}(L+g)} - 1\right) \end{bmatrix} + \sqrt{\frac{\psi_o}{\beta_c}}\left[C_4\left(e^{\sqrt{\frac{\beta_c}{\psi_o}}(L+g+L_c)} - e^{\sqrt{\frac{\beta_c}{\psi_o}}(L+g)}\right) - C_5\left(e^{-\sqrt{\frac{\beta_c}{\psi_o}}(L+g+L_c)} - e^{-\sqrt{\frac{\beta_c}{\psi_o}}(L+g)}\right)\right] + \right.$$
$$\left. \sqrt{\frac{\psi_o}{\beta_f}}\left[C_5\left(e^{\sqrt{\frac{\beta_f}{\psi_o}}(2L+g)} - e^{\sqrt{\frac{\beta_f}{\psi_o}}(L+g+L_c)}\right) - C_6\left(e^{-\sqrt{\frac{\beta_f}{\psi_o}}(2L+g)} - e^{-\sqrt{\frac{\beta_f}{\psi_o}}(L+g+L_c)}\right)\right]\right]$$

(4.50)

The governing equation which represents the temperature decay in a structure from $\overline{T}$ to T_s is

$$\frac{d\phi}{dt} + \tau_d \phi = 0 \tag{4.51}$$

where $\phi = T - T_s$ and $1/\tau_d = \frac{1}{C_p \rho_d}\left[\frac{\overline{S}}{R_T h} + \overline{h_e}\right]$.

This ODE represents the equation for temperature discharge, and its solution is given by

$$T(t) = T_s + \left(\overline{T} - T_s\right)e^{-(1/\tau_d)t} \tag{4.52}$$

where,$1/\tau_d$ is the decay time constant (the time needed for the thermal actuator to return to its initial position after being deflected is approximately $5/\tau_d$). $\overline{S}$ and $\overline{h_e}$ are the equivalent total shape factor and heat convection coefficient, respectively, and they are evaluated from S and h_e given that the average width $\overline{w}$ is approximated by averaging the equivalent area of the arms as

$$
\begin{aligned}
&\overline{w} = \left[\left(L + g \right) w_h + L_c w_c + L_f w_f \right] / \left[2L + g \right] \\
&\overline{S} = h\left(2t_v / h + 1 \right) / \overline{w} + 1 \\
&\overline{h_e} = \overline{w} h_{cu} + 2hh_{cs}
\end{aligned}
\tag{4.53}
$$

The approximate time. t_k , needed for a thermal actuator to decay from its lumped temperature, $\overline{T}$, down to $\kappa\%$ of T_s is given by

$$
t_k = Log\left(\frac{\overline{T} - T_s}{T_s[\kappa - 1]} \right)^{\tau_d} \tag{4.54}
$$

4.3.2 Verification Methodologies of the Proposed Theories

In this section, the validation of the proposed approximate methods and some other known techniques are presented. The verification of the obtained approximate rising time is performed by comparing it with results obtained by finite difference approximation method and exact solution of a special case. The steady state temperature profile of a thermal folded beam actuator was previously derived and experimentally confirmed in the literature [14], accordingly finite element modeling is sufficiently utilized in this work to validate the lumped model for cooling time responses. The verification of the proposed methods provided for extensive numerical simulations to evaluate the performance of fabricated devices both for temperature rising and cooling responses. This section presents simulations followed by discussions of the verification techniques.

4.3.2.1 SOI, PolyMUMPS and FLM Folded Beams Actuators

Thermal folded beam actuators can be fabricated using various technologies such as thin film deposition, DRIE, and laser machining. The performance of a device depends on the material and fabrication process. Figure (4.17-a) shows a folded beam actuator fabricated on an SOI wafer, and composed of four sandwiched layers; a 500 μm thick silicon handle wafer, 2 μm thick SiO2 with air gap, 100 μm thick silicon device structure, and metal coated pads. A PolyMUMPs folded beam actuator shown in Figure (4.17-b) has an additional dielectric Silicon nitride (Si_3N_4) layer sandwiched between the oxide layer and the handle wafer. The cross thermal resistance between the thermal micro-beam and the substrate is given by $R_T = t_v / k_v + t_n / k_n + t_s / k_s$, where, t_n and k_n are the thickness and thermal conductivity of Silicon nitride (Si_3N_4). The cross thermal resistance is more difficult to calculate for actuators fabricated from single layer substrates using surface micromachining such as Femtosecond laser micromachining (FLM) as shown in Figure (4.17-c). This is due to the uncertainty or variation of the air gap thickness after embedding the single layer folded beam actuator onto the workpiece layer.

In addition, although it is easy to accurately model material properties as function of temperature, in this research, only the resistance dependency on temperature at the lower range of the folded beam operating temperature is considered. This will facilitate establishing a comparison between the proposed approximate methods with other techniques, specifically at low input power.

In the following sections, the performance of the aforementioned fabricated folded beam actuators is assessed using numerical simulations. Furthermore, the mechanical performance of an SOI wafer fabricated folded beam actuator is experimentally analyzed using a non-contact MEMS profilometer and the obtained mechanical cycle is compared with the numerically evaluated thermal cycle which will be discussed in next sections.

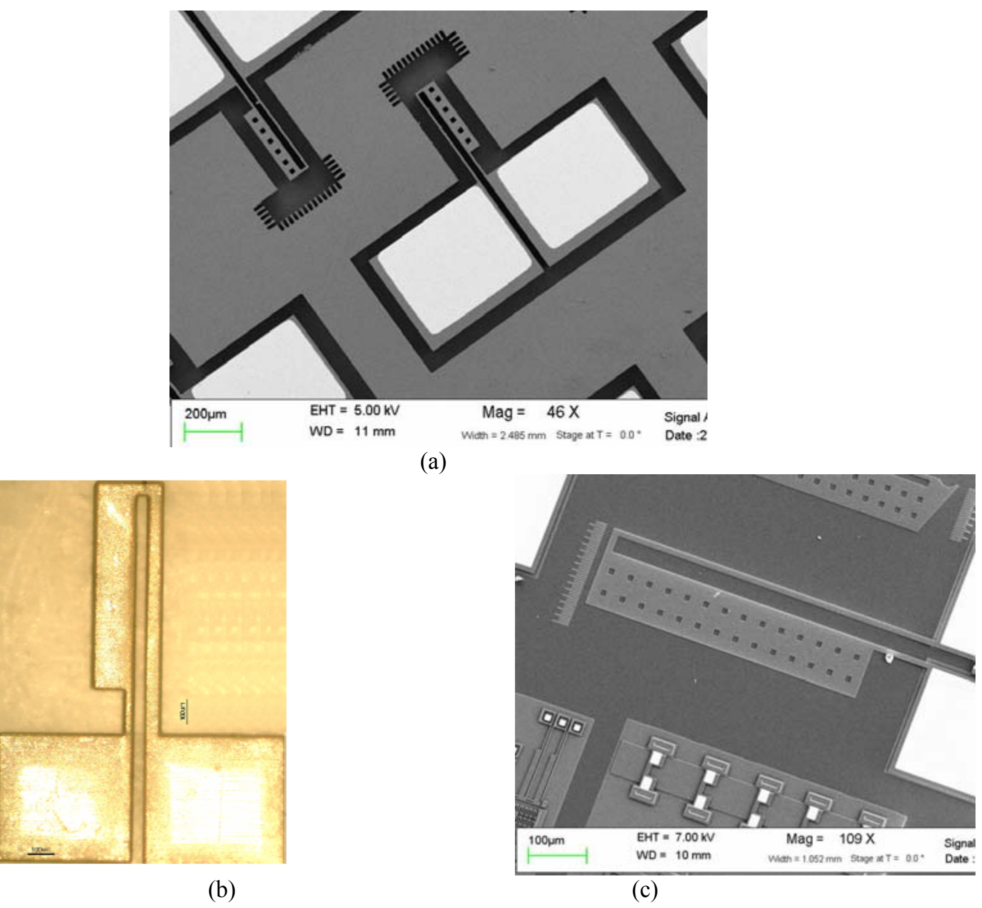

Figure 4.17 Three fabrication methods of folded beam thermal actuators. (a) DRIE with an SOI wafer, (b) PolyMUMPs, and (c) Nickel fabricated by FLM system and attached on PMMA substrate.

4.3.2.2 Verification of Trial Solution Method Using Finite Difference Approximation (FDA)

The general solution of a rising temperature distribution may be obtained by Forward-Time Centered-Space method (FTCS). For the thermal folded beam actuator in Figure (4.16), the finite difference representation of equations (4.31 and 4.32) can be expressed as

$$T_i^{n+1} = \left(\frac{{}^k\alpha_p \Delta t}{\Delta x^2}\right)\left(T_{i-1}^n - T_i^n\left(2 + {}^k\varepsilon\Delta x^2 - \frac{\Delta x^2}{{}^k\alpha_p \Delta t}\right) + T_{i+1}^n + {}^kT_\infty\, {}^k\varepsilon\Delta x^2\right) \quad \boldsymbol{k = f,c,h} \qquad (4.55)$$

where, *n* and *i* are integers that refer to time and space meshes, Δx and Δt are space and time grid resolutions, respectively. Time and space grids must be chosen to satisfy the Crank–Nicholson convergence condition. The non-homogeneity in the structure is accounted by the change in properties along spatial variable *x*. For a folded beam actuator, the parameters ${}^k\alpha_p, {}^k\varepsilon$ and ${}^kT_\infty$ change as the temperature profile marches across flexure, cold and hot arms. The continuity of flux and temperature at intermediate beam joints is automatically satisfied through space and time marching.

The derived finite difference equation (4.55) is applicable for thermal actuators with any number of serially connected line-shape beams $k \in I: 1,2,...,n$. Where the actuator with non-homogeneity in material and structure configurations can be analyzed by simply considering and changing ${}^k\alpha_p, {}^k\varepsilon$ and ${}^kT_\infty$ values while marching the *x*-domain. The rising temperature responses and time constants of V and U shape actuators are simulated and compared with our approximated methods as will be discussed in layer examples.

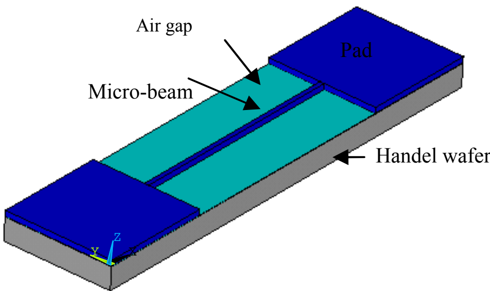

Figure 4.18 Solid model of an attached thermal actuator of uniform widths (I-shape).

4.3.2.3 Verification of Trial Solution Method for V-Shape Actuator

The approximate thermal response of a folded beam actuator, derived in section II.B, can be used to obtain the thermal response of V-shape actuator which is thermally equivalent to a single attached micro-beam shown in Figure 4.18. This is accomplished by simply setting uniform beam widths for the folded beam actuator $w_f = w_c = w_h$, yielding a thermal actuator with finite and sequentially connected micro-beams with uniform widths and with total length *L*. The approximate approach is verified by comparing it with the exact thermal response of a single micro-beam. The electrothermal behavior of an attached single line shape microstructure is represented by single heat conduction PDE. The transient and steady state temperature responses of a micro-beam thermal actuator have been investigated by Liwei [70], and the exact steady state temperature distribution without convection was given by

$$T_{s.s}(x) = T_\infty - (T_\infty - T_s)\frac{\cosh\left[\sqrt{\varepsilon}\left(x - L/2\right)\right]}{\cosh\left[\sqrt{\varepsilon}\left(L/2\right)\right]}. \tag{4.56}$$

The exact transient temperature distribution was given by [70]

$$T\left(x,t\right)=e^{-\alpha_p\varepsilon t}\sum_{n=1}^{\infty}e^{-\alpha_p\left(nx/L\right)^2 t}\sin\left(\frac{n\pi x}{L}\right)\left[\frac{2}{L}\int_0^L\left[T_s-T_{s.s}\left(x\right)\right]\sin\left(\frac{nx}{L}\right)dx\right]$$

(4.57)

The transient time constant τ_n is obtained from the transient solution as given by [70] is

$$\tau_n=\frac{\rho_d C_p}{\psi_o}\left[\left(\frac{S}{hR_T}-\frac{J^2\rho_o\xi}{\psi_o}\right)+\left(nx/L\right)^2\right]^{-1}. \tag{4.58}$$

The approximate solution obtained through the proposed methodology from equations (4.41-b and 4.44) are obtained as follow

$$\frac{d^2W\left(x,s\right)}{dx^2}-\left(\frac{s+\alpha_p\varepsilon}{\alpha_p}\right)W\left(x,s\right)+\frac{T_i}{\alpha_p}=0\cdot \tag{4.59}$$

Let $\tilde{W}\left(x,s\right)=a_o\left(s\right)+a_1\left(s\right)x+a_2\left(s\right)x^2$ giving that

$$W\left(0,s\right)=\frac{T_s-T_\infty}{s};W\left(2L+g,s\right)=\frac{T_s-T_\infty}{s} \quad . \tag{4.59-a}$$

The residual becomes

$$R\left(x,s\right)=\left[2a_2\left(s\right)+\frac{T_i}{\alpha_p}-\left(\frac{s+\alpha_p\varepsilon}{\alpha_p}\right)a_o\left(s\right)\right]-\left[a_1\left(s\right)\left(\frac{s+\alpha_p\varepsilon}{\alpha_p}\right)\right]x-\left[a_2\left(s\right)\left(\frac{s+\alpha_p\varepsilon}{\alpha_p}\right)\right]x^2 \quad . \tag{4.59-b}$$

The subdomain method is applied to minimize the error along the beam

$$\int_0^L Rdx=0 \qquad L\geq x\geq 0 \quad . \tag{4.59-c}$$

The undetermined coefficients are evaluated to be

$$a_o\left(s\right)=\left(T_s-T_\infty\right)/s\,, \quad a_1\left(s\right)=-La_2\left(s\right)$$

$$a_2(s) = \frac{\lambda_a s + \lambda_b}{s(\lambda_c s + \lambda_d)} \tag{4.60-a}$$

where

$$\begin{aligned} \lambda_a &= (T_s - T_\infty - T_i) \qquad & \lambda_b &= \alpha_p \varepsilon (T_s - T_\infty) \\ \lambda_c &= -5L^2/6 & \lambda_d &= \alpha_p (2 - 5\varepsilon L^2/6) \end{aligned} . \tag{4.60-b}$$

Taking the Laplace inverse of equation (4.59) gives the undetermined coefficients in time domain

$$a_o(t) = T_s - T_\infty, \qquad a_1(t) = -\sqrt{\lambda_c}\, a_2(t),$$

$$a_2(t) = \frac{\lambda_b}{\lambda_d} + \left(\frac{\lambda_a \lambda_d - \lambda_b \lambda_c}{\lambda_c \lambda_d} \right) e^{-(\lambda_d/\lambda_c)t} \tag{4.61}$$

where the general solution is given by the approximation

$$\tilde{T}(x;t) = T_\infty + a_o(t) + a_1(t)x + a_2(t)x^2 \tag{4.62}$$

The slowest rising time occurs when $\partial \tilde{T}(x;t)/\partial x = 0$, yielding that maximum temperature and slowest rising responses occur at $x = -a_1/(2a_2)$=L/2 . The steady state approximate rising temperature is

$$\tilde{T}(x;\infty) = T_s - \frac{\lambda_b \sqrt{\lambda_c}}{\lambda_d} x + \frac{\lambda_b}{\lambda_d} x^2 \quad . \tag{4.63}$$

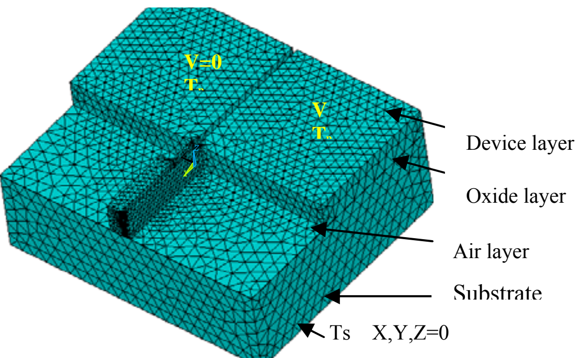

Figure 4.19 FEM model (tetrahedral mesh) and boundary condition of an SOI folded beam actuator.

As will be discussed in simulation subsection, the intensification of this special case is revealed by comparing it with the general exact solution and with the provided numerical approaches that are supported by FDA.

4.3.2.4 Verification of Lumped System Model Using Finite Element Modeling (FEM)

Finite element modeling (FEM) is mainly utilized in this research to compute the temperature discharging profile of thermal folded beam actuators. Also, the steady state temperature response is compared with the exact solution and FDA. It is computationally expensive to analyze the transient response of MEMS actuators with multi structural layers and a high aspect ratio using finite element software. The coupled field capability found in finite element software ANSYS 9 is utilized to obtain the dynamic and static responses of electrothermal folded beam actuators [92]. In ANSYS, the volumetric layers in solid models must have a continuous mesh at different material interfaces corresponding to a device model shown in Figure (4.19). After creating and

assembling the structures, material sets are defined for each volume, and a meshing procedure is globally generated for all volumes. Thermal and structural boundary conditions are applied; the initial temperature of all nodes is T_s while the pad and lower substrate layers have uniform temperature distribution of T_s at all the time. The natural convection coefficients are defined on upper and side faces of the beams with film temperature T_s. The input voltage V is applied across the pads and at different load steps in order to generate a pulsating heat along the folded beams.

The square input voltage consists of two regions; first, heating takes place during the excitation period (ON) and second, the cooling effect starts immediately at the OFF period after using the final temperature values as initial conditions. The FE model is mainly utilized to verify the cooling effect of an electrothermal actuator.

Table 4.5 Material properties of folded beam actuators [78, 69, 109 and 113].

	MUMPS			**SOI**		**FLM**		
Layers / **Parameters**	***Poly silicon***	***Si_3N_4***	***Si substrate***	***Si device***	***Si wafer handle***	***Machined nickel***	***PMMA, acrylic substrate***	***Air***
Density, ρ_d (Kg/m^3)	2330	3180	2330	2330	2330	8880	1190	0.524
Thermal conductivity, k ($Wm^{-1}\,{}^oC^{-1}$)	43	2.25	30	100	30	60.7	0.19	3.37e-2
Thermal Expansion, α ($10^{-6} \times {}^oC^{-1}$)	3.2	3.0	3.3	3.1	3.1	13.1	75	1.49e3
Thermal Capacity, C_p ($J\ Kg^{-1}\,{}^oC^{-1}$)	787	170	787	787	787	460	1450	1013
Temperature coefficient, ξ ($10^{-3} \times {}^o C^{-1}$)	1.25	-	1.25	1.25	1.25	6	-	-
Electrical resistivity, ρ_o ($\Omega.m$)	2.4e-5	10e10	2.4e-5	1.5e-4	2.5e-2	6.4e-8	1e14	3e13

The actuator reaches final steady state temperature at the end of heating period. Where the thermal-electric solid element, Solid69, is chosen to obtain the steady state temperature distribution and subsequently, Solid69 element is switched to Solid87 element that has transient thermal capability. The obtained steady state body temperature is applied as an initial condition for the cooling effect model where the transient mode is activated.

4.3.2.5 Charging and Discharging Time Simulations

The methodology of the simulations followed in this section is demonstrated by comparing the proposed methods among the well known techniques which were provided. The device model fabricated using the SOI wafer is utilized for two main purposes: first, simulation and experimental verification. Second, to study the performance of a folded beam actuator with polyMUMPS, SOI and Nickel folded beam actuators fabricated using FLM for various geometrical scales and material parameters. Tables 4.5 and 4.6 show the material properties and geometries used in this simulation. Initial temperatures of substrate lower face and contact pads are $T_i = 20^oC$ and $T_s \cong 20^oC$. The natural convection heat transfer coefficient of MEMS devices varies with geometrical size, surface roughness; device approximate values of natural convection obtained by [75] are utilized with their values generated in Table 4.7.

Table 4.6 Dimensions of folded beam (U) and line-shape (I) actuators measured in μm .

Parameter	MUMPS	U-SOI	FLM	I-SOI
air gap, t_v	0.75	2	5	2
thickness of substrate layer, t_s	675	300	1000	300
width of the hot arm , w_h	11	10	150	10
width of cold arm , w_c	100	52	1150	10
width of cold flexure arm, w_f	10	10	150	10
length of hot arm, L	598	370	3500	602
length of cold arm, L_c	498	271	2500	0
length of flexure arm, L_f	100	99	1000	0
structure thickness, h	1.5	100	25	100
gap distance between cold and hot arms, g	10	20	200	-
thickness of Si_3N_4 **layer,** t_o	0.6	-	-	-

Table 4.7 Natural convection coefficient used in simulation [75].

Natural convection coefficient ($Wm^{-2}K^{-1}$)	PolyMUMPs			SOI			FLM			SOI, Single lineshape
	f	***c***	***h***	***f***	***c***	***h***	***F***	***c***	***h***	
Face up, h_{cu}	107	67	107	107	67	107	43	23	43	43
Side wall, h_{cs}	11370	11370	11370	11370	11370	11370	504	504	504	504

4.3.2.6 Charging Simulation: Thermal Actuator with Beams of Uniform Widths

A special case study presented in subsection 4.4.3.2 has simplified the solution of the general temperature response for a folded beam actuator with I shape of uniform widths or thermally equivalent to single V-shape actuator analysis. A comparison of results between the steady state temperature profile, obtained from FEA (equation 4.55) and the exact solution (equation 4.45 or4.56), is presented in Figure (4.20-a) indicating that both methods are in good agreement given that the condition in equation (4.46) holds.

This steady state agreement is primarily important in validating the first step in the procedure for solving for the cooling rate of the lumped system. Where the temperature profile of the thermal actuator shall exhibit decay from the steady state temperature to the final temperature κT_s.

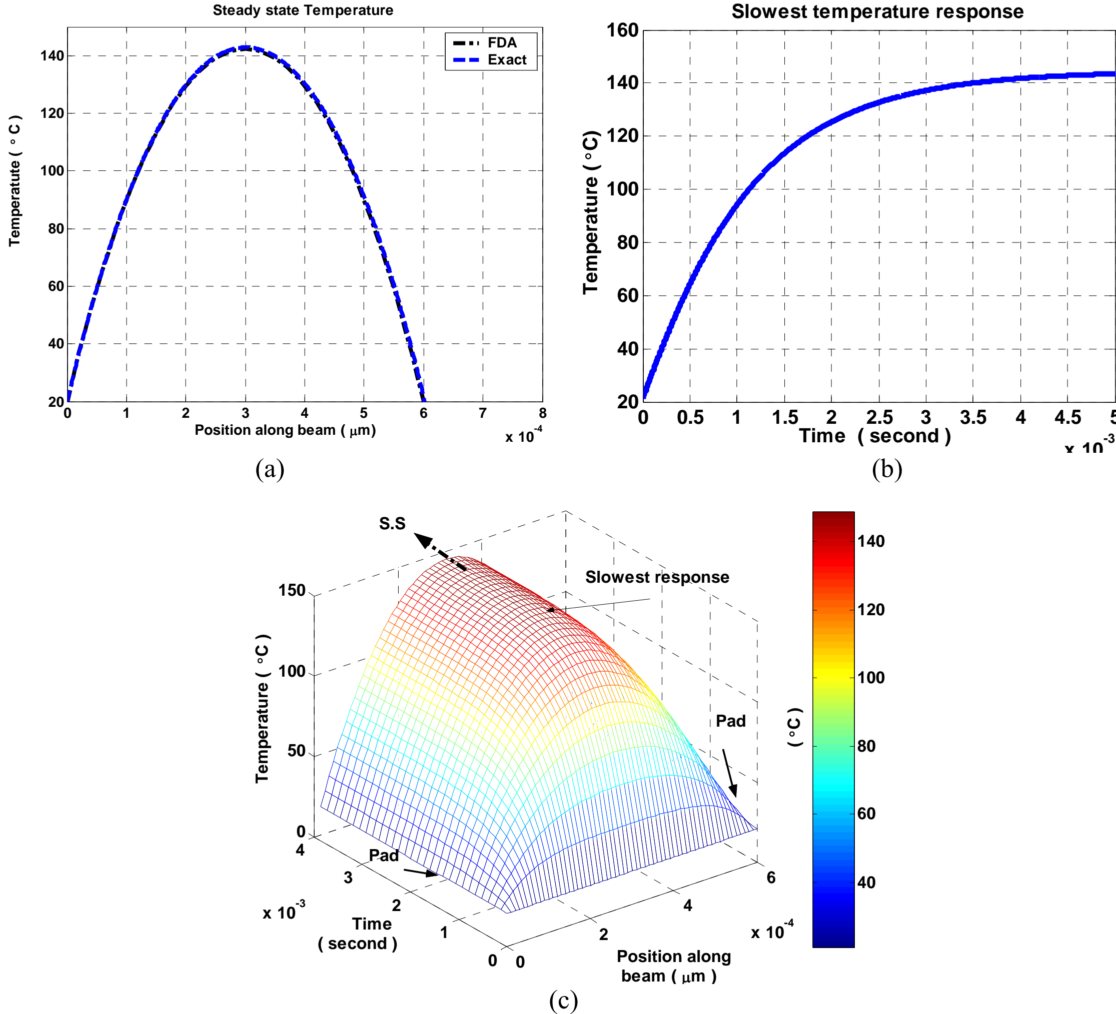

(a) (b)

(c)

Figure 4.20 Temperature response of a single SOI beam at 35mA current input (5V). a) S.S temperature profiles comparison between exact and FDA, b) temperature response $T(x,t)$ which is extracted by FDA and with mesh grid of $\Delta t = 0.5\times10^{-6}s,$, c) The $\Delta x = 10\times10^{-6}m$ slowest temperature response, $T_{\max}(t) = T(x = L/2;t)$, which is extracted from FDA.

Table 4.8 Settling time of a folded beam with uniform widths based on 98% of final value.

Method	**Thermal rising Time of Single Line-shape**
	heating (1 x 10^{-3}) second
FDA	0.4372
Exact	0.4236
Approximate	0.4393

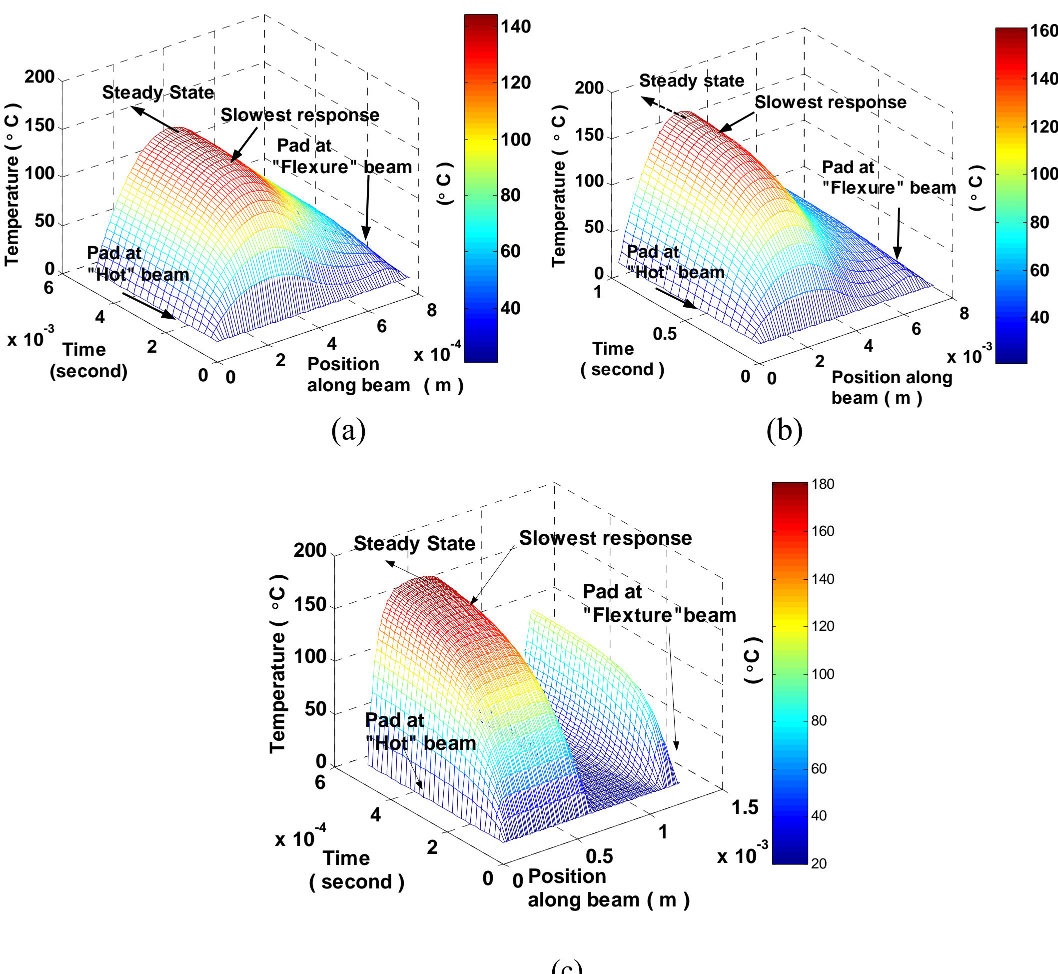

(c)

Figure 4.21 General temperature solution $T(x;t)$ of a folded beam actuator utilizing FDA. (a) SOI folded beam actuator at 50mA current input (4.4V) with $\Delta t = 0.5\times10^{-6}s$, $\Delta x = 10\times10^{-6}m$ (b) FLM folded beam actuator at 780mA current input (0.09V) with $\Delta t = 20\times10^{-6}s, \Delta x = 100\times10^{-6}m$, and C) PolyMUMPs folded beam actuator at 5mA current input (6.4V).

Figure (4.20-b) illustrates the general temperature response using FE approximation. The fastest temperature response occurs next to the pad boundary at which temperature is fixed.

However, the time required to reach steady state decreases as it approaches toward the micro-beam center has the slowest time response. The slowest time required to settle within 2% of the final value is depicted from temperature response at the midsection point as shown in Figure (4.20-c). Also, the analytic slowest time constant, τ_n, can be obtained at $(n=1, x=L/2)$. The approximate rising time constant can either be calculated directly from equation (4.42) or by choosing the largest time constant in equation (4.62). Table 4.8 summarizes a numerical comparison that shows an excellent agreement between FDA, exact and our approximate solution.

4.3.2.7 Charging and Discharging Simulations: Temperature Responses of Thermal Folded Beam Actuator Using FDA and Lumped Model

The finite difference approximation method is used to compare the temperature distribution for different material and geometric configurations. For a folded beam actuator, the rising temperature response according to step voltage input is obtained by applying equation (4-55). The temperature distributions of SOI, FLM, and PolyMUMPs folded beams have been simulated for the tabulated geometries and material properties as shown in Table 4.6 and plotted in Figure (4.21). The slowest thermal rising time of each folded beam is located around the center of hot arm. The maximum temperature

time response of a folded beam was also extracted for several step voltage inputs as shown in Figure (4.22). In general, rising temperature increases as the step voltage input increases due to the increase of temperature amplitudes. The derived lumped model is utilized to approximate the time required for the folded beam actuator to cool down to the initial condition T_s. In Figure (4.23), the decay response of the average temperature in equation 4.52 is simulated using the same excitation step voltage input of cases in Figure (4.22). A comparison between Figure (4.22-b) and Figure (4.23-b) shows that for a specified thermal cycle, the order magnitude of the decay time in the nickel folded

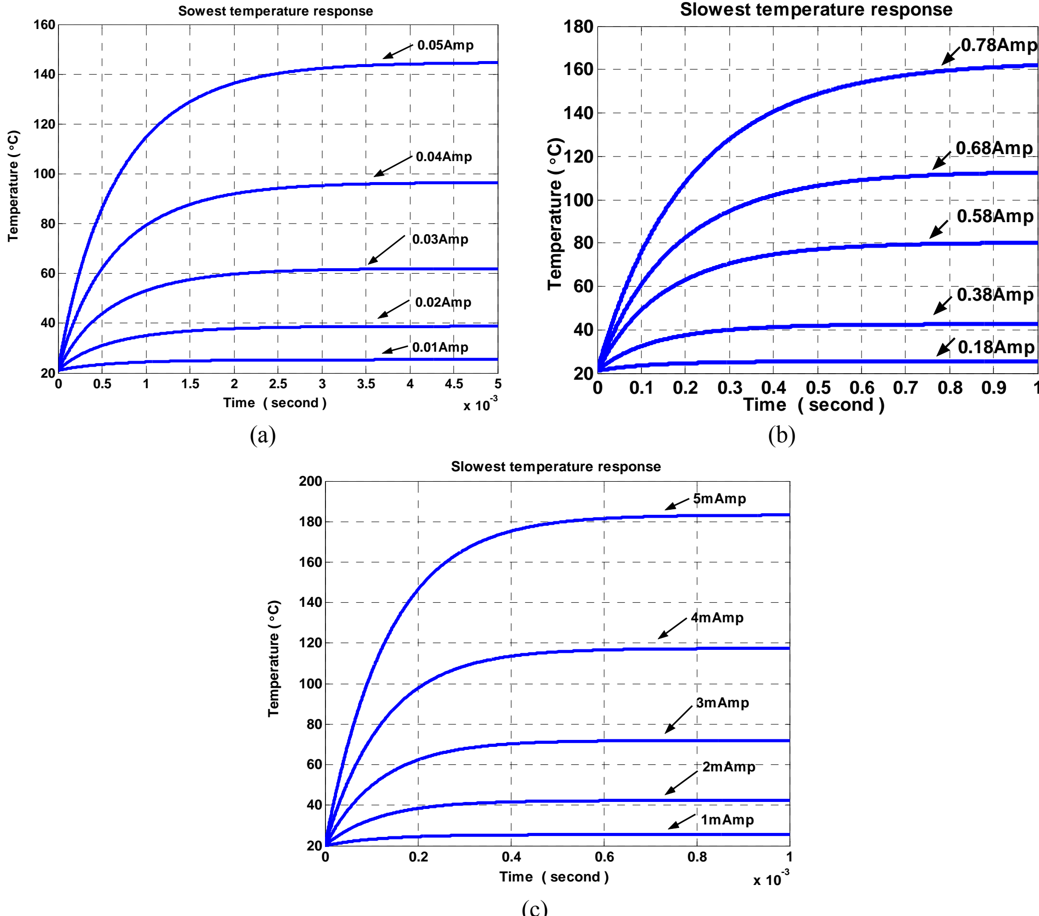

Figure 4.22 Slowest temperature response in a folded beam actuator using FDA and at different input current. (a) SOI, (b) FLM, and (c) PolyMUMPs.

beam actuator is around the rising time. This is due to the low amount of heat stored in the non thick metal layer providing that Nickel specific heat is lower than silicon. Similar conclusion can be drawn for the PolyMUMPs folded beam actuator whose thickness is 2μm. However, the SOI folded beam actuator whose device layer thickness is 100μm stores more heat, accordingly the decay time from steady state requires about two orders of more time.

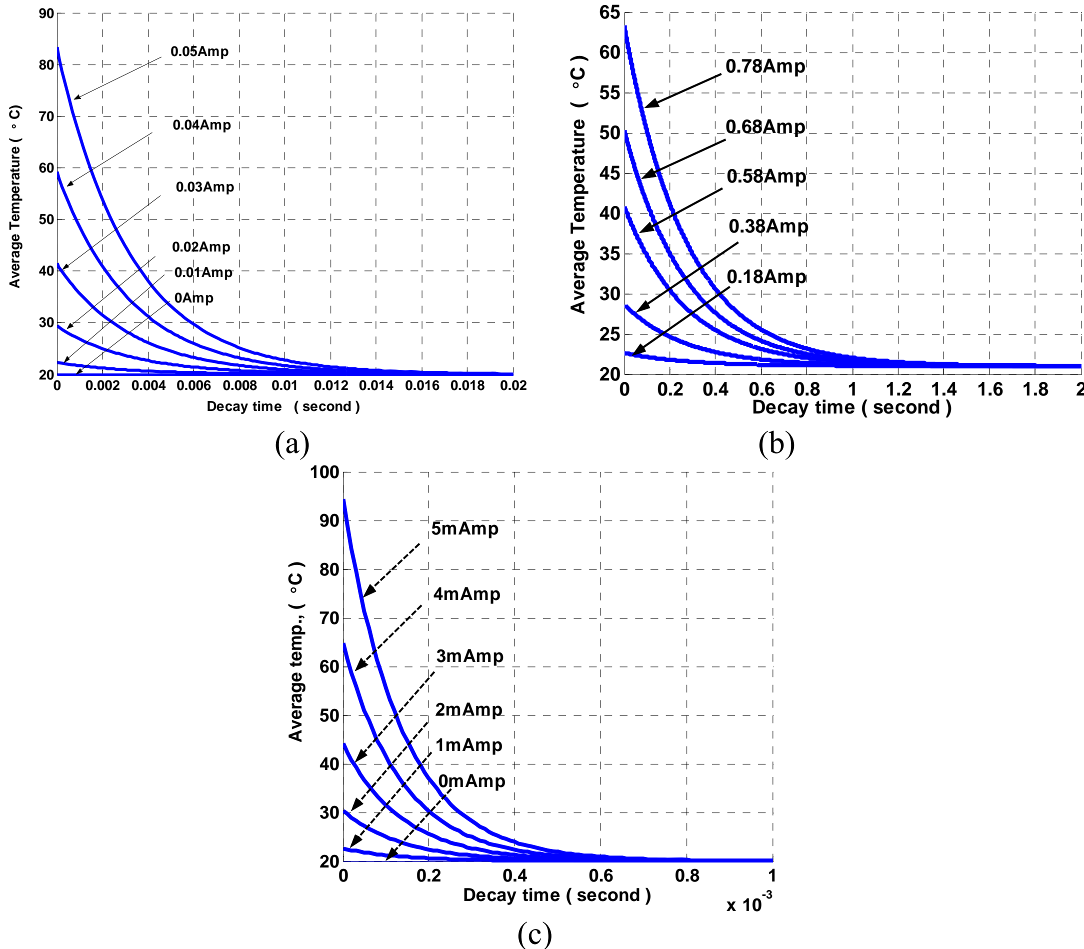

Figure 4.23 Cooling temperature response of the lumped folded beam actuators at different input current. (a) SOI, (b) FLM, and (c) PolyMUMPs.

4.3.2.8 Discharging Simulation: Temperature response of SOI Folded Beam Actuator Using FEM and Approximate Solution

The cooling effect in electrothermal actuators was approximated by a lumped model (equation 4.52) that is based on averaging the steady state temperature distribution along a device layer. The obtained exact S.S temperature distribution is thus compared with FDA and FEM. Figure (4.24-a) compares S.S temperature distributions of the SOI folded beam actuator at 4.4V step voltage input. Although exact and FDA

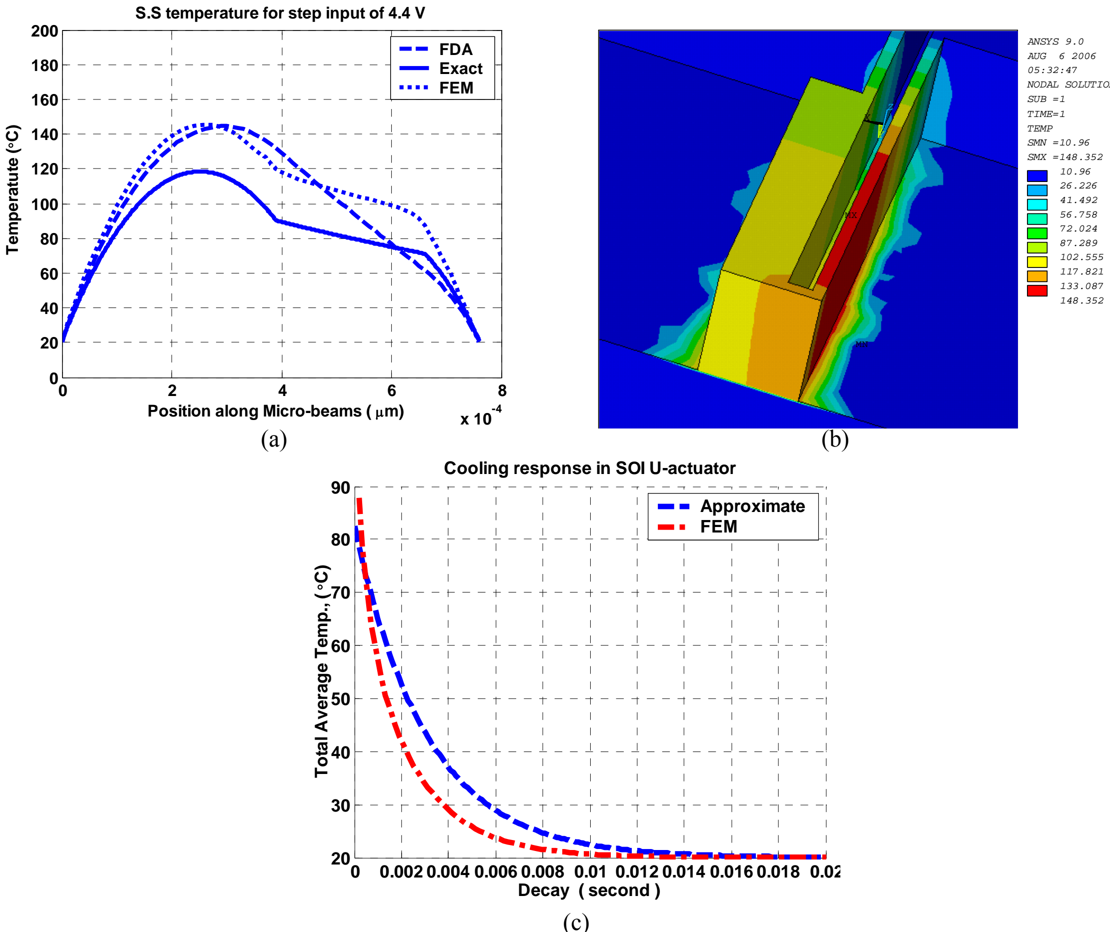

(a) (b)

(c)

Figure 4.24 Steady state and discharging analysis. (a) Comparison of temperature profiles among FDA, FEM, and exact models, and (b) FEM temperature distribution at a steady state at 4.4V. (c) Average transient cooling response after 4.4V square input and its comparison between lumped and FEM models.

were in good agreement for the beam with uniform widths as shown in Figure (4.18-a), both FEM and FDA exhibit a small temperature shift and different profiles.

These differences in folded beam's temperature response resulted from the fidelity of modeling approximation and the exact model assumptions. The derived exact and approximate models were based on high aspect ratio structures; however the thermal actuator with 100µm thick device layer is large compared to the 370µm long hot arm. The initial body temperature is applied after the input current is switched off as shown in Figure (4.24-b). For the purpose of comparisons, the averaged temperature of device layer's elements is plotted against time and compared with the FDA in Figure (4.24-c). Results show that the lumped method correlates well with the FEM even though both the methods.

4.3.4 Relationship between Measured Mechanical and Approximated Thermal Cycle Responses

The temperature profile measurement of MEMS devices requires a fast speed and high spatial resolution Infrared camera with a special optics. Instead of measuring the temperature profile, it is intended in this section to study and correlate the thermal cycle by observing the dynamic response of structures (electro-thermo-elastic). A commercial 3D MEMS dynamic profiler, Wyko/Veeco NT1100 DMEMS profiler [84], was used to measure the dynamical response of a attached folded beam actuator shown in Figure (4.17-a). The lateral deflection of a folded beam tip has been recorded by an interferometer position sensor that probes the full output cycle with $\delta = 5^o$ increment.

The input signal was $A\sin\left(\omega t+\beta\right)+A$, where A is 12V and β is zero. The open loop transfer function of the SOI folded beam actuator was extracted from the bode plot for a range of frequency f from 15Hz to 1015Hz at 50Hz step. Figure (4.25-a) shows the experimental and the best fit of magnitude Bode plot that show the ratio of maximum deflection to input voltage magnitude data at selected frequencies. The magnitude plot depicts a transition change in the actuator response at approximately ~265Hz. The tip deflections are attenuated at two slopes: ~1.4dB/decade and ~7.2dB/decade which correspond to ranges ~[15-65] Hz and ~[65-265] Hz , respectively. However, at frequencies higher than ~265Hz, the increase in input frequency produces excessive heat generation in the folded beam structure. Here, for ranges ~[265-965]Hz, the device cooling rate becomes less than the overall heat generation in folded beam structure and package. Thus, a DC deflection-offset increase of ~13dB/decade is observed with attenuation in peak to peak deflection response.

The linear system, which is observed to produce sinusoidal deflection for sinusoidal voltage excitation, could be approximated by fit model of three zeros and two poles

$$\frac{Y(s)}{V(s)}=\frac{\sum_{i=1}^{3}\left(s+z_i\right)}{\sum_{j=1}^{2}\left(s+p_i\right)} \tag{4.64-a}$$

An algorithm is developed to search for the locations of poles and zeros which are subjected to minimize the magnitude of a norm between experimental magnitudes

and the magnitude of the iterated locations. For a frequency range from 15Hz to1015 Hz, the optimal fit model function fine search gives

$$\frac{-0.0013s^3 + 5.281\ s^2 - 4299\ s - 125.5}{38.52\ s^2 - 22260\ s + 700500}. \quad (4.64\text{-b})$$

The model fit emphasizes that the overall electrothermal mechanical response is derivative over the experimented range of frequency. This is due to overheating (accumulation of heat) which results additive thermo-elastic expansions. The magnitude plot of the approximated open loop transfer function is compared to experimental data (Figure 4.25-a).

To show the normal operation and package heating up zone, it is useful to decompose the frequency response into two distinct frequency regions. The stable open loop models are fitted by first order transfer functions

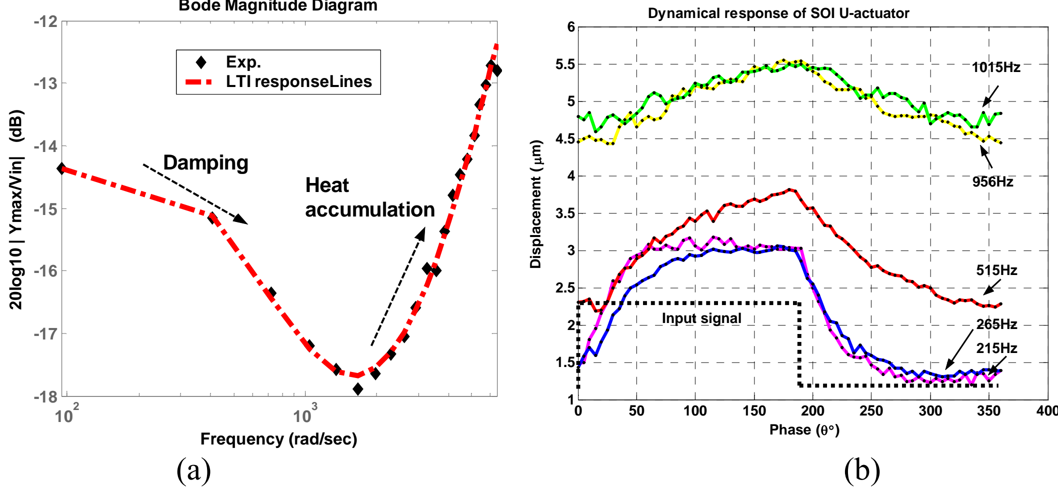

(a) (b)

Figure 4.25 Experimental dynamic response of the SOI thermal actuator for a range of frequencies from 15Hz to 1015Hz. (a) frequency response bode plot, and (b) deflection vs. phase for square signal input.

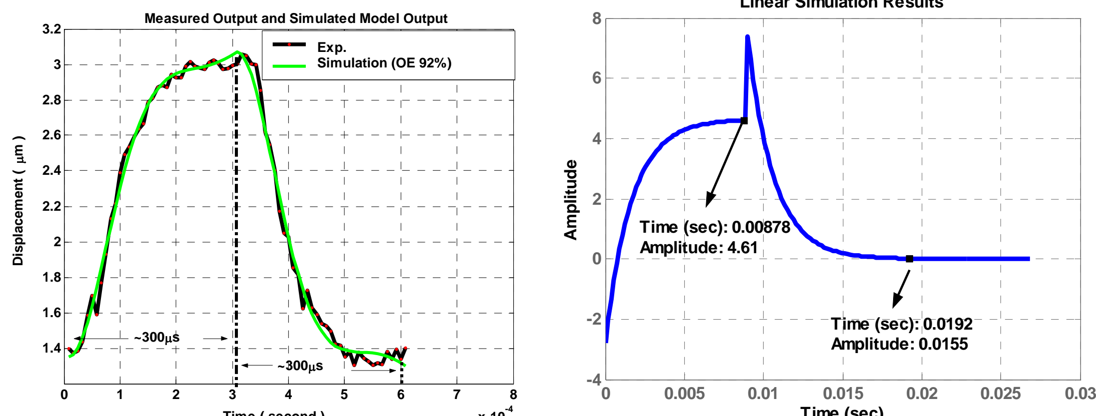

Figure 4.26 Identification of the SOI folded beam (a) Measured and fitted deflection response to 50% duty step input at f =265Hz., and (b) Mechanical response of the SOI folded beam actuator at 24V input with the result obtained from g_1 transfer function.

$$G(j\omega)=\begin{cases} g_1=\dfrac{-5.833\times10^{-5}\,j\omega+0.0589}{0.000505\,j\omega+0.3043}, 15\le f\le 265Hz \\ \\ g_2=\dfrac{-3.661\times10^{-5}\,j\omega+0.1193}{4.874\times10^{-5}\,j\omega+1.063}, 265\le f\le 1015Hz \end{cases} \tag{4.64-c}$$

A thermal folded beam actuator is one of the key elements in active MEMS devices such as microgrippers and optical attenuators. Figure (4.25-b) shows the structural dynamic response of the SOI folded beam actuator which was excited by a square input signal with 50% duty cycle for frequency ranges from 215Hz to 1015Hz. It is important to notice that the mechanical response at 215Hz shows that the device reached steady state deflection just after the ramping up region, however at $f\ge$ 265Hz, the ramping region interferes with retracting region without reaching a steady state. The main reason is that the excitation power frequency generates effective thermal cycle slower than mechanical cycle, i.e., the actuator is excited repeatedly before its structure completely responds. These successive signal overlaps accumulate heat and thus can

explain the deflection offset which is observed in either Bode plot or in step response in Figure (4.25). In addition, the frequency analysis showed that at $f = 265Hz$ the structure ramps and retracts without exhibiting a distinct steady state or dwell region. For this reason, it is essential to obtain a higher order dynamical model that can compute the approximate ramping and releasing time caused by structural heating and damping coupling. The structural dynamic response at square excitation signal $f = 265Hz$ and *A=24V* is fitted to an output error transfer function model with two zeros and three poles

$$\boldsymbol{Y}(\boldsymbol{s}) = \frac{89.92\ \mathrm{s}^2 + 2.263\times10^7\ \mathrm{s} + 1.891\times10^{11}}{\mathrm{s}^3 + 2.011\times10^4\ \mathrm{s}^2 + 5.473\times10^8\ \mathrm{s} + 1.026\times10^{12}}\boldsymbol{V}(\boldsymbol{s}) + \boldsymbol{e}(\boldsymbol{s}) \tag{4.65}$$

Using MATLAB identification toolbox [85], the optimized structural model parameters exhibit 92% fit with the measured data as shown in Figure 4.26-a. The open loop transfer function g_1 represents a model with $\sim 3\mu m$ offset that generates the structural response for a folded beam actuator at a significantly low energy accumulation. For this region, the structural response at 24V square input and at selected frequency shows no dwell time as shown in Figure (4.26-b).The significance of this region is that the time constants for both structural and thermal cycles are close to each other, with the thermal cycle being slower, as shown from Table 4.9. The computed time constants of heating and cooling responses are based on the settling time to the 98% of S.S temperature and 1.02% of initial temperature T_s.

The analytical thermal cycle analysis suggests that the folded beam actuator could operate safely with full cycle of charging and discharging without monitoring any

heating on the MEMS device layer for voltage input frequencies $f \leq 13.6$Hz. At higher frequency input, the average temperature stored on the thermal actuator increases due to the successive overlap. However, the accumulation of heat did not result in an observable mechanical offset as observed in the range of $15 \leq f \leq 265$ Hz. This can be explained by the dynamic coupling effects in thermo-elastic actuators. Purely elastic MEMS devices governed by high order transfer functions have frequency response that undergoes attenuation on the deflection. Meanwhile, additive heat storage on such devices causes additional deflection which is amplified when the total MEMS package overheats.

Moreover, it is observed that the folded beam actuator tends to saturate at frequencies higher than 1015Hz, i.e., the increase in frequency results in a more static deflection and a less ripple deflection as noticed in Figure (4.25-a and b). This response continues until structural dynamics is no longer observed and the folded beam actuator only generates static deflection as $\omega \to \infty$.

Table 4.9 Thermal and structural time constants comparison for SOI folded beam actuators at 24V.

	Thermal time constants		**Structural time constants**	
SOI Folded beam Actuator	**Heat** (s)	**Cool** **(s)**	**Ramp** (s)	**Retract** **(s)**
Approximate Lumped	0.00211	0.0057	--	--
Experimental	--	--	0.0022	0.0026

4.3.5 Discussion of Performance Analysis

The approximate method results in three fundamental time constants that correspond to the transient effect in the three arms of the folded beam actuator. The slowest 2% settling time of the SOI folded beam actuator based on the approximate method was 16msec for 4.4V input. Although the derived method was in excellent agreement with FDA in the case of uniform widths (Table 4.8), the FDA shows a small difference in the simulated heating time constant, which is 13msec. Also, small difference in method's results was observed in the steady state temperature profiles of folded beam when the folded beam started to discharge heat from average temperature of 82°C for an exact based solution. Meanwhile the FEM simulation indicates an average temperature of 100°C. Thus, the cooling time of the lumped model took longer than the simulated FEM with heating and cooling times of 15.6msec and ~13msec, respectively.

The transient analysis of the numerical approaches in FDA and FEM was primitively slow, often unstable and inaccurate due to several reasons: large size of model, coarse mesh grids in spatial and time, round off errors and ill conditioned matrices, limitations on algorithm stability and convergence, and insufficient mathematical approximations. The derived approximate and lumped models provide an analytical methodology that can quickly and accurately compute the thermal cycle. It is observed that the thermal cycle of E-T folded beam actuator explain the structural response and also indicate its thermal efficiency. In case of the experimented SOI folded beam actuator, the analytically approximated time constants of thermal charge

and discharge at 24V square input was 8.4msec and 22.8msec, respectively. The damping region of thermo-elastic frequency response showed that deflection ramp up time is 8msec and retracting time is 10.4msec. For the tested SOI folded beam actuator with device layer of 100 μm, the analytically approximated thermal cycle can operate at full charge and discharge (no overleaping) at ~13Hz and at 24V square input. This suggests that the reliability to thermal failure increases for a device operating at input power frequency less than full thermal duty. The approximate analytical methods could be utilized in optimizing the design of E-T.

Table 4.10 Heating and cooling settling time constants for several Silicon models.

	L μm	L_c μm	$w_h = w_f$ μm	w_c μm	t_v μm	**h** μm	**I mAmp**	**V Volt**	$T_{average}$	**Si heating**	**Si cooling**	**Substrate material**	**Convection from Table. 4.7**
										$4(1/\tau)_{max}$	$4t_k$		
Model 1	370	271	10	52	2	100	56	5.01	100.3	0.0067	0.0164	Silicon	No
Model 2	370	271	10	52	2	100	56	5.01	100.3	0.0067	0.0164	Silicon	Yes
Model 3	370	271	10	52	5	100	56	5.14	125.0	0.0085	0.0382	Silicon	Yes
Model 4	370	271	10	52	2	50	29	5.19	99.6	0.0060	0.0126	Silicon	Yes
Model 5	370	271	10	100	2	100	59	5.04	98.6	0.0110	0.0243	Silicon	Yes
Model 6	570	271	10	52	2	100	33.5	5.03	71.8	0.0100	0.0124	Silicon	Yes
Model 7	370	271	5	52	2	100	30	5.02	81.7	0.0911	0.0139	Silicon	Yes
Model 8	700	500	15	230	2	5	2.8	5.01	40.1	0.0031	0.0031	Silicon	Yes
Model 9	700	500	15	230	2	5	5.25	10.62	100.9	0.0031	0.0041	Silicon	Yes
Model 10	370	271	10	52	2	100	17	1.40	30.58	0.0097	0.1926	PMMA	Yes

Table 4.11 Heating and cooling settling time constants for several Nickel models.

	L μm	L_c μm)	$w_h = w_f$ μm	w_c μm	t_v μm	**h** μm	**I Amp**	**V Volt**	$T_{average}$	**Ni heating**	**Ni cooling**	**Substrate material**	**Convection from Table. 4.7**
										$4(1/\tau)_{max}$	$4t_k$		
Model 1	3500	2500	150	1150	5	25	0.700	0.074	52.67	0.9550	1.1646	PMMA	No
Model 2	3500	2500	150	1150	5	25	0.700	0.074	52.67	0.9550	1.1646	PMMA	Yes
Model 3	3500	2500	150	1150	20	25	0.700	0.075	54.52	1.0833	1.3452	PMMA	Yes
Model 4	3500	2500	150	1150	5	10	0.300	0.075	41.96	0.4251	0.4336	PMMA	Yes
Model 5	3500	2500	150	2250	5	25	0.730	0.075	50.38	1.0345	1.1781	PMMA	Yes
Model 6	4500	2500	150	1150	5	25	0.590	0.075	47.42	1.0007	1.1204	PMMA	Yes
Model 7	3500	2500	75	1150	5	25	0.390	0.074	51.93	0.9420	1.1519	PMMA	Yes
Model 8	700	500	15	230	2	5	0.090	0.074	31.91	0.0071	0.0057	Silicon	Yes
Model 9	700	500	15	230	2	5	0.138	0.134	52.33	0.0071	0.0075	Silicon	Yes
Model 10	3500	2500	150	1150	5	25	1.300	0.254	53.26	0.0372	0.0390	Silicon	Yes

The thermal duty cycle or the performance of folded beam actuators as a function of the voltage input, dimension and material properties are shown in Tables 4.10 and 4.11. The simulations were performed using properties and dimension configurations in Tables 4.5 and 4.6 unless changes are stated in models 1-10, as depicted in Tables 4.10 and 4.11. From the tabulated results, the following conclusions are drawn:

- It is observed that the influence of the conductive air gap, which is separated from a conductive substrate, has the most impact on thermal duty cycle. The increase of air gap will substantially increase both the discharge and charging time constants. More thermally conductive layers (e.g. substrate, small air gap, device layer) will also improve (speed up) the thermal cycle.
- The thickness of device layer significantly influences the thermal responses; the response of a device becomes faster as the thickness of a layer decreases.
- The charging and discharging time orders exhibit nonlinear behavior as model geometry and material change. In most cases, heating time is faster than cooling time. A more conductive substrate enhances discharging times if compared to charging time. However, both the cooling and rising time become of the same order for small scale devices.
- The effect of natural air convection is less important to temperature response at the presence of conductive air gap. The conduction in small scale devices dominates the convection heat transfer due to the quasi-static buoyant air flow [113]. It implies that the performance of a thermal actuator can be

enhanced by keeping the lower surface of the substrate at low temperature because most of the heat is dissipated into substrate via air gap.

- Although nickel has slow thermal cycle at meso scale, nickel or typical metallic substrates can be more desirable than silicon at small scales. This is relatively due to low power consumption and the decrease of thermal cycle time as a scale goes down.
- The increase of input power results in the increase of the average temperature which by intuition will cause the increase of thermal cycle.
- The thermal cycle reduces as the substrate thickness reduces under the assumption that the temperature of the lower surface of the substrate (package) is constant.
- For fixed input voltage, the increase of a hot arm length results in the increase of total resistance, which decreases the input power and the average state temperature. Consequently, the charging time increases and the discharging time decreases.
- The decrease of a hot arm and flexure widths increases the total resistance and decreases the input power for fixed input voltage. Although average temperature slightly decreases in narrow beams, the thermal cycle becomes slower.

- The increase of a cold arm length decreases the total resistance and increases the total input power. This effect causes a small drop in average temperature and increases the thermal cycle.

In the aforementioned models, one shall notice that in discharging time is as sensitive as to charging time. In summary, sensitivity and optimization analysis might be performed for the thermal cycle which is based on 98% heating and $\kappa - 1$ cooling times

$$\omega_T = Log\left(\frac{\overline{T} - T_s}{T_s[\kappa - 1]}\right)^{\tau_d} + 4/\min\left|\left[A_a \middle| A_b\right]^T\right| \quad . \tag{6.65}$$

4.4.6 *Summary of Transient Analysis Methods*

Novel approximate and lumped models based procedure developed was derived to analytically compute the charging and discharging temperature profiles of MEMS U and V-shape actuators. These procedures are used to quickly and efficiently calculate the thermal cycle of E-T actuators and showed good agreement with numerical approaches. These methods were also compared with the experimentally obtained results with excellent agreements. The obtained analytical expressions could be used for the optimum design of E-T MEMS devices based on their scale, boundary conditions and physical properties. An attached actuator conducts more heat to the substrate than a suspended actuator, and thus it can generate faster responses. Fast thermal and structural cycles can generally be achieved by scaling down the folded beam dimension, providing a thermally conductive substrate at low temperature, reducing the air gap between the device layer and the substrate, and last but not least, reducing input power

by either reducing input voltage amplitude or reducing the effective input duty cycle. Moreover, a folded beam actuator with a metallic device layer exhibit not only fast thermal cycle, but also low power consumption, which thermally makes it as an excellent alternative substitute of silicon. The discharging time of E-T actuator is generally higher than the charging time at high input voltage. However, it is feasible to not only design and achieve same order of magnitude in charging and discharging time, but also faster discharging can be suppressed.

4.4 Chapter Conclusions

We have arrived at closed expressions based on energy methods, described in chapter 2, which solve for both the transient and steady state temperature responses of the Multipurpose Electrothermal Microgrippers (METEG). Wherein the established methods are good agreement with experimental and numerical results. The performance of METEG is studied from the device material, geometry and thermal states. Particularly, thermal distribution and failures are much dependent on the availability of heat sink that cools down the tremendous generated heat. The presence of a thermal conductive substrates allowed maintaining low temperature profiles as compared to electrical power fed to the device. Those heat sinks are presented by air-gap, large handle wafer and large pads. Thus, the results shown explain the functionality of METEG during assembly processes that were described earlier in Chapter 3.

The analysis shows that it is possible to replace silicon with more effective material which could operate as an electro thermal building block. Hence, the designer may utilize the finding in selecting the proper device parameter for the intended application.

For example and in the design of end-effector for serial microassembly, one could design big attachment pads in order to sink heat resulted in active pick and place. Also, if the repeatability of pick and place is required to be fast, the designer may select low device layer thickness or project external heat sink so that the accumulated heat is less and the charging and discharging time is short. Another important application of the derived expression encompassed in designing distributed manipulators which were discussed in chapter 2. Specifically the careful study of thermal failures and performances of the building blocks and the integrated blocks could commence new active surface modules. That array could be capable of manipulating micro from one point to another by using the push action of the blocks.

Finally, the described approached are beneficial in understanding the capabilities of microassembly, wherein both deterministic serial and parallel manipulation relies on the capabilities of the module's performances. It is obvious that end-effectors design based on thermal actuation is a controllable problem which could, with the derived expression, be optimized and reverse engineered.

CHAPTER 5

SELF-ASSEMBLY AND PARALLEL MANIPULATION OF MICRO SYSTEMS

5.1 Introduction

The three dimensional scales are; first, meso-systems whose major devices and processes dimension are typically measured in millimeters, second, micro-engineering incorporates MEMS devices and processes that are measured in micrometers, third, nano-engineering is considered for processes resulting devices of defined structure or assembly in which nanometer is the most sensible unit of specifying dimension or tolerance. Researchers have utilized adhesion forces between micro-tip and micro-objects for contact handling, as found in simple pick and place processes [8]. Others aimed at reducing their effects during micro- manipulations [9]. Increasing the efficiency of grasping for micro part below limit of 50 micrometers is carried out in a submerged medium with controllable parameters [10]. The scaling effect of objects and microorganism could bring essential science upon the traditional manipulation method, wherein in the previous chapters, the scope of the dissertation aimed at developing techniques based on mechanical principals that often are implemental at macro scale devices. Hence, the assembly processes were much dependent on the design criteria

and configured automation. Examples included our designed end-effectors that are used for sequential micro assembly. However, such microassembly process becomes primitive at small scale due to the appearance of sticktion forces. Moreover, the serial microassembly is a slow and expensive process. Alternative method will be investigated in this chapter. The investigations are inspired by the following factors:

- With the available technologies thus far, the manual assembly is no longer viable at certain cut off dimension.
- Body surface interactions introduce significant mechanical forces that may change within mechanisms. Such phenomenal forces include contact forces, Van der waals, adhesion forces, electric dipoles, meniscus effect and Casimir forces.
- Scaling can change the relative dynamic of phenomena. For example, heat transfer and thermal response are often considerably faster than mechanical motion in micro scale as proven in previous chapter. Meanwhile the heat transfer in macro scale machine is slower than motion. Moreover, thermal expansion has less limiting influence in micro devices than macro scale devices.
- The reduction of volumetric deposition or removal leads to economic tradeoffs.

The difficulty of integrating micro-components in gas environment is primarily arising by the adhesive forces. Manipulation of parts on the order of 10 micron or smaller can be best investigated in a fluid medium utilizing laser trapping, dielectrophorcessis, etc [34]. While it is possible to fabricate miniature building blocks of conventional micro system, it appears that it will be difficult to overcome the adhesion effects in the conventional microassembly methods. Herein, it has been

envisioned that the next generation of sensors and actuators will instead utilize these scaling effect-adhesive forces in assisting the assembly processes. Methods developed for conventional macro scale assembly cannot be applied directly to microassembly. Thus this chapter investigates on the fundamental concepts of forces deriving microassembly process. Consequently, handling techniques, assembly and task planning of micromanipulations could be optimized by regulating the attraction forces.

5.2 Self-assembly Assisted by Adhesive Forces (Microphysics)

Micromanipulation of micro objects is predominant by micro physics of objects. In micro object manipulation, adhesion forces that are due to Van der waals, electrostatic and surface tension forces are dominant as compared with gravitational forces [37 and 38]. These forces, which appear on miniaturized objects (ex: less than 100um in dry environment), are considered either to handle manipulation tasks or as undesired forces. Many operation principles, such as self-assembly and assembly using capillary/surface tension forces, are primarily based on adhesion forces [39]. Researchers have utilized adhesion forces between micro-tip and micro-objects for contact handling as in simple pick and place [36]. Others aimed at reducing their effects during micro- manipulations [38]. Increasing the efficiency of grasping a micro part below limiting size of 50 micrometers is carried out in a submerged medium with controllable parameters [40].

The Effect of assembly Medium could depend on the choice of thermal and conductive liquids which facilitate the control of medium temperature and minimizes

the electrostatic perturbation [40]. Choosing a medium with high dielectric constant reduces the electrostatic force. Moreover, the capillary forces induced among micro parts and surfaces are cancelled in liquid medium [41].

Adhesion forces can be caused by electrostatic, Van der waals or surface tension. Electrostatic forces arise from charge transfer (triboelectrification) or charge transfer during micro-parts contact. Surface tension effects are a result of the interaction of layers of adsorbed moisture on two surfaces. Van der waals forces are due to instantaneous polarization of atoms and molecules due to quantum mechanical effects. More details about microphysical forces are summarized in Appendix A, wherein the variation of the total forces is studied from the available expressions which assist in understanding their relative contribution during assembly process.

5.3 Construction of 2½ D Structure: Principle of Self-assembly

Self-assembly based on DNA recognition can be defined as in the content of this research by the spontaneous organization of molecules or objects, under steady state or equilibrium conditions, into stable aggregates [32]. These 2D and 3D aggregates are not necessarily at the global minimum in energy. Here, the objects are driven by non-covalent forces that are selectively patterned to provide locking at the interface.

It has been envisioned in this research that the construction of the next generation of sensors and actuators will instead utilize these scaling effect-adhesive forces in assisting the assembly processes. Methods developed for conventional macro scale assembly cannot be applied directly to microassembly. In micro object

manipulation, adhesion forces that are promoted by van der Waals, electrostatic and surface tension forces are dominant as compared with gravitational forces [56 and 57]. These forces, which appears on miniaturized objects (ex: less that 100um in dry environment), are considered either to handle manipulation tasks or as undesired forces. Many operation principles, such as self-assembly and assembly using capillary/surface tension forces, are primarily based on adhesion forces [58].

In Figure (5.1), we suggest the basic building block of specified robotic structures. The spontaneous but probabilistic assembly of a large number of blocks is stimulated in either dry or wet medium. Four keys improve such selfassembly: (i) structural signature of the mated part's at the interface; (ii) interface area and shape, i.e. micro-scale forces; (iii) number of similar and dissimilar micro-parts; (iv) instantaneous orientation during the agitation depends on the aspect ratio of part. The process of self-assembly assisted by DNA concept could be thought of as a chemical process with known reactants and expected products. The basic blocks, shown in Figure (5.1), are arranged in unit cells and tethered by cantilever beams.

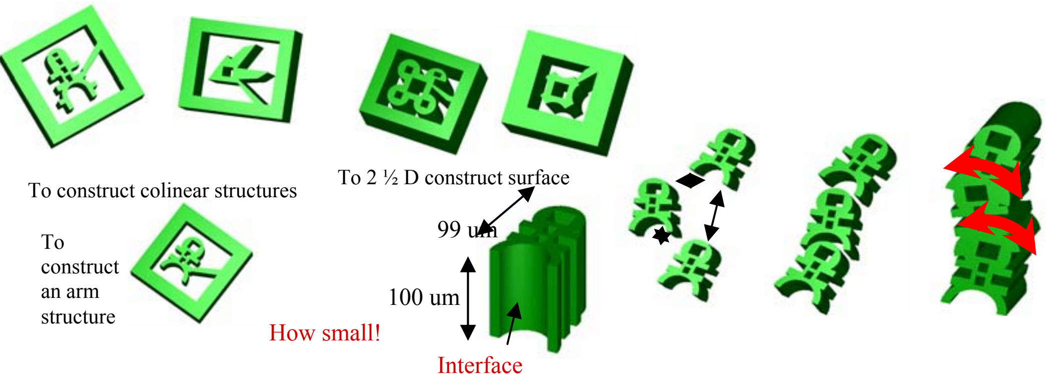

Figure 5.1 Solid models of encoded dust size parts.

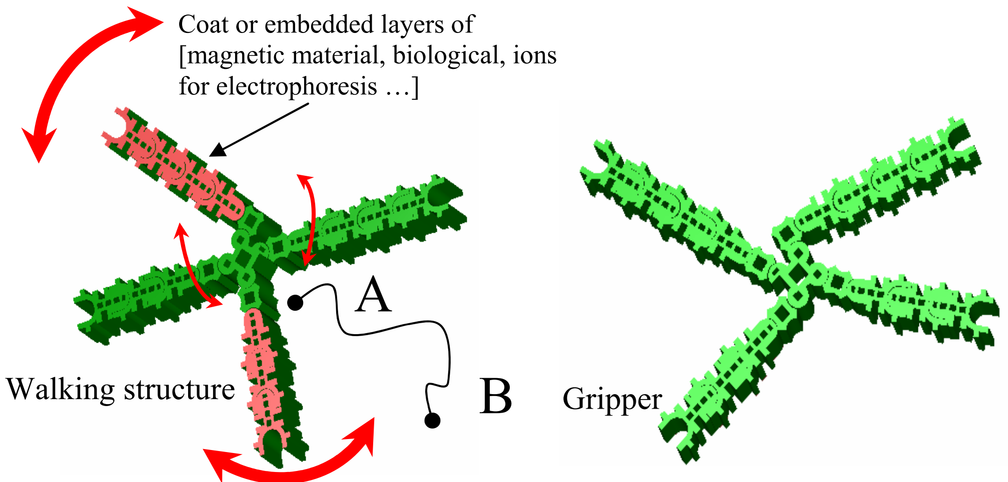

Figure 5.2 Solid model of self-assembled micro-robotic system.

These cells are fabricated in a single platform in massive quantities. The process of detethering the dust size parts from their fabricated platform is discussed in chapter 6. After singulating the dust size parts in the intended assembly platform, several patterns could be self-assembled assisted by microphysical force attraction which is maximum at the block's interfaces. Examples of possible assembly combinations are illustrated in Figure (5.2) which shows 2½ D walking micro-robot or microgripper which could be massively or partially patterned during self-assembly principal.

Building blocks are primarily constructed from passive components that could be fabricated from a single layer of different material. Such materials include silicon, stainless steel, shape memory alloy, magnet and others. Actuation methods of these microstructures are explored in the next two sections.

5.4 Self-assembly Strategies for Non-conventional Actuation and Translocation of Micro-structures

Actuating self-assembled micro structures can be achieved in to two ways. First, the relative motion of sub-objects with respect to each other in the micro structure, such as fixing parts on the structures and positioning others. An example includes using surface tension to hold certain components stationary on a surface, while the other structures are free to move under external forces. Second, the total transport of the micro structure relative to stationary reference.

Micro-Fluidic Techniques based on Micro total analysis system (μTAS [32]) utilizes a combination of electrokinetic transport mechanism for particle/species manipulation and bulk flow control. Phenomena which can be applied in transport MEMS structures are (i) electrophoresis which is the motion of the charged surfaces and macromolecules relative to a stationary liquid by an applied electric field (ii) electromosis which is the motion of ionized liquid relative to the stationary charged surface by an applied electric field.

On the other hand, electromagnetic actuation principle can be applied to micro-structure with ferrite properties responding to an external magnetic filed. This technique is utilized here to (i) Reinforce the connection among micro-parts constructing the micro-structures: the opposite magnetic polarity of the mated parts keeps the structure together; (ii) the total structure responds (attract/repulse) to the magnetic field. Thus creating a semi and dynamic magnetic field gradient could provide actuation to the mechanism.

The Motility of Microbiological species can also yield novel and promising approaches in transporting the assembled structures or micro-parts. For example, Bacteria colonies coating a micro structure can harmonically adjust their motion such that the structure moves from point "A" and settles around the survival point "B" in Figure (5.2). Other translocation or manipulation methods which could be utilized in translocating and actuating micro part include

- Micro-distributed manipulation system (μDMS) discussed in chapter 2: active surface modules (ASM) are discrete or continuous standalone manipulators where each individual actuator mechanisms are fixed or maneuverable in a domain and it is capable of performing different and/or identical tasks. The different modules form an array on which their collaborative actuations perform set of assembly tasks such as translation, flipping and rotation.
- Prehensile and Non-prehensile manipulations using micro-assembly work-cells: The prehensile manipulations include the group of METEG introduced in chapters 3 and 4; meanwhile the non-prehensile depends on the indirect mechanical contact between manipulator and translocated device. An example of non-prehensile includes the sticktion forces that appears between the end-effector and utilized in the assembly. Method for such non indirect forces includes controlled surface tension and sticktion forces [81], electrostatic force, blowing, etc.

- Surface and volumetric encoding: such as self assembly assisted by mechanical templating of micro-meso devices. Wherein, manipulating parts at micro level requires large forces to overcome the sticktion forces or requires techniques to control (reduce) sticktion force during assembly. Moreover, selfassembly based on agitation technique was first indirectly introduced earlier in chapter 3 during the development of hybrid assembly. Examples on self assembly assisted by agitation are also discussed later on this chapter. Other selective templating (bonding or attracting) include using chemical or photonic reaction codes, trapping using surface tension.

5.4.1 Micro-robotics Assisted by Bacteria Translocation

Surface translocation enables Bacteria to establish potential benefits including increased access to nutrients, avoidance of toxic substances, access to preferred colonization sites within hosts, and increased efficiency of transmission [61]. Bacteria movement in aqueous environment, mostly by swimming on the surface, has been broadly investigated [60 and 61] and utilized in this research. Thus, the next generation of manipulating robotic systems could be inspired or assisted by the translocations of microorganisms:

(i) *Swarming* depends on excessive development of flagella and partly on cell to cell interaction. Surface active substances in cretin concentrations inhibit swarming and swimming in liquid media of *Proteus* .One of the characteristics of

swarming is that cells move in the form of large draft or “bullet-shaped” colonies depending on the available moisture. Bigger rafts occur on drier agar as noticed on *Bacillus* colonies which are wondering in very dry plates. Cells measures roughly 10-30um and are arranged in large bundle which move quickly along continuous curve at approximately 10-15um/sec. ;

(ii) *Swimming* depends on flagella and fluid thickness, for example *Salmonella enterica*;

(iii)*Gliding* depends on intrinsic motive force and partly on cell to cell interaction, for example *Myxococcus spp*.;

(iv)Twitching depends on intrinsic motive force, for example *Pseudomonans* ;

(v) *Slidding* depends on spreading by expansion (i.e. growth and reduction friction); and

(vi)*Darting* or spread by ejection depends on growth in capsulated aggregate.

The development of miniaturized mobile robots is mainly dependent on scaling the on-board power supply. Fuel cells based on the thermodynamic of chemical combustion or reaction is being researched as a possible driving power. This is because of its high power conversion efficiency which reaches (35-70%) of direct chemical to electric reaction efficiency as in galvanic devices [62]. In direct methanol fuel cell DMFC, the length of time it delivers continuous power depends on the unit volume of packaged fuel with a net output of milliwatts. However, the most significant bottleneck for further miniaturization of mobile robots requires miniaturizing the on-board power source and motility mechanisms.

The directional motion of *Phototactic* algae with eye photoreceptor is stimulated by a collimated beam of light. Most of the organic structures such as bacteria exhibit self-propelled motion under appropriate conditions. Flagellum is hairlike structure that acts primarily as an organelle of movement in the cells of many living organisms. Flagella occur on cells of *Sperm*, *Cilium*, *Attila*, *Protist* (algae, fungi) and groups of Bactria. Most motile bacteria move by the use of flagella which is a single flagellum of rigid structure, 20nm in diameter, 15-20um long and protruding from cell surface. Helical motion is the default trajectory for organism moving at a low Reynolds number. This is because motion at low Reynolds number requires cyclic, symmetric deformation of body and each deformation causes the body to translate and rotate [59]. The axis of helical trajectory of *Chlaymdomonas reinhardtii* is stimulated and aligned with the direction of the light beam.

Researches have utilized polystyrene particles, which are immediately near the motile microorganisms; mainly bacteria, to calculate the mechanical drag force of microorganisms [63 and 64]. The Brownian motions of surface modified polystyrene particles are tracked using Laser racking Microheology (LTM). This enables calculating the drag force from the viscoelastic moduli measurements of the bacteria and from the Stokes' equations [64]

$$F_{drag} = 6\pi SaV\eta\left(\dot{\gamma}\right) \tag{5.1}$$

where, a accounts for minor radius of an approximated sphere, V, S , and $\eta\left(\dot{\gamma}\right)$ are the velocity, shape and the steady state shear viscosity at shear rate of $\dot{\gamma} = V/2a$. Some of non-Newtonian fluids, such as methylcellulose solutions, have steady state shear

viscosity that is empirically same as dynamic viscosity and can be found from the LTM measurements. The speed of swimming, *V,* of microorganism can also be calculated from Stokes' law [65]

$$V = a(2/9P_V\eta)^{1/2} \tag{5.2}$$

Where, P_V is the specific mechanical power. Stokes' Law is valid when Reynolds number is less than 0.5 [66].

Listeria monocytogenes bacterium can be slowed drown by methylcellulose as a viscoelastic thickening agent or by ideal viscous solution that would slow all biochemical rates [64]. Thick solution of high concentrations of methylcellulose (>1%) suppress large scale Brownian motion of bacteria and their tails. Where the ticking agent has caused additional Actin polymerization and thus generated larger force. The prediction force-velocity models of *Listeria* anticipate that the relation is exponential with negative exponent where it can pause its motion if the force is strong enough to deform cross-linked gels (0.1~1nN) [64]. However, bacterium of faster velocity is accompanied with low force. Where the bacterial tail binding complexes are long lived enough to become internally stretched and reduce the net generated force. Meanwhile, thickening the solution increases the internal straining and thus slow velocities accelerate the disassembly of these tails [64].

A summary is established in Table 5.1 showing the relation between the forces excreted by different species. A conclusion which can be drawn from the investigation is that the force is proportional to the specie's seize; hence there exist a range of species which can deliver enough power to manipulate human made micro structures.

Table. 5.1 Mechanical and control properties of some microorganism.

Micro-organisms	*Family taxonomy*	*Mechanism of motility*	*Unit size*	*speed*	*Unit force*	*Controllability*	*Ref.*
S. marcescens	bacteria	Flagellar/swarm	0.5 μm radius sphere	15 μm /s dragging spherical polystyrene bead of 10 μm radius	0.45pN	ethylenediaminetetraacetic acid to resume, copper ion to stop. Speed control: chemical and light.	[63] [67]
Listeria monocytogenes,	bacteria	Flagellar/swim	~0.5 μm radius.	(0.045 μm /s - 0.0073 μm /s)	(8.4pN -80pN) Upper band of 200pN.	(0.25%-0.75%) Methylcellulose.	[64]
Prorocenirum marial-labouriae	marine phytoplankton	Flagellar/swim	~6 μm radius	(171 μm /s	-	Nutrient	[68]

5.4.2 *Micro-robotic System Based on Micro Biological Organism*

The life of organisms depends on the probability of successful search for food, mates, appropriates temperature, correct pH, sunlight, concentration gradient and many other important factors [59]. For example, Bio-organisms with translocation ability are deemed to be one of the most promising on-board biomicromotors which are advantageous over human made actuators. This is not only because of high efficiency in directly converting chemical into mechanical energy, but also because the overall organism ranges from micro to nano in size. They are also capable of producing more complicated predictable motions which could be controlled as indicated in previous section.

The translocation of microorganism, such as the sliding of bacteria, could be potentially utilized as biomotors for micro-robotic systems. Figure (5.3) shows a

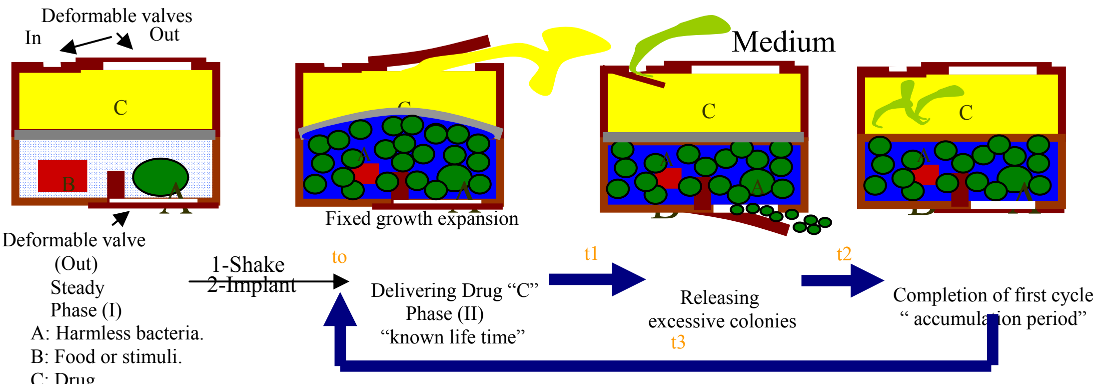

Figure 5.3 Biological Micro Pump (BMP) based on the translocation of microorganism in a control volume.

Biological- Micro-Pump (BMP), or alternatively *Bio-micropump*, concept for growing cultures of microorganism which could result in novel actuator and sensor devices. Example includes a disposable micro-pump drug delivery device based on bio-actuators encapsulated in a control volume.

5.4.3 Bio-Micropump (BMP)

The motility of micro organisms could provide the translocation mechanism for micro-robotic parts. In a controlled volume environment, the force excreted by a microorganism could be applied on an elastic membrane such that the motion results in an enclosed micro robotic system. For example, the volumetric change in the membrane could be utilized in providing the actuation tool for controlling the flow rate. The flow rate can either be continuous or discrete, depending on the design of release flap (actuator valve). Thus, it is possible to determine the cycle operation of drug release by considering factors such as amount of microorganism, stimuli, dimensions of micro-pump, fluid parameters, byproducts and stiffness of diaphragm and chamber. On board power for smart sensor and actuator for biomedical and industrial applications where

bio-micropump capsules based on microorganism actuation is fabricated to deliver a controlled amount of drug. This includes disposable drug delivery devices for respiratory and circulatory system. In particular, the benefit of using bacteria over other microorganism is might due to

- Taxonomy classifies wide range of harmless motile bacteria.
- Translocation combines different *mechanisms*: motile bacteria by use of flagella, helical Bactria rotating in spiral fashion, and gliding bacteria.
- Variation of size and rate of motion in bacteria and their colonies.

Several scale prototypes of non opportunistic pathogens BMP have been fabricated at UT-Arlington facilities. *Millimeter scale* microorganism based micro-pump is fabricated as follows:

i-Two hollow disks (chambers of height ~500um and ~1500um ,~3mm outer and ~1.5mm inner diameter) are diced from a glass tube using diamond sawing machine.

ii-Industrial rubber membrane (low stiffness and thickness) is sandwiched and glued between the two chambers.

iii-The larger chamber encapsulates two ingredients first, microorganism where spherical yeast particles is selected with its properties summarized in Table 5.2. Second, stimuli to initiate the growth of cells, wherein a mixture of smashed frozen-water and sugar are used.

iv-The chamber end ingredient are enclosed by class disk and kept at low temperature.

Table 5.2 Properties of Yeasts used in the controlling actuation for a tested BMP [88, 89 and 90]

Property	Note
Eukaryotic microorganisms (Fungi kingdom)	Mostly used in baking species is *Saccharomyces cerevisiae*
chemoorganotrophs	organic compounds as their energy source (glucose, ultra-violet irradiation)
Reproduction cycle is asexual and sexual by budding	formation of a new naturally genetically identical organism by the protrusion of part of another organism.
Cell cycle mechanism	similar to the cell cycle in human
Stress conditions:	haploid cells have simple life cycle and will generally die, diploid cells can reproduce (meiosis) and produce a variety of haploid spores, which can go on to mate reforming the diploid
pathogenic	Some species of yeast are opportunistic pathogens, where they can cause infection

v-The drug chamber is either hermitically sealed with a head containing a capillary tube or needle or left open for characterization purposes. Figure (5.4) shows a Bio-micropump powered by yeast, wherein the experiment is conducted at low temperature in order to prevent the budding process.

The chamber encapsulating the species are hermitically sealed, meanwhile a droplet of water is placed inside the open chamber. Increasing the temperature has stimulated budding process to occur at faster rate where the volume and gaseous output has pushed the separating membrane and then pushed the water, as shown in the sequenced pictures in Figure (5.4).

Another *centimeter scale* device but simplified model is presented on Figure (5.5). The device consists of two chambers separated by an elastic membrane. The first chamber with check valve encapsulates the microorganisms which are able to grow and react with specified external stimuli. The configuration allows single or countable cyclic modes depending on the availability of stimulus in the BMP external medium. In Figure (5.6) a meso scale BMP actuated by *Saccharomyces cerevisiae* which is a type of yeast,

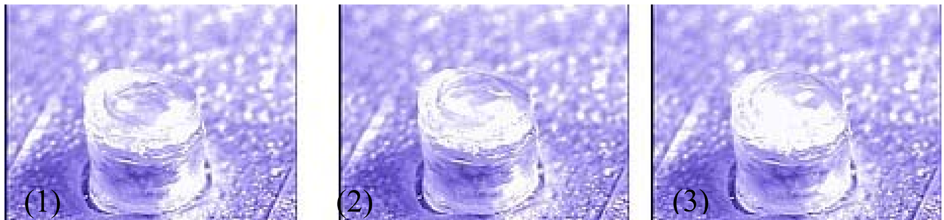

Figure 5.4 Micro scales BMP comprised of closed and open chambers.

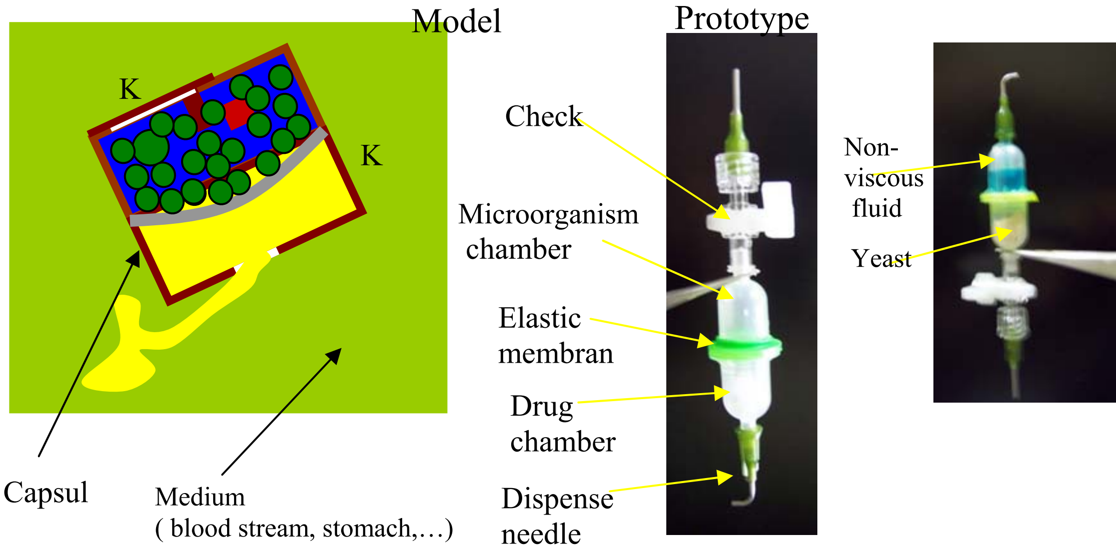

Figure 5.5 Macro prototypes of BMP (a) simplified model undergo cyclic fluid delivery. (b) Centimeter scale prototype.

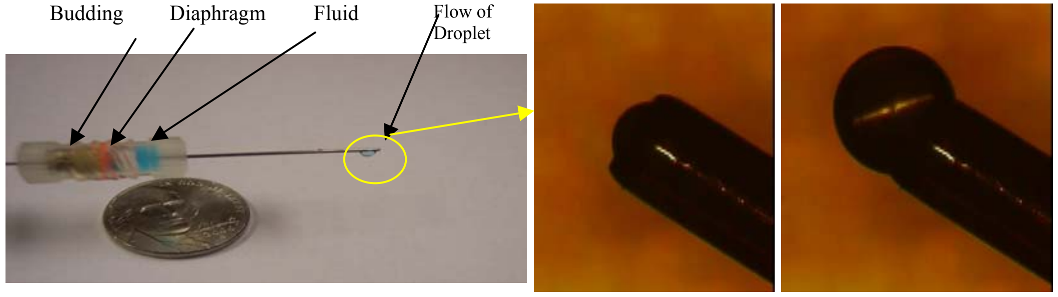

Figure 5.6 Meso-scale prototype of BMP (a) prototype. (b) Dispensing fluid from micro needle tip separated with 30s time elapse between the two microscopic images.

is fabricated and experimented for actuation. The device was able to pump the fluid at a constant rate and at controlled ON/OFF modes by keeping the devices preserved at low temperature stopped the reproduction of yeast, and thus halted the BMP action. An experimental setup for characterizing the efficiency of BMP is developed and shown in Figures (5.7). Where, the system can measure the chamber pressure and the maximum membrane deflection that correspond to the BMP constituents. In particular, the setup is utilized to qualitatively and quantitatively characterize the performance of BMP at different stimuli and microorganisms. Setup components, indicated in Figure (5.7), include (1) Pressure gauge to measure the amount of internal pressure inside chamber;(2) Displacement gauge to measure the maximum deflection of elastic diaphragm; (3)Z-stage for calibration and adjustment; (4) Controlled check valve;(5) Replaceable chamber; (6) disposable elastic diaphragm.

A proper culturing would embark the reproduction process in the Microorganism inside the capsule.

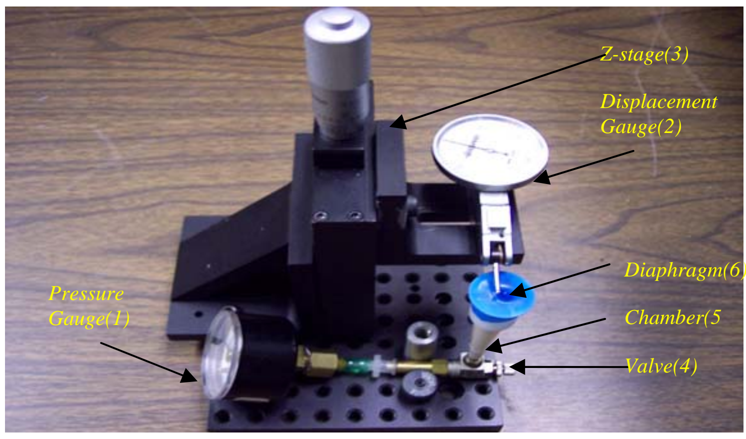

Figure 5.7 Proposed identification setup for performance measurement of BMP.

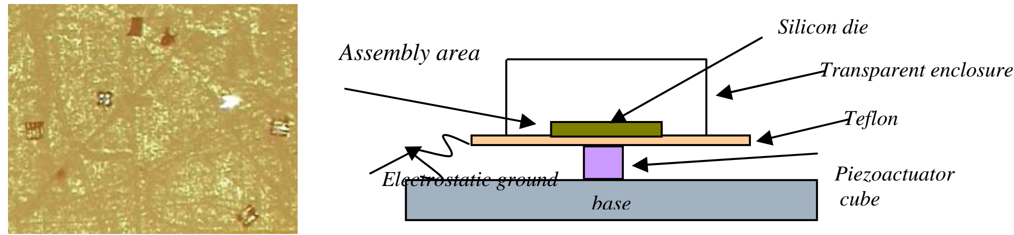

Figure 5.8 Schematic of a setup combining two processes: simultaneous parallel detethering and selfassembly of MEMS structures.

Depending on the microorganism, the pressure could be related to byproduct mostly gaseous caused by metabolism) or colony growth, expansion ...etc.

5.5 Feasibility Studies on Self-assembly

5.5.1 *Method Requirements*

We have deigned and fabricated dust size building block from SOI for Self-assembly based on DNA recognition to construct 2 ½D micro-robotic devices. The blocks occupy unit cells arranged in diced SOI die. These blocks are tethered to the device layer by a well-designed cantilever structure under which a principle of selective but monolithic detethering is developed. The Detethering requires agitation at specified large frequencies and amplitudes and is discussed in more detail in chapter 6.

The method considers the following key requirements

- Reconfiguration of assembled structure from basic building blocks;
- Fabrication of massive number of blocks in one platform.

The key issues needed to enhance the success if assembly depends on the block's design

- High Aspect ratio assist on stability;
- Large quantity increase the construction probability;
- Natural attraction forces at interface (short range forces);
- Repeated and symmetrical structures increase the successful spontaneous. interface

Simplified setup was built to provide platform for detethering and self assembly. Figure (5.8) shows a setup for monolithic tethering and assembly of MEMS structures. The procedure of self-assembly of dust size particles could be enhanced by observing and studying the probability of directional collusion under external forces. Specifically, the damping and sticktion effects limit the locomotion of micro-parts. And thus, powerful vibratory system might be needed to increase the probability of self-assembly. Herein, the probability of 2½ D into 3D self assembly, in dry and fluid medium, is low due to the microphysics accompanied in small feature sizes. Longer (low aspect ratio) and dense number of parts could enhance the assembly process. Our approaches is demonstrated in2 ½ structures, however 3D selfassembly is a recommendation for future research.

Large number of passive blocks is fabricated from SOI on 100 micron device layer with high aspect ratio, and shown in Figure (5.9). Where, the interfaces are of A and B parts are common with circle of 750 micron in diameter. The selected dimension allows micro parts to rest on larger area during the self assembly process.

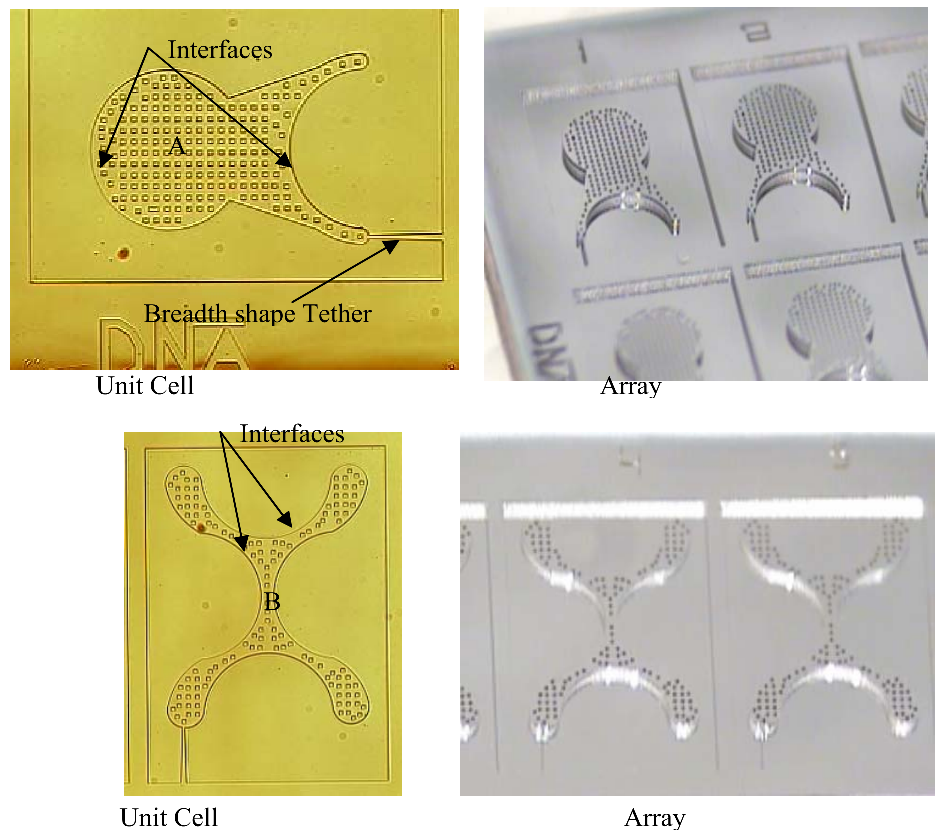

Figure 5.9 Micro-robotic building blocks of a fabricated on SOI.

5.5.2 *Concept of Self-assembly Assisted by Agitation*

This work propose methods for selfassembly assisted by dry/wet agitation which relies on

- Platform based on Micro-distributed manipulation system µDMS;
- Squeeze field forces and Brownian Motion;
- Designed collision traps.

The stiction forces between the silicon blocks and agitated hydrophobic surface is low and could be explained by weak existence of microphysical forces which are descried in Appendix A.

The agitation causes planar squeeze field forces enough to overcome the sticktion forces and allow the part to inherently undertake a Brownian motion. However, this Brownian motion could be directionally guided through surface forces generated by multi distributed point load actuators, such as piezoresonators. Parts, which are placed on an agitated assembly surface, stride toward a region with minimum forces. i.e, it describes the translocation over the energy field moving toward minimum energy location. Allowing the parts to randomly collide and interface at these specified regions, as shown in Figure (5.10). The attraction force can be reversed engineered such that it determines the manipulation trajectory of parts. The concepts of distributed manipulation, discussed in chapter 2, can be deployed to define the number and locations of vibratory loads on the assembly surface. Independent studies were performed to demonstrate the concept of trapping the micro part at site of minimum energy located in an agitated surface. Square traps of >1mm^2 in area were etched out on a 100um device layer of a 1cm^2 silicon dies. The centroid of bottom surface of die is attached to piezoresenator cube (PZT) which is

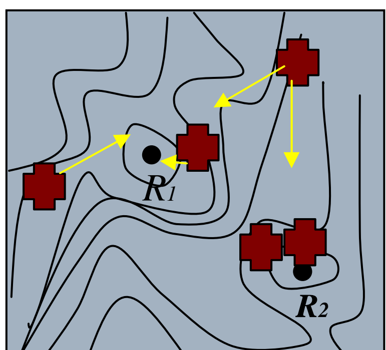

Figure 5.10. Schematic drawing of squeeze field with attraction regions *R's*.

oriented to vibrate normal to die surface. This high performance piezo actuator, provided by [123], is made of ceramic at sizes as small as 2 x 2 x 2 mm. The displacement is ~2.2 micron at 100V with blocking force and resonance frequency greater than 250N and 300kHz, respectively.

Tin20%-Gold80% metal layer of 25micron in thickness and $1mm^2$ in area is placed randomly on the surface of silicon die. In cleanroom environment it is observed that stiction forces (Van D. wall, electrostatic and surface tension) are comparably large to cause an obstacle for the motion of perform layer. A square signal at 50% duty cycle, 2kHz and 40V amplitude is fed to piezoactuator causing the surface to agitate upward and downward. This force was enough to overcome the sticktion forces and guide the motion to the minimum energy site located at the etched holes with total relocation time of 5.23second, as shown in Figure (5.11). This process describes self assembly by trapping and was directly utilized in hybrid assembly in sequential microassembly. However, the purpose of this demonstration, herein, is to implement the concept on flat assembly surfaces which have imaginary trapping sites capable of dragging micro part.

The effect microphysical forces are generally more apparent at smaller scale devices if inertia effect is negligible. Thus another study was performed for 250 x250x500um copper cubs. These blocks were machined on copper layer with porosity of (55%) using Femtosecond Bulk Micromachining System (FLM) [124]. This system comprises mainly of precision motorized and fully automated stages (XYZ) and focused Femtosecond laser set at (laser power of 150mW, laser spot of 100um and stages trajectories at 20mm/min. With the laser spot acting on the copper surface, successive

lines and squares were passed to ablated material and extract copper blocks, as shown in Figure (5.12). To template the cubes using an actively agitated surface, a silicon dies of 100 micron device layer and 400um handle wafer in thicknesses were selected. An array of circular holes was backside etched on handle wafer using DRIE and then the front side of die is attached to same type of piezo cube used earlier. Holes dimensions are constrained such that several diameters are fabricated. Diameter is arranged on the silicon backside ranging from 200um to 400um with 400um cavity in depth, as shown Figure 5.13.

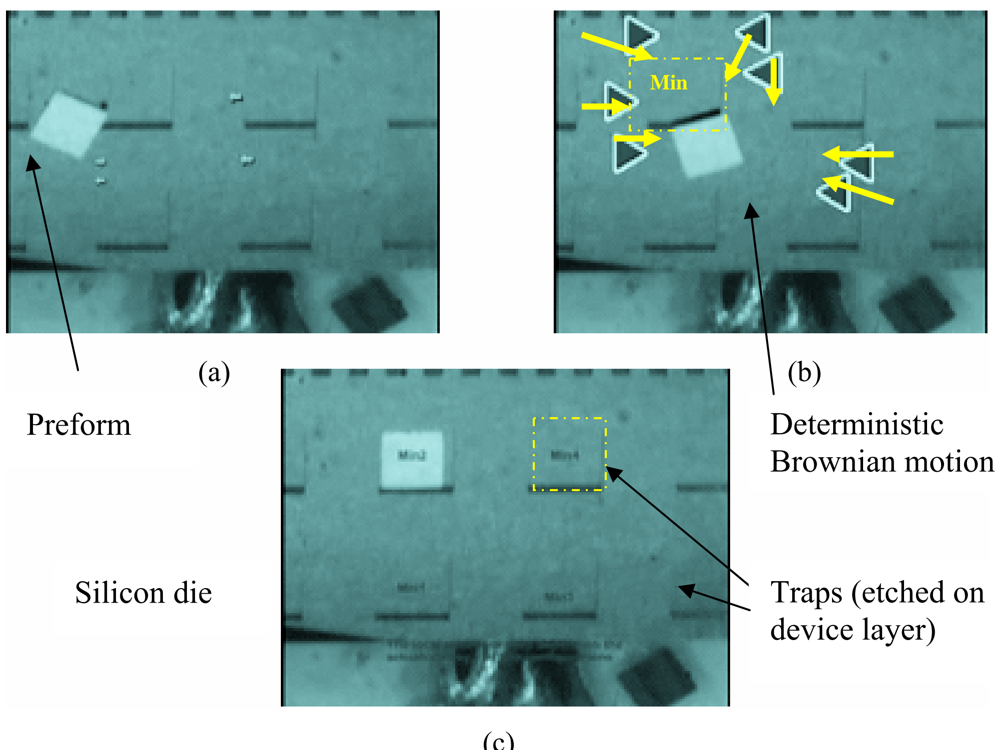

Figure 5.11 Trapping Meso-scale parts of large sticion forces (a) A perform placed randomly in an etched silicon die. (b) Guiding the Brownian motion by agitation. (c) Trapping preform at the minimum energy sites.

Figure 5.12 Machining on 55% porous copper layer used in assembly assisted by agitation.

In the first demo, five copper blocks of $250x250x500um^3$ were randomly placed on the surface of back silicon substrate. A square input waveform at 50% duty cycle, 100Hz and 30V amplitude is then fed to piezoactuator. Where, 0.46 second was the time needed for the cubes, in Figure (5.13), to relocate themselves on the nearest site which has both proper dimension greater than 200um and has minimum energy. Because these sites have minimum energy (often different from zero) within the vicinity of agitated surface, it is possible to transmit force into this site if the actuation conditions are changed. For example, the inertia of copper blocks as compared to their surface forces allowed the abrupt force acting normally on the parts to displace its location. Where, the time took to change a group of minimum energy sites to another was 0.09second, as shown in Figure (5.14). Given that the piezoactuator vibratory frequency was changed from 100lHz into 400 kHz and at continuous mode.

5.5.3 *Self-assembly Based on DNA Recognition and Assisted by Wet and Dry Agitations*

A method based on dry agitation is proposed in this research and the process might be justified from Fig.(15.5) and summarized as follow

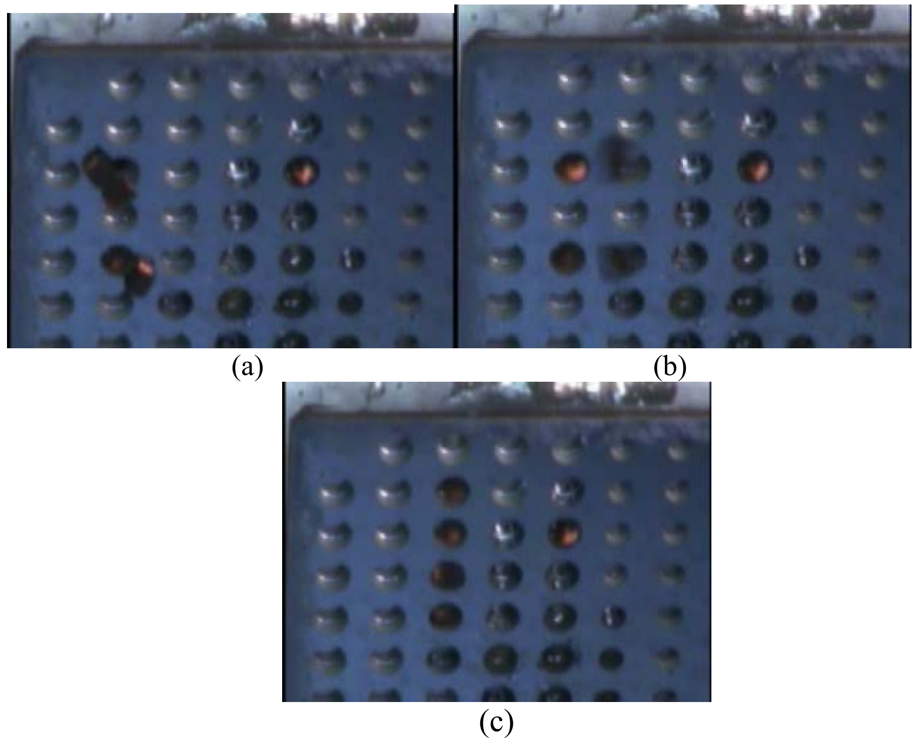

Figure 5.13 Trapping small scale parts of large sticktion forces: (a) randomly placed copper blocks, (b) instantaneous image taken during agitation and trapping. (c) After trapping.

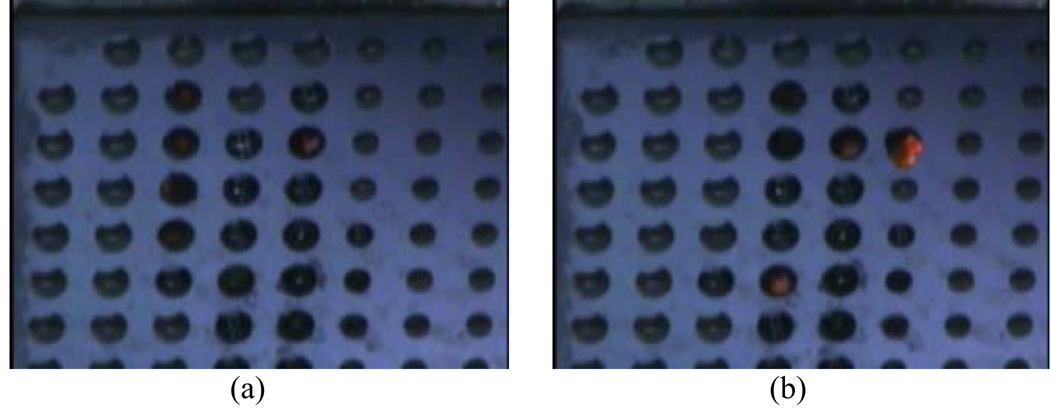

Figure 5.14 Relocating the parts from one trap to another using two different agitation conditions. (a) Locations from conditions described for figure 5.13 and at 100 kHz vibratory frequency. (b) Relocation into new binding site for 400kHz.

(i) Repulsive layer decreases the sticktion between the blocks and agitated surface.

(ii) The agitation causes planar squeeze field forces with some minimum energy regions.

(iii) The agitation overcomes the sticktion forces.

(iv) Parts move toward the minimum energy sites.

(v) Parts randomly collide causing interfacing between the micro-parts.

Key issues which require further investigation on the selfassembly based on dry agitation is due to complexity of the problem, specifically

- Design of the setup and obtaining the resonating (set of frequency and magnitudes) conditions at which motion and assembly starts.
- Reverse engineering the problem and knowing the effect of system parameter including but not limited to plate rigidity, environment, selection of surfaces, effect of scaling, surface roughness or sticktion forces), surface inclination.

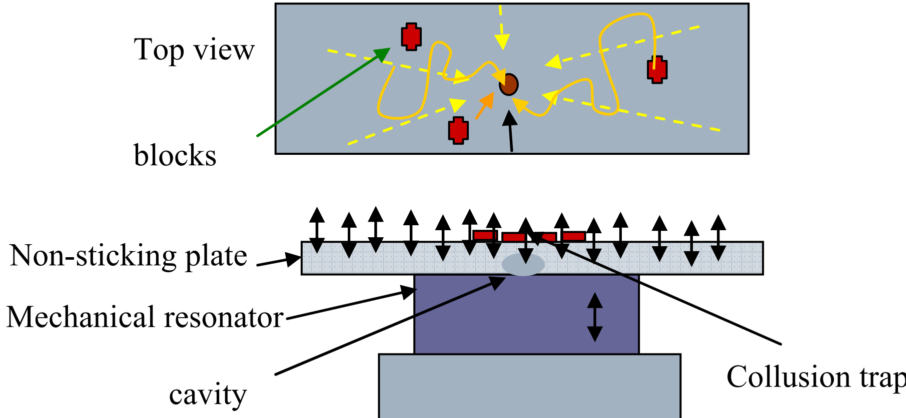

Figure 5.15 Schematic for self assembly assisted by dry agitation.

On the other hand, self-assembly assisted by wet agitation is a concept we develop and is based on the surface tension between a floating micro-part and liquid, wherein agitation creates directional forces enough to mobilize parts into minimum energy sites. The advantage of this method is based on minimizing sticktion forces in cases of hydrophobic vs. hydrophilic interaction. The process of self assembly is based on the existence of local minimum sites at which parts may collide

(i) Parts are freely floating on layer/meniscus the as a result of surface tension (repulsive).

(ii) The agitation imposes distributed surface energy whose local/global minimum are reflected from solid to liquid layer. Hence, this agitation causes planar squeeze field forces on the liquid layers.

(iii)Parts move toward the minimum energy sites at which they randomly collide causing interfacing between the micro-parts.

Figure (5.16) shows two schematics of self assembly assisted by wet agitations in a layer and meniscus. The challenges of this method is encompassed on identifying the effect of system parameter on the self assembly process including but not limited to setup design, properties of liquid and assembled parts, sizes of layers/meniscus relative to parts, interfacial tension analysis, identification of frequencies and amplitude of assembly. The experiments conducted in this section are performed to proof the concept at tuned conditions. The reliability of the method has not been investigated at broader design of experiments.

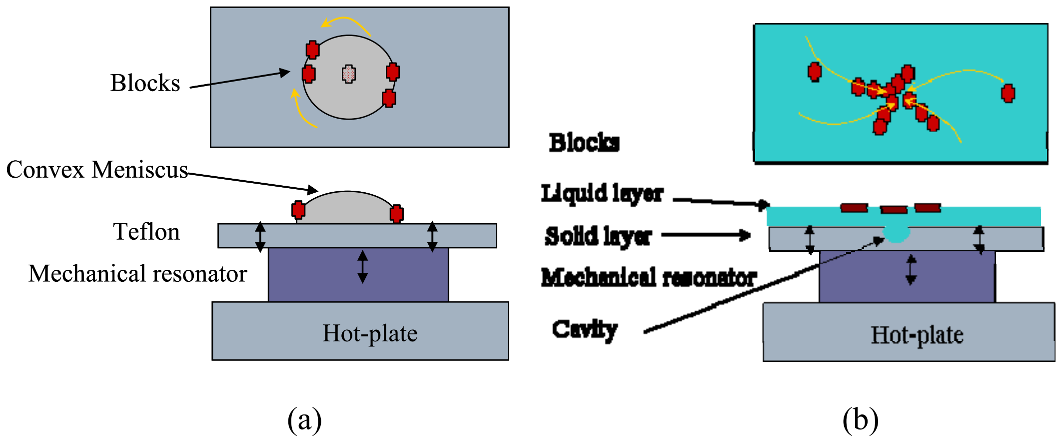

Figure 5.16 Schematic of self assembly assisted by wet agitation. (a) Meniscus based assembly. (b) Floating based assembly.

Experiments on parallel assembly are conducted using 2½D structures. The silicon building blocks of O-C shape were properly deteathered using ultrasonic device and then collected on a teflon plate attached onto a piezo actuator. A droplet of purified water is dispensed on the hydrophobic teflon plate causing convex meniscus. The blocks are dropped on this water droplet where blocks had arranged themselves on the droplet perimeter, as shown in Figure (5.16-a). The Teflon is agitated upward and downward using piezoactuator at 200V, causing the parts to come closer as frequency increases. Once the interfaces lock each other, the water is slowly evaporated using a hot plate placed below the assembly setup.

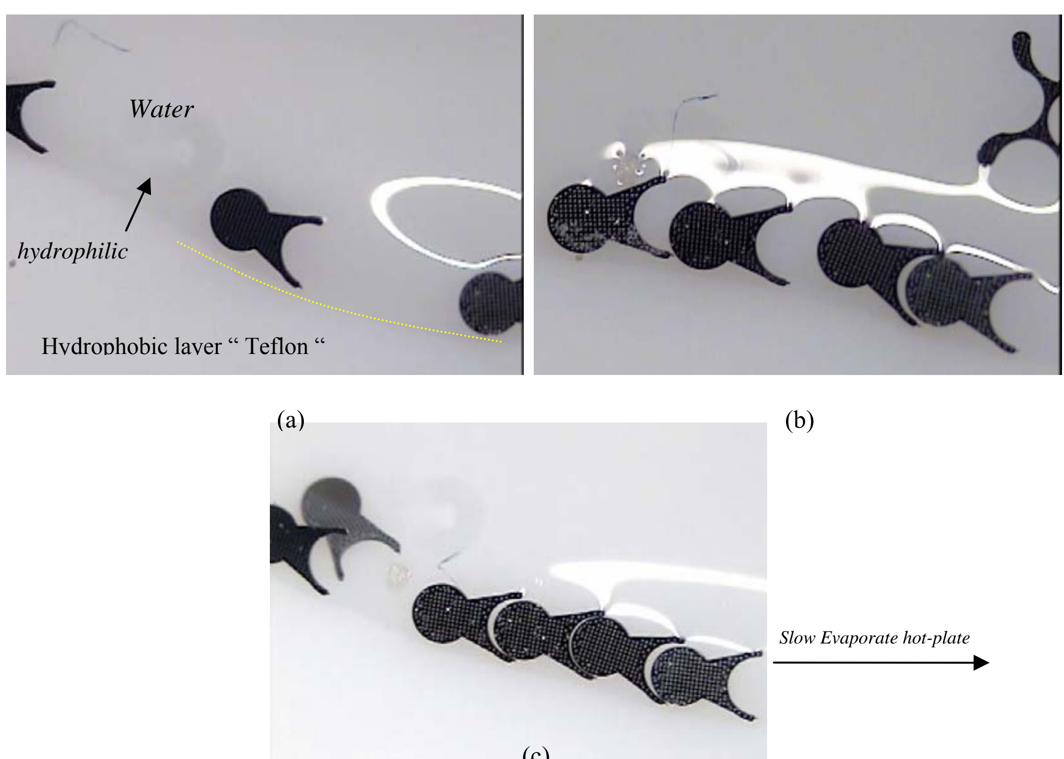

Figure 5.17 Self assembly of aggregate under wet agitation (a) Blocks floating on water meniscus (Arbitrarily thrown on the droplet). (b) Agitation of the platform collects the blocks at certain sites (the least vibrating site) (c) Increasing agitation frequency will further collide blocks.

Figure (5.17) shows a series of connected blocks locked mainly by a weak Van der wall forces. This serially connected structure is an example of reconfigurable swarm robots which could have potential applications in micro robotic and micro automation. The crucial question which should be answered is how well-connected are the micro assembly under pure microphysical forces such that it could be later considered for actuations.

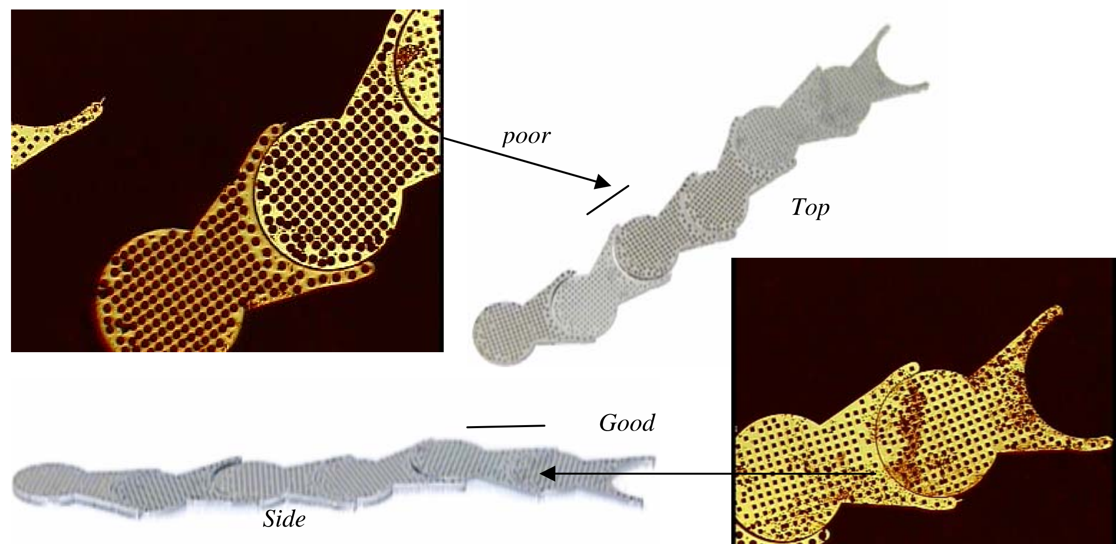

Figure 5.18 Preliminary results in self-assembly assisted by wet agitation for DNA configured micro parts.

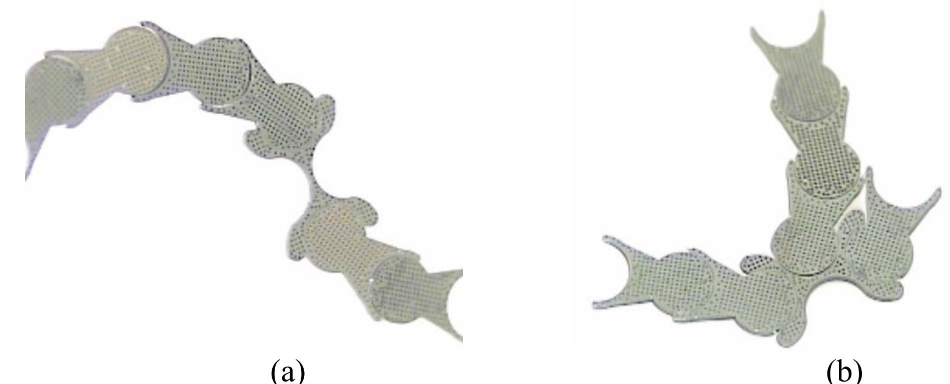

Figure 5.19 Preliminary results in self-assembly assisted by agitation for DNA configured micro parts. (a) One successful assembly based on dry agitation. (b) One successful assembly of wet to dry agitation.

The principles, followed in dry agitation, is similar to those described in previous section, wherein the micro parts are placed on a Teflon of circular surface which has small through hole at its center. To ensure the uniformity of the vibratory agitation, a circular speaker diaphragm is used to provide the upward and downward agitation. Herein, the Teflon surface is glued to the speaker diaphragm and then the

micro parts are randomly placed on the surfaces. For a harmonic signal of relatively few hundred Hertz, the parts started moving toward the through holes, wherein after several trial, one possible aggregate was captured and displayed in Figure (5.18-a). The drawback of the apparatus used is the low frequency response region of the speakers. Thus it is recommended to replace this agitation actuator with large piezocube capable of delivering large amplitudes at wide range of frequencies.

On the other hand, similar experiment is implemented for an agitated Teflon plate placed at the speaker diaphragm. Where, a small cavity is hollowed out on the back side Teflon centroid. Herein, other key block, Block “B” in Figure (5.9), is deliberately attached to the opposite flat side of the Teflon surface and above the cavity. Where, the weak surface tension is established between a single block “B” and Teflon surface by performing a very thin layer of moisture. This will inherently prevent the Brownian motion of block “B”. The connecting arm blocks “A”, in Figure 5.9, are randomly placed on surfaces. Then the surface is agitated allowing parts “A” to collide part “B” at the surface centroid. One of the successful assemblies was achieved and displayed in Figure (5.19-b).

It has been suggested earlier to utilize several actuation methods on such micro-robotics assembly. Including Electromagnetic, translocation assisted by biological species, chemical encoding…etc. A feasibility study is performed to measure the ability of the assembly to resist disturbance and the micro parts ability to move relative to each other. Preliminary investigation was performed on assembly in Figure (5.20-a) by

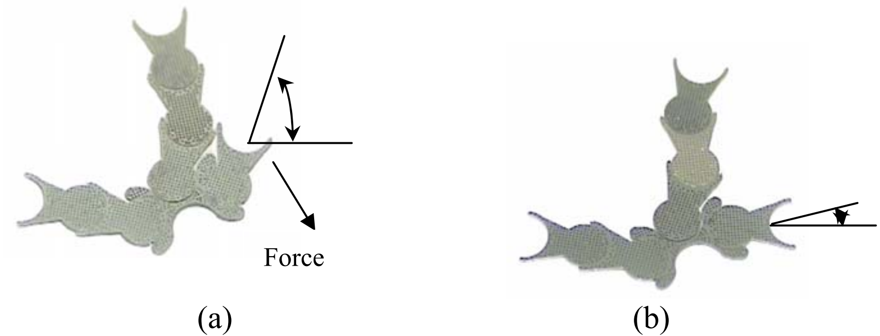

Figure 5.20 Effect of disturbance on self assembled aggregates. (a) Before applying force. (b) After applying force.

mechanical pushing one arm of the micro-robot in favor of rotating it around the interface. It was observed that small force could maintain the structure undisturbed while the subcomponent are relatively moved around the interface pivot , as noticed in Figure (5.20-b).

5.6 Chapter Summary and Conclusions

This chapter conceives new methodologies and concepts for parallel self-assembly assisted by law of natures. The scope of the art followed herein encompassed investigating new translocation and actuation mechanisms borrowed from different fields including biology, solid mechanics, and fluid mechanic. It was found that the stochastic elf-assembly can be constrained and planned to produce favorable structures. DNA based and agitation techniques were the motives for first determining the possible shape of constructed systems. And second, the deriving field which likely defined the manipulation paths. Moreover, the inboard power supply of microrobotic system is one of the most essential challenges facing the advance on the industry of smart sensor and

actuator. However, we have experimentally proved the feasibility of actuating devices at minimum losses during energy conversion. Where, the energy or the motility of the species was utilized to drive a novel custom made micropump. Thus, the constructed micro robotic system can be actuated or translocated by parallel micro organisms.

Finally, the parallel manipulation has enabled multiple constructions of structures at minimum cost, unlike serial microassembly discussed in chapter 3.

CHAPTER 6

SELECTIVE AND MONOLITHIC DETETHERING METHOD FOR MESO- MICRO DEVICES

6.1 Introduction

The vastly growing fabrication techniques have increased the need for microassembly techniques aiming at constructing complex structures, hybrid, integrated electronic and Microelectromechanical MEMS devices. The success of a developed technology depends not only on its capability to deliver the amount of parallel or sequential process flows, but also on the complexity of performing the assigned tasks at minimum sensory and at high precision.

One particular manipulation task in MEMS, for example and in most situations, is to release the microstructures or device from wafers or dies on which they are fabricated. In addition, it is required do not lose the devices during the fabrication process sequences. This is addressed by often including different mechanical structures or thethers in the design to anchor the devices in the same device layer frame which is rigidly attached on the wafer or die level.

The traditional approach of detethering structures from the body relies on mechanically probing the stiff structure to break the tethers. This method suffers from drawbacks including slow yield, requirement for sensory vision feedback and it might not result in

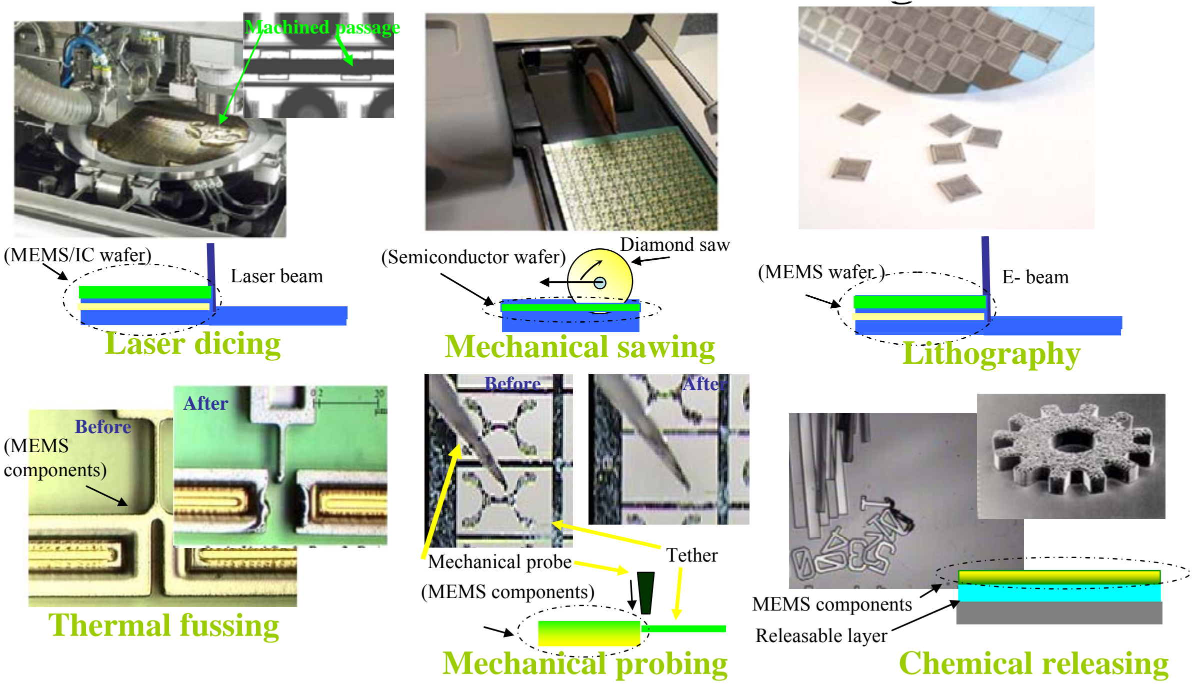

Figure 6.1 Method for releasing MEMS and semiconductors.

complete and fine separation of the devices from the tethers. Alternative techniques employed to release devices shown in Figure (6.1) such thermal diffusion of tethers [142], laser dicing [139], mechanical sawing [140], mechanical probing, lithography [141] and chemical releasing [143] suffer from similar drawbacks. Releasing MEMS devices by etching away the sacrificial layer [114] enables parallel release. However, etching has limited applications and requires preferred fabrication steps which may overlap with the design requirements. Moreover, removing MEMS devices using sacrificial layer is incorporated in the fabrication process.

The purpose of this chapter is to investigate techniques for parallel and selective release of the Micro to Meso devices discussed in previous chapters. The need for finding fast and reliable method to release MEMS and electronic parts is emerging,

where the current methods of dicing or mechanical probing for releasing parts become primitive processes for large quantities. Therefore, an invention which generally relates to methods for releasing MEMS structures, semiconductor and integrated circuit devices after manufacturing is introduced.

A methodology followed by applications and apparatus for detethering multiple miniaturized components and microelectronics from their platforms is disclosed in this chapter. The method provides a mechanism for parallel and selective detethering of suspended micro-meso scale parts. Reverse engineering the mechanical design of the tethers could provide specific fracture conditions at which detethering can take place under controlled vibratory agitation. The material presented is arranged by first building the theory of parallel and selective releasing and then validating the proposed methodology through numerical simulations and experiments.

6.2 Method Contributions

A novel platform is discussed for not only releasing MEMS components and electronic devices, but also to identify procedures, applications and methods which could be efficiently utilized for industrial and research purposes.

The detethering method presented in this research was developed in order tor control the process of singulating microelectromechanical and semiconductor devices. The method process flow can be described through the following steps. , First, the proper design of flexible tethers for each device encapsulated in a unit cell. Second, devices are massively fabricated on their layers. Third, the devices are preferentially

arranged in an array of cells and attached to the cell frame by the tethers. Fourth, the array pattern and their tethers comprise a body of structural layers that is attached to a controlled vibratory agitation system. Fifth, a range of waveform signals are introduced to the system to generate the desired and critical dynamical responses on the tethered devices. Sixth, the dynamical response of the tethers results in generating fracture stresses at the defined locations on the tethers. The fracture stresses define the destructive conditions which should be reversed engineered depending on a range of factors. These factors are not limited to materials and geometries of tethers and devices, structural damping constants, and fabrication processes. The damping constants can further determine the amplitudes of stresses for detethering purposes.

The design of the tethers should provide a designated range of destructive conditions at least less than and different from the fracture conditions of the actual device components. Thus, the required destructive conditions are defined apriori for each or for a batch of unit devices. By providing controlled agitations to the fabricated array of cells will result in massively and simultaneously but selectively detether devices from their body if they have the same fracture conditions. The selective and massive releasing allow several batches of identical devices or a properly selected set of devices to be detethered on the same platform by choosing appropriate agitation conditions.

The vibratory agitation system operates at the preferred dynamical excitation responses, and compatible with the specified range of frequencies/amplitudes needed to provide destructive conditions in the tethered devices. Controlled vibration is obtained

from a set of high performance piezoactuatoros (however other devices could be used as well).

The structures of tethers are not limited to a specific geometry but include groups of cantilever beams with tip mass at free end. The tether geometries could be linear breadth tapered cantilevers, prismatic cantilever beams, tapered cantilever beams of truncated wedges, tapered cantilever beams of truncated cone, doubly-tapered cantilever beams, group of cantilever beams truncated at different shape-functions. According to the tether shape, the devices will exhibit clean fractures at the tether free-end. The maximum stress concentration will occur at the tether neck due to notches designed and fabricated at the neck of the tether.

The pulling direction of the piezoactuator in an agitation system is transmitted at different angles with respect to the layout of the tethered devices. The apparatus include a rigid but rotary disc with stopping-mechanism to partials the inertia transmitted to tether anchors, causing several directional in-plane agitations.

The array arrangement of cells fabricated on the agitated body may be further selectively detethered. Particularly, subgroups of a group of devices, which share identical and relative distractive conditions, are selectively detethered by controlling the orientation of in-plane agitations. The method may be implemented at different scales and at different levels including but not limited to cell level, package level, die level, wafer level and circuit board level.

The proposed design of the tethers considering the suspended mass and the cells and arrays gives could potential be used as for sensory and actuation purposes. New

sensors and actuators may be obtained; for example, a safety inertial sensor fabricated from at least one conductive layer and a proof mass which could be double tethered and anchored thus establishing two necks with the proof mass. The anchors of the tethers are part of two isolated pads across which a signal is applied. The developed circuit is open if the designed destructive conditions of tethers and proof mass combination are externally excited, where the excitations define crucial or harsh operating conditions at which the fracture takes place at the said necks. The circuit complexity required for signal processing and conditioning is considerably reduced. The functionality of the inertial sensor relies on a mechanical signature designed for specified external conditions. A potential application of this inertial device is a disposable and replaceable safety switch that might be fabricated on the same wafer level and for different signatures.

6.3 Applications for the Method

The described detethering method will be applied to releasing MEMS structures, semiconductor and integrated circuit devices after manufacturing. The method is an enabling concept which provides a novel process for massively separating the miniaturized integrated circuit devices from their anchors and the apparatus may be incorporated in an assembly process-line. This is an advantageous approach to cross-link the process of manufacturing massive numbers of devices and the post-manipulation processes that include singulation, orientation and presentation.

In addition, the method provides a novel procedure to release MEMS structures after manufacturing. For example, MEMS devices fabricated on the device layer of silicon on insulator by (Direct Reactive Ion Etching) DRIE may be massively arranged in array of cells in which each unit device is properly tethered to the device layer frame. The vibratory agitations may be used to release the devices by breaking the tethers at their necks.

The detethering process as an enabling technology could augment the development of both a small number and massive quantities of released modules or devices for post assembly. In particular, a preprocess that is needed to provide a platform for selfassembly, templating and sorting. Application examples include detethering of massive quantities of light emitting diodes (LEDs), laser detectors and modules for building robotics systems. Moreover, the methodology may be implemented for the design of a range of sensors and actuators. Specifically, the destructive detethering technique may be implemented in single packaged device(s) under forced or natural agitations, where the functionality of the packaged device relies on releasing the attached parts at the free ends. An example includes the proposed mechanical inertial switch which may be utilized in existing applications related to systems safety. Finally, the methodology of releasing by mechanical signature enables paradigms in applied sciences in micro-electromechanical engineering. Methods of inverse or reverse engineering and optimization of vibrating structures could be studied from their performance efficiencies at different agitation conditions. Particular studies

include but not limited to structural vibration of small objects, fracture strength of small objects and control of agitation system.

6.4 Description of the Method

The approach generally relates to a mechanical mechanism utilized in detethering MEMS structures, integrated circuits and similar devices after fabrication. . The methodology and apparatus for monolithic and selective detethring along with some applications is presented. Further investigation on the system parameters aids in insightfully understanding the design and characterization of a tethered device. The variation of parameters leads to wide range of desired operating conditions and may also lead to the design and development of different tether shapes.

6.4.1 *General Concept of the Detethering Method*

The steps followed in determining the fracture conditions for a specific group of tethered devices, such as those in Figure (6.2), may preferentially require prior modeling knowledge either through numerical simulations and/or experimental evaluation. Certain conditions should constrain the intended to be limited to embodiments shown. Generic guidelines to be considered for defining the design parameters include avoid malfunctioning the device, the range of vibratory agitation signals should be feasible with the available actuators, it is preferred to design a notch at the tether free end such that it can easily break during agitation; but the tether should be strong enough to hold device during manufacturing and handling processes, the unit cell

shall be as much as possible compact and comparable to device size. The concept is based on applying external oscillatory displacement to the layer's platform which encapsulates the tethered devices. Each device is tethered to the cell's frame. Large number of cells constitutes the layers on which devices are fabricated and their schematic could for example be embodied in Figure (6.2). The later embodiment comprises of device anchored at different angles and tether shape which enables unique signatures for each identical group of cells. Shaking the entire fabricated layer by a directional displacement transmits forces to tethered devices and the effect of the inertia of the small device is not neglected for displacements excited at high frequencies and amplitudes.

Figure (6.3) depicts an example of a breadth shape cantilever tether which has constant thickness and linear width that is maximum at the anchor. The minimum width is located at the free end of the cantilevered tether at which a device is connected. The neck and the orientation of device form a notch whose angle creates maximum stress concentration. The mechanical fracture signature, defined here by a specified system resonance frequency, depends on many parameters like those shown in Figure (6.3).

The fracture conditions of the described notch is not trivial but may be related to the following factors. (1) Agitation of entire fabricated layer is same as the agitation of each unit cell at their anchors. The applied displacement at the anchors forces the devices to oscillate at different phase and amplitude and could be explained by the equivalent model describing an agitated unit cell as shown in Figure (6.4).

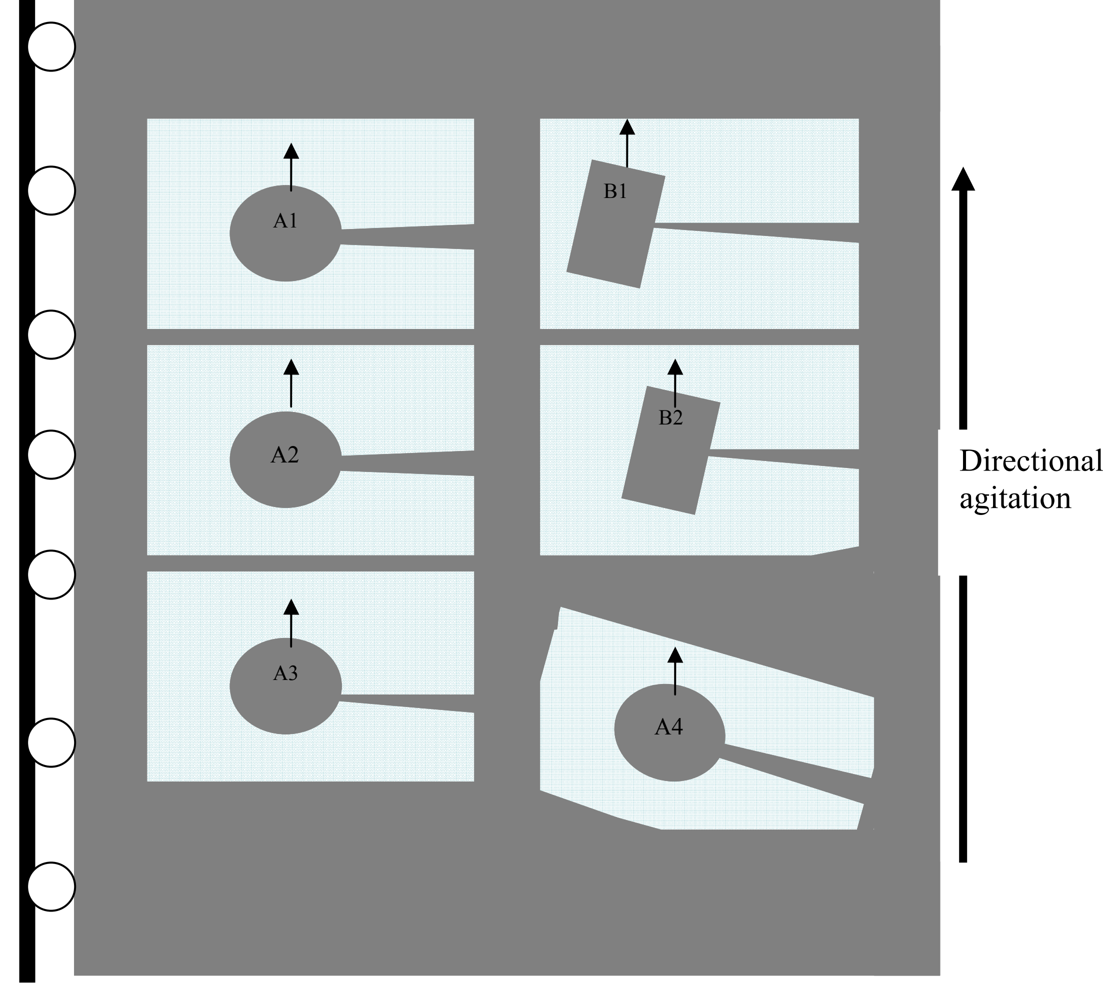

Figure 6.2 Schematic for an array of two different devices fabricated on same platform.

Numerical and analytical methods could be used to find the sensitivity of parameter changes to the fracture conditions as will be seen in later sections.

The maximum relative displacement between the base excitation and the device center of gravity is caused by transverse inertia and results in maximum bending energy at the notch.

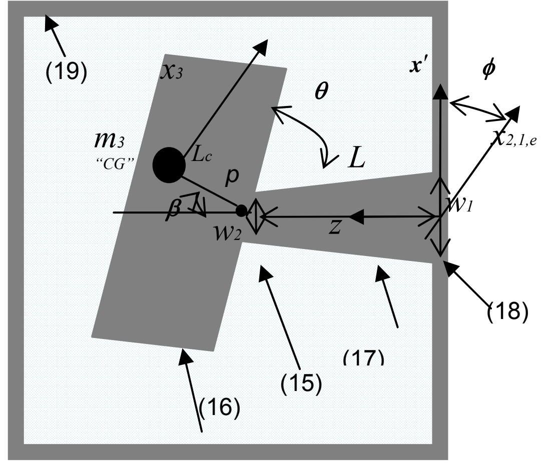

(15) Neck or notch.
(16) Device.
(17) Tether.
(18) Anchor.
(19) Cell frame.

z Lateral coordinate along cantilever beam.
$\boldsymbol{x'}$ Axial coordinate perpendicular to z.
$\boldsymbol{v}$ Deflection of elastic axis in $\boldsymbol{x'}$ direction.
$\boldsymbol{L}$ Length of cantilever beam.
$\boldsymbol{A}(z)$ Cross section of cantilever beam at z.
$\boldsymbol{I}(z)$ Moment of inertia of cross-section about the perpendicular to the plane of bending at z.
$\boldsymbol{p}(z,t)$ Load per unit length.
$\boldsymbol{\beta}$ Angle of CG-shift from beam lateral coordinates.
$\boldsymbol{\phi}$ Angle between the excitation coordinate and $\boldsymbol{x'}$.
$\boldsymbol{\theta}$ Angle of stress concentration.

Figure 6.3 Schematic of a tethered device in a unit cell. (a) Top view of a device fabricated in unit cell.

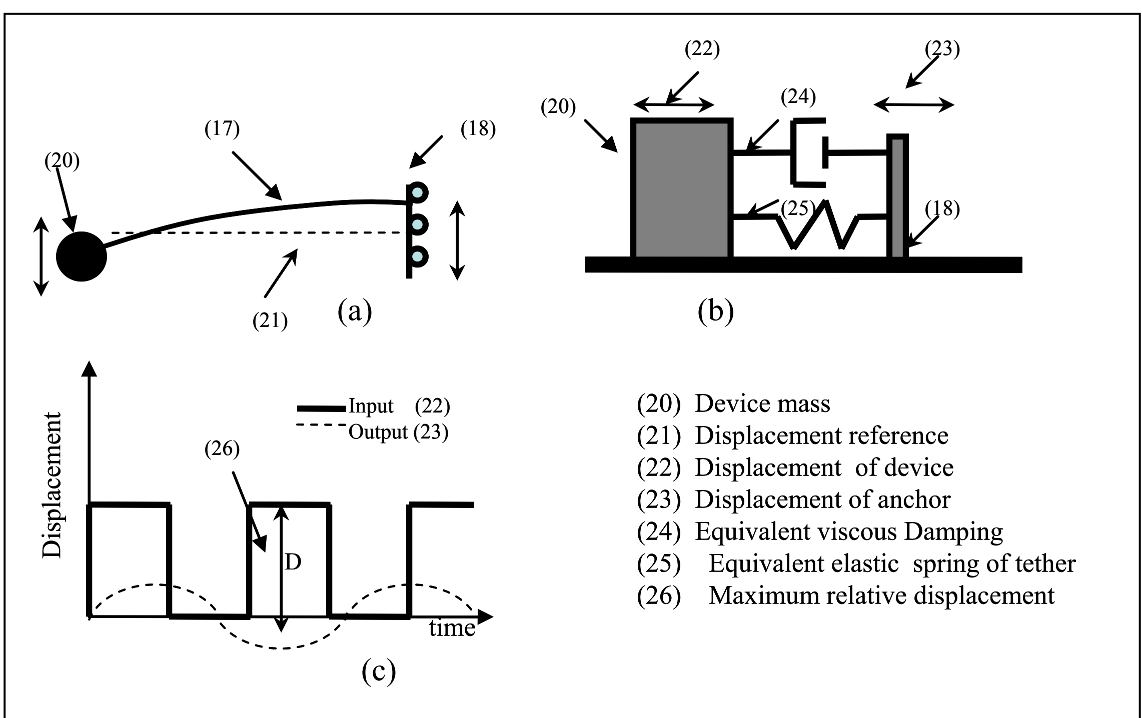

Figure 6.4 Illustrations for mechanical modeling and time response of a tethered device: (a) Illustration of a single cantilever tether being vertically agitated. (b)Spring-mass lumped model of a unit cell under damping (c) illustration of input output displacements.

This condition may cause fracture if the localized stress exceeds the fracture stress. (2) The device center of mass is dislocated from the tether neck. Thus the dynamic bending moment is acting at the notch whose effect is proportional to the dislocation and the transmitted inertia. The fracture is more likely to occur at the latter conditions. (3) The dynamic response of the tether and device system exhibits maximum stress concentration at the system resonance frequencies. The amplitude and resonance frequency of the system is chosen to determine the fraction stress of device from the tether.

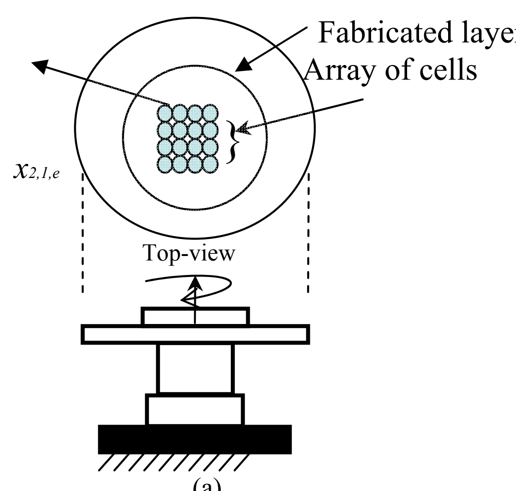

(a).

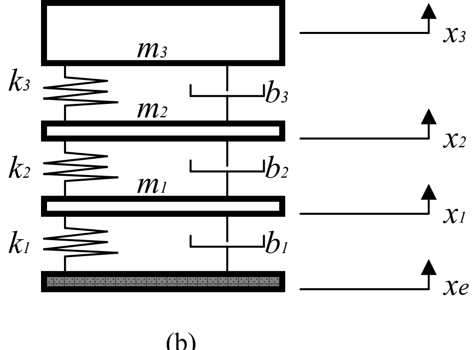

(b)

x_e Coordinate of Actuator excitation

x_1 Coordinate of Non-sticking plate

x_2 Coordinate of array-plate

x_3 Coordinate of device center of mass

k_3/b_3 Equivalent spring/damping constants at cantilever end

k_1/b_1 Equivalent spring/damping constants of rotary plate.

k_2/b_2 Equivalent spring /damping constants of array-plate.

m_1 Point mass of rotary plate

m_2 Point mass of array plate

m_3 Point mass of device at center of gravity CG

m_c Mass of cantilever

(c)

Figure 6.5 General schematic of a vibratory agitation system: illustration of total system dynamical model including fabricated devices: (a) Schematic drawing of the devices placed on the setup.(b) Equivalent model.(c) Some important modeling parameters for total system dynamical modeling.

Specifically, the vicinity of modal frequencies to cause fracture at the weakest points in the tether but not on the devices structures should be selected to be different from detethering conditions in other devices. Selecting piezo-actuator as the main driver for vibratory system allows for the selection of different harmonic excitation signals. For example, one could use harmonic trigonometric or square signals to excite piezo actuators. Figure (6.4) shows schematically an agitation concept that relates the excited anchor and device motions configured in lumped or measured motions.

6.4.2 *Vibratory Agitation System*

The embodiment described in Figure (6.5 or 6.6) generally illustrates the vibratory agitation system which is essential to comprehend the invented dethering methods. It is worth mentioning here that the system is capable of providing controlled directional agitation in x, y and z. The barrier, indicated in schematic with number (15), is optional and used to induce frequent impact with the agitating wafer. Particular use is to enable the releasing at low frequencies and for small scale devices where the inverse design of the tether might prove to be difficult.

The system consists of three main subsyetms: (1) First, high performance actuators capable of providing relatively large agitation displacements at high frequencies. Here, oscillatory displacements are provided by two stacked piezoactuators. Planar vibratory motion is transmitted at different directions with respect to the tether anchors, depending on the angle between the tether base and the rotary disc.

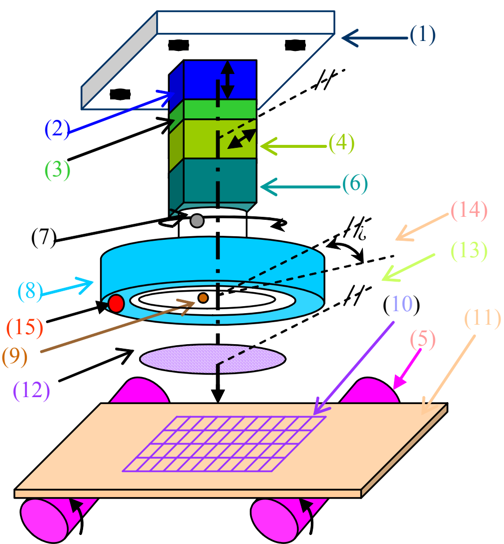

(1) A support fixture.
(2)Piezoactuator agitating out of plane.
(3) Intermediate adapter between piezoactuator.
(4) Piezoactuator agitating in plane.
(5) Feeding wheels.
(6) Intermediate adapter between piezoactuator and rotary disc.
(7) Locking mechanism.
(8) Rotary disc and wafer holder.
(9) Wafer clamping mechanism (suction).
(10) Templates to sort the released devices.
(11) A non sticking conveyer belt.
(12) Wafer.
(13) Axis of alignment.
(14) Adjustable angle of rotation.
(15) Barrier.

Figure 6.6 Major components of a top-down vibratory agitation system: an illustration in industrial process-line.

The other stack of piezoactuators transmits an out of plane vibratory motion. The planar agitation and in plane fractures are commonly designed to guide the detethering locations. (2) Second, a subsystem consisting of a rotary disc with a holder used to rigidly hold the fabricated devices. This system is responsible for providing the additional feature of dethering a subgroup of identical devices. The clamping and rotary mechanisms should be designed with minimum frictional damping between parts.

6.4.3 *Monolithic Detethering Concept*

Parallel releasing of identical or different devices is achievable if the operating conditions simultaneously generate fracture stress in the described devices. A schematic demonstration of this concept is depicted in Figure (6.2). For example, devices A1 and

A2 are identical and experience same anchor excitation and thus fracture should occur simultaneously for both. This concept may also be explained using the dynamic response of different devices as illustrated in Figure (6.7). If the areas below the normalized relative displacement overlap above the minimum yield stress conditions, then there exists at least one input frequency which simultaneously excites the fracture conditions of devices with overlapped areas.

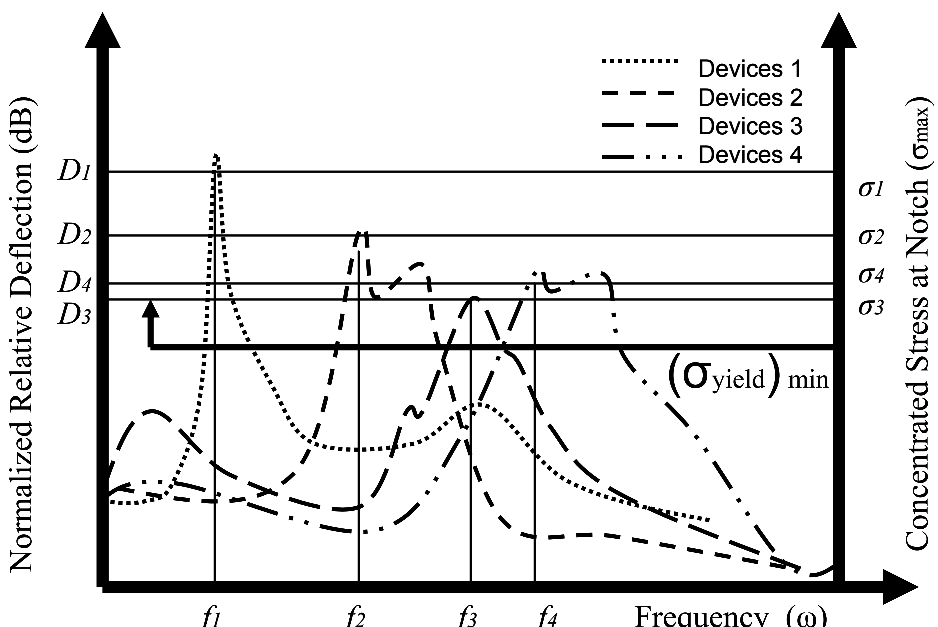

Figure 6.7 Concept of selective and monolithic detethering attained from frequency response and stress analysis.

6.4.4 *Selective Detethering Concept*

Selective detethering can be implemented for devices which either have identical or different structures. The technique is possible by changing the dynamic responses of the cell units under same external agitation. Figure (6.2) illustrates

identical devices A1, A2 and A3. However, the tethers of group A1 and A2 are different from that of A3, thus selective but different destructive frequencies may be defined to release devices A3. Similar scenario occurs in detethering devices B1 and B2.

The same approach for detethring from same group could be applied even if the device and tether designs are identical but the orientation of the unit cell is different from other same units. Rotary concepts allow transmitting in plane agitation at different angles with respect to tether anchors. Thus, the vibration vector is decomposed and ‘less’ agitation is experienced by the device if the angle is not fully transverse with the tether. Consequently, partial vibratory agitation may be planned for identical cells if they are arranged at different angles with respect to motion direction of actuator. For example, the group of devices A1, A2 and A4 are identical in the design of tether and design of devices. A situation in which it is assumed that the current illustration sufficiently allows A1, A2 to be simultaneously detethered under planar agitation, where A4 is not detethered because only partial displacement is transmitted to device. However, A4 can be detethered if the cell angle is reoriented at an angle which makes planar agitation acting at a situation similar to the successful detethring of A1 and A2. This re-orientation is accomplished by the rotating the disc.

Figure (6.7) is applicable to a group of four devices fabricated on the same tray with each group of devices having unique detethering conditions that do not overlap with the other groups. Such illustration may be useful for the designer to evaluate the detethering process in order to define the critical frequencies upon which successfully parallel and selective detethering take place.

6.4.5 *Notes on Other Applications of Detethering*

The proposed detethering method does not only bridge fabrication and production processes, but also enables the development of new sensors and actuators. The first application is to incorporate the method and setup in a process-line illustrated in Figure (6.6). After fabrication, the devices may be selectively released in massive quantities by using the techniques. Then the process flow continues for post assembly, where auxiliary subsystem may be introduced to support the process flow in industrial or research plants. The second application is the safety inertial sensor based on the invented methodology. A doubly tethered proof-mass, illustrated in Figure (6.8), which has at least one conductive layer, are anchored to the pads, wherein the said pads completes the circuits to which inertial sensor is connected. The logic of said sensor is "Closed" circuit unless a destructive vibratory agitation is applied to detether the mass and opens the said circuit. The significant application of the claimed inertial sensor is that it can be installed as a disposable packaged device to secure the safety of other circuits and structures at harsh environments. Its advantages over other available devices, such as accelerometers and force sensors are: has a simple principle that relies only on the mechanical signature, can withstand a wide range of harsh conditions, the design complexity of circuit is considerably reduced, the size of sensor is compact, reliable and could be easily packaged and it is cost effective.

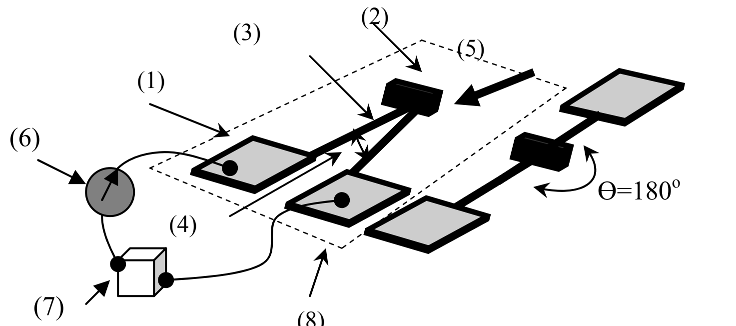

(1) Conductive pad.
(2) Proof mass.
(3) Tethers.
(4) Angel separating double tethers Θ.
(5) External Dynamical load (inertial force).
(6) Electrical signal.
(7) Other circuits.
(8) Packaged unit cell.

Figure 6.8 Inertial-switch sensor: posseses mechanical signatures that are excited at certain vibratory harsh-environment.

Other applications encompass using the method to provide a large quantity of detethered components to be used in a self-assembly process. For example, Figure (6.9) shows key features of a MEMS block fabricated from silicon on insulator by DRIE process. Based on the assembly principle, the blocks are stochastically organizing themselves to form certain robotics systems based on the DNA recognition concept.

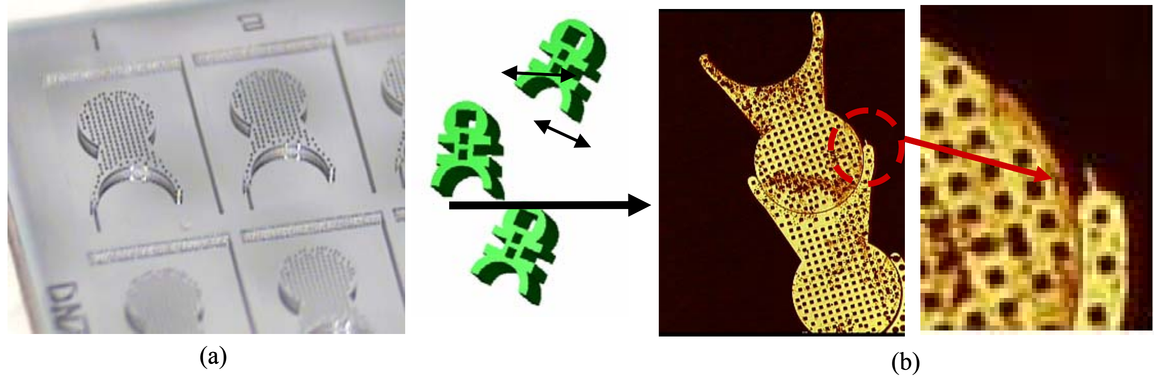

Figure 6.9 An application on the need for releasing massive MEMS blocks: (a) Building blocks are fabricated and tethered, (b) The massively detethered blocks are utilized in DNA based selfassembly.

6.4.6 *Summary of the Method*

A method for parallel and selective tethering of suspended Meso- micro-parts is introduced from system to subsystem levels. The preferred embodiment in accordance with current invention consists of three stacked subsystems. Figure (6.5) or Figure (6.6) embodies a setup comprising of (1) an actuator blocks to provide controlled vibratory agitations at several frequencies and amplitudes. Here, cubes of stacked piezoactuator*s* are sandwiched between a rigid frame and a rotary disc. (2) The rotary disc utilized to changes the angle of in plane agitations direction with respect to tethered devices. The disc comprises: mechanical clamper mounted on the said disc and used to firmly hold the fabricated layer, and mechanical stopper used to firmly hold the said disc at specified angle. (3) An array in which suspended devices are arranged within cells on the device layer of fabricated layer.

Cells of encapsulating micro-parts are encoded by a unique fracture conditions that is related to the vibration of a group of devices, wherein detethering characteristic are strongly dependent on the tether shapes, tether material properties, notch placed at the free end of said tether, device geometry, device mass and its center of gravity location.

For example, a linearly breadth cantilever beam is a recommended tether designed for MEMS structures. It could be fabricated on silicon device layer of MEMS structure by DRIE process, wherein the said cantilever beam is depicted in Figure (6.3). The point mass of device is attached to the beam’s neck at the free end with an angle that causes stress concentration. Therefore, fracture conditions are described at yield

strength that is caused by maximum relative deflection of neck as measured to anchor deflection. This simple measure and design criterion for fracture may be best contained within the resonance frequency of a system of tethered device; comprising the dynamics of tether and device.

A single packaged inertial sensor is one inertial application on the detethring of devices under controllable destructive conditions. Two electrode-tethers are fabricated with their free ends attached to a proof mass. Figure (6.8) shows the said inertial sensors whose electrodes and proof mass are completing some auxiliary or electronic circuits. At specified external agitations, the stress constriction result in breaking the electrodes necks, wherein the circuit is open and the signal is cut from the other said circuits.

6.5 Design and Verification Methods

The experimental studies on the detethering MEMS devices fabricated on SOI have proven the feasibility of the releasing method. Up to now, however, there are no mathematical theories describing the fracture stresses of micro cantilever beam under dynamical vibration. In this section, we attempt to understand the effect of harmonic excitation on tethered micro to meso devices. In particular, the variation of stress is studied from the design parameter of tethered devices. We provide basic mechanisms sufficient to enable the reader to refine problem optimization and reverse engineering the design of tether (inverse the design). Finite element analysis is discussed with the effort of supporting the proposition claimed in the pervious sections. Furthermore, the describing wave equations of one of the claimed tether shape are derived with the merit of understanding the dynamical properties from governing mathematical equation.

6.5.1 Experimental Feasibility Studies

Feasibility studies on the selective and parallel detethering are obtained for devices fabricated on device layer through direct ion etching of SOI. Where the silicon devices are attached to cells frame using a linearly tapered cantilever. These devices are arranged large quantities in unit cells as shown in Figure (6.10-a), wherein, small dust size silicon blocks have thickness of 100 micron and average length of 100 micron. Each cell has a unit device whose sacrificial layer is chemically released. While, the device is kept anchored to the device layer frame with a tether on same device layer.
These blocks should be properly released without leaving flashes of tether, wherein the application of behind introducing massive and selective quantity of clean blocks where discussed in previous chapter. Specifically, the problem illustrates the need of introducing massive self assembly for construction of micro robotic systems, such as arms for microrobot.

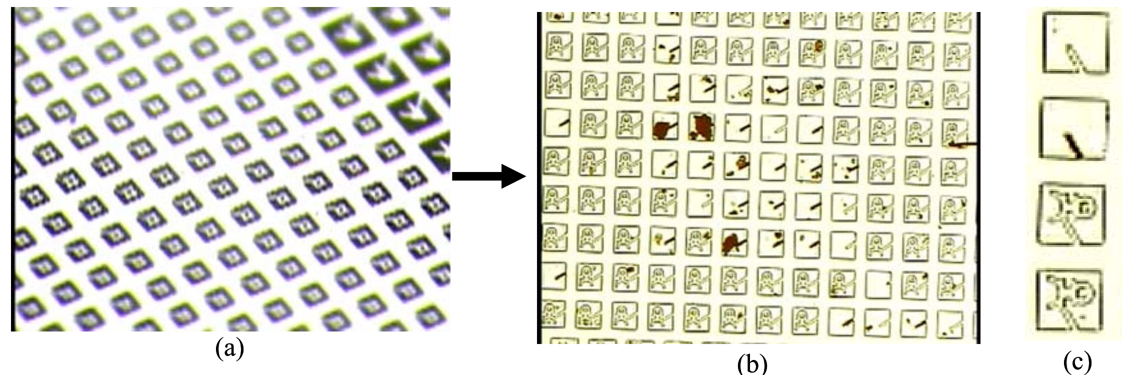

Figure 6.10 Blocks tethered by breadth cantilever beam and results on detethering based on vibratory agitation: (a) massive number of dust size blocks are fabricated on device layer of 1cm^2 SOI die, (b) specific blocks are detethered, (c) zoom in at tethered and detethered unit cells.

The platform which carries theses cells is a silicon die of ~1cm^2 in area and has total thickness of ~400 micron (including the handle wafer). Figure (6.10-b) shows a preliminarily experimental verification of massive detethering, wherein small sizes of MEMS blocks fabricated on silicon on insulator (SOI) are detetherd based on vibratory agitation. A zoom in some of the released part is shown in Figure (6.10-c), where it is clear that the devices has weakest point at maximum stresses occurred at the notch.

Obviously, the parts are solid block which are difficult to damage at normal resonance frequency of tethered devices. Further measurement requires experimental identification of the fracture conditions for different geometries, like those fabricated on SOI in Figure (6.11).

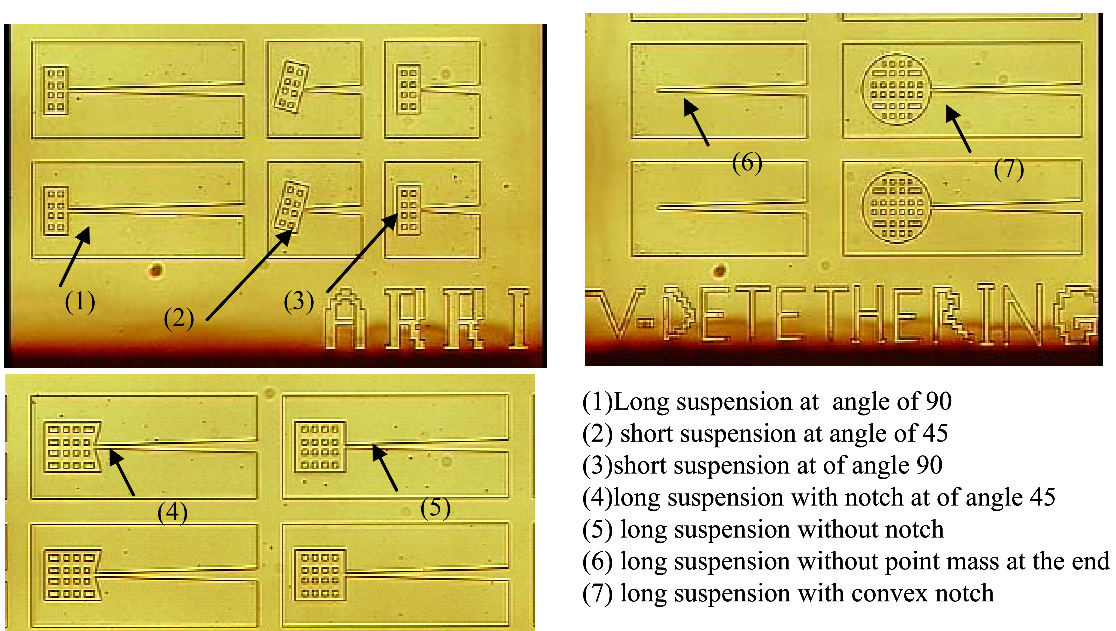

Figure 6.11 MEMS blocks fabricated from silicon in insulator using DRIE: tethers have different notches at the free end of breadth cantilever beam.

Where, we introduce different length of tethers and different notch angles. It is important to notice here that the motion profile of the resonating device could be captured by 3D MEMS profilometer, upon which more implicit analysis is brought with the identification of fracture conditions. Experimentally, there is no unique fracture stresses of a device may vary according to micro geometry [118]. Hence, the experimental investigation combined with numerical simulation is important in fully understanding fracture signatures.

6.5.2 *Numerical Simulations*

The methods followed in analyzing the fracture conditions of tethered devices are supported by numerical simulations based on Finite element modeling. Herein, the modal and harmonic analysis are performed for several examples with the favor of validating the claims mentioned earlier. The examples illustrated in the analysis are models for devices fabricated from silicon on insulator. The device layer thickness is of 100 micron and has density and modulus of elasticity of 2330Kg/m^3 and 169Gpas, respectively. The damping and external loading are assumed zero unless otherwise mentioned.

In particular, the method concepts are approached in the following categories:

- Modal analysis of several types of tethers under tip loading in which three examples are discussed: cantilever beam of uniform cross section and under a tip loading, a wedge cantilever beam and linearly tapered beam. The effect of changes

in geometrical parameters is also demonstrated to enable the understanding of tether shape.

- Harmonic analysis embodied on laterally agitating unit cells under dynamical load of known amplitudes and frequencies. A sinusoidal displacement input is fed to the structure and swept over range of frequencies. The maximum stress (Von Misses) concentrations are calculated at tether neck for the range of frequencies. Different comparisons are made in illustrative examples:

    1- Harmonic analysis of the stress concentration at neck for different tether shapes and at range of frequencies.

    2- Harmonic analysis for complex devices are sought to distinct the fracture conditions between tethers and the devices.

    3- Array of identical and different cells are agitated in one platform.

    4- The effect of external damping constants on the detethering, associated for example by the air, is compared for that of vacuumed agitation.

6.5.2.1 Modal Analysis

The scope of this analysis is to generate a fast look up table for simple types of cantilever tethers. The resonance frequencies or modal are defined for anchored tether which experiencing impulse force exerted at the device. Thus exciting the different natural frequencies at which system might severely respond. The modal analysis does not directly imply the fracture conditions rather than generally defining a range of frequencies at which devices may fracture. The exact analysis should be obtained from

the harmonic analysis discussed later. This is because the anchors of cantilever beams are fixed in modal analysis while it is vibrating due to agitation. Table 6.1 discusses the effect of beam shape on the first five natural frequencies of tethered block. It can be found that the modals are sensitive to the length and cross sectional uniformity of the tethers, wherein the resonance frequencies drops as the length increases and as the cross sections narrows at the free end of the tethers.

6.5.2.2 Harmonic Analysis

Understanding the effect of the inertia of micro component on the detethering can be simulated using finite element modeling. The scope of this analysis is to evaluate the sensitivity of maximum stresses to tether shape and device inertia properties.

Table 6.1 Look up table of basic tethers with mass at free end.

Model	**Modal (Hz)**	**Notes**	**Models and modal shape**
1	29177. 0.21046E+06 0.12565E+07 0.26396E+07 0.69081E+07	1-uniform rectangular cantilever beam of size (20x20)x250 $um^3$and thickness of 100um. 2-device is a block which has dimension of (200x400)um^2 and thickness of 100um. 3-Modal 1,2,4&5 cause transverse bending at neck. 4- Modal 3 is compressive. 5- Modal 1 is the principal mode upon which primary design should be based.	(model) (modal 1) (modal 2) (modal 3) (modal 4) (modal 5)

Table 6.1-continued.

Model	Modal (Hz)	Notes	Models and modal shape
2	19450. 0.11683E+06 0.10786E+07 0.19777E+07 0.52975E+07	1-wedge cantilever beam: base width is 20um, neck width is 10um, length is 250um and thickness of 100um. 2-Device is a block which has dimension of (200x400)um^2 and thickness of 100um. 3-Modal 1,2,4&5 cause transverse bending at neck. 4- Modal 3 is compressive. 5- modal 1 is the principal mode upon which primary design should be based.	(model) (modal 1) (modal 2) (modal 4)
3	9937.5 57304. 0.51161E+06 0.78153E+06 0.13840E+07	1-wedge cantilever beam: base width is 20um, neck width is 10um, length is500um and thickness of 100um. 2-Device is a block which has dimension of (200x400)um^2 and thickness of 100um.	
4	9551.7 94374. 0.76489E+06 0.19753E+07 0.52952E+07	1-wedge cantilever beam: base width is 20um, neck width is 10um, length is250um and thickness of 100um. 2-Device is a block which has dimension of (400x400)um^2 and thickness of 100um.	
5	19297. 0.11473E+06 0.10769E+07 0.19736E+07 0.52871E+07	1-wedge cantilever beam: base width is 20um, neck width is 10um, length is250um and thickness of 100um. 2-Device is a block at angel of 114°,which has dimension: base of 200 um, height of 400um and thickness of 100um.	

The steady state stress response is simulated for a sinusoid displacement of 10um in amplitude. The models depicted in Table 6.1 are reconsidered in the harmonic analysis. The fixed anchor is replaced with a movable degree of freedom that represents the motion of a unit cell in the fabricated platform. The agitation signal is swept over a range of frequencies (5-25000 kHz) and the response is captured in LogLog plot shown in Figure (6.12). The following observations are drawn from results on the plot

Within the range of excitation, two modes are observed for model 1, 2, 4 & 5 which share the same tether length. However, model 3 which has double length exhibits doubled the total modals into four. Moreover, the longer the tether the more flexible it will become causing the device to resonate at lower frequencies. For example, the principal modal of model 3 is 40kHz and at 7.6Gpas. Meanwhile principal modal of model 2 occurs at 70kHz and at higher stress concentration of 128Gpas.

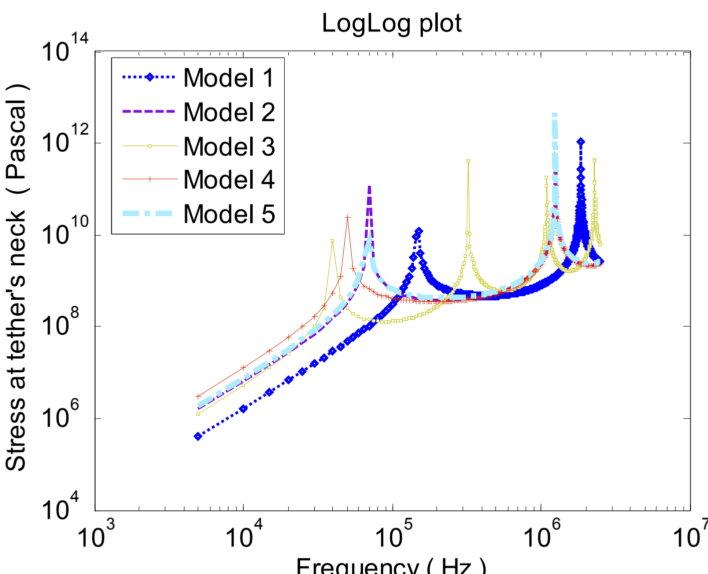

Figure 6.12 Harmonic response of Von Mises stress for neglected damping coefficients.

- Additional mass results in fracture at lower frequencies but without necessarily causing higher stresses, where the effect of inertia is clear for first principal mode and neglected for higher mode. For example, model 2 has inertia of 1.8398×10^{-7}N with the center of gravity laterally shifted from tether neck and with principal mode and maximum stress at (70kHz, 128GPas). Meanwhile model 4 has double the inertia but with first mode and maximum stress pair of (50kHz, 24GPas)
- The wedge cantilever beam introduces a neck at the device layer body which generally results in amplifying the stress consternation for the first mode set. This can be observed by comparing models 1 and 2 with frequency stress pairs of {(145kHz, 9.43GPas), (1855kHz, 1042GPas)} and {(70kHz, 128GPas), (1250kHz, 286GPas)} respectively.
- The notch angle caused by positioning the device relative to the tether neck axis does not change the mode frequencies but slightly changes the magnitude of maximum stress. A comparison between models 2 and 5 shows the following frequency stress pairs {(70kHz, 128GPas), (1250kHz, 286GPas)} and {(70kHz, 7.6GPas), (1245kHz, 4504GPas)} respectively.

The modal stresses of a complete structure are displayed for several frequencies and amplitudes and shown in Figure (6.13). In model 2, the stress concentration is close to the device body resulting in a fracture free from leftover tethers. However, model 1 shown in Figure (6.13) shows that the first principal stress concentration takes place at a

distance from the neck edge and thus the released body could include some portion of tether. Resonating at higher frequencies results in the different the beam will buckle, wherein the stress concentration will change accordingly as could be depicted from the first three modal of model 2, as show in Figure (6.13).

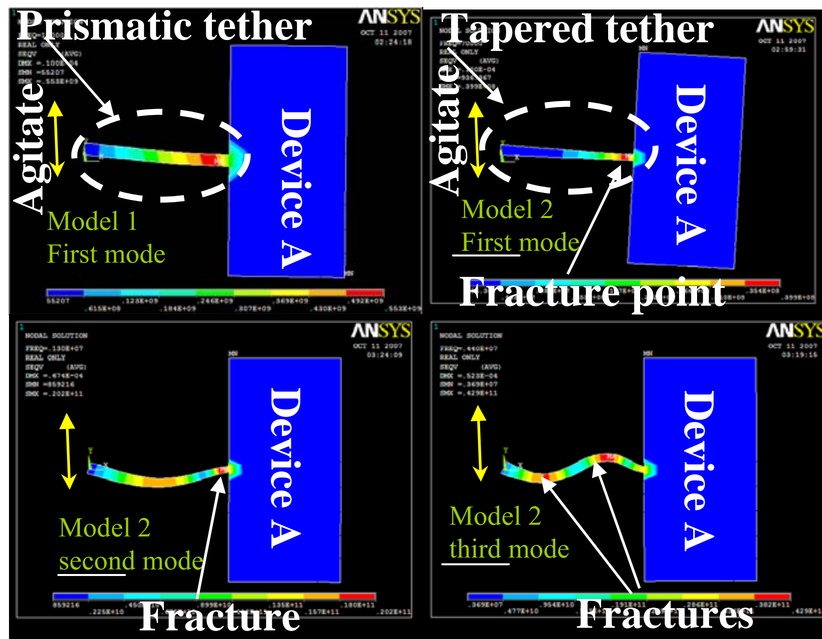

Figure 6.13 The stress harmonic response plotted for modals of model 1 and 2.

It is preferred that fracture takes place at first mode and always at the neck. However, at higher modes the location of maximum stress may result in fracture at intermediate locations on the tether. In the previous simulation, the damping was neglected assuming that material damping and air damping are insignificant. The effect of external viscous damping caused by air is studied and the harmonic frequency response of stress is plotted for several damping ratios as shown in Figure (6.14).

Damping assists in reducing the amplitude of maximum stress generated at the neck. Thus, it might be of an interest to perform the detethering process at certain viscous damping conditions which can be externally introduced to the agitated system. For example, MEMS detethering could be performed in vacuum in order to attain high amplitudes at resonance.

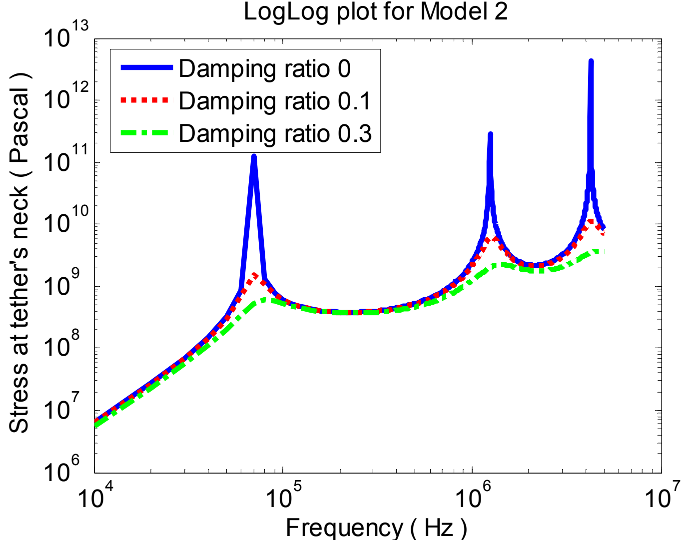

Figure 6.14 Harmonic response of model 2 at different damping ratios.

6.5.2.3 Monolithic Detethering Using Harmonic Analysis for Array of Complex Devices

The purpose of this simulation is to obtain a set of frequencies that selectively and monolithically detether devices. A microgripper is encapsulated in a unit cell of 1.25 x 1.75 mm^2 and anchored to the frame by a wedge cantilever beam as shown in Figure (6.15). The tether used in the array is same for model 2 as discussed in Table 6.1. The array of identical cells is arranged in one platform and then laterally excited by harmonic signals of fixed amplitude and varying frequency. The harmonic stress concentration at the neck is recorded and plotted for the various resonating frequencies.

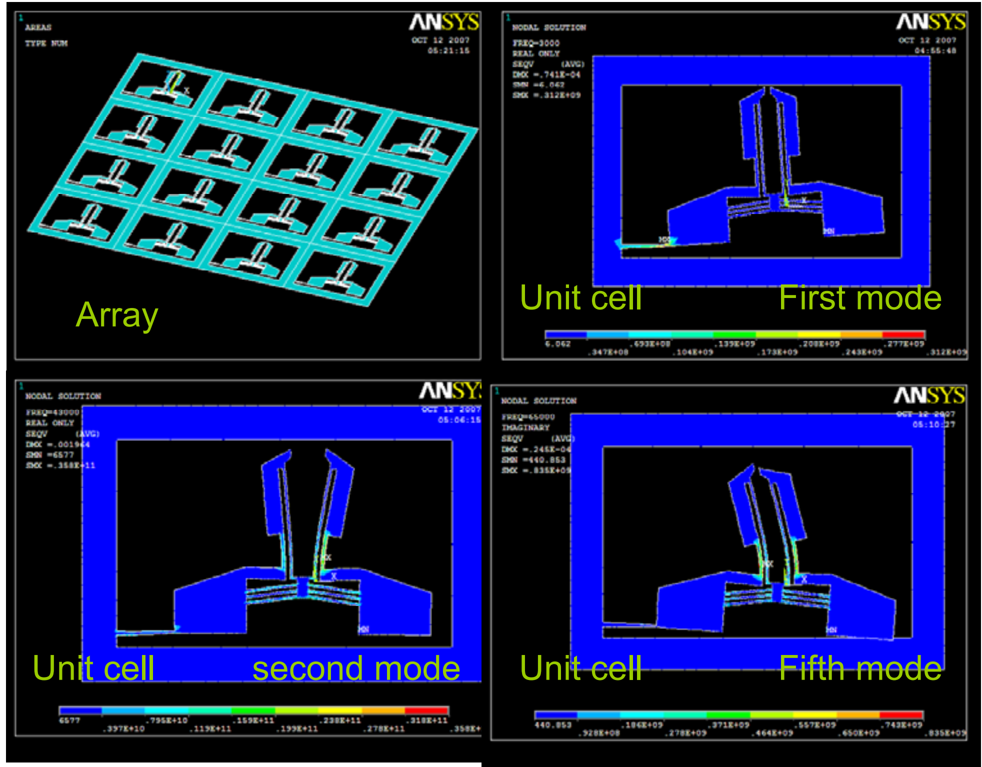

Figure 6.15 Harmonic Von Mises stresses at modal frequencies for agitated unit cells.

The FEM model and simulations in Figure 6.15 present the stress distribution (Von Mises) for a unit cell. The frequency plot of the unit cell is shown in Figure (6.17) for cells in group number (1) is shown in Figure (6.16). It is clear that the tether intensively resonates at different mode especially at high frequencies. For example, the first mode shown in Figure (6.13) has maximum stresses only at the tether neck but the stress distribution on the total device leaves it undamaged at that particular input frequency. However, the scenario changes for higher modes, for example at third and fifth modes where the agitations cause undesired stresses in the device which may result in structural or other damage to the device possibly rendering it unusable.

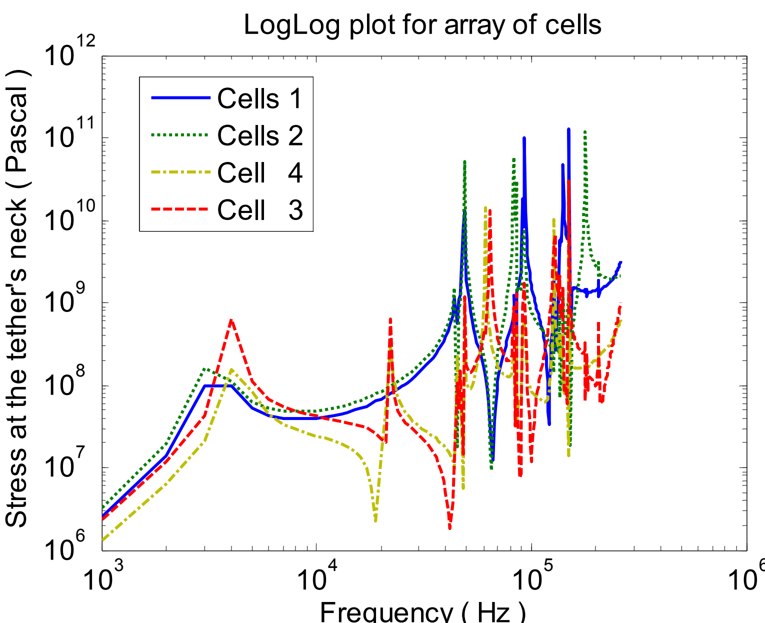

Figure 6.16 Harmonic responses of stresses measured at the tether neck for devices in figure 6.17.

6.5.2.4 Monolithic and Selective Detethering Using Harmonic Analysis for Array of Complex Devices

The selective detethering concept relies on modifying the structure of the tethers or their orientation with respect to the agitation axis. In Figure (6.17), the microgrippers are identical but tethered in four groups. Unit cells 1 has microgrippers tethered by a tether model 2 at 90° from side wall. Unit cells 2 encapsulate a microgripper with the tether attached at an angle with respect to the frame side wall. Cells 3 and 4 have longer tethers attached at two different angles as shown in Figure (6.17).

The harmonic responses of the stresses computed at the tether necks are plotted for a range of input frequencies and shown in Figure (6.16). The following are observed:

- In cells group 1, the direction of agitation is normal to the tether longitude where the tether in group 2 is at an angle relative to agitation

direction. Given the geometrical consideration of the device, the pattern of the harmonic response did not change but rather shifted in magnitude. The inertia transmitted to the center of gravity of the device has been amplified by the rotation. This verifies the ability of controlling the amount of transmitted load for given fixed agitation conditions.

- The same microgripper tethered by a longer wedge beam and anchored at different angle has multi modal frequencies and different pattern. A conclusion that supports the possibility of finding conditions at which selective detethering could take place for identical devices.

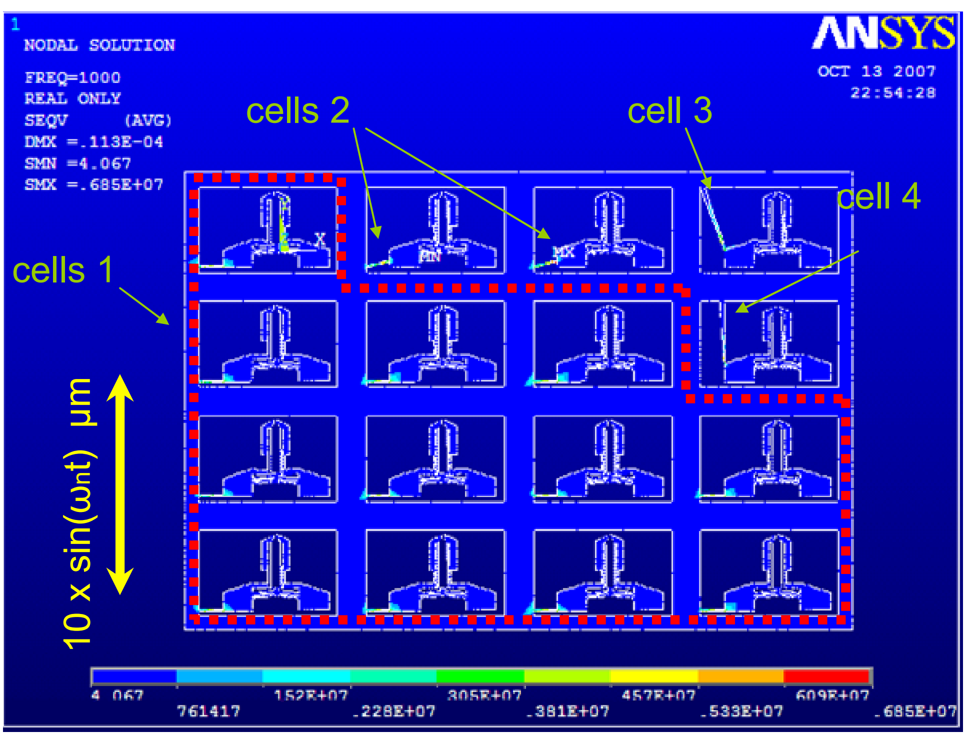

Figure 6.17 Array of identical devices anchored by different tethers.

6.5.3 *Mathematical Considerations for the Bending Vibration of Clamped-free Beams under Agitation*

It has been shown in [117] that the "*fundamental natural frequency of a discrete to continuous system is inversely proportional to the gravitational acceleration divided by maximum static deflection, raised to the ½ power*". Accordingly, it becomes easier to define the maximum stresses from the analytical natural frequencies of tethered devices. Therefore, obtaining the fundamental frequency equation of tethered devices could be sufficient to evaluate the maximum stresses generated at the anchor.

The structure of the tethers is not limited to but includes groups of cantilever beams with tip mass at free end such as linear breadth tapered cantilevers, prismatic cantilever beams, tapered cantilever beams of truncated wedges, tapered cantilever beams of truncated cone, doubly-tapered cantilever beams, and group of cantilever beams truncated at different shape-functions.

Depending on the unit cells fabricated platform, the effects of in and out of plane agitation directions should be studied for each tethered device. An example of clamped-free tethers is a uniform Prismatic Beam shown in Figure (6.18). The Bernoulli-Euler equation used to analyze the behavior of the beam considers a uniform cross-sectional beam under transverse vibration and neglects shear, bending, and rotational inertia. Under free transfer load at the device, the differential equation is given by [115, pp312]

$$EI\frac{\partial^4 v}{\partial z^4} + A\rho\frac{\partial^2 v}{\partial t^2} = 0 \tag{6.1}$$

The cantilever beam frequency is iteratively computed from $\cos(k_n l)\cosh(k_n l) = -1$ where $k_n^4 = \frac{\omega_n^2 \rho A}{EI}$. For the first few modes, the natural frequencies are obtained from $k_n l$ =[1.8751, 4.6941, 7.8548, 10.996].

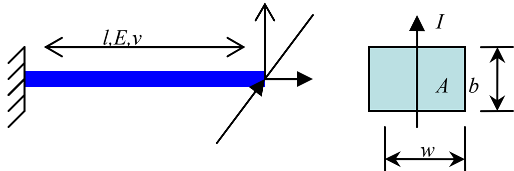

Figure 6.18 Uniform cross section cantilever beam without mass at the end.

It is necessary to study the in-plane vibration (in y-direction) as shown in Figure 6.19 of the beam which might be excited by random agitation. The natural frequency, given by $\omega_n = \frac{\lambda}{l^2}\sqrt{\frac{EI_o}{\rho A_o}}$, could be evaluated by Bernoulli-Euler theory, where I_o and A_o are the second moment of inertia and cross sectional area at the root. The exact values of the correction factor λ for the three lowest frequencies of vibration are [5.315, 15.202 and 30.09] [115, pp85].

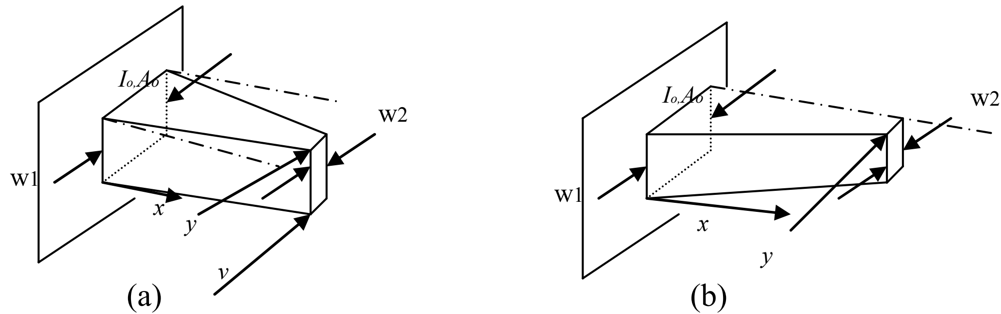

Figure 6.19 Schematic drawing of clamped free tethers (a) linear tapered beam (b) trapezoidal linear beam.

On the other hand, the exact analysis of beam differential equation in an agitated environment is modeled from the differential equation of vibration of fixed lateral beam of variable cross-section [115, 116]

$$\frac{\partial^2}{\boldsymbol{x}^2}\left\{\boldsymbol{EI}(\boldsymbol{x})\frac{\partial^2 \boldsymbol{v}}{\partial \boldsymbol{x}^2}\right\}+\boldsymbol{A}(\boldsymbol{x})\boldsymbol{\rho}\frac{\partial^2 \boldsymbol{v}}{\partial \boldsymbol{t}^2}=\boldsymbol{p}(\boldsymbol{x},\boldsymbol{t}) \tag{6.2}$$

where E is the homogenous modulus of elasticity with constant value, and $\boldsymbol{p}(\boldsymbol{x},\boldsymbol{t})$ and $\boldsymbol{\rho}$ are the load per unit length and density, respectively. For a linearly and symmetrical tapered beam of constant thickness h, the cross-sectional area and the cross sectional-moment of inertia with respect to neutral axis through the centroid of beam at location of point x are given by

$$A(x)=w_2h+\frac{(L-x)}{L}(w_1-w_2)h\,;\quad \boldsymbol{w}_1>\boldsymbol{w}_2$$

$$I(z)=\frac{h}{12}\left(w_2+\frac{(L-x)}{L}(w_1-w_2)\right)^3;\quad \boldsymbol{w}_1>\boldsymbol{w}_2 \tag{6.3}$$

where, width of cantilever beam at anchor and free end are $\boldsymbol{w}_1$ and $\boldsymbol{w}_2$, respectively, and h is the thickness of cantilever beam. A micro-part of point mass $\boldsymbol{m}_3$ is assumed to be acting at point p at the free end in free vibration conditions; i.e. $\boldsymbol{p}(\boldsymbol{x},\boldsymbol{t})=0$. The micro-part is rigidly connected to the free end of the elastic beam whose bending moment and shear force are assumed to be at point p

$$\frac{Ehw_2^3}{12}\left.\frac{\partial^3 v(x,t)}{\partial x^3}\right|_{x=L}-\left(\frac{Eh(w_1-w_2)w_2^2}{4L}\right)\left.\frac{\partial^2 v(x,t)}{\partial x^2}\right|_{x=L}=m_3\left.\frac{\partial^2 v(x,t)}{\partial t^2}\right|_{x=L};\quad \boldsymbol{w}_1>\boldsymbol{w}_2$$

$$\left.\frac{\partial^2 \boldsymbol{v}(\boldsymbol{x},\boldsymbol{t})}{\partial \boldsymbol{x}^2}\right|_{\boldsymbol{x}=\boldsymbol{L}}=0 \tag{6.4}$$

The beam support is fixed to the cell frame layer which is under agitation with displacement x_2. The effect of axial agitation along y-direction is neglected and the lateral component is only considered to be effective. The beam is initially resting and the remaining boundary and initial conditions are written with respect to coordinate y

$$\begin{gathered} v(0,t) = x_2(t)\cos(\phi) \\ \frac{\partial v}{\partial x}(0,t) = \frac{\partial x_2(t)}{\partial x}\sin(\phi) = 0 \\ \frac{\partial v}{\partial t}(x,0) = v(x,0) = 0 \end{gathered} \tag{6.5}$$

where ϕ is an adjustable angle portraying the angular measurement between the directional agitation x_e and support axis x'. On considering the governing partial equation with the variable cross-section, the equation is rewritten as

$$\left(w_2 + \frac{(L-x)}{L}(w_1 - w_2)\right)^2 \frac{\partial^4 v}{\partial x^4} + \frac{6(w_1 - w_2)^2}{L^2}\frac{\partial^2 v}{\partial x^2} + \frac{12\rho}{E}\frac{\partial^2 v}{\partial t^2} = 0 \ . \tag{6.6}$$

Upon imposing variable transformation of $\xi = w_2 + (L-x)(w_1 - w_2)/L$ and function transformation of $f(\xi,t) = v(\xi,t) - x_2(t)\cos(\phi)$, the general equation becomes

$$a_0\xi^2 \frac{\partial^4 f}{\partial \xi^4} + 6a_0\frac{\partial^2 f}{\partial \xi^2} + \frac{\partial^2 f}{\partial t^2} = -\cos\phi\frac{d^2 x_2}{dt^2}; \quad a_0 = \frac{E(w_1 - w_2)^4}{12\rho L^4}, \quad w_1 > w_2 \tag{6.7}$$

The initial and boundary conditions are then transformed into

$$\begin{gathered} \partial f/\partial t(\xi,0) = \cos\phi dx_2/dt(t=0) = 0 \qquad f(\xi,0) = \cos\phi x_2(t=0) = 0 \\ f(\xi = w_1,t) = 0\,,\ \partial f/\partial z(\xi = w_1,t) = 0 \qquad \partial^2 f/\partial \xi^2(\xi = w_2,t) = 0 \\ w_2 a_1 \frac{\partial^3 f(\xi = w_2,t)}{\partial \xi^3} + 3a_1\frac{\partial^2 f(\xi = w_2,t)}{\partial \xi^2} + \frac{\partial^2 f(\xi = w_2,t)}{\partial t^2} = -\cos\phi\frac{dx_2^2}{dt^2}; \\ a_1 = \frac{Ehw_2^2(w_1 - w_2)^3}{12m_3L^3} \end{gathered} \tag{6.8}$$

The agitation function x_2 is piecewise differentiable function of at least of order two. This signal is approximately obtained by solving the structural dynamic of the lumped system illustrated in Figure (6.5). Then, the system solution is imposed on the exact cell-subsystem analysis which is described by the general nonlinear P.D.E of mixed conditions in equation (6.8). Before analytically solving the general equation, lumped system and approximate cell-subsystem dynamics must be derived as shown in the next section.

6.5.4 Lumped Modeling of Vibrating Cells in a Vibratory System

The structural model of the total setup can be represented by a system of spring mass and dampers under base excitation x_e. The transmitted effective agitating signal x_2 is exciting the unit cell which encapsulates the hanging microstructure. Upon writing the three ordinary differential equations of the system dynamics, x_1, x_2 and x_3 are written as functions of the total system parameters and base excitation

$$X_1(s) = \frac{-(AD-BC)G}{\Delta(s)} X_e(s),\ X_2(s) = \frac{AEG}{\Delta(s)} X_e(s), \qquad X_3(s) = \frac{-BEG}{\Delta(s)} X_e(s),$$
$$\Delta(s) = CBF + AE^2 - ADF \tag{6.9}$$

where

$$\begin{aligned} &A=m_3s^2+b_3s+k_3 \quad B=-(b_3s+k_3) \quad C=-(b_3s+k_3) \quad D=m_2s^2+(b_2+b_3)s+k_2+k_3; \\ &E=-(k_2+b_2s) \quad F=m_1s^2+(b_1+b_2)s+k_1+k_2 \quad G=b_1s+k_1 \end{aligned} \tag{6.10}$$

Depending on the cantilever beam shape, the equivalent spring constant could be found for different tether shapes. For example, using Bernoulli equation for a uniform cross sectional beam and constant width under a point load at the free end yields an

approximate stiffness of $k_3 = 3Ew^3h/(4L^3)$ [115, 117]. On the other hand, the stiffness of a linearly tapered beam shown in Figure (6.19), can be approximated from bending energy of bending moment M caused by a virtual load Q at the free end with corresponding deflection δ. The stiffness is given by

$$k_3 \approx \frac{Q}{\delta} = \frac{Q}{\int_0^L \frac{M\partial M/Q}{EI(x)}dx} = \frac{Ehw_2^2\left(w_1^3 - w_2^3 - 3w_1^2w_2 + 3w_2^2w_1\right)}{L^3\left(w_1^2 - 4w_1w_2 + 3w_2^2 - 2w_2^2\log(-w_2L) + 2w_2^2\log(-w_1L)\right)} \quad . (6.11)$$

The deflection of the device in a lumped system is obtained from derived expressions in equation (6.10). Several test models are developed to evaluate the deflection of the device relative to the overall changes in the system parameters and shown in Table 6.2. The illustrated examples are depicted for a linearly tapered beam with spring constant given in (6.11). The models are harmonically excited by *A x sin(wt)*. The important conclusion that can be drawn from simulation in Figure (6.20) is the sensitivity of system to parameter changes. The basic fracture condition of a fabricated platform is fixed for the tethered devices if their ambient/packaged viscous-effect is controlled. But, the change of fixture damping and spring constants alter the harmonic excitation at the tether anchor and thus result in undesired fracture conditions. Thus, it is important for the designer to be aware of the possible changes in the agitation system parameters. It is preferred to have a rigidly assembled agitation system to prevent any undesirable effects on the agitation system performance due to system assembly.

Table 6.2 Test lumped models for tethered devices in vibratory agitation system.

Simulated Model	Parameters	Notes
S1	L=500um, w1=w2=20um, m1=3.895e-4, M2=0.0029, m3=1.8398e-8, b1=b2.125, b3=19e-9, k1=k2=1e9, k3=270N/m^3	Uniform cross section, tether spring constant is calculated from equation. Rigid plate and wafer.
S2	L=500um, w1=20um, w2=10um, m1=3.895e-4, M2=0.0029, m3=1.8398e-8, b1=b2.125, b3=19e-9, k1=k2=1e9, k3=58 N/m^3	Linearly tapered, tether spring constant is calculated from equation
S3	L=500um, w1=20um, w2=10um, m1=3.895e-4, M2=0.0029, m3= 3.6796e-8, b1=b2.125, b3=19e-9, k1=k2=1e9, k3=58 N/m^3	Linearly tapered, double device mass.
S4	L=500um, w1=20um,w2=10um,m1=3.895e-4, M2=0.0029, m3=1.8398e-8, b1=b2=0, b3=0, k1=k2=1e7, k3=58 N/m^3	Linearly tapered, neglected apparatus damping, vacuum agitation, but apparatus are stiff.
S5	L=500um, w1=20um,w2=10um,m1=3.895e-4, M2=0.0029, m3=1.8398e-8, b1=b2=0, b3=.4, k1=k2=1e9, k3=58 N/m^3	Linearly tapered, neglected apparatus damping, viscous agitation, but apparatus are rigid.

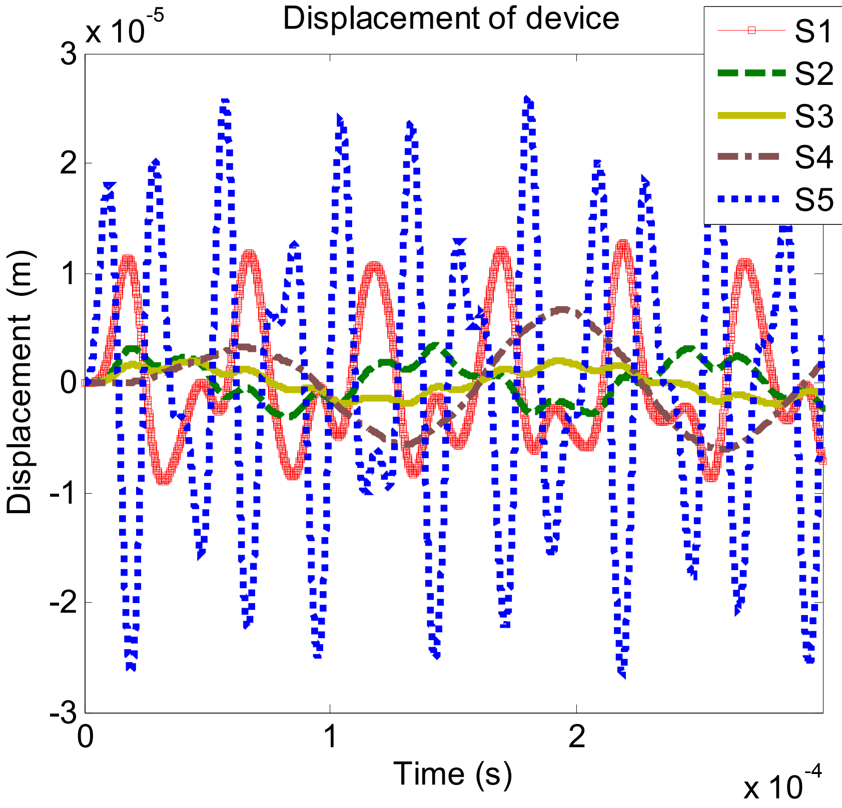

Figure 6.20 Time response analysis of device displacement for a lumped model. A=10micron and *w*=40kHz and the device deflection is simulated for realistic system values.

6.6 Chapter Conclusions

Alternative methods for releasing MEMS and semiconductor parts were developed with the focus of selectively increasing the yield process. The methods have been analyzed and experimentally verified employing fabricated MEMS parts, where large quantity of Meso to Micro blocks were detethered and then introduced in selfassembly of Micro robotic system. The selective and parallel releasing methodology was also validated using finite element methods to perform harmonic analysis and identify the fracture stresses of the tethered devices. Specifically, a fracture signature could be uniquely defined for cantilever designs that have maximum stresses at the device attachment location.

The importance of the detethering methodologies over current technologies could be summarized as follows

- Programmability as the tether design is invertible, identifiable and controllable.
- Simplicity in its implementation and apriori design considerations.
- Flexibility as it can be implemented for different applications.
- Clean since it does not require lubrication and does not induce heat or particles.
- Accuracy in releasing selectively and at sub-micron resolution.
- Scalability as it can be approached at wafer level, die level, and device level.
- Cost efficiency since the required apparatus are of low cost.
- Time efficiency for simultaneous massive release.

CHAPTER 7

CONCLUSIONS AND FUTURE WORK

7.1 Dissertation Summary and Conclusions

In this dissertation, interdisciplinary studies on the multi-scale manipulation and actuation techniques identified explored new methodologies on the microassembly world. The scaling effect has been utilized to enhance the capabilities of serial and parallel assembly tasks. The thermal behavior was utilized – efficiently to construct active devices capable of performing the basic tasks required for serial assembly. Additional capabilities were introduced and illustrated by integrating sensing and heat sources, in multipurpose electrothermoelastic microgrippers (METEG) and also externally introduced configuring a 3D assembly station with compressive force sensor and hotplate. The performance of METEG was better understood through modeling, simulation and identification experiments leading to the introduction of new platforms for experimental identification, numerical techniques and analytical methodologies. These techniques are used to plan the structural and thermal behaviors according to the assembly requirements. It was concluded that the METEG structures comply a range of satisfactory response enabling them to have fast charge and discharge thermal cycle, to identify the thermal and structural failure zones, to provide large deflections and large forces to meet assembly requirements.

The methods followed in the dissertation initiated and explored new research activities on parallel assembly through self-assembly assisted by DNA recognition concept. Wherein, methods of constructing micro-robotic systems were researched according to the following four principles. First, designed building blocks which are uniquely or deterministically interface during the assembly processes. Second, introduced and researched an enabling technology which introduces a large number of parts that are selectively released to an assembly platform. Third, introduced enabling methods for stochastic assembly driven by actively excited surfaces. Fourth, investigated possible actuation techniques. Several concepts were analyzed including possibility of constructing 2½D robots from configured micro-to meso scale blocks; active surfaces can deterministically mobilize substructures through agitation of surfaces with traction squeeze field topography; and methods for releasing micro and meso scale parts from their fabricated layers. Contributions of the dissertation are summarized in the following:

- Developed Novel End-effectors with compliant structures for deterministic microassembly work-cells:
    - Pick and place of heterogeneous micro-part.
    - Active and Passive assembly modes.
    - Joule heating generates uniform pressure and reduction of adhesive forces.
    - Sensory feedback for control.
    - Demonstrated serial to hybrid microassembly.

- Developed Analytical Models and Numerical Synthesis for performance analysis of METEG MEMS devices:
  - Steady state temperature distribution of METEG components.
  - Comprehensive analysis of Microgripper "combined structures in METEG".
  - Analogous Multiphysics modeling techniques of METEG.
  - Thermal Cycle responses.

- Developed Concepts for Micro Self-assembly and manipulation strategies inspired by DNA recognition and assisted by active surface manipulation.
- Developed mathematical concepts based on energy cost functions for micro-distributed manipulation system (μDMS).

- Experimental methodologies:
  - Identified the static and dynamical performance of the elastic and the electrothernoelastic METEG MEMS devices.
  - Investigated techniques for packaging and attaching the released electrothernoelastic MEMS devices.
  - Demonstrated selective detethering technique for micro to meso scale MEMS parts on die and wafer levels.
  - Introduced self-assembly mechanism in dry and wet agitation.

7.2 Future Work

Throughout the dissertation research, several novel concepts were developed. The majority of the research findings were verified and demonstrated through experimental and numerical simulation. Nevertheless, the amount of knowledge for the explored research could be further extended. Based on the material presented in this dissertation, the following are recommendations for continued and future research:

- Analyze the nonlinear mechanical static response of gripper thermal actuator by deriving equations for: force and moment equilibrium, nonlinear large displacement and strain of structures, geometrical and boundary conditions and numerical solution for the set of the obtained nonlinear equations.
- Continue the investigation on Bio-Micropump (BMP), particularly develop simplified mathematical models for fluid and structural coupling.
- Continue the investigation on the translocation and actuation of Micro devices through bio-on-board-power-supply. Particular studies should explore utilizing the bacteria to actuate and control the mobility of micro- and Nano-structures.
- Continue research to improve implement and experimentally verify the newly developed concept of Micro-distributed manipulation System.

- New emerging science and engineering paradigms can be investigated and developed based on the presented research. For example, the inverse design of mechanical signatures of vibrating cantilever such that the natural or forced agitations are utilized to maximize failures at desired region.

APPENDIX A

MICROPHYSICS AT MICROSCALE

A.1 Van der Waals (Atomic) Forces

It is the force acting between atoms generated by instantaneous polarization of atoms and molecules due to quantum mechanical effects such as orientation effect, excitation effect and dispersion effect [35,39]. Dispersion effect is dominant and the generated forces are called London forces. This Van der Waals force is generally attractive in nature but decays rapidly to zero away from a surface. The origin of the London Van der Waals force lies in the instantaneous dipole generated by the fluctuation of electron cloud surrounding the nucleus of electrically neutral atoms. The forces between macroscopic object can be derived from the interaction forces between two particles provided the three following hypothesis [39]: additives, uniform material properties and continues medium. These assumptions gives the total macroscopic van der Waals forces, F_{VDW} , between two macroscopic bodies

$$F_{VDW} = -\rho_1 \rho_2 \int_{V_1} \int_{V_1} \nabla w dV_1 dV_2 \tag{A-1}$$

The negative sign emphasize the fact that the force is attractive. The notations ρ_i and V_i represent the number of particles per unit volume and the volume of each body (i=1, 2), respectively. Here, the total force is the gradient of the interaction potential w is a function of separation ,d , between the object's particles and is given by [39]

$$w(d) = \frac{C}{d^6} \tag{A-2}$$

where C is a material dependent interaction constant which relates to bodies materials and the medium which separate them. This constant relates to Hamaker constant H by the following approximation [37,39]

$$H = \pi^2 C \rho_1 \rho_2 . \tag{A-3}$$

The volumetric integration does not have an analytical solution, except in a few special cases. Therefore, in most cases the integrals have to be approximated using numerical methods and complexity reduction methods as in using divergence theorem to perform surface integral instead of volumetric integration [39].

The total force of van der Waals interactive energy for two flat surfaces can analytically be obtained as follows

$$\frac{F_{VDW}}{A} = \frac{H_{123}}{6\pi d^3} \tag{A-4}$$

where, A & d are the planar surface area and the separation distance, respectively. H_{123} is the Hamaker constant for substance "1" and "2" in the presence of medium "3". For cylinder-planner surface contacts, the Van der Waal force is given by

$$\frac{F_{VDW}}{l} = \frac{H_{123} R^{1/2}}{16\sqrt{2} d^{5/2}} \tag{A-5}$$

where, l & d are the length and diameter of the cylindrical part, respectively.

For two microscopic spherical particle of radii R_1 and R_2, the non retarded interaction force is given by[36]

$$F_{VDW} = \frac{HCR_1R_2}{3} \left[\frac{8R_1^2R_2^2 - \left[C^2 - (R_1 - R_2)^2\right]\left[C^2 - (R_1 + R_2)^2\right]}{\left[C^2 - (R_1 - R_2)^2\right]^2 \left[C^2 - (R_1 + R_2)^2\right]^2} \right] \tag{A-6}$$

where C is the distance between centers, and the Hamaker constant is rewritten as $H = \pi^2 n^2 \lambda$ (where n is the number of atoms per cm^3). λ is the London-Van der Waals constant. Note that we van obtain from (A-6) the non retarded force between a sphere of radius R and an infinite half space separated by a distance d of a near a flat surface is[35]

$$F_{VDW} = \frac{H}{6}\left[\frac{R}{d^2} + \frac{d}{2(d+2R)^2} - \frac{1}{d} + \mathbf{ln}\frac{1}{d+2R}\right] \overset{(d<<R)}{\approx} \frac{RH}{6d^2} \qquad \text{(A-7)}$$

When the plane-surface has a roughness of b, the van der Waals force between sphere and a rough plane is reduced [38] according to

$$F_{VDW} = \left(\frac{d}{d + b/2}\right)^2 F_{VDW} \qquad \text{(A-8)}$$

The directional interactive forces occur between a sphere of radius a R_1 and rectangular block of dimensions (a,b,c) corresponding the Cartesian coordinate (x,y,z), respectively. Let the nominal separation between the two particles be (x_o, y_o, z_o) then forces are given by [36]

$$(F_l)_{VDW} = \int_{z_o-c/2}^{z_o+c/2}\int_{y_o-b/2}^{y_o+b/2}\int_{x_o-a/2}^{x_o+a/2} \frac{n^2\pi\lambda}{4R^3}\left[\frac{2RR_1}{(R+R_1)^4} + \frac{2RR_1}{(R-R_1)^4} + \frac{1}{(R+R_1)^2} - \frac{1}{(R-R_1)^2}\right] l dx dy dz$$

(A-9)

where, l is the coordinate (x or y or z) and $R = \sqrt{x^2 + y^2 + z^2}$. This force is computed under the assumption that the sphere center passes the block center and bisects its faces into equal halves. This force drops to its minimum as the block surfaces at a corner

make 45° with a tangential surface at the sphere. Where is can be easily found that the force between a sphere and an infinite half space is larger than sphere and a block and their magnitude becomes approximately equal when the separation distance is very close. The expressions describing Van der Waal force can be optimized such that either maximized or minimized during assembly process. For example one method to reduce the Van der Waals includes coating the surface with metal.

A.2 Surface Tension and Capillary Forces

The tangential stresses in the surface layer of liquid is known as the surface tension which analogously defined by stress in elasticity [43]. This stress must be balanced either by external forces or volumes stresses in the body.

Key issues in surface tension self assembly rely on first, on the geometry design of the binding site which control the hydrocarbon shape and the corresponding configuration at which global minimum energy is held [41]. And thus, providing unique alignment and orientation. Calculating the surface energy E between two surfaces S & P is obtained by the first order approximation model which is based on the linear relationship between the interfacial energy and the interfacial areas [41]. The energy can be computed by

$$E = \sigma\left(|S| + |P| - 2|S \cap P|\right) \tag{A-10}$$

where $|S|$, $|P|$ and $|S \cap P|$ denotes the substrate and part binding site and their overlap area, respectively. σ is the lubricant-aqueous interfacial tension.

A.3 Coulomb Forces or Charge-Charge Interactions

The inverse-square Coulomb force between charged atoms, ion or micro-parts is one of the strongest physical forces and even stronger than most of chemical bonding [37]. The Coulomb force interaction, F_{ES}, between two charges Q_1 and Q_2 is derived from free energy, $w(r)$, is

$$F_{ES} = -\frac{dw(r)}{dr} = -\frac{d}{dr}\left(\frac{Q_1 Q_2}{4\pi\varepsilon_o \varepsilon r}\right) = \frac{Q_1 Q_2}{4\pi\varepsilon_o \varepsilon r^2} \quad \text{(A-11)}$$

where r, ε_o and ε are the particle radius, dielectric permittivity of free space (8.854×10^{-12} Js) and dielectric permittivity of medium, respectively. The electrostatic force acting on a charge Q_1 at a distance *r* can also be expressed from electric field, E_1 *(Vm^{-1})*

$$F_{ES} = E_1 Q_2 = \frac{Q_1}{4\pi\varepsilon_o \varepsilon r^2} Q_2 \quad \text{(A-12)}$$

It is easy to show that the Coulomb force on a charge *e,* near a spherical structure (spherical micro-part) containing net charge *Q* uniformly distributed on is same as a point charge *Q.*

Electrostatic force can occur between a charges sphere of radius R_1 and uncharged conductive sphere of radius R_2 is given by [38]

$$F_{ES} = \frac{\pi(\varepsilon_m - \varepsilon_o)}{4\varepsilon_o(\varepsilon_m + \varepsilon_o)}\left(\frac{2R_1R_2}{R_1 + R_2}\right)^2 \sigma^2 \quad \text{(A-13)}$$

Where σ and ε_m are the electric charge density of surface and medium permeability, respectively. The electrostatic force between a conductive plate and a charged sphere is obtained by setting $R_2 \to \infty$,

$$F_{ES} = \frac{\pi R_1^2 \sigma^2}{\varepsilon_o} \tag{A-14}$$

In many situations, it is desired to eliminate the static charged. Methods of elimination includes first, voltage impress which is generated by high voltage increase at electrodes. Second, self-discharge type charge elimination. Third, generating of ions by radiation ionization. Fourth, choosing medium of high dielectric constant, $\varepsilon_r = \varepsilon / \varepsilon_o$, such as water which has ε_r =80.

A.4 Pull-off Forces

The deformation between two micro objects depends on the surface free energy of adhesion (contacted surface). The resulted force represents the necessary force to detach both objects [40]. Surface energy is defined by the work necessary to form unit area of surface by processes of division. For one component liquid, the surface energy is equal to surface tension.

In solid or crystals, both surface tension and surface energy are not equal but related [43]. The combined surface energy, W_{123} ,of solid objects 1, 2 and the medium 3 can be estimated from interfacial energy, γ ,of materials [38]. The attractive force between two rigid macroscopic spheres of radii R_1 and R_2 is a result of Derjaguin approximation [37]

$$F_{st} = 2\pi W_{132} \frac{R_1 R_2}{R_1 + R_2} \quad \text{(A-15)}$$

Where W_{123} is estimated by [40]

$$W_{123} \simeq 2\left(\gamma_3 + \sqrt{\gamma_1\gamma_2} - \sqrt{\gamma_1\gamma_3} - \sqrt{\gamma_2\gamma_3}\right). \quad \text{(A-16)}$$

For example, in case of silicon contact ($\gamma = 1400\, m.J.m^{-1}$), the surface energies in water ($\gamma = 72\, m.J.m^{-1}$) and air ($\gamma \sim 0\, m.J.m^{-1}$) are $2800\, m.J.m^{-1}$ and $1670\, m.J.m^{-1}$, respectively.

The pull-off force, F_p, of elastic spherical objects 1 and 2 of radii in medium -3- was obtained by "JKR" theory [37]. Special cases include: first, two identical spheres of radius R in liquid has adhesion force of $F_{st} = 2\pi R\gamma_{SL}$, second, two identical spheres in vacuum $F_{st} = 2\pi R\gamma_S$, third, sphere on flat surface in vacuum $F_{st} = 4\pi R\gamma_S$,and fourth, sphere on flat surface in vapor $F_{st} = 4\pi R\gamma_{SV}$.

REFERENCES

[1] G. D. Skidmore, E. Parker, M. Ellis, N. Sarkar, and R. Merkle, "Exponential Assembly," *Nanotechnology*, 12, pp. 316-321, 2001.

[2] J. Reiter, M. Terry, K. F. Böhringer, J. W. Suh, and G. T. A. Kovacs, "Thermo-bimorph Microcilia Arrays for Small Spacecraft Docking," *ASME Int'l Mechanical Eng. Congress and Expo.,* pp. 57-63, 2000.

[3] K. F. Böhringer, V. Bhatt, and K. Goldberg, "Sensorless Manipulation Using Transverse Vibrations of a Plate," *IEEE Int'l Conf. on Robotics and Automation*, pp. 1989-1996, May 1995.

[4] S. E. Lyshevski, *MEMS AND NEMS, Systems, Devices, and Structures*, 1st Ed., CRC PRESS, 2002.

[5] K. F. Böhringer, "Surface Modification and Modulation in Microstructures: Controlling Protein Adsorption, Monolayer Desorption, and Micro-Self-Assembly," *Journal of Micromechanics and Microengineering,* Vol.13, pp. 1971-1988, July 2003.

[6] J. T. Feddema, A. J. Ogden, L. K. Warne, W. A. Johnson, D. Armour, "Electrostatic/electromagnetic gripper for micro-assembly," *World Automation congress, Proc. of the 5th biannual*, pp. 268-274, 2000.

[7] P. Lambert, P. Letier, and A. Delchambre, "Capillary and surface tension forces in the manipulation of small parts," *Proc. of the 5th IEEE int'l Sympo. on assembly and task planning*, pp. 54-59, 2003.

[8] J. T. Feddema, Patrick Xavier, Russell Brown, "Micro-Assembly Planning with van der Waals Force," *International symposium on assembly and task planning*, porto, Portugal, pp. 32-38, July 1999.

[9] F. Arai, D. Andou, T. Fukuda, "Adhesion forces reduction for micro manipulation based on micro physics," *Proceeding of IEEE, Tech. Dig. Pf MEMS '96 workshop.* 354-359, 1996.

[10] M. Gauthier, B. Lopez-Walle, C. Clevy, "Comparison between micro-objects manipulations in dry and liquid mediums," *Proceedings 2005 IEEE International Symposium on Computational Intelligence in Robotics and Automation*,`pp.701-7012 June 27-30, 2005.

[11] P.J Swanson, R. R Burridge, D.E Koditschek, "Global asymptotic stability of a passive juggler: parts feeding strategy," *Proc. 1995 IEEE Int. Conf. on Robotics and Automation* ," pp.1314-1318.

[12] Y. Aiyama, T. Arai, "Dexterous manipulation with general manipulation methodology," *Intelligent Robots and Systems '96, IROS 96, Proceedings of the 1996 IEEE/RSJ International Conference on*, pp. 905 – 910, 1996.

[13] Allegro, S., *Automatic Microassembly by Mean of Visually Guided Micromanipulation*, PhD Thesis, EPFL, Lausanne, 1998.

[14] M. Erdmann, M. T. Mason. "An exploration of sensorless manipulation. In *Proc. IEEE International Conference on Robotics and Automation,"* pp.1569-1574, San Francisco, CA, Apr. 1986.

[15] Y. Hatamura, H. Morishita, " Direct Coupling System Between Nanometer World and Human World," *Micro Electro Mechanical Systems*, IEEE, pp. 203-208, 1990.

[16] M. Mitsuishi, K. Kobyashi, T. Nago, Y. Hatamura , T. Sato, B. Kramer, " Development of Tele-Operated Micro-Handling/Machining System Based on Information Transformation," *Proc. 1993 IEEE/RSJ Int. Conf. on Intelligent Robots and Systems*, pp. 1473-1478,1993.

[17] A. Codourey, M. Rodriguez, I. Pappas, " Human Machine Interaction for Manipulation in the Microworld," *Proc. 15th IEEE International Workshop on Robot and Human Communication*, Tsukuba, Japan, Nov. 11-14, 1996.

[18] A. Sulzmann, J. M. Breguet, J. Jacot, " Micromotor Assembly using High Accurate optical Vision Feedback for Microrobot Realtive 3D displacement in Submicron Range," *Proc. 1997 Int. Conf. On Solid-State Sensors and Actuators (Transducers 97)* , pp. 279-282, 1997.

[19] T. Sato, T. Kameya , H. Miyazaki, Y. Hatamura, " Hand-eye System in the Nano Manipulation World," *Proc. 1995 IEEE int. Conf. on Robotics and Automation*, pp. 59-66,1995.

[20] K. Koyano, T. Sato, "Micro object handling System with Concentrated visual Field and New handling Skills," *Proc. IEEE Int. Conf. on Robotics and Automation*, pp. 2541-2548, 1996.

[21] J. Y. Feddema, R. W. Simon, "CAD-Driven Microassembly and Visual Servoing," *Proc. 1998 IEEE Int. Conf. on Robotics and Automation*, pp. 1212-1219, Belguim, May 16-21, 1998.

[22] M. T. Mason, "Automatic planning of fine-motions: Correctness and completeness," in *Proc. 1984 IEEE Int. Conf. on Robotics and Automation*. pp. 492-503. Atlanta, GA, Mar., 1984.

[23] K. F. Böhringer, V. Bhatt, and K. Goldberg, "Sensorless Manipulation Using Transverse Vibrations of a Plate," *IEEE International Conference on Robotics and Automation (ICRA)*, vol. 2, pp. 1989-1986, Nagoya, Japan, May 21-27, 1995.

[24] K. F. Böhringer, B. R. Donald, R. Mihailovich, and N. C. MacDonald, "Sensorless Manipulation Using Massively Parallel Microfabricated Actuator Arrays," *IEEE International Conference on Robotics and Automation (ICRA)*, vol. 1, pp. 826-833, San Diego, CA, May 8-13, 1994.

[25] J. E. Luntz, W. Messner and H. Choset, "Closed-Loop Operation of Actuator Arrays," Proc. of 2000 IEEE International Conference on Robotics & Automation. pp 3666 – 3672, 2000.

[26] J.E. Luntz, W. Messner, and H. Choset, "Discrete actuator array vectorfield design for distributed manipulation," *Proc. of the 1999 IEEE International Conference on Robotics & Automation*, pp.2235 – 2241, 1999

[27] H. Moon, J.E. Luntz, “Manipulating a flat object against stationary barrier using airflows,” *Proc. of the 2006 IEEE International Conference on Robotics and Automation*, pp. 1737–1742, 2006.

[28] S. Konishi and H. Fujita, “A Conveyance the Concept of System Using Air Flow Based on Distributed Micro Motion Systems,” *JMEMS*, V. 3, pp. 54-58, 1994.

[29] A. Huang, et. al., “Application of MEMS Devices to Delta Wing Aircraft: From Concept Development to Transonic Flight Test,” *AIAA,* 2001.

[30] K. Pister, R. Fearing, and R. Howe, “A planar air levitated electrostatic actuator system,” in *Proc.* of *the IEEE Microelectromech. Syst.,* Napa Valley, CA, Feb. 1990, pp. 67-71.

[31] K. F. Böhringer, “Surface Modification and Modulation in Microstructures: Controlling Protein Adsorption, Monolayer Desorption, and Micro-Self-Assembly,” *IOP Journal of Micromechanics and Microengineering* 13(4), July 2003.

[32] B. Randall Donald, K. M. Lynch and D. Rus, (2001) Algorithmic and Computational Robotics: New Directions, A K Peters, Ltd.

[33] T. Sato, K. Koyano, M. Nakao, Y. Hatamura, “Novel Manipulator for Micro Object Handling Interface Between Micro and Human Worlds,” *Proc. Of 1993 IEEE/RSJ int. Conf. on intelligent Robots and Systems*, pp. 1674-1680, 1993.

[34] S. Allegro, *Automatic Microassembly by Mean of Visually Guided Micromanipulation*, PhD Thesis, EPFL, Lausanne, 1998.

[35] S. Johansson, “Technology for Microassembling,” *Proc. 1997 Materials for Mechanical Optical Microsystems Symposium*, pp. 3-13, 1997.

[36] A. Mensuishi, M. Carroza, C. Ristori, G. Tiezzi, and P. Dario, "A workstation for Manipulation of Micron sized objects," *Proc. 8th int. Conf. on Advanced Robotics*, pp. 253—258, 1997.

[37] J.Y. Feddema, P. Xavier, R. Brown, "Micro-Assembly Planning With Van der Waals Force," *Proc. Of 1999 IEEE international Symposium on Assembly and Task Planning (ISATP'99)*. pp. 32-38, 1999.

[38] M. B. Cohn, K.-F. Bohringer , J. M. Novorolski, A. Singh, , Keller, C. G. K. Y. Goldberg, R. T. Howe, " Microassembly technologies for MEMS," *SPIE Micromachining and Microfabrication,"* Sept. 1998.

[39] F. Arai and T. Fukuda, "A new pick up and release method by heating for micromanipulation," *Proc. of IEEE tenth annual international workshop on MEMS '97*, pp. 383-388, 1997.

[40] J. T. Feddema, A. J. Ogden, L. K. Warne, W. A. Johnson, D. Armour, "Electrostatic/electromagnetic gripper for micro-assembly," *World Automation congress, Proc. of the 5th biannual*, pp. 268-274, 2000.

[41] W. Riethmuller and W. Benecke, "Thermally excited silicon microactuators," *IEEE Trans. on Electron Devices*, Vol. 35, Issue 6, pp.758–763, June 1988.

[42] P. lambert, P. Letier, and A. Delchambre, "Capillary and surface tension forces in the manipulation of small parts," *Proc. of the 5th IEEE int'l Sympo. on assembly and task planning*, pp. 54-59, 2003.

[43] Y. Zhou and B. J. Nelson, "The Effect of Material Properties and gripping forces on micrograsping," *Proc. of IEEE int'l conf. on robotics and automation*. pp. 1115-1120, 2000.

[44] S. E. Lyshevski, (2002) *MEMS AND NEMS, Systems, Devices, and Structures*, 1st Ed., CRC PRESS.

[45] J. T. Butler, V.M. Bright, and W. D. Cowan, "Average power control and positioning of polysilicon thermal actuators," *Sensors and Actuators*, Vol. 72, pp. 88–97, 1999.

[46] A. A. Geisberger, N. Sarkar, M. Ellis, and G. D. Skidmore, "Electrothermal properties and modeling of polysilicon microthermal actuators," *J. of Microelectromechanical Systems*, Vol. 12(4), pp. 513–523, 2003.

[47] L. Que , J.-S. Park, Y.B. Gianchandani, "Bent-beam electro-thermal actuators for high force applications," Microelectromechanical systems (MEMS), *IEEE International Conference*, pp. 31–36, 1999.

[48] B. R. Donald, K. M. Lynch and D. Rus, (2001), Algorithmic and Computational Robotics: New Directions, A K Peters, Ltd.

[49] J. E. Luntz, W. Messner and H. Choset, "Closed-Loop Operation of Actuator Arrays," Proc. of 2000 IEEE International Conference on Robotics & Automation. pp 3666 – 3672, 2000.

[50] J. E. Luntz, W. C. Messner, H. Choset, " Discrete Actuator Array Vectorfield Design for Distributed Manipulation," *ICRA* 1999: pp. 2235-2241.

[51] K. F. Böhringer, B. Donald, B. Mihailovirch, and N. MacDonald, "A Theory of Manipulation and Control for Microfabricated Actuator Array," *In Proc. IEEE International Conference on Robotics and Automation*, pp. 102-107, 1994.

[52] J. W. Suh, R. B. Darling, K. F. Böhringer, B. R. Donald, H. Baltes, G. T. A. Kovacs, "Fully Programmable MEMS Ciliary Actuator Arrays for Micromanipulation Tasks," *IEEE International Conference on Robotics and Automation (ICRA),* pp. 1101-1108, San Francisco, CA, April 2000.

[53] J. Reiter, M. Terry, K. F. Böhringer, J. W. Suh, Gregory T. A. Kovacs, "Thermo-bimorph Microcilia Arrays for Small Spacecraft Docking," *ASME International Mechanical Engineering Congress and Exposition (IMECE), Micro-electro-mechanical Systems (MEMS),* vol. 2, pp. 57-63, Orlando, FL, November 5-10, 2000.

[54] M.l Gauthier, B. Lopez-Walle, C. Clevy, "Comparison between micro-objects manipulations in dry and liquid mediums," *Proceedings 2005 IEEE International Symposium on Computational Intelligence in Robotics and Automation*,`pp.701-7012 June 27-30, 2005.

[55] Y.B. Gianchandani and K. Najafi, "Bent-Beam Strain Sensors," *IEEE J.* of *Microelectromechanical Systems*, Vol. 5, pp. 52-58, March 1996.

[56] J.N. Israelachvili, (1992), Intermolecular and Surface Forces, 2nd Ed., Academic Press.

[57] F. Arai, D. Andou, T. Fukuda, “Adhesion forces reduction for micro manipulation based on micro physics,” *Proceeding of IEEE, Tech. Dig. Pf MEMS ’96 workshop.* 354-359, 1996.

[58] M. Savia, Q. Zhou, H. N. Koivo, “Simulating adhesion forces between arbitrarily shaped objects in microhano-handling operations,” *Proc. of 2004 IEEE International conference on intelligence robotics and systems*, pp. 1722-1727, 2004.

[59] H. C. Crenshaw, “A new look at locomotion in microorganisms: Rotating and translating,” *Am. Zool.* 36, pp. 608–618. 1996.

[60] J. Henrichsen. “Bacterial Surface Translocation: a Survey and a Classification,” *Bacteriological Reviews*, pp. 478-503. 1972.

[61] I. Brown and C. C. Hase, “Flagellum-Independent Surface Migration of *Virio cholerae* and *Escherichia coli*,” *Journal of Bacteriology*, pp. 3784-3790, 2001.

[62] S. Yao, X. Tang, C. Hsieh, Y. Alyousef, M. Vladimer, G. K. Fedder, C. H. Amon, “Micro-electro-mechanical systems (MEMS)-based micro-scale direct methanol fuel cell development,” *Energy* 31, pp. 636–649, 2006.

[63] B. Behkam and M.Sitti, “Bacterial flagella-based propulsion and on/off motion control of microscale Objects,” *Applied physic letter,* 90, 2007.

[64] J.L. McGrath, N.J. Eungdamrong, C.I. Fisher, F. Peng, L. Mahadevan, T.J. Mitchison, and S.C. Kuo, “The force-velocity relationship for the actin-based motility of *Listeria monocytogenes,” Curr. Biol,*13, pp.329-332. 2003.

[65] D. B. Dusenery, “Minimum size limit for useful locomotion by free-swimming microbes,” *Proc. Natl. Acad. Sci.* Vol. 94, pp. 10949–10954, 1997.

[66] L. Karp-Boss, E. Boss, P. A. Jumars, “Nutrient fluxes to planktonic osmotrophs in the presence of fluid motion.,” *Oceanogr. Mar Biol Annu Rev* 34: pp. 71–107, 1996.

[67] F. Neidhart, J. Ingraham, K. Low, B. Magasanik, M. Schaechter, and H. Umbarger, *Escherichia Coli and Salmonella Typhimurium: Cellular and Molecular Biology*, (American Society for Microbiology, Washington, DC, 1987), p. 732.

[68] D . Kamykowski, R. E. Reed, G. J. Kirkpatrick, “Comparison of sinking velocity, swimming velocity, rotation and path characteristics among six marine dinoflagellate species,” *Marine Biology* 113, pp. 319-28, 1992.

[69] Q. Huang and N. Ka Shek Lee, Analysis and design of polysilicon thermal flexure actuator, J. Micromech. Microeng. 9 (1999) 64–70.

[70] Li. Lin , M. Chiao, Electrothermal responses of lineshape microstructures, Sensors and Actuators A 55 (1996) 35-41.

[71] D. M Brnas, V. M. Bright, Design and performance of a double hot arm polysilicon thermal actuator, Proc. SPIE, vol3224,1997, pp.296-306.

[72] L. P, Slimane C K, Romanowicz B and Renaud P, Modelization and characterization of asymmetrical thermal microacuators *J. Micromech. Microeng.* 6 (1996) 134–137.

[73] L. Lin and M. Chiao Electrothermal responses of lineshape microstructures *Sensors Actuators* A 1996, pp 55 35–41.

[74] Zs. Geretovszky a, L. Kelemen b, K. Piglmayer, Temperature distribution in multilayers covered by liquid layer and processed by focused laser beam, Applied Surface Science 106,1996, pp. 422-428.

[75] N. Mankame and G. Ananthasuresh1, Comprehensive thermal modeling and characterization of an electro-thermal-compliant microactuator, J. Micromech. Microeng. 11, 2001, pp.452–462.

[76] D. Polder and M. Hove, "Theory of radiative heat transfer between closely spaced bodies," *Phys. Rev.* B 4, 1971, pp. 3303–14.

[77] J. Jonsmann, O. Sigmund, and S. Bouwstra, "Compliant electro-thermal microactuators," *Proc. MEMS'99,* 1999, pp 588–593.

[78] C.D. Lott, T.W. McLain, J.N. Harb, L.L. Howell, "Modeling the Thermal Behavior of a Surface-micromachined Linear-displacement Thermomechanical Microactuator," *Sensors and Actuators*, A, vol. 101, (2002), p. 239 .

[79] S. Kiwan, M. A1-Nimr and M.A1-Sharo'a, "Trial solution methods to solve the hyperbolic heat conduction equation," *Int. Comm. Heat Mass Transfer*, Vol. 27, No. 6, pp. 865–876, 2000.

[80] M. Mayyas & P. Shiakolas, "A Study On The Thermal Behavior Of Electrothermal Microactuators Due To Various Voltage Inputs," *Proceedings of IMECE 2006*," Paper No. IMECE2006-15321, Chicago IL, November 2006.

[81] M. Mayyas, P. Zhang, W. H. Lee, P. Shiakolas and D. Popa, "Design Tradeoffs for Electrothermal Microgrippers", *ICRA07*, April 2007, Roma, Italy.

[82] M. Mayyas, W.H. Lee, D.O. Popa, P. Shiakolas, P. Zhang, H. E. Stephanou. "Comprehensive Electrothermal Modeling of a Thermal Microgripper," *TEXMEMS VII International Conference on MEMS*, El Paso, TX, September 2005.

[83] M. Mayyas, Panos Shiakolas and Woo H. Lee, "Thermal Cycle of an In-plane Folded Beam Electrothermal Microactuators: Approximate Solution and Lumped Models", submitted to *journal of heat transfer*.

[84] 3D MEMS profiler, "WYKO NT1100" www.veeco.com .

[85] MATLAB 7.2, The MathWorks Inc, http://www.mathworks.com/.

[86] L. Ljung, *System Identification*, second edition, Prentice Hall, 1998.

[87] AE801 force sensor element specifications available at: http://www.sensorone.com/AE801_Spec.asp

[88] S. Ostergaard, L. Olsson, J. Nielsen, "Metabolic Engineering of Saccharomyces cerevisiae," *Microbiol. Mol. Biol. Rev*. 64: pp. 34-50 . 2000.

[89] C.P. Kurtzman, Molecular taxonomy of the yeasts., Yeast. 10(13):pp. 1727-40. 1994.

[90] F. Yeong, "Severing all ties between mother and daughter: cell separation in budding yeast," *Mol Microbiol* 55 (5), 2005, pp. 1325-31

[91] D. Popa, R. Murthy,A. Das, W. Lee and H. Stephanou, "High Yield Automated MEMS Assembly," *in Proc. of IEEE CASE Conference*, September 2007.

[92] ANSYS Inc. Southpointe. 275 Technology Drive.Canonsburg, PA. 15317. http://www.ansys.com/products/cfx.

[93] G. D. Skidmore, E. Parker, M. Ellis, N. Sarkar, and R. Merkle, " Exponential Assembly," Nanotechnology, 12, 2001, pp. 316-321,

[94] A. Das, P. Zhang; W. Lee, D. Popa, and H. Stephanou "μ3: Multiscale, Deterministic Micro-Nano Assembly System for Construction of On-Wafer Microrobots," *Robotics and Automation, 2007 IEEE International Conference on* 10-14 April, 2007, pp. 461 – 466.

[95] M. B. Cohn, K. F. Böhringer, J. M. Novorolski, A. Singh, C. G. Keller, K. Y. Goldberg, R. T. Howe, "Microassembly Technologies for MEMS," *SPIE Conf. on Micromachining and Microfabrication Process Technology* IV, pp. 2-16, Santa Clara, CA, September 1998.

[96] S. E. Lyshevski, MEMS AND NEMS, Systems, Devices, and Structures, 1st Ed., CRC PRESS, 2002.

[97] M. Carrozza, A. Eisinberg, A. Menciassi, D. Campolo, S. Micera and P. Dario, "Towards a force-controlled microgripper for assembling biomedical microdevices," *J. Micromech. Microeng.* 10 (2000).

[98] M. Marius, Blideran, G. Bertsche, W. Henschel, D. P. Kern, "A mechanically actuated silicon microgripper for handling 3 micro- and nanoparticles," *Microelectronic Engineering* ,2006, pp.1382-1385.

[99] K. Ivanova, T. Ivanov, A. Badar a, B. E. Volland, I. W. Rangelow , D.Andrijasevic, F. Su¨mecz, S. Fischer, M. Spitzbart, Werner B., I. Kostic, "Thermally driven microgripper as a tool for micro assembly," *Microelectronic Engineering*, ,2006, pp.1393-1395

[100] S.S. Sastry, M. Cohn b, F. Tendick, “Milli-robotics for remote, minimally invasive surgery,” *Robotics and Autonomous System*s 21,1997, 305-316.

[101] G. Kerschena, K. Wordenb, A. F. Vakakisc, J. Golinval, “Past, present and future of nonlinear system identification in structural dynamics,” *Mechanical Systems and Signal Processing* 20, 2006, pp. 505–592.

[102] N. Lobontiu, E. Garcia, Mechanics of Microelectromechanical systems, Kluwer Academic Publishers, 2005.

[103] R. Volpe and P. Khosla, “A Theoretical and Experimental Investigation of Explicit Force Control Strategies for Manipulators,” *IEEE Transactions On Automatic Control*, No 11 1997.

[104] R. Volpe and P. Khosla, “Analysis and Experimental Verification of a Fourth Order Plant Model for Manipulator Force Control,” *IEEE Robotics &Automation Magazine*.

[105] AE801 force sensor element specifications available at: http://www.sensorone.com/AE801_Spec.asp

[106] J. K. Luo, A. J. Flewitt, S. M. Spearing, N. A. Fleck, “Comparison of microtweezers based on three lateral thermal actuator configurations,” *J. Micromech. Microeng.* 15 1294–1302, 2005.

[107] C. Shiang Pany and W. Hsu, “An electro-thermally and laterally driven polysilicon microactuator,” *J. Micromech. Microeng.* 7 1997, pp. 7–13.

[108] L. Field, L. Diane, P. Burriesci, P. Robrish, R. Ruby, “Micromachined 1 × 2 optical-fiber switch,” *Sensors and Actuators* A 53 ,1996, pp.311-315.

[109] Material proprieties are available at www.matweb.com.

[110] H. R, Sameoto D, Hubbard T, et al., "Time and frequency response of two-arm micromachined thermal actuators," *J. Micromech. Microeng* 13 (1): 40-46 JAN, 2003.

[111] M. Pai and N.C. Tien, "Low voltage electrothermal vibromotor for silicon optical, bench applications," *Sensors and Actuators*, 83 ,2000, pp.237–243.

[112] D. Popa, B. Kang, J.T. Wen, H.E. Stephanou, G. Skidmore, and A. Geisberger, "Dynamic modeling and input shaping of thermal bimorph MEMS actuators," *ICRA 2003*, pp. 1470–1475.

[113] D. Yan et al., Modeling of two-hot-arm horizontal thermal actuator, *J. Micromech. Microeng*. 13,2003, pp. 312–322.

[114] Patel , et al., 2007, Methods for depositing, releasing and packaging micro-electromechanical devices on wafer substrates, United States Patent 6969635, October 23, 2007.

[115] E. Voltera, E. Zachmanoglou, *Dynamics of Vibrations*. Columbus, Charles E. Merrill Books, Inc., 1965.

[116] S. Lin, S. Lee, B. Chen, "Closed-form solutions for the frequency shift of V-shaped probes scanning an inclined surface," *Applied Surface Science* 252 (2006) 6249–6259.

[117] C. W. Bert, "Relationship Between fundamental natural Frequency and Maximum Static Deflection For Various Linear Vibratory System," *Journal of Sound and Vibration*, 1993 162(3), pp. 547-557.

[118] D. Son, Jong-jin Kim, T. Won Lim, D. Kwon, “Evaluation of fracture properties of silicon by combining resonance frequency and microtensile methods,” *Thin Solid Films* 468 (2004) .pp. 167– 173.

[119] Y. Oh, W. Lee, G. Skidmore, “Design, optimization, and experiment of compliant microgripper,” *Proceedings of IMECE03*, pp. 44013.

[120] W. Lee, B. Kang, Y. Oh , H. Stephanou, A. C. Sanderson, G. Skidmore, and M. Ellis, “Micropeg Manipulation with a Compliant Microgripper,” *Proceedings of the 2003 IEEE International Conference on Robotics & Automation*, Taipei, Taiwan, pp. 3213-3218.

[121] J. Sin, W. Lee, D. Popa, and H. Stephanou, “Assembled Fourier Transform Micro-spectrometer,” *Proc. of SPIE* Vol. 6109, 2006.

[122] D. Popa, H. Stephanou, “Micro and Meso Scale Robotic Assembly”, in *SME Journal of Manufacturing Processes*, vol. 6 No. 1, 2004, 52-71.

[123] PI , web site is available at: http://www.physikinstrumente.com.

[124] Microfabrication laboratory at the University of Texas of Arlington, available at: http://biomems.uta.edu/.

[125] J. Saheb, J. Richard, R. Meingan, M. Sawan, and Y.Savaria, “System Integration of High Voltage Electrostatic MEMS Actuators,” *IEEE-NEWCAS Conference, 2005.* pp.155- 158

[126] E. Sergey, E. Lyshevski, (2002), *MEMS and NEMS: Systems, Devices, and Structures*, first edition, CRC.

[127] N. Maluf, (1999), *An Introduction to Microelectromechanical Systems Engineering*, 2nd_Edition, Artech House on Demand, page 83.

[128] P. B. Koeneman, I. J. Busch-Vishniac, and K. L. Wood, “Feasibility of Micro Power Supplies for MEMS,” *JMEMS*, VOL. 6, NO. 4, 1997, pp. 355-362.

[129] M. Mayyas, (2004), *Wafer Surface Reconstruction and Characterization for Motion Compensation in a Femtosecond Laser Micromachining System* , MS thesis, U. T. Arlington.

[130] L.C. Hsu, V. George, D.O. Popa, W.H. Lee, M. Mayyas, P. Zhang, H. Stephanou, J.C. Chiao. “3D Microassembly Station,” *in Proceedings of TexMEMS VII, El Paso,* Texas, September 2005.

[131] Provided by Zyvex Corporation, website is available at http: //www.zyvex.com/ Products/UMWS_001a.htm.

[132] S. T. Smith and R. M. Seugling, “Sensor and actuator considerations for precision, small machines,” *Precision Engineering*, Volume 30, Issue 3, 2006, pp. 245-264.

[133] Texas Microfactory™ at Automation & Robotics Research Institute, website available at: http://www.arri.uta.edu/facilities.html.

[134] M. McCormick, E. Chowanietz, A. Lees, “Microengineering design and manufacture using the LIGA process,” *Engineering Science and Education Journal*, Volume 3, Issue 6, 994, pp. 255 – 262.

[135] D. Popa, D., H. Byoung, S. Jeongsik, Z. Jie, "Reconfigurable micro-assembly system for photonics applications," *ICRA* Volume 2, Issue , 11-15 2002 pp. 1495 – 1500.

[136] T. Udeshi, , K. Tsui, K., "Assembly sequence planning for automated micro assembly," *ISATP*,19-21, 2005, pp.98 – 105.

[137] G. Skidmore,M. Ellis, A. Geisberger, K. Tsui, K. Tuck, R. Saini,T. Udeshi, M. Nolan, R. Stallcup,J. II Von Her, "Assembly technology across multiple length scales from the micro-scale to the nano-scale," *Micro Electro Mechanical Systems, 2004. 17th IEEE International Conference on. (MEMS)*, 2004, pp.588 – 592.

[138] G.D Skidmore, M. Ellis, E. Parker, N. Sarkar, R. Merkle, "Micro-assembly for top-down nanotechnology," *Micromechatronics and Human Science*, Oct. 2000 pp. 3 – 9

[139] T. A. Mai, R Housh, B Richerzhagen, K. Stay, S. SA, "Fusion of Diamond blade saw with water jet-guided laser technology to yield revolutionary dicing solution," *SEMICON* Europa 2007.

[140] J. A. Plaza, M. J. Lopez, A. Moreno, M. Duch and C. Cané, "Definition of high aspect ratio glass columns," *Sensors and Actuators A: Physical,* Volume 105, Issue 3, 15, 2003, pp. 305-310.

[141] S. Chung, Y. Im, J. Choi and H. Jeong, "Microreplication techniques using soft lithography," *Microelectronic Engineering*, Volume 75, Issue 2, August 2004, Pages 194-200.

[142] C. Yu-Shan, C. Kwan-Shi , R. Johnstone, M. Parameswaran, "Fuse-tethers in MEMS: theory and operation," *Electrical and Computer Engineering, 2005*, page(s): 1517- 1520.

[143] R. C. Cole, R. E. Robertson, A. D. Yarbrough, Method of HF vapor release of microstructures, US patent No. 460738 filed on 1999-12-14.

BIOGRAPHICAL INFORMATION

Mohammad A. Mayyas (1978- current) received the B.S. degree in mechanical engineering from Jordan University of Science and Technology, Irbid, Jordan, in 2001, the M.S.M.E and Ph.D degrees all in mechanical engineering from The University of Texas at Arlington, from 2003-2007. Mr. Mayyas is the recipient of many awards and fellowships: Best undergraduate project award for Mechanical engineering, Jordan-Amman 2000; IEAST scholarship, Germany-Freiburg, 2000; author of second best conference paper in TeXMEMS VII, El Paso 2005; coauthor of the best Symposium Paper Award, Nano- & Micro-Smart Systems Symposium, Adelaide, Australia, 2006; Hashemite University Doctoral Fellowship, 2003-2006; Hermanns Doctoral Fellowship 2004-2007; STEM fellowship from Automation & Robotics Research Institute 2005-2007. Mr. Mayyas biography appeared on Marquis Who's Who in America, 2008.

He is a co-inventor of a provisional U.S patent and author/coauthor of several journal and referreed conference publications. His research interests include synthesis, analysis and control of MEMS; modeling, identification and simulation of coupled field systems; microassembly methodologies; packaging techniques; micro-actuations and manipulation techniques; mechatronics system; micro-robotics systems; algorithms for micro-surfaces reconstruction and reverse engineering; and image processing.